

# **Green route synthesis of metal based nanoparticles and their composites with polymers for industrial applications**



**Thesis submitted in partial fulfilment  
for the award of Degree of**

Doctor of Philosophy

by

**Vartika Srivastava**

**DEPARTMENT OF BASIC SCIENCES & HUMANITIES**

**RAJIV GANDHI INSTITUTE OF PETROLEUM TECHNOLOGY  
JAIS – 229304, India**

**Enrolment No. PC16-001**

**2021**





Department of Basic Sciences & Humanities  
Rajiv Gandhi Institute of Petroleum Technology  
(An Institution of National Importance)

**CERTIFICATE**

It is certified that the work contained in the thesis titled “**Green route synthesis of metal based nanoparticles and their composites with polymers for industrial applications**” by **Vartika Srivastava** has been carried out under my supervision and that this work has not been submitted elsewhere for a degree.

It is further certified that the student has fulfilled all the requirements of Comprehensive, Candidacy and SOTA.

Dr. Abhay Kumar Choubey  
Department of Basic Sciences & Humanities  
Rajiv Gandhi Institute of Petroleum Technology  
Jais – 229304, India





Department of Basic Sciences & Humanities  
Rajiv Gandhi Institute of Petroleum Technology  
(An Institution of National Importance)

**DECLARATION BY THE CANDIDATE**

I, **Vartika Srivastava**, certify that the work embodied in this thesis is my own bonafide work and carried out by me under the supervision of **Dr. Abhay Kumar Choubey** from August 2016 to April 2021, in the **Department of Basic Sciences & Humanities** at Rajiv Gandhi Institute of Petroleum Technology, Jais. The matter embodied in this thesis has not been submitted for the award of any other degree. I declare that I have faithfully acknowledged and given credits to the research workers wherever their works have been cited in my work in this thesis. I further declare that I have not wilfully copied any other's work, paragraphs, text, data, results, etc. reported in journals, books, magazines, reports, dissertations, theses, etc. or available at websites and have not included them in this thesis and have not cited as my own work.

**Date:**

**Vartika Srivastava**

**Place:**





Department of Basic Sciences & Humanities  
Rajiv Gandhi Institute of Petroleum Technology  
(An Institution of National Importance)

**CERTIFICATE BY THE SUPERVISOR**

It is certified that the above statement made by the student is correct to the best of my knowledge.

**Dr. Abhay Kumar Choubey**  
Associate Professor

**Dr. Amritanshu Shukla**  
Head of Department





Department of Basic Sciences & Humanities  
Rajiv Gandhi Institute of Petroleum Technology  
(An Institution of National Importance)

**CERTIFICATE**

It is certified that the work contained in the thesis titled “**Green route synthesis of metal based nanoparticles and their composites with polymers for industrial applications**” by Ms. **Vartika Srivastava** has been carried out under my supervision. It is also certified that she fulfilled the mandatory requirement of TWO quality publications arose out of her thesis work.

It is further certified that the two publications (copies enclosed) of the aforesaid Ms.

Vartika Srivastava have been published in the Journals indexed by –

- (a) **SCI**
- (b) **SCI Extended**
- (c) **SCOPUS**
- (d) **\*Non-indexed journals**
  - 1.4.1.1 (Only in special cases)
  - 1.4.1.2

(\*Please enclosed DPGC resolution in this regard)

**Dr. Abhay Kumar Choubey**  
Associate Professor

**Dr. Atul Sharma**  
Convener, DPGC



## COPYRIGHT TRANSFER CERTIFICATE

**Title of the Thesis: Green route synthesis of metal based nanoparticles and their composites with polymers for industrial applications**

**Name of the Student: Vartika Srivastava**

### COPYRIGHT TRANSFER

The undersigned hereby assigns to the Rajiv Gandhi Institute of Petroleum Technology, Jais all rights under copyright that may exist in and for the above thesis submitted for the award of the “*Doctor of Philosophy*”.

**Date:**

**Place:**

**Vartika Srivastava**

**Note:** However, the author may reproduce or authorize others to reproduce material extracted verbatim from the thesis or derivative of the thesis for author's personal use provided that the source and the Institute's copyright notice are indicated.



**RAJIV GANDHI INSTITUTE OF PETROLEUM TECHNOLOGY, JAIS  
FOR SUBMISSION OF Ph.D. THESIS PERSONAL DETAILS**

Name of Student: **Vartika Srivastava**

Enrolment No.: **PC16-001** Term of Registration: **2016-2017**

Category of Registration: **Full Time**

Fulfilled required Minimum Residence period: **4 Semesters/ 5 Semesters / 6 Semesters**

Supervisor: **Dr. Abhay Kumar Choubey**

Department: **Basic Sciences & Humanities**

Title of Thesis: **Green route synthesis of metal based nanoparticles and their composites with polymers for industrial applications**



## **Acknowledgments**

*First and foremost, I would like to express my deepest and sincere gratitude towards my research supervisor Dr. A.K. Choubey for his constant encouragement and guidance. He has been helping me out and supported me throughout the course of this research work. I also thank him for his trust and patience on me and giving me scientific freedom to explore various research ideas.*

*I thank RGIPT, Jais for providing scholarship and giving necessary infrastructures to carry out my research work.*

*I want to thank all the faculty members of the Department of Basic Sciences and Humanities, RGIPT for their continuous support. I also want to express my gratitude to Dr. Shivanjali Sharma for her inputs in our collaborative research work.*

*I would like to thank various institutes in India such as NBRI Lucknow, IIT-Kanpur, CDRI-Lucknow and MNIT-Jaipur. These institutes allowed me to perform the collaborative work and use their central facilities on payment basis.*

*I am grateful to Dr. Aradhana Mishra, NBRI-Lucknow for allowing me for the collaborative work in her lab, which gave an exposure to newer areas of research that produced research articles in my work.*

*I would like to thank all the current and former members of my lab for creating and maintaining such a friendly environment. Special thank goes to my senior lab mate Dr. Reena.*

*I sincerely thank all my friends and seniors, Arijit, Komal, Dr. Shama Perween, M.K. Jha, Somendra Singh, Praveen Maurya, and Dr. R.R. Ujjwal for making such a stressful journey smooth and memorable one. Each moment that I spent with them is a part of nostalgia. Special thanks to my friend Mukarram for being my constant support through out this journey. I have missed few names also but I thank all of them whom I have interacted, developed a friendship during my RGIPT days. I duly acknowledge each and every non teaching staff at RGIPT for indirectly contributing to my research by saving my time.*

*Most of all, I would like to thank my parents and my family, for believing in my aspirations and always letting me follow my dreams and passion. I thank my sister Ritika for always being there by my side, whatsoever the*

*situation may be. I thank my husband Abhayankar for making me believe in myself and pushing me to get into this Ph.D. programe.*

*My parents are my constant source of power and their faith in me has propelled me to cross all the hurdles swiftly. They deserve all the credits for each success of mine.*

*....Vartika Srivastava*





*Dedicated*  
*to my*  
*Beloved Parents*



## Preface

Nanomaterials are at the sharp end of the booming field of nanotechnology. The distinctive properties of these materials owing to their size make these materials worthier and necessary in many domains of human activity. The dissertation work presented here highlights the application of these materials for environmental remediation, petroleum industry application and for biological application as well. Green synthesis of these materials is beneficial over other conventional methods. Green route aims at executing sustainable process and generating minimum waste. The process involves use of non-toxic precursors and gentle reaction conditions and therefore, is continuously being promoted to be applied in the field of nanotechnology for maintaining environmental sustainability.

The research work carried out is presented in the form of thesis consisting of eight chapters.

Chapter 1 gives an introduction of nanotechnology, nanomaterials, types of nanomaterials, nano-polymer composites, their synthesis and applications.

Chapter 2 explains the synthesis of  $\alpha$ -MnO<sub>2</sub> nanoparticles using the leaf extract of *Ficus retusa* as reducing agent. The synthesized material was used for removal of methyl orange and methyl red dyes by the process of adsorption.

In chapter 3,  $\alpha$ -MnO<sub>2</sub> nanoparticles were embedded into the matrix of polymer membrane prepared using polyvinyl alcohol along with chitosan. This novel membrane was used as photocatalyst for degradation of cationic dyes such as eosin yellow and methylene blue.

Chapter 4 is also an extension of chapter 2 where  $\alpha$ -MnO<sub>2</sub> nanoparticles have been applied for improving the rheological properties of water-based drilling fluid.

Chapter 5 deals with the synthesis of CuO nanoparticles using the leaf extract of *Ficus retusa*. These nanoparticles were used to enhance the adsorptive properties of pure polymer hydrogel beads prepared using chitosan. The modified chitosan beads act as an excellent adsorbent for anionic dyes such as congo red and eriochrome black T.

Chapter 6 describes synthesis of silver nanoparticles using plant extract obtained from *Citrus sinensis*. The obtained nanoparticles were used for degradation of congo red. The silver nanoparticles were also investigated for their antibacterial and antifungal properties.

In Chapter 7, zinc oxide nanoparticles have been synthesized using the leaf extract of *Moringa oleifera*. The ZnO nanoparticles were used as an adsorbent for removal of congo red dye from its aqueous solution. The adsorptive property of ZnO nanoparticles was further improved by doping the material with Cu.

The last chapter i.e., chapter 8 exhibits the conclusions of the research and highlights the major contribution of the work along with the future prospects.





# Table of contents

|   |      |
|---|------|
| Table of contents .....   | i    |
| Table of figures.....   | ix   |
| List of tables .....  | xvii |
| Abbreviations .....   | xxi  |
| Notations.....  | xxv  |
| Chapter 1: Introduction.....  | 29   |
| 1.1    Background.....  | 29   |
| 1.1.1    Carbon based nanostructured materials.....   | 30   |
| 1.1.2    Metal-based nanostructured materials .....   | 30   |
| 1.1.3    Dendrimers .....   | 31   |
| 1.1.4    Nanofibers .....   | 31   |
| 1.1.5    Nanocomposites .....   | 32   |
| 1.2    Chemistry of nanomaterials.....  | 33   |
| 1.3    Metal-based nanomaterials .....  | 34   |
| 1.3.1    Metal/metal oxide nanomaterials .....  | 34   |
| 1.3.2    Metal oxide-nanocomposites.....  | 35   |
| 1.4    Synthesis of nanomaterials/ nanocomposites .....   | 36   |
| 1.4.1    Synthetic techniques of metal-based nanomaterials.....   | 36   |
| 1.4.2    Synthesis of polymer matrix nanocomposites .....   | 45   |
| 1.5    Characterization techniques for analysis of nanomaterials and polymer matrix<br>nanocomposites ..... | 45   |
| 1.5.1    X-ray diffraction analysis .....   | 46   |

|         |  |    |
|---------|--|----|
| 1.5.2   | Scanning electron microscopy .....   | 47 |
| 1.5.3   | Transmission electron microscopy .....   | 47 |
| 1.5.4   | UV-Vis spectroscopy .....  | 48 |
| 1.5.5   | Fourier transform infrared spectroscopy.....   | 49 |
| 1.5.6   | Brunauer-Emmett-Teller surface area analysis.....  | 49 |
| 1.5.7   | Dynamic light scattering analysis .....  | 50 |
| 1.5.8   | Thermogravimetric analysis.....  | 50 |
| 1.6     | Applications of nanomaterials/nanocomposites .....   | 51 |
| 1.6.1   | Application of metal-based nanomaterials/nano-polymer composites for<br>wastewater treatment ..... | 52 |
|         | Water pollution .....  | 52 |
| i.      | Methylene blue.....  | 55 |
| ii.     | Congo red.....   | 56 |
| iii.    | Methyl red.....  | 56 |
| iv.     | Methyl Orange .....  | 57 |
| v.      | Eriochrome Black T .....   | 58 |
| vi.     | Eosin yellow.....  | 58 |
| 1.6.1.1 | Adsorption.....  | 60 |
| 1.6.1.2 | Chemical reduction .....   | 62 |
| 1.6.1.3 | Photocatalysis.....  | 62 |
| 1.6.2   | Application of nanomaterial in development of drilling fluid.....                                  | 63 |
| 1.6.3   | Application of nanomaterials as antimicrobial agent.....   | 64 |
|         | References.....  | 67 |

|  |     |
|--|-----|
| Chapter 2: Study of adsorption of anionic dyes over biofabricated crystalline $\alpha$ -MnO <sub>2</sub> nanoparticles.....  | 79  |
| 2.1 Introduction .....   | 79  |
| 2.2 Novel aspect of the work.....  | 81  |
| 2.3 Materials and method .....   | 82  |
| 2.3.1 Materials .....  | 82  |
| 2.3.2 Synthesis of $\alpha$ -MnO <sub>2</sub> nanoparticles.....   | 82  |
| 2.4 Removal of dyes using $\alpha$ -MnO <sub>2</sub> nanoparticles.....  | 83  |
| 2.5 Results and discussion.....  | 84  |
| 2.5.1 Characterization of $\alpha$ -MnO <sub>2</sub> nanoparticles .....   | 84  |
| 2.5.2 Adsorption studies .....   | 89  |
| 2.5.3 Adsorption kinetics.....   | 92  |
| 2.5.4 Adsorption isotherm .....  | 95  |
| 2.5.5 Adsorption thermodynamics .....  | 101 |
| 2.6 Reusability of adsorbent.....  | 103 |
| 2.7 Conclusions .....  | 104 |
| References .....   | 106 |
| Chapter 3: Novel PVA/Chitosan composite membrane modified using biofabricated $\alpha$ -MnO <sub>2</sub> nanoparticles for photocatalytic degradation of cationic dyes ..... | 115 |
| 3.1 Introduction .....   | 115 |
| 3.2 Materials and method .....   | 118 |
| 3.2.1 Materials .....  | 118 |
| 3.2.2 Fabrication of membrane.....   | 118 |
| 3.2.3 Characterization.....  | 119 |

|   |  |     |
|---|--|-----|
| 3.3   | Photocatalytic activities .....  | 119 |
| 3.4   | Results and discussion .....   | 120 |
| 3.4.1   | Characterization of PVA/CS-MNPs membrane .....   | 120 |
| 3.4.2   | Removal of dyes .....  | 124 |
| 3.4.3   | Mechanism of degradation.....  | 128 |
| 3.4.4   | Effect of pH.....  | 129 |
| 3.4.5   | Effect of concentration of $\alpha$ -MnO <sub>2</sub> nanoparticles within membrane..... | 130 |
| 3.4.6   | Effect of initial dye concentration.....   | 131 |
| 3.4.7   | Kinetics of photocatalytic reaction .....  | 133 |
| 3.5   | Recyclability of catalyst.....   | 135 |
| 3.6   | Comparison of PVA/CS-MNPs membrane with other photocatalysts .....                       | 136 |
| 3.7   | Conclusions.....   | 137 |
|   | References.....  | 139 |
| Chapter 4: Application of manganese dioxide nanoparticles synthesized via green route<br>for improved performance of water-based drilling fluids..... |  |     |
| 4.1   | Introduction.....  | 145 |
| 4.2   | Experimental .....   | 149 |
| 4.2.1   | Drilling fluids preparation.....   | 149 |
| 4.2.2   | Drilling fluids testing before and after hot rolling .....                               | 150 |
| 4.2.3   | Evaluation of rheological parameters .....   | 151 |
| 4.2.4   | Filtration testing .....   | 152 |
| 4.3   | Results and discussion .....   | 153 |
| 4.3.1   | DLS study of water-based drilling fluid .....  | 153 |

|       |  |     |
|-------|--|-----|
| 4.3.2 | Rheological parameters of $\alpha$ -MnO <sub>2</sub> nanoparticles containing mud formulations.....  | 154 |
| 4.3.3 | Low pressure-low temperature filtration .....  | 157 |
| 4.3.4 | High pressure-high temperature fluid loss .....  | 160 |
| 4.3.5 | Effect of concentration of $\alpha$ -MnO <sub>2</sub> nanoparticles on pH and electrical conductivity .....  | 161 |
| 4.4   | Conclusions .....  | 162 |
|       | References .....   | 164 |
|       | Chapter 5: Investigation on enhancement of adsorptive property of pure chitosan beads by immobilization of biofabricated CuO nanoparticles for wastewater treatment..... | 171 |
| 5.1   | Introduction .....   | 171 |
| 5.2   | Materials and method .....   | 173 |
| 5.2.1 | Chemicals used.....  | 173 |
| 5.2.2 | Plant material and extraction .....  | 173 |
| 5.2.3 | Green synthesis of CuO nanoparticles .....   | 174 |
| 5.2.4 | Preparation of CS/CuO nano-beads.....  | 174 |
| 5.2.5 | Material characterization .....  | 175 |
| 5.3   | Adsorption experiments.....  | 175 |
| 5.3.1 | Effect of pH .....   | 177 |
| 5.3.2 | Effect of dyes' initial concentration .....  | 177 |
| 5.3.3 | Effect of dosage concentration .....   | 177 |
| 5.3.4 | Effect of contact time .....   | 177 |
| 5.4   | Results and discussion.....  | 177 |
| 5.4.1 | Characterization of CuO nanoparticles and CS/CuO nano-beads.....   | 177 |

|   |   |     |
|---|---|-----|
| 5.4.2   | Mechanism of adsorption of dyes .....                               | 182 |
| 5.4.3   | Effect of pH.....   | 184 |
| 5.4.4   | Effect of dosage concentration.....                                 | 185 |
| 5.4.5   | Effect of initial dye concentration.....                            | 187 |
| 5.4.6   | Effect of contact time.....   | 189 |
| 5.4.7   | Adsorption isotherm.....  | 190 |
| 5.4.8   | Adsorption kinetics .....   | 195 |
| 5.5   | Conclusions.....  | 198 |
|   | References.....   | 200 |
| Chapter 6: Green synthesis of biogenic silver particles, process parameter optimization and application as photocatalyst in dye degradation.....205 |   |     |
| 6.1   | Introduction.....   | 205 |
| 6.2   | Experimental .....  | 207 |
| 6.2.1   | Materials .....   | 207 |
| 6.2.2   | Synthesis of Ag nanoparticles.....                                  | 207 |
| 6.3   | Stability of Ag nanoparticles at different pH and temperature ..... | 209 |
| 6.4   | Antimicrobial assay of Ag nanoparticles .....                       | 209 |
| 6.4.1   | Antibacterial activity assessment.....                              | 209 |
| 6.4.2   | Antifungal activity evaluation.....                                 | 210 |
| 6.5   | Photocatalysis .....  | 210 |
| 6.6   | Results and discussion .....  | 211 |
| 6.6.1   | Characterization of Ag nanoparticles.....                           | 211 |
| 6.6.2   | Effect of pH on the stability of Ag nanoparticles .....             | 217 |
| 6.6.3   | Stability of nanoparticles at different temperatures .....          | 217 |

|       |  |     |
|-------|--|-----|
| 6.6.4 | Antibacterial assay result.....  | 218 |
| 6.6.5 | Antifungal assay result .....  | 220 |
| 6.6.6 | Mechanism of synthesis of silver nanoparticles using orange peel.....  | 222 |
| 6.6.7 | Photocatalysis .....   | 224 |
| 6.7   | Conclusions .....  | 227 |
|       | References .....   | 229 |
|       | Chapter 7: Kinetic and isothermal study of effect of transition metal doping on adsorptive property of zinc oxide nanoparticles synthesized via green route using <i>Moringa oleifera</i> leaf extract ..... | 235 |
| 7.1   | Introduction .....   | 235 |
| 7.2   | Materials and method .....   | 237 |
| 7.2.1 | Materials .....  | 237 |
| 7.2.2 | Synthesis of plant extract.....  | 237 |
| 7.2.3 | Biosynthesis of pure ZnO nanoparticles and Cu doped ZnO nanoparticles<br>238   |     |
| 7.2.4 | Adsorption experiments.....  | 239 |
| 7.3   | Results and discussion.....  | 240 |
| 7.3.1 | Characterization of biosynthesized ZnO nanoparticles.....  | 240 |
| 7.3.2 | Optimization of adsorption parameters .....  | 246 |
| 7.3.3 | Optimization of pH.....  | 246 |
| 7.3.4 | Optimization of contact time .....   | 247 |
| 7.3.5 | Optimization of adsorbent dose.....  | 247 |
| 7.3.6 | Optimization of congo red dye concentration .....  | 247 |
| 7.3.7 | Kinetic study.....   | 248 |

|   |     |
|---|-----|
| 7.3.8 Isotherm study.....                           | 249 |
| 7.4 Conclusions.....                                | 252 |
| References.....                                     | 254 |
| Chapter 8: Conclusions and future prospective ..... | 257 |
| List of Publications .....                          | 261 |

## Table of figures

|  |    |
|--|----|
| Figure 1.1: Eco-friendly and cost-effective route for the green synthesis of nanoparticles using plants extract.....   | 42 |
| Figure 1.2: Structure of methylene blue.....   | 55 |
| Figure 1.3: Structure of congo red.....  | 56 |
| Figure 1.4: Structure of methyl red.....   | 57 |
| Figure 1.5: Structure of methyl orange.....  | 57 |
| Figure 1.6: Structure of eriochrome black T.....   | 58 |
| Figure 1.7: Structure of eosin yellow.....   | 59 |
| Figure 1.8: Flowchart for synthetic route, characterization and application of metal-based nanoparticles synthesized through green route.....  | 66 |
| <br>   |    |
| Figure 2.1: FESEM images of synthesized MNPs at different temperatures (a) 80°C, (b) 200°C, (c) 400°C, (d) 600°C and (e) 800°C. (f) EDX analysis of $\alpha$ -MnO <sub>2</sub> nanoparticles synthesized at 800°C temperature..... | 85 |
| Figure 2.2: XRD pattern of MNPs synthesized at different temperatures.....   | 86 |
| Figure 2.3: TGA of MNPs synthesized at 800°C.....  | 88 |
| Figure 2.4: FTIR spectra of biofabricated MNPs.....  | 89 |
| Figure 2.5: Adsorption-desorption isotherm of BET surface area analysis of MNPs....  | 89 |
| Figure 2.6: Effect of (a) pH and (b) concentration of MNPs on removal of dyes.....   | 91 |
| Figure 2.7: Time-dependent UV-Visible absorption spectra for the removal of (a) methyl orange and (b) methyl red dye from their aqueous media at room temperature. (c) Removal of dyes at different contact time.....              | 91 |
| Figure 2.8: (a) Pseudo first order and (b) Pseudo second order kinetics for adsorption of dyes over MNPs in linear regression analysis.....  | 93 |

|  |     |
|--|-----|
| Figure 2.9: Representation of kinetic models for adsorption of methyl orange and methyl red dyes over MNPs in non-linear regression analysis. ....   | 94  |
| Figure 2.10: Representation of Langmuir, Freundlich and Temkin isotherm models for MNPs in non-linear regression analysis. ....  | 97  |
| Figure 2.11: (a) Langmuir, (b) Freundlich and (c) Temkin isotherm for adsorption of methyl orange and methyl red dyes over MNPs using linear form of models. ....  | 98  |
| Figure 2.12: Effect of initial concentration of dyes (methyl orange and methyl red) on dye adsorption and percentage of dye removal using 30 mg of adsorbent. ....   | 100 |
| Figure 2.13: Effect of temperature on adsorption of methyl orange and methyl red (a) Equilibrium constant for methyl orange on MNPs as function of temperature, (b) Van't Hoff plot for exchange of methyl orange with MNPs, (c) Equilibrium constant for methyl red on MNPs as function of temperature and (d) Van't Hoff plot for exchange of methyl red with MNPs. .... | 103 |
| Figure 2.14: Recyclability of MNPs in the removal of methyl red and methyl orange dyes. ....   | 104 |
| <br>   |     |
| Figure 3.1: FTIR spectra of membrane of (a) PVA, (b) PVA-CS and (c) PVA-CS/MNPs. ....  | 122 |
| Figure 3.2: Comparison of (a) tensile strength, (b) strain, and (c) toughness of pure PVA, PVA/CS and PVA/CS-MNPs membrane of varying concentrations. ....   | 123 |
| Figure 3.3: Photographs of PVA/CS-MNPs membrane (a) Composite 1, (b) Composite 2 and (c) Composite 3. ....   | 124 |
| Figure 3.4: FESEM images (a) PVA/CS membrane (without MNPs), (b) Composite 1, (c) Composite 2 and (d) Composite 3. ....  | 124 |

|  |     |
|--|-----|
| Figure 3.5: UV-Vis spectra of degradation of eosin yellow and methylene blue dyes at different time interval. ....   | 125 |
| Figure 3.6: Eosin yellow fluorescence spectra (at $\lambda_{ex}$ : 520, 500 and 480 nm) at different time intervals of 0, 30, 60 and 90 min. ....  | 126 |
| Figure 3.7: Methylene blue fluorescence spectra (at $\lambda_{ex}$ : 660, 640 and 620 nm) at different time intervals of 0, 30, 60, 90 and 120 min. ....   | 126 |
| Figure 3.8: Schematic diagram showing the possible charge separation and transfer during photocatalytic degradation of eosin yellow/methylene blue dyes. ....  | 129 |
| Figure 3.9: Percentage of removal of eosin yellow dye on varying its initial concentration. ....   | 132 |
| Figure 3.10: Percentage of removal of methylene blue dye on varying its initial concentration. ....  | 132 |
| Figure 3.11: Pseudo first order kinetics for the degradation of eosin yellow dye using different composites of PVA/CS-MNPs membrane.....   | 134 |
| Figure 3.12: Pseudo first order kinetics for the degradation of methylene blue dye using different composites of PVA/CS-MNPs membrane.....   | 134 |
| Figure 3.13: Percentage degradation of eosin yellow and methylene blue dyes at different cycles. ....  | 136 |
| Figure 4.1: Schematic of hot rolling process.....  | 151 |
| Figure 4.2: Rheological parameters of drilling fluids before and after hot rolling at 100°C temperature for 16 hours (AV = Apparent viscosity, PV = Plastic viscosity, YP = Yield point, GS = Gel strength, GS-0 = Initial GS and GS-10= 10 minutes or final GS). .... | 155 |
| Figure 4.3: Viscosity vs shear stress curves of drilling fluid samples after hot rolling. ....   | 157 |

|   |     |
|---|-----|
| Figure 4.4: Low pressure-low temperature fluid loss of drilling base mud and nanoparticles containing mud formulations before and after hot rolling at 100°C temperature. ....                      | 159 |
| Figure 4.5: FESEM and EDX analysis of filter cake formed by low pressure-low temperature filtration test of base mud (a and b) and mud with 0.10 w/v % of MNPs (c and d). ....                      | 159 |
| Figure 4.6: Filter cake obtained by API filtration test (a) base mud and (b) mud with 0.20 w/v % of MNPs.....   | 160 |
| Figure 4.7: High pressure-high temperature fluid loss of nanoparticles containing mud formulations before and after hot rolling. ....   | 160 |
| Figure 4.8: pH and electrical conductivity of drilling fluids before hot rolling (a and b) and after hot rolling (c and d) at 100°C temperature (both measured at room temperature i.e., 25°C)..... | 161 |
| <br>  |     |
| Figure 5.1: Preparation of CS/CuO nano-beads. ....  | 175 |
| Figure 5.2: (a) XRD of CuO nanoparticles and (b) TGA of of CuO nanoparticles, pure chitosan beads and CS/CuO nano-beads.....  | 180 |
| Figure 5.3: FTIR spectra of pure chitosan beads, CuO nanoparticles and CS/CuO nano-beads. ....  | 181 |
| Figure 5.4: FESEM images of (a) CuO nanoparticles, (b) chitosan beads and (c) CS/CuO nano-beads. EDX of (d) CuO nanoparticles, (e) chitosan beads and (f) CS/CuO nano-beads. ....                   | 181 |
| Figure 5.5: Mechanism of adsorption of (a) congo red and (b) eriochrome black T dyes over CS/CuO nano-beads.....  | 183 |
| Figure 5.6: Effect of initial pH of solution on removal of dyes.....  | 185 |

|   |     |
|---|-----|
| Figure 5.7: Effect of adsorbent dosage on the removal of congo red and eriochrome black T dyes using (a) chitosan beads and (b) CS/CuO nano-beads (for 50 mg L <sup>-1</sup> dyes concentration).....   | 187 |
| Figure 5.8: Effect of initial concentration of dyes (congo red and eriochrome black T) on its removal using (a) CS/CuO nano-beads and (b) chitosan beads. ....  | 188 |
| Figure 5.9: Images showing adsorption of congo red and eriochrome black T dye solutions of varying concentrations over (a) CS/CuO nano-beads and (b) chitosan beads respectively. UV-Vis spectra of removal of (c) congo red and (d) eriochrome black T dye (10 mg L <sup>-1</sup> ) using 1.0 g of adsorbents..... | 190 |
| Figure 5.10: (a) Langmuir, (b) Freundlich and (c) Temkin isotherm for adsorption of congo red and eriochrome black T dye over CS/CuO nano-beads. ....   | 193 |
| Figure 5.11: Representation of Langmuir, Freundlich and Temkin isotherm models for CS/CuO nano-beads in non-linear regression analysis. ....  | 195 |
| Figure 5.12: (a) Pseudo first order kinetics and (b) Pseudo second order kinetics of adsorption of congo red and eriochrome black T dyes over CS/CuO nano-beads.....  | 197 |
| Figure 5.13: Representation of kinetic models for adsorption of congo red and eriochrome black T dyes over CS/CuO nano-beads through non-linear regression analysis. ....   | 198 |
| <br>  |     |
| Figure 6.1: UV-Vis absorption spectra of AgNPs synthesized after 30 minutes in solution (a) without extract, (b) $K_{Ext/Ag} = 0.5$ , (c) $K_{Ext/Ag} = 2.5$ and (d) $K_{Ext/Ag} = 5.0$ .....   | 212 |
| Figure 6.2: UV-Vis absorption spectra of AgNPs synthesized over a period of time (a) [Extract] = 0 ppm, NaBH <sub>4</sub> was used as reducing agent, (b) $K_{Ext/Ag} = 0.5$ , (c) $K_{Ext/Ag} = 2.5$ and (d) $K_{Ext/Ag} = 5.0$ .....  | 213 |
| Figure 6.3: XRD pattern of AgNPs synthesized using $K_{Ext/Ag}$ ratio = 5.0.....  | 214 |

|   |     |
|---|-----|
| Figure 6.4: Hydrodynamic diameter of AgNPs (a) $K_{Ext/Ag} = 0.5$ , (b) $K_{Ext/Ag} = 2.5$ and (c) $K_{Ext/Ag} = 5.0$ .....   | 215 |
| Figure 6.5: SEM images of synthesized AgNPs (a) without extract, (b) $K_{Ext/Ag} = 0.5$ , (c) $K_{Ext/Ag} = 2.5$ and (d) $K_{Ext/Ag} = 5.0$ .....   | 216 |
| Figure 6.6: EDX spectrum of AgNPs (a) $K_{Ext/Ag} = 0.5$ , (b) $K_{Ext/Ag} = 2.5$ and (c) $K_{Ext/Ag} = 5.0$ .....  | 217 |
| Figure 6.7: Hydrodynamic diameter and polydispersity index of AgNPs with changing (a) pH and (b) temperature.....   | 218 |
| Figure 6.8: Antibacterial activity of biogenic AgNPs against (A) <i>P. syringae</i> , and (B) <i>P. aeruginosa</i> (1) peel extract, (2) $K_{Ext/Ag} = 0.5$ , (3) $K_{Ext/Ag} = 2.5$ and (4) $K_{Ext/Ag} = 5.0$ (in both the cases).....                      | 219 |
| Figure 6.9: Images showing mycelial growth of <i>A. brassicicola</i> on PDA medium containing nanoparticles synthesized using (a) $K_{Ext/Ag} = 0$ (peel extract), (b) $K_{Ext/Ag} = 0.5$ , (c) $K_{Ext/Ag} = 2.5$ and (d) $K_{Ext/Ag} = 5.0$ .....           | 221 |
| Figure 6.10: Percentage of inhibition of fungal ( <i>A. brassicicola</i> ) growth using AgNPs having (1) $K_{Ext/Ag} = 0.5$ , (2) $K_{Ext/Ag} = 2.5$ and (3) $K_{Ext/Ag} = 5.0$ . ....  | 221 |
| Figure 6.11: A schematic illustration of the mechanism for formation and stabilization of AgNPs using orange peel (a) Redox reaction showing mechanism of reduction of $Ag^+$ ions to $Ag^0$ by ellagic acid and (b) Capping and stabilization of AgNPs. .... | 224 |
| Figure 6.12: Time dependent UV-Vis spectra for the catalytic degradation of congo red dye using silver nanoparticles (a) in absence and (b) in presence of sunlight. (c) The plot of $\ln A_0/A_t$ versus time for the degradation of congo red. ....         | 227 |
| Figure 7.1: FTIR spectra of pure ZNPs and Cu doped ZNPs. ....   | 240 |
| Figure 7.2: XRD spectra of (a) pure ZNPs and (b) Cu doped ZNPs. ....  | 241 |

|  |     |
|--|-----|
| Figure 7.3: (a and c) FESEM images, (b and d) EDX spectrum of ZNPs and Cu doped ZNPs respectively.....   | 243 |
| Figure 7.4: FTIR spectrum of pure ZNPs and Cu doped ZNPs. ....   | 244 |
| Figure 7.5: TGA curves of (a) pure ZNPs and (b) Cu doped ZNPs. ....  | 245 |
| Figure 7.6: TEM images of (a) pure ZNPs and (b) Cu doped ZNPs.....   | 246 |
| Figure 7.7: Effect of (a) pH, (b) time, (c) adsorbent dose and (d) dye concentration on percent removal of congo red. ....                               | 248 |
| Figure 7.8: (a and b) Pseudo first order and (c and d) Pseudo second order kinetics for adsorption of congo red dye over synthesized nanoparticles. .... | 249 |
| Figure 7.9: (a) Langmuir, (b) Freundlich and (c) Temkin isotherm for adsorption of congo red over ZNPs and Cu doped ZNPs .....                           | 252 |



## List of tables

|  |     |
|--|-----|
| Table 2.1: Kinetic model equations used to study dye adsorption onto MNPs.....   | 93  |
| Table 2.2: Kinetic model parameters calculated using linear regression analysis of methyl orange and methyl red dye adsorption on MNPs .....                             | 94  |
| Table 2.3: Kinetic model parameters calculated using non-linear regression analysis of methyl orange and methyl red dye adsorption on MNPs .....                         | 94  |
| Table 2.4: Equilibrium model equations used to investigate methyl orange and methyl red dye adsorption over MNPs .....   | 97  |
| Table 2.5: Adsorption isotherm models and their coefficients calculated using linear regression analysis for methyl orange and methyl red dye adsorption onto MNPs ..... | 99  |
| Table 2.6: Non-linear regression analysis of adsorption isotherm models for methyl orange and methyl red dye adsorption onto MNPs .....                                  | 99  |
| Table 2.7: Comparison of adsorption capacity of methyl orange dye with other reported adsorbents .....   | 100 |
| Table 2.8: Comparison of adsorption capacity of methyl red dye with other reported adsorbents .....  | 101 |
| Table 2.9: Thermodynamic parameters for adsorption of methyl orange and methyl red dye on MNPs at pH 2 .....   | 102 |
| <br>   |     |
| Table 3.1: Amount of nanoparticles in the studied PVA/CS-MNPs membrane with corresponding designations .....   | 119 |
| Table 3.2: ESI-MS of dye solutions before and after the removal of dyes .....  | 128 |
| Table 3.3: Effect of pH on photocatalytic degradation of dyes.....   | 130 |
| Table 3.4: Rate constant for photodegradation of eosin yellow and methylene blue dyes using varying composition of membrane and initial concentration of dyes.....       | 135 |

|   |     |
|---|-----|
| Table 3.5: Photocatalytic degradation of methylene blue dye using different photocatalysts.....   | 137 |
| Table 3.6: Photocatalytic degradation of eosin yellow dye using different photocatalysts .....  | 137 |
| Table 4.1: Concentration of nanoparticles in the studied drilling fluids with corresponding codes.....  | 150 |
| Table 4.2: Zeta potential (at room temperature) of xanthun gum (0.05 w/v %), MNPs (0.05 w/v %), and a combination of xanthan gum (0.05 w/v %) and MNPs (0.05 w/v %); each dispersed in deionized water..... | 154 |
| Table 5.1: BET analysis of pure chitosan beads and CS/CuO nano-beads .....  | 182 |
| Table 5.2: Comparison of percentage of dye removal over varying concentration of adsorbents .....   | 186 |
| Table 5.3: Comparison of percentage of dye removal on varying the initial concentration of dyes.....  | 189 |
| Table 5.4: Linear regression analysis of adsorption isothermal models for congo red and eriochrome black T dye adsorption over CS/CuO nano-beads.....   | 194 |
| Table 5.5: Interpretation of adsorption isotherm models using non-linear regression analysis for congo red and eriochrome black T dye adsorption over CS/CuO nano-beads .....                               | 194 |
| Table 5.6: Kinetic models parameter study of congo red and eriochrome black T dyes on CS/CuO nano-beads using linear regression analysis.....   | 197 |

|   |     |
|---|-----|
| Table 5.7: Kinetic models parameter study of congo red and eriochrome black T dyes adsorption on CS/CuO nano-beads using non-linear regression analysis ..... | 198 |
| Table 6.1: Composition of sample solutions .....  | 208 |
| Table 6.2: Effect of different concentrations of peel extract on Z-average and zeta potential of AgNPs .....  | 215 |
| Table 6.3: Zone of inhibition (Mean± SD) exhibited by AgNPs against gram negative bacteria ( <i>P. syringae</i> and <i>P. aeruginosa</i> ) .....              | 220 |
| Table 6.4: Fungal growth (colony diameter, mm) in presence of AgNPs synthesized using variable $K_{Ext/Ag}$ .....   | 222 |
| Table 7.1: Kinetic models parameter study of congo red dye adsorption on undoped and Cu doped ZNPs .....  | 249 |
| Table 7.2: Various adsorptions isothermal models for congo red dye adsorption interpreted by correlation coefficients and adsorption parameters.....          | 252 |



## Abbreviations

|       |   |   |
|-------|---|---|
| Φ300  | : | Dial reading from a viscometer at 300 rpm   |
| Φ600  | : | Dial reading from a viscometer at 600 rpm   |
| AHR   | : | After hot rolling                           |
| API   | : | American Petroleum Institute                |
| AV    | : | Apparent viscosity                          |
| BET   | : | Brunauer-Emmett-Teller                      |
| BHR   | : | Before hot rolling                          |
| BJH   | : | Barrett–Joyner–Halenda                      |
| BM    | : | Base mud                                    |
| Bt    | : | Bentonite powder                            |
| Cal.  | : | Calculated                                  |
| CB    | : | Conduction band                             |
| CMNC  | : | Ceramic matrix nanocomposite                |
| CR    | : | Congo red                                   |
| CS    | : | Chitosan                                    |
| DLS   | : | Dynamic light scattering analysis           |
| EBT   | : | Eriochrome black T                          |
| EDX   | : | Energy dispersive x-ray                     |
| EY    | : | Eosin yellow                                |
| FESEM | : | Field emission scanning electron microscopy |
| FL    | : | Fluid loss                                  |
| FTIR  | : | Fourier transform infrared spectroscopy     |
| FWHM  | : | Full width half maxima                      |

|       |   |   |
|-------|---|---|
| GS-0. | : | Gel strength after 10 s                           |
| GS-10 | : | Gel strength after 10 min.                        |
| HPHT  | : | High pressure-high temperature                    |
| IUPAC | : | International Union of Pure and Applied Chemistry |
| JCPDS | : | Joint Committee for Powder Diffraction Standards  |
| LPLT  | : | Low pressure-low temperature                      |
| MB    | : | Methylene blue                                    |
| MR    | : | Methyl red  |
| MMNC  | : | Metal matrix nanocomposite                        |
| MNPs  | : | $\alpha$ -MnO <sub>2</sub> nanoparticles          |
| MO    | : | Methyl orange                                     |
| NPs   | : | Nanoparticles                                     |
| PAC   | : | Polyanionic cellulose                             |
| PDA   | : | Potato dextrose agar                              |
| PDI   | : | Poly dispersity index                             |
| PHBS  | : | Pre-hydrated Bentonite Slurry                     |
| PMNC  | : | Polymer matrix nanocomposite                      |
| PV    | : | Plastic viscosity                                 |

|        |   |                                  |
|--------|---|----------------------------------|
| PVA    | : | Polyvinyl alcohol                |
| RMSE   | : | Root mean square error           |
| SEM    | : | Scanning electron microscopy     |
| SPR    | : | Surface plasmon resonance        |
| TEM    | : | Transmission electron microscopy |
| TGA    | : | Thermogravimetric analysis       |
| Theo.  | : | Theoretical                      |
| UV-Vis | : | Ultraviolet-Visible spectroscopy |
| VB     | : | Valence band                     |
| XRD    | : | X-Ray diffraction                |
| YP     | : | Yield point                      |
| ZNPs   | : | Zinc oxide nanoparticles         |



## Notations

|                                      |   |                              |
|--------------------------------------|---|------------------------------|
| eV                                   | : | Electron volt                |
| m <sup>2</sup> /g                    | : | square meter per gram        |
| nm                                   | : | nanometer                    |
| Hz                                   | : | Hertz                        |
| Å                                    | : | Angstrom                     |
| cm                                   | : | centimetre                   |
| KJ                                   | : | kilo Joule                   |
| KV                                   | : | kilo Volt                    |
| cP                                   | : | centipoise                   |
| lbs/100 ft <sup>2</sup>              | : | pounds per 100 square feet   |
| mV                                   | : | Millivolt                    |
| rpm                                  | : | rotations per min.           |
| v/v                                  | : | volume per unit volume       |
| w/v                                  | : | weight per unit volume       |
| µm                                   | : | micrometre                   |
| g                                    | : | gram                         |
| h                                    | : | hour                         |
| M                                    | : | mole                         |
| mM                                   | : | millimole                    |
| Wt %                                 | : | weight percent               |
| kJ/m <sup>3</sup>                    | : | kilo Joule per metre cube    |
| g mg <sup>-1</sup> min <sup>-1</sup> | : | gram per milli gram per min. |
| J mol <sup>-1</sup> K <sup>-1</sup>  | : | Joule per mole per Kelvin    |
| m/z                                  | : | mass to charge ratio         |

|              |   |                              |
|--------------|---|------------------------------|
| $\theta$     | : | Braggs' angle                |
| $\nu$        | : | frequency                    |
| KHz          | : | Kilo Hertz                   |
| min.         | : | minute                       |
| $L g^{-1}$   | : | litre per gram               |
| $L mg^{-1}$  | : | litre per milligram          |
| M            | : | molar                        |
| $mg L^{-1}$  | : | milligram per litre          |
| cps/ev       | : | centipoise per electron volt |
| $mg L^{-1}$  | : | milligram per litre          |
| ppm          | : | parts per million            |
| $^{\circ}C$  | : | degree centigrade            |
| $\mu L$      | : | microlitre                   |
| $\mu m$      | : | micrometre                   |
| a.u.         | : | Atomic unit                  |
| $kJ/m^3$     | : | kilo Joule per metre cube    |
| MPa          | : | Mega pascal                  |
| $mg g^{-1}$  | : | milli gram per gram          |
| $cm^3/g$     | : | centimetre cube per gram     |
| $g mol^{-1}$ | : | gram per mole                |





# Chapter 1: Introduction

---

## 1.1 Background

Nanotechnology constitutes a dynamic area of research and development which has expanded its application in various domains of technology as well as techno-economic sector. Nanoparticles (NPs) and nanostructured materials possess regulatable morphological features like shape, size, surface area and physiochemical properties such as conductivity, melting point, wettability, catalytic property, light absorption, which enables them to perform better as compared to their bulk counterparts. Like micrometer, picometer etc., nanometer is also an international system of units, which changes the value of macroscopic unit by orders of magnitude. In fundamental, nanomaterials are a term used for the particles in dispersed/agglomerated state having external dimension in the size range of 1-1000 nm [Balzani, 2005; Zhu et al., 2011]. The dimensions of these nanomaterials are very small as compared to the characteristic length of scale which imparts them certain peculiar physical properties based on quantum phenomenon [Love et al., 2005; Whitesides, 2005].

The progress of research in the area of nanomaterials is considered as one of the most demanded and versatile fields of research in physics, chemistry, biology and various areas of engineering [Edelstein and Cammaratra, 1998]. The reduction in the size of conventional materials in the range of nanoscale permits the amendment of properties and the materials in the nano range exhibits specific optical, mechanical and electrical properties.

Owing to its regulatory properties, nanomaterials are now being used for various purposes as catalyst, photocatalyst, drug carrier, antimicrobial substance, energy

storage material, phase change material, filler and adsorbent [Farre et al., 2009; Yoshimatsu et al., 2008]. These materials can also be used to design certain novel materials using the existing ones with the objective of improving its performance. In the recent time, nanomaterials have been widely used to counter various environmental challenges including wastewater treatment, energy production, sensing of pollutants, etc. [Perreault et al., 2015].

Over the last two decades, global efforts are being carried out on exploring theoretical as well as experimental concept of synthesis, characterization, growth and application of these nanomaterials and their composite in multidisciplinary field.

Nanomaterials can be classified into different groups which are as follows:

#### **1.1.1 Carbon based nanostructured materials**

As the name suggests, these nanomaterials are mainly comprised of carbon in the form of tubes, ellipsoids or hollow sphere. Carbon nanomaterials in the shape of sphere and ellipsoid are called as fullerenes, while cylindrical nanomaterials are referred to as nanotubes. These particles have found their application in different fields such as electronics, energy applications and biological applications and also as sensors [Choudhary et al., 2014].

#### **1.1.2 Metal-based nanostructured materials**

The metal-based nanomaterials consists of quantum dots (QDs), metallic nanomaterials (nano gold, nano silver, etc.) and metal oxides such as titanium oxide, zinc oxide, etc.

A quantum dot may be defined as a semiconductor crystal having a closed pack structure and size in the range of 1-100 nm. The change in the size of quantum dots modifies their optical and electrical properties. QDs are constituted of elements lying in the range of group III-V, II-VI or IV-VI of the periodic table of the elements. These

materials possess magnificent fluorescence properties, which enable them to be used as nano sensors and biosensors. These QDs may also be used as an active component in nanostructured complexes [Bakirhan and Ozkan, 2019; Jha, 2018].

In the recent times, metal nanoparticles have gained tremendous attention due to their unusual properties owing to its nano size and higher density of the surface of its edges [Fernández-García et al., 2004]. Metallic nanoparticles possess physiochemical properties, higher stability and reactivity, which makes them potent carrier for performing different activities. These nanomaterials can be synthesized in numerous ways, which modify its morphology as well as incorporate functional groups into its structure that permits them to conjugate with ligands of drugs and antibodies and thus makes it a potential to be used in the areas of biotechnology, drug delivery, magnetic separation and also for diagnostic imaging. Metal oxide nanomaterials have attracted a great deal of attention because of their large applications in various fields like catalysis, sensors and environmental remediation like adsorption and degradation of various contaminants from aqueous media [Oskam, 2006].

### **1.1.3 Dendrimers**

The branched element of polymers in the nanosize is referred to as dendrimers. The surface of dendrimers terminates into innumerable chains, which is altered to be used for different purposes such as catalysis. The three-dimensional structure of dendrimers assists formation of cavities in its interior that can be used to hold the molecules of drugs and then release it at the desired location. In this way, dendrimers are efficiently being used for drug delivery as well.

### **1.1.4 Nanofibers**

Nanofibers are termed as one-dimensional nanomaterials, which include nanotubes, nanorods, nanofibers and nanowires. These nanofibers have wide range of distinctive

applications in various devices related to electronics, chemical sensors, photonics, drug carrier, hydrogen storage, batteries, etc. [Zhao et al., 2011; Li et al., 2011; Mahapatra et al., 2011]. The presence of electronic states of defined density within in small size of nano range is responsible for the variation in the optical, magnetic and electric properties of these one dimensional nano fibers from their bulk phase. Nanofibres also have the ability to be used as an insulator, a semiconductor and even as a conductor [Singh and Ali, 2010]. Lot of research has been conducted on methods of synthesizing metal oxide nanowires possessing novel properties [Shen et al., 2009; Li et al., 2010; Comini et al., 2009].

### **1.1.5 Nanocomposites**

Nanocomposites are those materials, which possess more than one phase and one of its phase scales in the nano range from 1-100 nm. Based on dispersed phase and dispersed matrix used, nanocomposites can be broadly classified as below.

- **Ceramic matrix nanocomposites**
- **Metal matrix nanocomposites**
- **Polymer matrix nanocomposites**

#### **1.1.5.1 Ceramic matrix nanocomposites (CMNCs)**

Ceramic matrix nanocomposites (CMNCs) are referred to as the materials which are composed of one or more distinct ceramic phase in addition to any other nano component. The addition of ceramic adds to the wear resistance and stability of material at high temperature and harmful chemicals but at the same time it also reduces the brittleness and toughness of material, which restricts its application in industries. Example of CMCs is incorporation of materials such as fibers or platelets into the ceramic matrix to reduce its brittleness and its durability against fracture.

### **1.1.5.2 Metal matrix nanocomposites (MMNCs)**

Metal matrix nanocomposites (MMNCs) are also a multiphase material in which one of the phases is made from a metal or alloy and some nanomaterial is implanted into its matrix as a reinforcement material. MMNCs possess high ductility, tensile strength, toughness young modulus and therefore, it is very fondly used in industries such as aerospace and automobile industry.

Although MMNCs have their advantages but certain demerits are also associated with them which includes their high production cost, high porosity with low wear resistance and weak bonding.

### **1.1.5.3 Polymer matrix nanocomposites (PMNCs)**

Polymer matrix nanocomposites consist of a matrix of a polymer or a copolymer having nanofillers dispersed in it. Nanofillers are mainly of three types (a) 1D nanofillers, which are basically nanomaterials having linear structure like nanotubes, (b) 2D nanofillers designated to layered nanosized particles viz. montmorillonite, and (c) 3D nanofillers, which are distinctly powdered nanomaterials like silver nanoparticles. The interactive forces operating between the nanofillers and polymer matrix at molecular level induce certain alterations in the properties of polymer.

The prominent characteristics of PMNCs are enhanced mechanical properties, low gas permeability, high abrasion resistance and thermal stability.

Among all the nanocomposites mentioned above, the most distinguished section of research in the recent times is PMNCs. PMNCs have several unique properties such as variations in dimensions, ability to form films, and activated functionalities [Lofrano et al., 2016; Jordan et al., 2005].

## **1.2 Chemistry of nanomaterials**

Chemistry operates within materials at any scale. Nano-chemistry deals with

chemistry of materials at the atomic level. There are two important outlooks of nano-chemistry. The first one is related with understanding of chemical properties of particles at atomic level. The second one is about utilizing this understanding for the synthesis, growth, alteration and stability of each nanoparticle along with the determination of the mechanism of formation of complex nanostructures. Moreover, the changes in the properties of materials on reducing its size to nano scale is a dynamic feature of nanoparticles. The change in the properties of material with size can be validated by several examples. It has been reported that an inert material gold loses its inertness and acts as a chemical catalyst at nano scale [Thompson et al., 2007]. The variation in properties of nanomaterials from its bulk phase has been shown by exhibiting Cu nanowires as fully transparent conductive electrodes which are opaque in bulk form [Guo et al., 2013].

### **1.3 Metal-based nanomaterials**

#### **1.3.1 Metal/metal oxide nanomaterials**

Recently, metal /metal oxide nanoparticles are considered to be the most important field which has gained attention of lot of researchers owing to its distinct structure, morphology and chemistry. Metal elements form several types of oxides, which acquire different geometries and behave typically like a metallic semiconductor or insulator. The properties of metal oxides such as optical, magnetic, electrical, electrochemical, mechanical, catalytic, etc. alters on reducing the size of material to nano range [Vayssieres, 2004]. The reduction of size of metal oxides leads to nano scale enhancement of properties as compared to bulk material or may even give rise to novel properties.

Metal-based nanomaterials are used as adsorbents for removal of dyes from industrial wastewater. These adsorbents are highly efficient and low cost material that are widely

used for the removal of dyes from the wastewater. Among the metal oxide nanoparticles, zinc oxide, magnesium oxide and copper oxide have been studied in detail and are found to be very promising to be used as adsorbent for removal of dyes from their aqueous solutions. These metal oxide nano-adsorbents are found to be way more effective as compared to conventional adsorbents owing to its higher surface to volume ratio. High surface to volume ratio strengthens the interaction between the adsorbate and adsorbent. The surface chemistry of nano adsorbent is influenced by the pH of the solutions. The use of metal oxide nanoparticles as adsorbents offer several advantages like less toxicity, higher chemical stability and surface area, easier synthesis routes over the conventional ones. These properties of metal oxide nanomaterials compel the researchers to prioritize them over conventional ones [**Kumar and Chawla, 2014; Rajput et al., 2016**].

### **1.3.2 Metal oxide-nanocomposites**

Other than metal/metal oxides being used for wastewater treatment, researchers are also focusing on utilizing hydrogel biopolymer for treating industrial wastewater. Wastewater treatment can also be carried out by using hydrogels owing to its properties such as higher ability to expand, low interfacial tension, hydrophilic nature, selective permeability, and adsorptive property [**Alvarez-Lorenzo and Concheiro, 2002; Şen and Avci, 2005; Roy et al., 2010a,b**]. Although metal/metal oxide has several advantages to be used effectively for water treatment, but it also has certain disadvantages such as tendency to agglomerate, which makes it unsuitable for dispersion and reduces its adsorptive property. These issues can be overcome by using metal oxide nanoparticles as fillers in hydrogel nano polymers to achieve better adsorption properties [**Aghajani et al., 2017**]. The use of metal-based NPs in the matrix of polymer assists the enhancement of stability and hydrophilic property of hydrogels [**Banerjee et al., 2017**;

**He et al., 2011]**.

## **1.4 Synthesis of nanomaterials/ nanocomposites**

### **1.4.1 Synthetic techniques of metal-based nanomaterials**

Metal-based nanoparticles can be synthesized using several techniques reported by several researchers over the past decades. The challenging aspect of synthesis is controlling the shape, size, and morphology of materials. There are several methods available for synthesis of nanomaterials, which are based on either of the two approaches: (i) Top-down approach, and (ii) Bottom-up approach.

Top-down approach is applied in techniques such as lithographic techniques (involving UV, optical field, scanning method, use of electron, ion or laser beam) and mechanical techniques (like grinding) to produce nanoparticles of desired shape and size using the bulk material. Although top down approach has certain advantages but it also possess few limitations which includes difficulty in synthesizing smallest possible structure. Moreover, it is also challenging to maintain the uniformity and quality of nanomaterials using this method [**Dick, 2008**].

On the contrary, “Bottom up” approach utilizes the chemical properties of molecules and enables the atoms to aggregate and form larger structure. Bottom up approach is used for the crystallization of material from its liquid solution or vapor source which leads to synthesis of uniform nano size material. The most common methods which utilizes this approach are chemical synthesis involving biofabricated synthesis, self-assembly, laser induced assembly, film deposition.

Although nanoparticles can be synthesized using either of the approaches but synthesis of nanomaterials through bottom up approach is not only cost effective but also have absolute precision and minimum energy requirement as compared to top down approach [**Chaudhuri and Paria, 2012**]. The process of synthesis of metal-based nanomaterials

can be broadly classified into two sections i.e., physical and chemical methods.

#### **1.4.1.1 Physical method**

Physical methods are referred to those processes which utilizes high energy treatment for producing nanomaterials in the solid or gas phase. The types of physical methods involves sputtering, vapor deposition, laser ablation, electro deposition etc.

#### **1.4.1.2 Chemical method**

Chemical method promotes synthesis of nanomaterials from the basic level i.e., atom by atom to cluster by cluster. Chemical synthesis method can be bifurcated under two heads i.e., thermodynamic approach or kinetic approach. Thermodynamic approach directs the synthesis process in three steps (i) formation of saturated solution, (ii) nucleation, and (iii) growth. While kinetically, nanoparticles are generated by either carrying out the process within limited boundary or limited amount of precursor. Chemical methods are more beneficial over physical methods as it allows the synthesis of nanoparticles of desired shape, size and morphology. There are several chemical methods which are being applied for synthesis of nanoparticles which includes precipitation method, hydrothermal, reflux etc.

##### **i. Hydrothermal Method**

Hydrothermal method is used in case of heterogeneous phase reactions in which the process is carried out in presence of aqueous solvents in the condition of high temperature and pressure. The objective of reaction is the direct crystallization of metal oxide from its solution. The hydrothermal synthesis of metal oxide is carried out at temperature below 300°C because of the fact that the maximum value of ionic product of water is in the temperature range of 250-300°C. The major benefit of using hydrothermal method over other methods is this method is efficient for synthesizing metal oxides in all shape, size, phase and form [Byrappa and Adschiri, 2007]. Moreover, metal oxide powder

synthesized through this method are in their purest form having narrow size distribution [Panda et al., 2006].

### **ii. Precipitation Method**

Precipitation method is also used for synthesizing metal oxide nanomaterials. The advantages of this method include energy consuming process and a very low cost nature. In this method, pH adjustment is done to precipitate solid material from its solution. A supersaturated solution is used for precipitation of particles through homogenous or heterogeneous nucleation and then growth occurs through diffusion or Ostwald ripening. The kinetics of reaction control the particle size distribution along with the morphology of nanomaterials. The parameters, which play a vital role in the precipitation method, are concentration of reactants, pH of solution, reaction temperature, and order of mixing the reactants [Rao and Mullar, 2005].

### **iii. Reflux Method**

Reflux method is a technique in which reaction is carried out at lower temperature condition as compared to the hydrothermal synthesis. This method is used when the boiling point of solvent is low to prevent any loss. The temperature of the refluxing depends on the temperature at which dissolution of starting material occurs. This technique can be applied in sol-gel, precipitation, or any other method.

Although both physical and chemical methods are used extensively for synthesis of nanomaterials but there are certain major drawbacks associated with these methods. The physical method needs consumption of higher amount of energy for its execution which makes the process costly. In addition to this, the yield of production is also very low that makes it even more overpriced [Shedbalkar et al., 2014]. Although chemical method is advantageous in terms of energy requirement as the reduction step requires very less energy and leads to generation of nanoparticles with narrow particle size distribution

[Albanese et al., 2012]. But the significant drawback associated with this method is that it is hazardous for the environment as harmful and toxic chemicals used in this method possess serious threats to nature, and are responsible for carcinogenicity and cytotoxicity. The use of chemical methods is not only hazardous for environment but also responsible for generating several health issues. The use of perilous chemicals (hydrazine or potassium bitartrate) leads to carcinogenicity, genotoxicity, and cytotoxicity [Nath and Banerjee, 2013; Kharisov et al., 2016]. Because of the health and environmental hazards posed by the chemicals, chemical method is restricted in its utilization. In addition to this, other drawbacks associated with using physical and chemical methods are expensive set up, requirement of skilled operators, instability of nanomaterial and regeneration of materials synthesized. Therefore, it is the need of hour to develop a method, which is not only cost effective and energy saving but also proves to be biocompatible and generates nanoparticles of varying shape, size and morphology [Kulkarni and Muddapur, 2014].

#### **1.4.1.3 Green synthesis of nanomaterial**

Keeping the practical situation into consideration, it is necessary to synthesize improved nanomaterials, which can meet the issues mentioned above. With the objective of satisfying the limitations, researchers have now shifted their focus from conventional methods of synthesis to synthesis of nanomaterials via green route. Biofabrication of nanomaterials is gaining a lot of importance in the current scenario. Basically, biological method is a regulated, controlled, hassle free process, which boosts the eco-friendliness of this method. Green route of synthesis hinders the generation of toxic/unwanted by-products through setting up a sustainable and eco-friendly procedure that promotes usage of non-toxic solvent and renewable feedstock. The selection of an ideal solvent system and precursor is necessary to achieve the target. Green synthesis of nanomaterials can be mediated through several biological materials (e.g., microorganisms and plant

extract). The product obtained through this green route synthesis is referred to as biogenic nanoparticles. The methodologies used in this approach are dependent on several parameters which may be temperature, pressure, solvent, and pH of the system. For the preparation of metal-based nanoparticles (metal/metal oxide), the use of plant extract is prioritized over microorganisms. It is so because of the diversity of plant kingdom, which provides infinite number of phytochemicals present in their extract. Phytochemicals such as ketones, aldehydes, amides, flavonoids, terpenoids, steroids, phenols, carboxylic acid including ascorbic acid are found in different part of the plants. These phytochemicals are extracted from the plants and are used as precursor for synthesis of nanomaterials. Therefore, it can be concluded that, biogenic synthesis of nanomaterial is the most convenient method for preparation of metal-based nanoparticles. The method is not only environment friendly but is also uneconomical, and energy saving. The key points, which are considered for synthesis of nanoparticles, are selection of eco-friendly solvent, an efficient reducing agent and a non-toxic stabilizing agent.

The biomediated synthesis of nanomaterials is evolving as a favorable technique over conventional methods of synthesis [**Singh et al., 2016**]. The biological synthesis route is gaining much importance because of its ability to synthesize materials in nano size with minimum energy consumption, low cost and ease of scaling up to higher level [**Dhuper et al., 2012**]. Biological synthesis can be accomplished using various natural sources (such as algae, bacteria, fungi, yeast, plant extract and waste materials) as precursor for fabrication of nanomaterials having widespread application [**Shivaji et al., 2011; Stephen and Macnaughtont, 1999; Chan and Mat Don, 2013; Syed et al., 2013; K et al., 2011; Akhtar et al., 2013; Kanchi et al., 2014**]. The biological molecules coat the surface of nanoparticles enabling them biocompatibility over NPs

synthesized using other methods [Hakim et al., 2005; Mukherjee et al., 2001; Tripp et al., 2002]. Biogenic approach of nanoparticle synthesis helps in modulating the size and morphology of nanomaterials [Riddin et al., 2010; Schröfel et al., 2014]. For example, fungal biomass was used to prepare Ag nanoparticles. The size of Ag nanoparticles was in the range of 20-30 nm. The growth of the biomass on the surface of which nanoparticles were growing continued to grow, which proves that nanoparticles were non-toxic in nature [Mukherjee et al., 2001].

Besides microorganisms, extract prepared using plant (leaf, stem, seeds, flower, peel, latex, etc.) are also used effectively as a reducing and stabilizing agent for synthesis of nanomaterials. In the biosynthesis of nanostructured materials, the concept of energy saving “Green chemistry” has been used with the objective of developing eco-friendly nanoparticles, and is referred to as “Green synthesis” [Pal et al., 2019]. The use of microorganisms and plants is the premier substitute for generation of nanoparticles with desirable properties. Plants can be termed as chemical factories provided by nature which are available free of cost with negligible maintenance required. On the other hand, preservation of microbial culture is a complex process [Hulkoti and Taranath, 2014]. Therefore, it can be concluded that the use of plant extract for synthesis of nanoparticles is advantageous over microorganisms. Moreover, the kinetics of plant assisted synthesis route is much higher than other biosynthetic techniques. Different part of plants viz. stem, root, leaf, peel and fruit have been reported to be used for green synthesis of nanoparticles because of the wide range of phytochemicals present in each part of the plants [Iravani, 2011]. Extract prepared using the leaves of *Jasminum sambac* was applied for the synthesis of Ag, Au, and Ag-Au alloy nanoparticles [Yallappa et al., 2015]. Similarly, the synthesis of Au nanoparticles having triangular, spherical and hexagonal shape using olive leaf extract at a temperature higher than the chemical

method has also been reported [Khalil et al., 2012]. Iron-polyphenol (Fe-P) nanoparticles were also reported to be synthesized using the phytochemical present in the leaves of *Eucalyptus tereticornis*, *Melaleuca nesophila* and *Rosemarinus officinalis* [Wang et al., 2014]. The polyphenol present in the leaves of these plants reacted with the ferric chloride solution to form ferric-polyphenol nanoparticles of varying shapes. Several metal-based nanoparticles such as gold, silver, platinum, titanium, zinc, iron, etc. have been synthesized effortlessly using green approach [Singh et al., 2018].

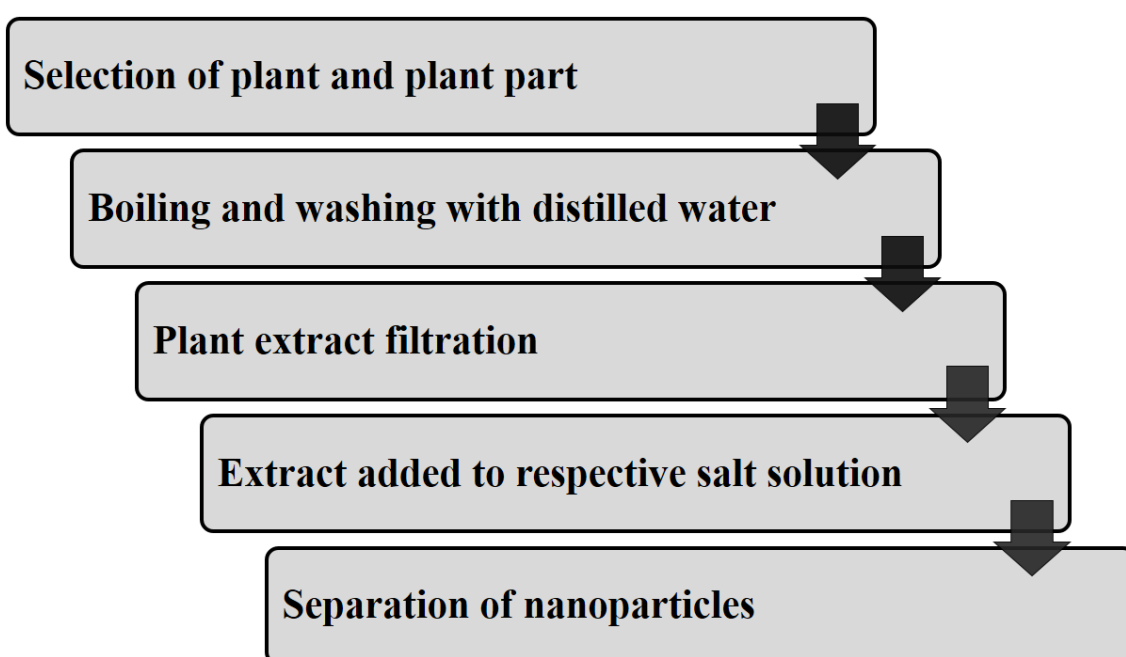


**Figure 1.1: Eco-friendly and cost-effective route for the green synthesis of nanoparticles using plants extract.**

Following nanoparticles have been synthesized in this study and applied in different fields:

**i. Ag nanoparticles**

The prime necessity for synthesis of Ag nanoparticles is a solution of silver metal ions and a reducing agent. The most harmless and cost-effective reducing agent, which can be utilized in as a reducing agent, is a mixture of biomolecules such as polysaccharides, amino acid, phenols, terpenes, saponins and proteins. These biomolecules are not only

used for reduction of salt solution but also stabilizes the biofabricated nanoparticles. Plant extract of several species have been used for fabricating silver nanoparticle such as *Saccharum officinarum* [Chaudhari et al., 2012], *Cinamomum camphora* [Huang et al., 2008], *Capsicum annuum* [Li et al., 2007], *Helianthus annuus* [Dubchak et al., 2010] *Aloe vera* [Chandran et al., 2006b], *Medicago sativa* [Lukman et al., 2011] and several others. For synthesizing morphology regulated and stable Ag nanoparticles the phytochemicals present in the plant act as capping as well as reducing agent. The synthesis of silver nanoparticles has also been reported by using methanolic extract of *Eucalyptus hybrid* [Dubey et al., 2009]. Almost all the parts of the plant such as seeds of *Jatropha curcas* [Bar et al., 2009] and skin of tomatoes [Carbone et al., 2020] have been extracted and used for fabrication of silver nanoparticles.

#### ii. ZnO nanoparticles

In the past few years, research efforts have been focused on ZnO nanoparticles all over the globe due to its widespread application in biomedical field, wastewater treatment, optics and electronics. ZnO nanoparticles possesses a band gap of 3.37 eV and a binding energy of 60 meV, which enable them to be used as catalyst, antiinflammatory agent, in the process of wound healing and also as UV filter. Plant parts like seeds, leaves, roots, flowers, etc., are used for the fabrication of ZnO nanoparticles. ZnO nanoparticles have been reported to be synthesized using the leaves of *Azadirachta indica* [Bhuyan et al., 2015], flower and leaves of *Vitex negundo* [Ambika and Sundrarajan, 2015]. ZnO nanoflowers have also been synthesized using *B. licheniformis* has also been used by scientists for synthesizing ZnO nanoflowers and these nanoflowers exhibit excellent photocatalytic activity for degradation of methylene blue dye. *Lactobacillus plantarum* extract assisted the synthesis of moderately stable ZnO nanoparticle having zeta potential value [Selvarajan and Mohanasrinivasan, 2013].

### iii. MnO<sub>2</sub> nanoparticles

The most abundant element present on the surface of earth is discovered to be Mn. It is found to be twelfth most common element on earth. Among various 3d transitional metal oxides, Mn oxides hold specific position because of the possibility of several variants, which are different in composition and structure such as MnO, Mn<sub>2</sub>O<sub>3</sub>, Mn<sub>3</sub>O<sub>4</sub>, etc. MnO<sub>2</sub> finds its application in different areas ranging from solar cells and batteries, catalysis, molecular and ionic sieving, optoelectronics, magnetic storage devices to water treatment and purification. Various scientists and researchers have worked on green synthesis of MnO<sub>2</sub> nanoparticles (MNPs) and have reported their outlook on the method reported by them. A study reported the synthesis of Mn nanoparticles by reduction of manganese acetate using methanolic extract of lemon and then the fabricated nanoparticles were used and further stabilized with the help of turmeric curcumin [Jayandran, et al., 2015]. In this work, the reaction was carried out in a pH range of 3-4 and temperature ranging from 50-60°C. MNPs having particle size of 19.2 nm have also been prepared by using the aqueous leaf extract of *Kalopanax pictus* for reduction of potassium permanganate [Sathiyamoorthi et al., 2015]. Kumar and co-workers described the synthesis of MnO nanoparticles of varying sizes using aqueous extract of *Syzygium aromaticum* as reducing as well as stabilizing agents [Kumar et al. 2017]. Manganese nanorods having average size of 40-50 nm have been reported to be synthesized using the leaf extract of *Phyllanthus amarus* [Prasad and Patra, 2017]. In other study, peel extract of *Ananas comosus* was employed for preparing Mn<sub>3</sub>O<sub>4</sub> nanoparticles in the size range of (10-35 nm) for application [Assaikkutti et al., 2016].

### iv. CuO nanoparticles

In the recent times, scientists have focused on the investigation of using copper oxide nanomaterials for different purposes in different areas such as gas sensors, food preservation, catalysis, waste treatment, dye removal, effective antimicrobial and

antioxidant, photovoltaic device, solar energy converter, super conductor and in agriculture as well [Jiang et al., 2015; Fatah et al., 2018; Sundar et al., 2018; Sone et al., 2017]. In addition to this, CuO nanoparticles exhibited exclusive, antimicrobial, antioxidant and anticancer efficacy, which facilitates them to be used in biomedical applications. Several plants are reported, which have been used for the synthesis of copper oxide nanoparticles. CuO nanoparticles were synthesized using plant extracts of *Oak fruit hull* (Jaft) [Sorbiun et al., 2018], *Rosa canina* fruit [Hematti et al., 2018], *Olea europaea* leaf extract [Sulaiman et al., 2017], *Azadirachta indica* [Sharma et al., 2018], *Moringa oleifera* [Galan et al., 2018] leaf extract, *Abutilon indicum* [Ijaz et al., 2017] leaf extract, *Euphorbia chamaesyce* leaf extract [Maham et al., 2017], *Ferulago angulate* (schlecht) boiss [Shayegan et al., 2018].

#### **1.4.2 Synthesis of polymer matrix nanocomposites**

Nanoparticles of varying size are fillers that are reinforced into the matrix of polymer to diminish certain limitations of polymers and also to enhance some of the properties. The addition of nanoscale fillers into the matrix of polymer improves its mechanical and physical properties, which increases the applicability of polymers for different purposes [Reynaud et al., 1999; Young et al., 2012]. The combination of polymer material with nanomaterials forms innovative composites having novel properties. Uniformly distributed nano sized filler generates supremely large interfacial area per unit volume between nanomaterial and polymer. Moreover, the distance between nano-elements also reduces to molecular dimensions.

#### **1.5 Characterization techniques for analysis of nanomaterials and polymer matrix nanocomposites**

There are several analytical techniques which are being employed for characterization of metal-based nanomaterials and nano-polymer composites. In this section, the basic

principles of techniques used for characterization of synthesized materials has been put forward. The techniques used for investigation of metal-based nanomaterials as well as nano-polymer composites are x-ray diffraction (XRD), scanning electron microscopy (SEM), transmission electron microscopy (TEM), Ultraviolet-Visible light absorption spectroscopy (UV-Vis), thermo gravimetric analysis (TGA), Infrared spectroscopy (FT-IR), dynamic light scattering (DLS), and Brunauer-Emmet-Teller (BET) surface area.

### 1.5.1 X-ray diffraction analysis

The structural characterization of nanocrystalline substance is carried out using x-ray diffraction technique. This analytical technique is employed to investigate the structural phase along with the crystallite size of nanomaterial. The crystalline phase of material is identified by examining the diffraction pattern recorded with x-ray diffractometer using Cu K $\alpha$  radiation ( $\lambda = 1.5418 \text{ \AA}$ ). X-ray diffraction follows the principle of Bragg's law, which is represented by the equation mentioned below.

$$n\lambda = 2d\sin\theta \quad \dots\dots\dots (1.1)$$

Where, d represents the interplanar distance between lattice planes of miller indices, and  $\lambda$ , wavelength of the incident x-ray and  $\theta$ , Bragg angle.

The widths of the peaks assist in determining the size distribution and defects in the nanocrystal. The peak width broadens with decrease in the size of nanocrystal. The size of nanocrystals is calculated from the peak width of diffraction pattern using the Debye-Scherrer equation mentioned below.

$$D = \frac{0.9\lambda}{\beta\cos\theta} \quad \dots\dots\dots (1.2)$$

In the above **equation 1.2**, D represents the mean size of crystals,  $\lambda$ , wavelength of the incident x-ray, B, full width half maxima (FWHM) value of the peaks in radian, and  $\theta$ , Bragg's angle.

The XRD pattern of a material, Cu/Cu<sub>2</sub>O synthesized via green route was recorded and diffraction pattern confirmed the presence of mixed phases of copper (Cu) and copper oxide (Cu<sub>2</sub>O) [Sampaio et al., 2020]. Similarly, XRD analysis was also used for characterizing the biofabricated TiO<sub>2</sub> nanoparticles which confirmed their successful synthesis [Rajendhiran et al., 2020].

### 1.5.2 Scanning electron microscopy

SEM is used for examining the morphology of the synthesized materials. This technique provides the images of the surface of samples by detecting the signals generated from interaction of the electron incident on the surface of the sample. When the incident electron hits the surface of sample, secondary electrons possessing energy lesser than 50 eV is emitted from the surface. The efficiency of surface to emit secondary electrons depends on several factors such as geometry, chemical composition and characteristics of surface and bulk. Thus, SEM analysis gives an elaborated information about the chemical composition, surface topology as well as morphology. SEM technique is extensively used by researchers to study the morphology of materials. FESEM technique was used to represent the rod shape morphology of  $\alpha$ -FeOOH and  $\alpha$ -Fe<sub>2</sub>O<sub>3</sub> nanomaterials of about 30 nm diameter and 400 nm length [Marinho et al., 2014].

A polymer matrix nanocomposite was prepared by reinforcing the nano Al<sub>2</sub>O<sub>3</sub> into the matrix of glass fiber. FESEM images of the samples were taken to identify the failures and strengthening morphology of the composite [Mahato et al., 2020].

### 1.5.3 Transmission electron microscopy

TEM is an instrument used for structural and chemical characterization of materials. It possesses high spatial resolution and has ability to image atoms at a very high resolution of 0.1 nm, which is even smaller than the interatomic distance. The quantitative chemical analysis from single crystal can also be done by focusing the electron beam to a diameter

smaller than 0.3 nm. The TEM images of nano-hydroxyapatite and polymer nanocomposite were captured to show the change in morphology with/without non-ionic surfactant. The data showed more of nano-particle agglomerates in presence of non-ionic surfactant than those synthesized without it [Rop et al., 2019].

#### 1.5.4 UV-Vis spectroscopy

To study the optical and electronic properties of materials, UV-Vis spectroscopy is the simplest and most useful technique. The basic principle of this technique is the absorbance of light due to the electronic transition taking place in specimen under study. The wavelength of light essential for this transition to take place lies in the UV and visible region of electromagnetic spectrum. The technique is completely based on Lambert Beers' law according to which the absorbance is related as follows:

$$A = \log \frac{I_0}{I_t} \quad \dots\dots\dots (1.3)$$

$I_0$  and  $I_t$  are the intensities of incident and transmitted rays of light respectively.

The intensity of absorption (A) is recorded by UV-Vis spectrometer as a function of wavelength.

$$A = \epsilon cx \quad \dots\dots\dots (1.4)$$

Where, x represents sample path length, c, concentration of solution and  $\epsilon$ , molar extinction coefficient ( $\text{mol}^{-1}\text{cm}^{-1}$ ).

This characterization technique gives the preliminary information about particle size distribution and band gap of semiconductor metal oxide nanoparticles. UV-Vis spectroscopy is used to study the optical and electronic properties of nanoparticles [Saha and Bhuia, 2013]. UV-Vis spectrometry was applied to analyze  $\text{Fe}_2\text{O}_3/\text{SnO}_2$  nanocomposite for calculating band gap and investigating the absorption shifting of edges [Xia et al., 2008].

### **1.5.5 Fourier transform infrared spectroscopy**

Fourier transform infrared spectroscopy (FTIR) technique is a vibrational spectroscopic technique used for determining the availability of functional groups of the sample. The functional group is determined by characterizing the structural properties of the molecules. The working principle of FTIR is the measurement of IR light ray transmitted through the sample. IR spectroscopy discovers the vibrational modes in the molecules while photon mode in nanoparticles by means of suitable selection rule. Determined by the properties of their crystal symmetry. The vibrational or photon frequencies of nanoparticles change when the nanoparticles with the molecules or ions present on the surface of polymer. This modification in the frequencies gives details about the interaction between nanoparticles and molecule of other material.

The green synthesis of ZnO nanoparticles has been reported by Kumar and co-workers. The FT-IR spectroscopic analysis was carried out in the range of 500-4000  $\text{cm}^{-1}$ . The vibrational peak obtained from the analysis confirmed the formation of ZnO nanoparticles [Kumar et al., 2020]. FTIR spectra was also carried out of a nanocomposite to show the grafting of acrylic acid/ammonium acrylate (monomer) on to the surface of cellulose and nano-hydroxyapatite [Rop et al., 2019].

### **1.5.6 Brunauer-Emmett-Teller surface area analysis**

BET technique is applied to ascertain the specific area of nanomaterials and nano-polymer composites. The surface area is estimated by carrying out the physical adsorption of  $\text{N}_2$  gas over the surface of sample. The amount of gas adsorbed on to the surface of the sample measured by volumetric flow method corresponds to the monolayer coverage on its surface. The analysis is done at the temperature of liquid nitrogen. This analytical technique successfully determines the surface area, pore volume and diameter and pore density of the material analyzed. The synthesis of  $\text{CeO}_2$  nanoparticles through electro

spinning method has been reported earlier. The surface area of these nanoparticles determined using BET surface area analyzer was found to be larger than  $100 \text{ m}^2\text{g}^{-1}$  [Moller et al., 2018]. Similarly, mesoporous halloysite nanotubes were modified by  $\text{CuFe}_2\text{O}_4$  nanoparticles. Nitrogen adsorption and desorption method was used to calculate pore size and pore volume of  $\text{CuFe}_2\text{O}_4$ @HNTs. BET surface area of HNTs was compared with that of  $\text{CuFe}_2\text{O}_4$ @HNTs [Maleki et al., 2019].

### 1.5.7 Dynamic light scattering analysis

DLS also known as photon correlation spectroscopy or quassi-elastic light scattering is a technique which is used for estimating the size of particles in a solution through the scattering of light. The solution of nanoparticles is subjected to a beam of monochromatic light. The scattering of light takes place which is fluctuated due to the Brownian motion exhibited by the particles in solution. DLS is a sensitive and powerful tool which provides information about the hydrodynamic diameter of particles along with the polydispersity index of the material. The tool is also helpful in measuring the aggregation of nanoparticles occurring within the solution and thereby evaluates the stability of solution. A crosslinked polyethylene amine and triphosphate (PEI-TPP) nanoparticles were prepared for gene delivery. The average size of these nanoparticles was evaluated using DLS based particle size analyzer [Huang et al., 2014]. The applications of dynamic light scattering techniques in characterizing and developing the nanoparticles has also been elaborated in several articles [Carvalho et al., 2018].

### 1.5.8 Thermogravimetric analysis

TGA is a method, which is used for examining the thermal stability of the materials. It is a method that helps in recording the changes in the properties of material (both physical and chemical) with increase in temperature. The change in the mass of the sample as a result of decomposition, oxidation, or loss of water molecules or volatile substances

attached to the surface of sample is represented in the form a graph plot between temperature (or time) versus mass percentage of sample. TGA is basically a tool, which is used to derive the information regarding decomposition profile, thermal stability of material, life expectancy and moisture/volatile content. TGA analysis is used for obtaining the information regarding surface coatings of nanoparticles along with the purity of the sample [Mansfield et al., 2014]. Laboureur alongwith his co-workers studied the oxidation of Aluminum nanopowder through TGA method, which is useful for research on several parameters like heating rate, composition of oxidizing gas or mass of sample [Laboureur et al., 2019].

### **1.6 Applications of nanomaterials/nanocomposites**

A review on green synthesis of nanoparticles has been reported in the present chapter. Various metal/metal oxide nanoparticles such as silver, zinc oxide, metal doped zinc oxide, copper oxide, manganese oxide have been synthesized in this work using plant extract as precursor. Literature review exhibits the development in the field of synthesis of nanomaterial and characterization of abovementioned nanomaterials using different analytical techniques. Apart from synthesis, basic principle of evolution, along with the merits of using this technique for synthesis has been discussed in brief. These nanomaterials are also used for the preparation of polymer nanocomposite. The nanomaterials and polymer matrix nanocomposites synthesized in the laboratory are characterized using various analytical techniques. The techniques used for analysing these materials have been elaborated in this chapter. The incorporation of nanomaterials into the matrix of polymer enhances the ability of polymer to remove undesired dye from water bodies. In addition to synthesis, the environmental application of these nanomaterials in the process such as adsorption, catalytic reduction and photocatalysis for dye removal has been discussed in detail. The nanomaterial was also being tested for

its application in petroleum industry in assisting the shale formation by using these materials as an additional additive for enhancing the rheological properties of water-based drilling fluid.

Nanomaterials are of great interest for researchers because of their fascinating properties within the size range of less than 100 nm. The properties exhibited by nanomaterials are entirely different from their bulk counterpart. The decrease in size of materials leads to increase in the number of particles and therefore, mobility of surface atom is higher as compared to the inner atoms. Based on its unique properties, the application of nanomaterial ranges from medicinal field to various modern industries.

Researchers have applied nanomaterials in the area of wastewater treatment [Zhang et al., 2016], bio medical field [Tripathi et al., 2019], catalysis, information technology, petroleum industry and so on. These are also used as sensors in electrochemical, magnetic and optical field [Liu et al., 2018]. In addition to this, nanomaterials are also applicable in the area of energy storage devices in the form of electrodes and aids the assembling of batteries [Gogotsi and Penner, 2018].

The study presented in this dissertation work primarily focuses on the application of metal/metal oxide nanoparticles synthesized via green route for wastewater treatment. These metal-based nanomaterials have also been used for the fabrication of polymer-nanocomposite, which possess excellent ability to remove the organic dyes from its aqueous solutions through different methods. Other than wastewater treatment, nanomaterials have also been found to be used to enhance the properties of drilling fluid as mentioned earlier in petroleum industry.

### **1.6.1 Application of metal-based nanomaterials/nano-polymer composites for wastewater treatment**

#### **Water pollution**

There is a global increase in population in the past decades which is accompanied by

increase in the demand for fresh water supply. The reduction in the availability of fresh water is either due to wastage of fresh water, which has led to water crisis or secondly, water pollution is a significant threat that is responsible for scarcity of fresh water. The increasing scarcity of water bodies will eventually lead to water crisis all over the globe. The water bodies available on the surface seems to be insufficient to bear the rising urge of water. The extensive quantity of water required by industries for its functioning competes with ever rising water requirement by the huge section of population residing the drought prone regions all over the world. It is estimated that the population of drought prone areas is expected to reach approximately 33% of the total world's population by 2025. The increasing population will lead to increase in global consumption of fresh water, thereby, making it necessary to treat the industrial wastewater to make it fit for human consumption and for other purposes.

The presence of hazardous substances in the water bodies leads to drastic chemical and biological changes in the aquatic ecosystem, which threatens the aquatic life. In addition to the disturbance in aquatic ecosystem, the polluted water also pose serious health threats to mankind [**Iram et al., 2010; Kerkez and Bayazit, 2014**]. Therefore, it is very necessary to recycle the water bodies contaminated with inorganic pollutants such as heavy metal ions and organic pollutants like phenol, carbon tetrachloride, benzene etc. as well as organic dyes including congo red, rhodamine, methyl blue, methyl orange, etc. [**Chowdhury and Yanful, 2010; Bhoumik et al., 2011; Yang and He, 2011; Cao et al., 2010**]. The degree of treatment of wastewater determines the potential usage of treated water for different purposes. With the objective of addressing this issue, the focal point of the research work is synthesis of cost effective metal-based nanoparticles through green route, which can be used for removing organic dyes from wastewater.

## **Water pollution by dyes**

The organic dyes and pigments as coloring agent released in water bodies as effluents are used in several industries viz. leather, paper, food, and plastics. According to the estimation of World Bank, one of the largest sources of water pollution in the world is textile industry, which contributes approximately 20% of global industrial waste released into the water bodies. Textile dyeing industries releases around 72 chemicals, which are toxic in nature and needs to be removed from water bodies. The process of production of textile involves dyeing, rinsing and finally treatment of textiles that involves usage of large amount of fresh water. The water used in these processes are then released as such into the water bodies without any treatment. Wastewater released from these industries are often at high temperature and pH further magnifies the problem. After the discharge of dyes into the water bodies, these dyes decompose into toxic products like carbon monoxide, hydrogen chloride, nitrogen dioxide and carbon dioxide. In addition to dyes, textile manufacturing industries also releases hazardous products like aromatic amines, ammonia, alkali salts, heavy metals, and pigments, all of which are carcinogenic in nature. It is very necessary to either remove or decompose these dyes present in wastewater into simpler and non-toxic forms. Dye molecules are composed of two major units: chromophores, and auxochromes. Chromophores renders color to the dyes while auxochromes not only act as supplements to chromophore but is also responsible for its solubility in water. The complex aromatic structure of dye molecules does not allow it to dissociate easily and renders stability to them, which hinders the biodegradation of dyes [Gupta and Suhas, 2009]. Even the smallest concentration of dye (as much as  $1.0 \text{ g L}^{-1}$ ) transmits color to drinking water and make it unfit for consumption by human beings. The toxicity of dye molecules may lead to dysfunction of internal organs such as kidney, liver, brain and central nervous system.

Moreover, organic dyes and pigments hinder the sunlight to penetrate the water bodies and thereby reducing the efficiency of photosynthesis, which ultimately effects the growth of aquatic flora.

Dyes are broadly classified into following three types:

1. Cationic dye,
2. Anionic dye, and
3. Non-ionic dyes

Some of the common dyes, which are being discharged in water bodies and act as water pollutants are mentioned below.

**i. Methylene blue**

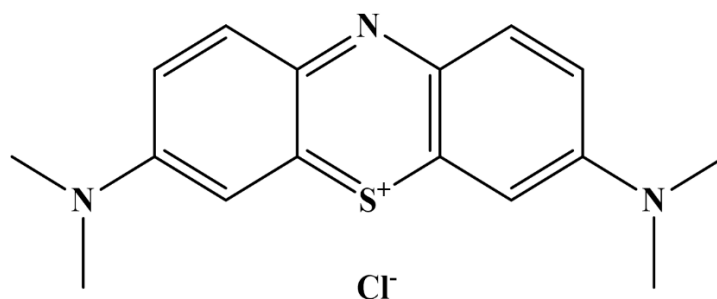


**Figure 1.2: Structure of methylene blue.**

Methylene blue (MB) S is a cationic azo dye having formula  $C_{16}H_{18}N_3SCl$  ( $319.85 \text{ g mol}^{-1}$ ). It is a heterocyclic aromatic compound, which is broadly used in the field of analytical chemistry as an indicator for redox titrations. It is also used in Diels Alder reaction as a photosensitizer for creating singlet oxygen. The consumption of methylene blue has number of health hazards including nausea, vomiting, diarrhea, etc. Repetitive consumption of the dye may lead to dizziness, high fever, irregular heartbeat, unusual tiredness, pale blue skin colour, etc.

## ii. Congo red

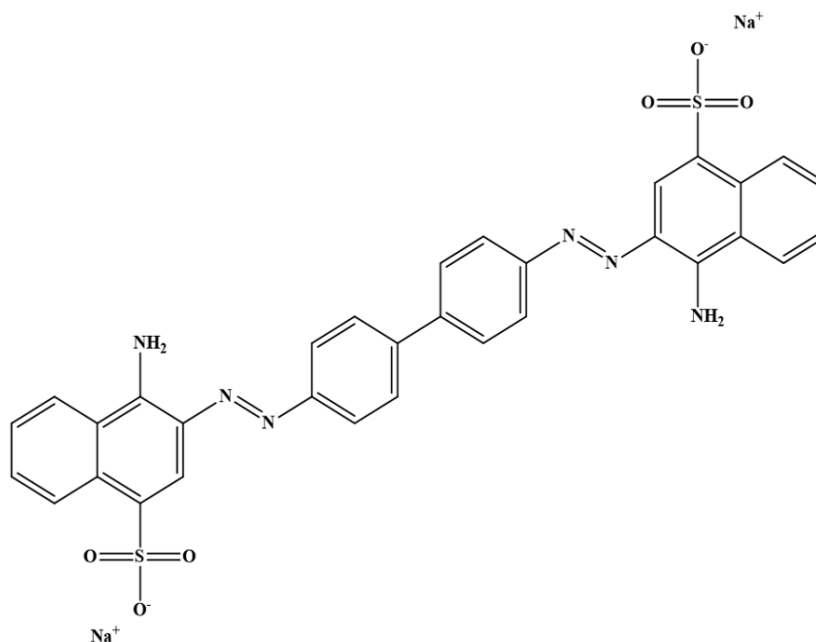


**Figure 1.3: Structure of congo red.**

Congo red (CR) is an anionic diazo dye, which is red in basic medium but as the solution of the dye turns acidic, its colour changes from red to blue. The chemical formula of the dye is  $C_{32}H_{22}N_6Na_2O_6S_2$  having molecular weight  $696.665 \text{ g mol}^{-1}$ . Congo red dye is majorly used as a staining agent in biological assays and also as an indicator in the titrimetric analysis. The consumption of congo red may lead to several health concern as it is a potential carcinogen and mutagen.

## iii. Methyl red

Methyl red (MR) dye is also known as C.I. Acid 2. It is an azo dye having chemical formula  $C_{15}H_{15}N_3O_2$ . It turns red in acidic medium and orange in the alkaline medium. Methyl red dye is extensively used in the paper printing and textile industries. It plays a vital role in sonochemical destruction of hydrocarbon pollutants. It acts as a health hazard causing irritation in the respiratory and digestive tract when swallowed/inhaled. On getting exposed to methyl red externally, it leads to eye and

skin irritation and itching.

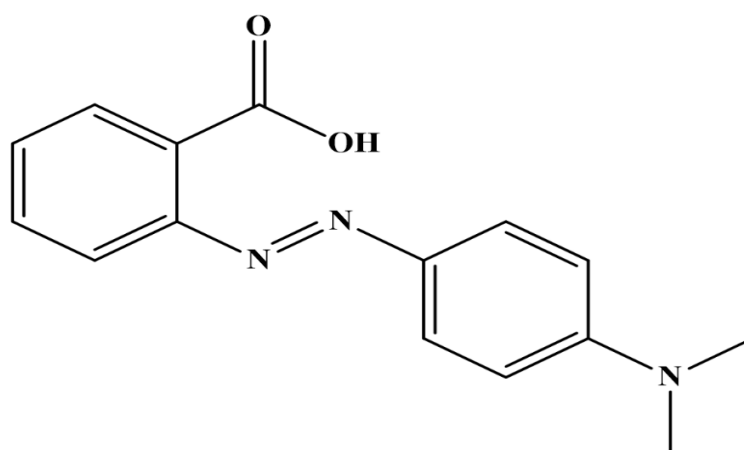


**Figure 1.4: Structure of methyl red.**

#### iv. Methyl Orange

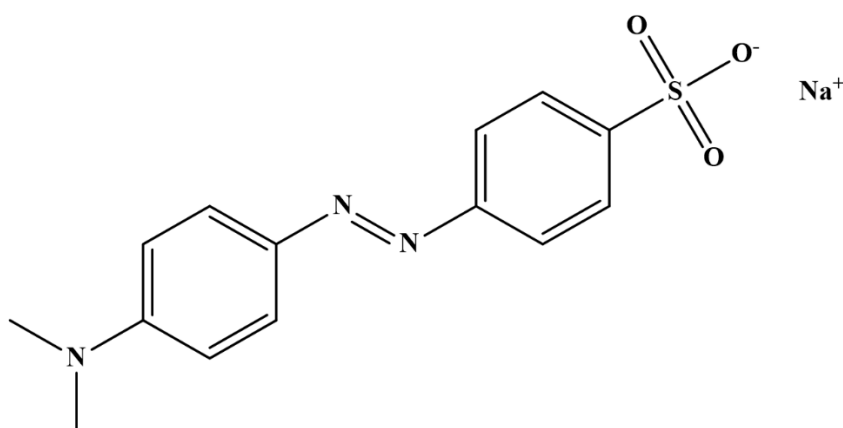


**Figure 1.5: Structure of methyl orange.**

Another dye methyl orange (MO) having chemical formula  $C_{14}H_{14}N_3NaO_3S$  is used most frequently in the titrations as a pH indicator because of its tendency to change its colour with change in pH. Swallowing of Methyl orange may causes nausea, vomiting and diarrhoea. It is highly toxic and acts as carcinogenic agent.

v. **Eriochrome Black T**

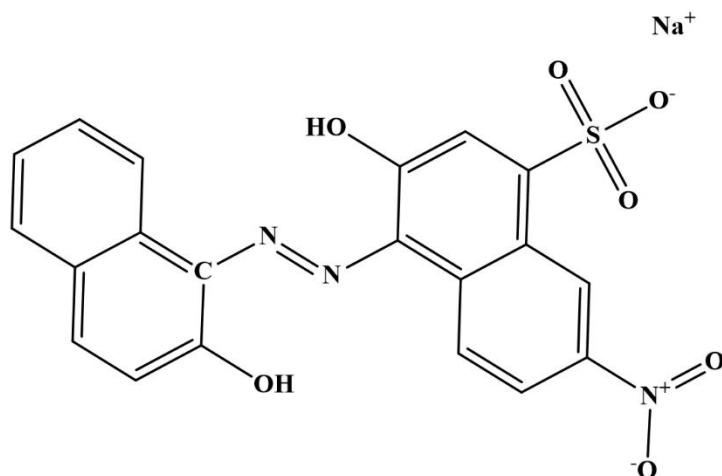


**Figure 1.6: Structure of eriochrome black T.**

Eriochrome Black T (EBT) is an azo dye having molecular formula  $C_{20}H_{12}N_3O_7SNa$ . It is used as an indicator in the complexometric titrations viz. process of determination of water hardness. Eriochrome Black T has the ability to change its color from blue in deprotonated state to red on forming a complex with calcium or magnesium, or any other metal ion present in hard water. EBT is mainly used in textile industry for dyeing silk, wool and nylon. Exposure to EBT leads to eye and skin irritation and its inhalation/ingestion may cause irritation of digestive/respiratory tract.

vi. **Eosin yellow**

Eosin yellow (EY) commonly known as C.I 45380. Acid Red 87 having chemical formula  $C_{20}H_6Br_4Na_2O_5$  is used most commonly as a stain in histology specifically as H and E stain. It is also used as a staining agent in Papanicolaou stain and other cytologic stains. EY is applied in organic synthesis too as a photosensitizer. Similar to other mentioned dyes, eosin yellow also acts as a pollutant and creates serious health issues. Exposure to eosin yellow causes irritation in the eyes, mucous membrane and skin. The exposure to eosin yellow even for a short duration leads to cheliitis, irritation and

stomatitis and the prolonged exposure leads to dermatitis.

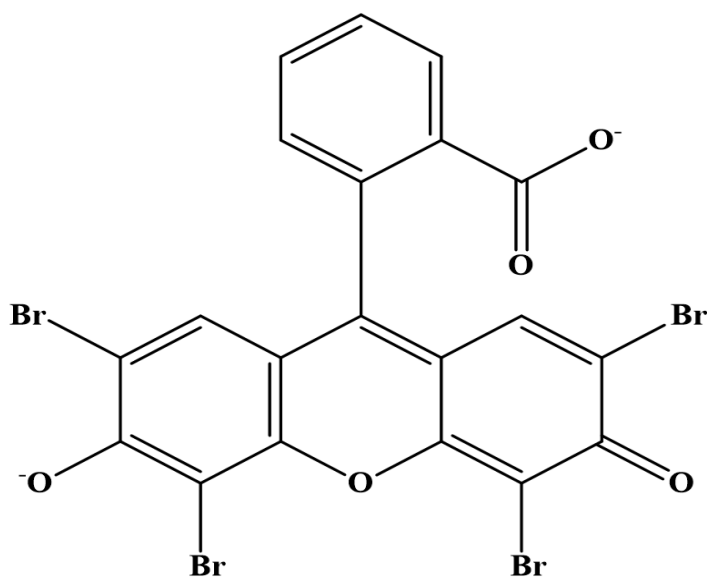


**Figure 1.7: Structure of eosin yellow.**

The toxic elements such as heavy metal ions, organic compounds and dyes released from the industries are being treated through several ways. The treatment methods utilize chemical, physical, biological and other emerging technologies for treating the wastewater effectively. Over the past decades, researchers have employed several methods like ion exchange method, precipitation, catalysis, photocatalysis, solvent extraction, adsorption etc. for removal of these contaminants and avail the fresh water from natural resources. As mentioned above, nanotechnology has been found to be a promising solution for environmental remediation. The application of nanomaterials can be seen as an effective method for the removal of contaminants owing to its structure and morphology. Now a days, nanoscience is effectively used in water treatments in various forms such as nanofiltration membrane, nano catalyst, nonporous materials, nanomaterials in the form of magnet and sensors. Several technology developers have asserted these nanotechnologies to be the most efficient and cost-effective technologies for the treatment of wastewater [Hillie et al., 2006]. The pores present on the surface of

nanomaterials enable them to be used for processes like ion exchange, separation and purification, catalysis, etc. The usage of nanomaterials may be preferred over conventional filters owing to their availability in abundance at cheaper price, lesser energy consuming process and ability of treating wastewater containing higher organic content. Among the different types of nanomaterials, metal-based nanomaterials and polymer nanocomposites act as good catalyst as well as adsorbing agent for wastewater treatment. In the present study, following methods have been explored for removal of dyes using nanomaterials and nano-polymer composites:

#### **1.6.1.1 Adsorption**

Adsorption is a process similar to surface tension effective for separating solid substances dissolved (even in the trace amounts) in water bodies. The bonding requirements of atoms present in the bulk phase of materials are saturated by formation of bonds (ionic or covalent) with adjoining atoms. However, the peripheral atoms are not counter balanced by other atoms on their outer surface and therefore, experience a deficiency of bonds, which make them energetically favourable to attach themselves with whatever atom available to attain a saturated state.

Depending upon the type of attachment between the surface of adsorbate and adsorbent, adsorption may be of two types, which are physisorption and chemisorption.

Physisorption is referred to as type of adsorption in which weak intermolecular force of attraction is responsible for attachment of adsorbate with adsorbent, however, chemisorption involves a chemical reaction between surface and the adsorbate. New chemical bonds are formed between the functional groups of adsorbent and adsorbate. Most commonly, physisorption is responsible for reduction in concentration of dyes and metal ions from wastewater. Over the years, researchers have used several materials as adsorbents, but the efficiency of these conventional adsorbents is limited owing to its

limited surface area, lack of selectivity, and the adsorption kinetics.

Nowadays, nanoadsorbents have been appeared as an alternate source for conventional adsorbents. Metal oxide nanoadsorbents are widely studied due to their unique properties compared to their bulk counterpart [Nassar, 2012]. Arising out of their ultrafine size, large surface area, associated sorption sites, short intra-particle diffusion, high density of corner or edge surface sites, tunable pore size, chemical stability and non-toxicity, metal oxide nano adsorbents offer significant improvement in the field of adsorption [Qu et al., 2013].

### **Factors affecting adsorption**

The process of adsorption is controlled by various factors mentioned below:

- **Surface area of adsorbent**

Surface area of adsorbents has an impact on its adsorptive capacity. Smaller the particle size of material, greater is the surface area and hence, greater the adsorptive capacity of material.

- **Contact time/residence time**

Contact time refers to the duration for which the adsorbent remains in contact with the solution of adsorbate. The longer the contact time, higher is the removal of metal ions/dyes from their solution. Rate of reaction is higher at the beginning of reaction and decreases sharply with time.

- **Particle size of adsorbent**

The internal diffusion and mass transfer limit of adsorbate penetration into the adsorbent is controlled by the particle size. The reduction in the size of particle increases the rate of adsorption. This is because as the external surface area of adsorbate increases, more

number of molecules gets exposed to the active sites of adsorbent, which fastens the process of adsorption.

- **Solubility of solute (adsorbate) in liquid**

The ease of removal of substance from its aqueous solution increases as the solubility of substances in water decreases. A non-polar substance is removed more easily than the polar solvent due to its low affinity for water molecules.

- **pH**

pH of the solution has a significant impact on the process of adsorption and hence, it is a major parameter, which controls the process. The adsorption of dye is dependent on the charge present on its surface adsorbate and adsorbent. In this regard, pH plays a crucial role in ionization process generating charges suitable for adsorption to take place.

#### **1.6.1.2 Chemical reduction**

Chemical reduction of dyes is another method that can be applied for removal of dyes from water bodies. Chemical reduction is yet another emerging technique, which can be used for removing azo dyes and organic contaminants such as nitroarenes through their transformation into products which are easily biodegradable and non-toxic [Razo-Flores et al., 1997; Aditya et al., 2015]. The chemical reduction of organic dyes is carried out effectively by applying nanomaterials as catalyst.

#### **1.6.1.3 Photocatalysis**

The dyes and other organic compounds released in water bodies can be effectively degraded through photocatalytic degradation using polymer nanocomposites. The hazardous contaminants, which are non-biodegradable, can be treated using this method to degrade these compounds. This type of catalysis is operated for the generation of electron-hole pairs, which produces free radicals. Free radicals are ultimately responsible

for carrying out secondary reactions. During this process two reactions occur simultaneously; oxidation reaction takes place from photo generated holes and reduction occurs from photo generated electrons. In the past few years, a lot of research has been conducted on degrading organic pollutants through heterogeneous photocatalysis. The process of photocatalysis is inspired by natural process of photosynthesis. Recently, a film composed of CdS and carboxymethyl starch was successfully designed and used for photocatalytic degradation of dyes [Xue et al., 2020]. Similarly, there is another work reported on PAN nanofibrous membrane which was modified with Fe complexes and used as photocatalyst (Li et al., 2020).

### **1.6.2 Application of nanomaterial in development of drilling fluid**

Drilling fluids are the most significant component of drilling industry having multiple functions to be performed simultaneously. Drilling operation is basically the process of drilling a hole from the superficial layer to the reservoir which is accomplished with the help of drilling bit attached to a long chain of drill pipe. These drilling bits are continuously subjected to rotation and weight load which breaks the rocks into small fragments referred to as “drill cuttings”. These cutting needs to be removed from there for the drilling process to occur smoothly. To remove these cuttings, drilling fluid is circulated from the surface to the drilling holes from where it lifts the cuttings and then reaches back to the surface. The cuttings are removed from drilling fluid on the surface using powerful pumps and then the drilling fluid is again circulated into the bore and the cycle goes on. In addition to this, drilling fluid also performs number of functions which involves suspension of drill cuttings, maintaining the stability of borehole, lubrication and cooling of drilling bits, reducing the pay zone damage, removal of cuttings from the downhole and managing the pressures of subsurface formations. The inadequate cleaning of holes leads to creation of beds which poses problem in drilling operations. The

appropriate hole cleaning depends on the rheological properties (drilling fluid weight, apparent viscosity, plastic viscosity, yield point, gel strength) of drilling fluid. Nanotechnology has also been applied to the drilling industry in the same manner as it is contributing significantly in other industries. Nanomaterials have been tested by researchers for its ability to be used as a drilling fluid additive with the objective of enhancing the stability of wellbore. The use of nanoparticles leads to production of smart fluid which has optimal properties to remain stable under harsh environment. The incorporation of nanomaterials into the drilling fluid shuts off the movement of water between formation and wellbore. It is not advisable to apply usual drilling method of relying on filter cake to minimize the fluid loss in shale formation with nanodarcy (nd) permeability. Therefore, researchers have now started exploring nanoparticles which can be included into the drilling fluid to block the pores present in the shale and reduce the filtration loss. Hence, the challenges bumping into the drilling industry can be conquered by formulating drilling fluid containing nanoparticles. The effect of raising ageing temperature on rheological and filtration properties of TiO<sub>2</sub> modified drilling fluid was studied in detail [Beg et al., 2020]. Bismuth ferrite nanoparticles were also used as an additive to the drilling fluid to enhance its properties so that it can be used effectively for drilling operations by [Perween et al., 2019]. Various other work have been reported on utilization of nanoparticles in smoothening the process of drilling operation [Aramendiz and Imqam, 2019; Liu et al., 2020; Saffari et al., 2018].

### **1.6.3 Application of nanomaterials as antimicrobial agent**

Bacterial infections are the origin of severe infections and deaths. The most common treatment of bacterial infections is intake of antibiotics, which is not only cheap but also work wonders for the eradication of bacterial infection. However, several researchers have reported that the use of antibiotics develops bacterial strains, which is resistant to

multi drugs. Moreover, a super bacterium has developed these days due to excessive use of antibiotics, which is resistant to almost all the antibiotics. The mechanism of working of antibiotics is designed in a way so that it targets the bacteria at three stages of their growth namely cell wall synthesis, translational machinery and DNA replication machinery. Unfortunately, bacteria possess the ability to develop resistance against each of these modes of action. Therefore, there is a need to develop something which can work with some other mechanism against bacteria. With the vision of developing new method, which works effectively against bacterial growth, nanomaterials have been implicated to obstruct bacterial growth. The available literature reveals that nanoparticles are highly efficient as antibacterial agents. The mechanism of action of nanoparticles is it makes direct contact with the bacterial cell wall which facilitates these materials to penetrate the cell and therefore, makes it difficult for bacteria to develop resistance. There are three possible mechanisms of action of NPs which can be executed simultaneously to inhibit bacterial growth: oxidative stress induction [**Gurunathan et al., 2012**], metal ion release [**Nagya et al., 2011**], or non-oxidative [**Leung et al., 2014**] mechanisms. The nano dimensions of these material enable it to demonstrate wide spectrum antibacterial properties against both gram positive and gram negative bacteria. Ramalingam and co-workers reported the efficacy of Ag nanoparticles to inhibit the growth of gram negative bacteria such as *Escherichia coli* and *Pseudomonas aeruginosa* [**Ramalingam et al., 2016**]. Magnesium fluoride and yttrium fluoride nanoparticles were used as an effective antimicrobial agent [**Lellouche et al., 2012a; Lellouche et al., 2012b**].

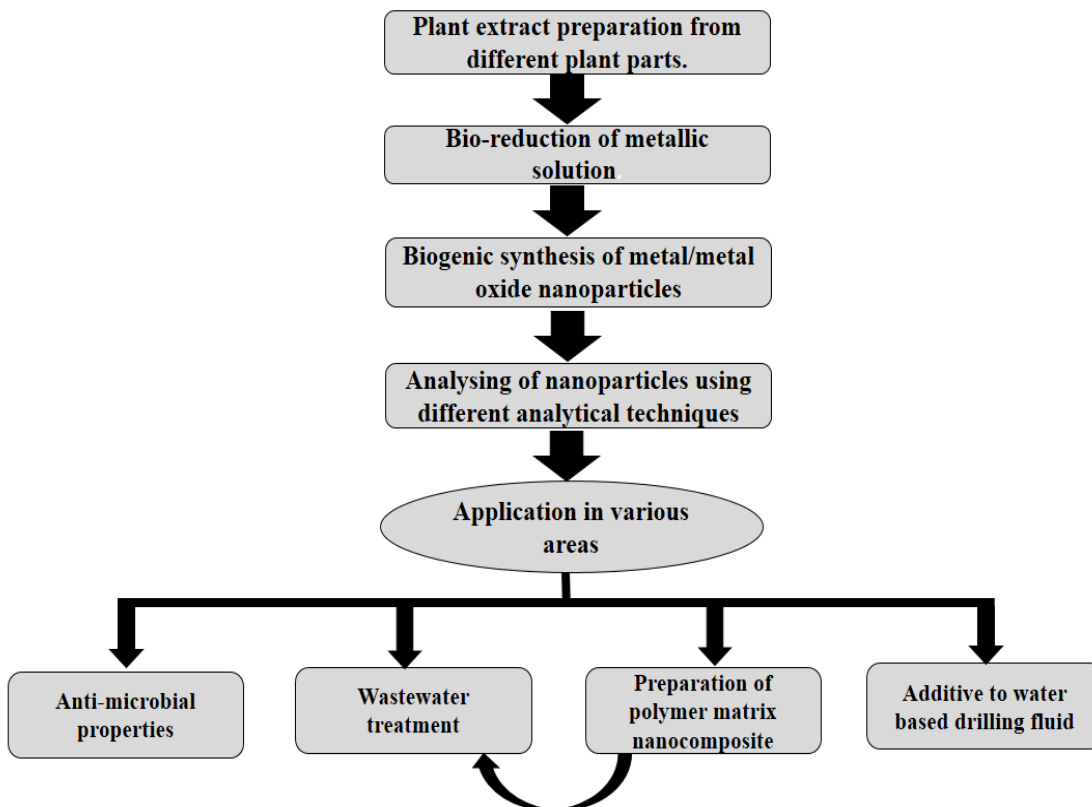


**Figure 1.8: Flowchart for synthetic route, characterization and application of metal-based nanoparticles synthesized through green route.**

## References

- Aditya, T., Pal, A., Pal, T. (2015). Nitroarenes reduction: a trusted model reaction to test nano catalysts. *Chemical communication*, 51, 9410-9431.
- Aghajani, M., Maruf, S.H., Wang, M., Yoshimura, J., Pichorim, G., Greenberg, A., Ding Y. (2017). Relationship between permeation and deformation for porous membranes. 526, 293-300.
- Akhtar, M.S., Panwar, J., Yun, Y.S. (2013). Biogenic Synthesis of Metallic Nanoparticles by Plant Extracts. *ACS Sustainable Chemistry and Engineering*, 1, 6, 591-602.
- Albanese, A., Tang, P.S., and Chan, W.C. (2012). The effect of nanoparticle size, shape, and surface chemistry on biological systems. *Annu. Rev. Biomed. Eng.*, 14, 1 —16.
- Alvarez-Lorenzo, C., Concheiro, A. (2002). Reversible adsorption by a pH- and temperature-sensitive acrylic hydrogel. *Journal of Controlled Release*, 80, 1-3, 247–257. doi:10.1016/s0168-3659(02)00032-9
- Ambika, S., Sundrarajan, M. (2015). Antibacterial behaviour of *Vitex negundo* extract assisted ZnO nanoparticles against pathogenic bacteria. *J. Photochem and Photobio. B*, 146, 52-7. doi: 10.1016/j.jphotobiol.2015.02.020.
- Aramendiz, J., and Imqam, A. (2019). Water-based drilling fluid formulation using silica and graphene nanoparticles for unconventional shale applications. *J Petro. Sci. and Eng*, 179, 742-749.
- Assaikkutti, A., Bhavan, P.S., Vimala, K., Karthik, M., Cheruparambath, P. (2016). Dietary supplementation of green synthesized manganese-oxide nanoparticles and its effect on growth performance, muscle composition and digestive enzyme activities of the giant freshwater prawn *Macrobrachium rosenbergii*. *J.Trace Elements Med. and Bio*, 35, 7–17. doi:10.1016/j.jtemb.2016.01.005.
- Bakirhan, N.K., and Ozkan, S.A. (2019). Quantum dots as a new generation nanomaterials and their electrochemical applications in pharmaceutical industry. *Handbook of nanomaterials for Industrial Applications*, 520-529.
- Balzani, V. (2005). Nanoscience and nanotechnology: A personal view of a chemist. *Small*, 1, 278–283.
- Bar, H., Bhui, D.K., Sahoo, G.P. et al. (2009). Green synthesis of silver nanoparticles using seed extract of *Jatropha curcas*. *Colloids Surfaces A: Physico chem Eng Asp*, 339, 1–3, 1, 134-139. <https://doi.org/10.1016/j.colsurfa.2009.07.02>.
- Beg, M., Kumar, P., Choudhary, P., Sharma, S. (2020). Effect of high temperature ageing on TiO<sub>2</sub> enhanced drilling fluids: A rheological and filtration study. *Upstream Oil and Gas Tech*, 5, 100019.

Bhoumik, M., Maity, A., Srinivasu, V.V., and Onyango M. S. (2011). Enhanced removal of Cr (VI) from aqueous solution using polypyrrole/Fe<sub>3</sub>O<sub>4</sub> magnetic nanocomposite. *J. Hazard. Mater.*, 190, 381-390.

Bhuyan, T., Mishra, K., Khanuja, M., Prasad, R., Varma, A. (2015). Biosynthesis of zinc oxide nanoparticles from *Azadirachta indica* for antibacterial and photocatalytic applications. *Mat. Sci in semiconductor process*, 32, 55-61.

Byrappa, K., and Adschiri, T. (2007). Hydrothermal technology for nanotechnology. *Prog. Cryst.Growth Charact. Mater.*, 53, 117-166.

Cao, G., Su, L., Zhang, X., and Li, H. (2010). Hydrothermal synthesis and catalytic properties of  $\alpha$ - and  $\beta$ -MnO<sub>2</sub> nanorods. *Mater. Res. Bull.*, 45, 425-428.

Carbone, K., AngeliA, A.D. et al. (2020). Microwave-assisted synthesis of catalytic silver nanoparticles by hyperpigmented tomato skins: A green approach. *LWT-Food Science and Technology*, 133,110088.

Carvalho, P.M., Felicio, M.R., Santos, N.C., Goncalves, N., and Domingues, M.M. (2018). Application of light scattering techniques to nanoparticle characterization and development. *Frontiers in chem*, 6, 237.

Chan, Y.S., Mat Don, M. (2013). Biosynthesis and structural characterization of Ag nanoparticles from white rot fungi. *Materials Science and Engineering: C*, 33, 1, 282-288.

Chandran, S.P., Chaudhary, M., Pasricha, R. et al. (2006). Synthesis of gold nanotriangles and silver nanoparticles using *Aloe vera* plant extract. *Biotechnol Prog*, 22, 2, 577-83. <https://doi.org/10.1021/bp0501423>

Chaudhari, P.R., Masurkar, S.A., Shidore, V.B., Kamble, S.P. (2012). Biosynthesis of silver nanoparticles using *Saccharum officinarum* and its antimicrobial activity. *Micro Nano Lett*, 7, 646–650.

Chaudhuri, R. G., and Paria, S. (2012). Core/shell nanoparticles: classes, properties, synthesis mechanisms, characterization, and applications. *Chem. Rev*, 112, 2373–243.

Choudhary, N., Hwang, S., and Choi, W. (2014). Carbon nanomaterials: A review. *Handbook of Nanomaterials Properties*, 709-769.

Chowdhury, S.R., and Yanful, E. K. (2010). Arsenic and chromium removal by mixed magnetite- maghemite nanoparticles and the effect of phosphate on removal. *J. Environ. Man*, 92, 2238-2247.

Comini, E., Faglia, G., Ferroni, M., Ponzoni, A., Vomiero, A., and Sberveglieri, G. (2009). Metal oxide nanowires: preparation and application in gas sensing. *J. Mol. Catal. A: Chem*, 305, 170–177.

- Dick, K. A. (2008). A review of nanowire growth promoted by alloys and non-alloying elements with emphasis on Au-assisted III-V nanowires. *Prog. Cryst. Growth Charact. Mater*, 54, 138-173.
- Dhuper, S., Panda D., and Nayak, P. (2012). *Nano Trends: J Nanotech. App*, 13, 16-22.
- Dubchak, S., Ogar, A., Mietelski, J.W., Turnau, K. (2010). Influence of silver and titanium nanoparticles on arbuscular mycorrhiza colonization and accumulation of radio caesium in *Helianthus annuus*. *Span J Agric Res*, 1,103–108.
- Dubey, M., Bhadauria, S., Kushwah, B.S. (2009). Green synthesis of nanosilver particles from extract of *Eucalyptus hybrida* (safeda) leaf. *Dig. J Nanomater Biostruct*, 4, 537–543.
- Edelstein, A.S., and Cammaratra, R.C. (1998). *Nanomaterials: synthesis, properties and applications*. Second Edition, CRC Press, New York.
- Farre, M., Gajda-Schranz, K., Kantiani, L., and Barcelo, D. (2009). Ecotoxicity and analysis of nanomaterials in the aquatic environment. *Anal. Bioanal. Chem*, 393, 81–95.
- Fatah, A.F., Hamid, N.A. (2018). Physical and chemical properties of LSCF-CuO as potential cathode for intermediate temperature solid oxide fuel cell (IT-SOFC). *Malaysian, J. Fund. Appl. Sci*, 14, 391–396.
- Fernández-García, M., Martínez-Arias, A., Hanson, J. C., and Rodríguez, J. A. (2004). Nanostructured oxides in chemistry: characterization and properties. *Chem. Rev*, 104, 4063-4104.
- Galan, C.R., Silva, M.F., Mantovani, D. (2018). Green Synthesis of Copper Oxide Nanoparticles Impregnated on Activated Carbon Using *Moringa oleifera* leaves extract for the Removal of Nitrates from Water. *Can. J. Chem. Eng*, 9999, 1–9.
- Gogotsi, Y., Penner, R.M. (2018). Energy Storage in Nanomaterials – Capacitive, Pseudocapacitive, or Battery-like? *ACS Nano*, 12, 3, 2081–2083.
- Guo, H., Lin, N., Chen, Y. et al. (2013). Copper Nanowires as Fully Transparent Conductive Electrodes. *Sci Rep*, 3, 2323.
- Gupta, V. K., and Suhas. (2009). Application of low-cost adsorbents for dye removal – A review. *J. Environmental Management*, 90, 2313–2342.
- Gurunathan, S., Han, J.W., Dayem, A.A., Eppakayala, V., Kim, J.H. (2012). Oxidative stress-mediated antibacterial activity of graphene oxide and reduced graphene oxide in *Pseudomonas aeruginosa*. *Int J. Nanomedicine*, 7, 5901-14.
- Hakim, L.F., Portman, J.L., Casper, M.D., Weimer, A.W. (2005). Aggregation behavior of nanoparticles in fluidized beds. *Powder Technology*, 160, 3, 149-160.

He, L., Fullenkamp, D.E., Rivera, J.G., and Messersmith, P.B. (2011). pH responsive self-healing hydrogels formed by boronate–catechol complexation. *Chem Commun. (Camb)*, 47, 26, 7497–7499.

Hematti, S., Mehrazin, L., Hekmati, M., Izadi, M., Veisi, H. (2018). Biosynthesis of CuO nanoparticles using *Rosa canina* fruit extract as a recyclable and heterogeneous nanocatalyst for C-N Ullmann coupling reactions. *Mater. Chem. Phys*, 214, 527–532.

Hillie, T., Munasinghe, M., Hlope, M., and Deraniyagala, Y. (2006). *Nanotechnology: Water and Development, Global Dialogue on Nanotechnology and the poor: Opportunities and Risks*. Meridian Institute.

Huang, J., Lin, L., Li, Q et al. (2008). Continuous-flow biosynthesis of silver nanoparticles by lixivium of sundried *Cinnamomum camphora* leaf in tubular microreactors. *Ind Eng Chem Res*, 47, 6081–6090

Huang, X., Shen, S., Zhang, Z., Zhuang, J. (2014). Crosslinked polyethylenimine-tripolyphosphate nanoparticles for gene delivery. *Int. J. Nanomed*, 9, 4785.

Hulkoti, N.I., Taranath, T.C. (2014). Biosynthesis of nanoparticles using microbes—a review. *Colloids Surfaces B Biointerfaces*, 121, 474–483.

Ijaz, F., Shahid, S., Khan, S.A., Ahmad, W. (2017). Green synthesis of copper oxide nanoparticles using *Abutilon indicum* leaf extract: Antimicrobial, antioxidant and photocatalytic dye degradation activities. *Trop. J. Pharm. Res*, 16, 743–753.

Iram, M., Guo, C., Guan, Y., Ishfaq, A., and Liu, H. (2010). Adsorption and magnetic removal of neutral red dye from aqueous solution using Fe<sub>3</sub>O<sub>4</sub> hollow nanospheres. *J. Hazard. Mater*, 181, 1039-1050.

Iravani, S. (2011). Green synthesis of metal nanoparticles using plants. *Green Chem*, 13, 2638–2650. <https://doi.org/10.1039/C1GC15386B>.

Jayandran, M., Haneefa, M., Balasubramanian, V. (2015). Green synthesis and characterization of Manganese nanoparticles using natural plant extracts and its evaluation of antimicrobial activity. *J. Applied Pharmaceutical Sci*, 1, 105–110. doi:10.7324/JAPS.2015.501218.

Jha, M. (2018). Current trends in industrial Scale synthesis of quantum dots and its application in electronics. *Handbook of nanomaterials for Industrial Applications*, 381-385.

Jiang, T., Wang, Y., Meng, D., Yu, M. (2018). Facile synthesis and photocatalytic performance of self-assembly CuO microspheres. *Superlattice. Microst*, 85, 1–6, 17.

Jordan, J., Jacob, K.I., Tannenbaum, R., Sharaf, M. A. and Jasiuk, I. (2005). Experimental trends in polymer nanocomposites – a review. *Mater. Sci. Eng. A*, 393, 1–11. 10.1016/j.msea.2004.09.044.

- K, S.K., R, A., Arumugam, P., Berchmans, S. (2011). Synthesis of Gold Nanoparticles: An Ecofriendly Approach Using *Hansenula anomala*. ACS Applied Materials and Interfaces, 3, 5, 1418-1425.
- Kanchi, S., Kumar, G., Lo, A.Y., Tseng, C.M., Chen, S.K., Lin, C.Y., and Chin, T.S. (2014). Exploitation of de-oiled jatropha waste for gold nanoparticles synthesis: A green approach. Arabian Journal of Chemistry, 11, 2, 247-255.
- Kerkez, O., and Bayazit, S. S. (2014). Magnetite decorated multi-walled carbon nanotubes for removal of toxic dyes from aqueous solutions. J. Nanopart. Res, 16, 2431.
- Khalil, M.M.H., Ismail, E.H., El-Magdoub, F. (2012). Biosynthesis of Au nanoparticles using olive leaf extract: 1st Nano Updates. Arabian Journal of Chemistry, 5, 4, 431-437.
- Kharisov, B.I., Kharissova, O.V., and Ortiz-Mendez, U. (2016). CRC concised encyclopedia of nanotechnology, CRC Press.
- Kulkarni, N., and Muddapur, U. (2014). Biosynthesis of metal nanoparticles: A review. J. Nanotechnol, 1 —8.
- Kumar, N., Irfan, G., Udayabhanu, Nagaraju, G. (2020). Green synthesis of zinc oxide nanoparticles: Mechanical and microstructural characterization of aluminum nanocomposites. Materials Today: Proceedings.
- Kumar, R., and Chawla, J. (2014). Removal of Cadmium Ion from Water/Wastewater by Nano-metal Oxides: A Review. Water Quality, Exp Health, 5, 215-226.
- Kumar, V., Singh, K., Panwar, S., Mehta, S.K. (2017). Green synthesis of manganese oxide nanoparticles for the electrochemical sensing of p-nitrophenol. International Nano Letters, 7, 123–131. doi:10.1007/s40089-017-0205-3.
- Laboureur, D., Glabeke, G., and Gouriet, J.B. (2019). Aluminum nanoparticle oxidation by TGA/DSC. J. Thermal Ana. and Calorim, 137,1199-1210.
- Lellouche, J., Friedman, A., Lahmi, R., Gedanken, A., Banin, E. (2012a). Antibiofilm surface functionalization of catheters by magnesium fluoride nanoparticles. Int. J. Nanomedicine, 7, 1175–1188.
- Lellouche, J., Friedman, A., Gedanken, A., Banin, E. (2012b). Antibacterial and antibiofilm properties of yttrium fluoride nanoparticles. Int. J. Nano-medicine, 7, 5611–5624.
- Leung, Y.H., Ng, A.M., Xu, X., Shen, Z. (2014). Mechanisms of antibacterial activity of MgO: non-ROS mediated toxicity of MgO nanoparticles towards *Escherichia coli*. Small, 10, 6, 1171-83.
- Li, B., and Wang, Y. (2010). Facile synthesis and photocatalytic activity of ZnO-CuO nanocomposite. Superlattice Microst, 47, 615-623.

Li, F., Dong, Y., Kang, W., Cheng, B., Cui, G. (2020). Enhanced removal of azo dye using modified PAN nano fibrous membrane Fe complexes with adsorption/visible driven photo catalysis bifunctional roles. *Applied Surface Science*, 404, 206-215.

Li, S., Shen, Y., Xie, A et al. (2007). Green synthesis of silver nanoparticles using *Capsicum annuum* L. extract. *Green Chem*, 9, 852–858.

Li, X., Meng, G., Xu, Q., Kong, M., Zhu, X., Chu, Z., and Li, A. P. (2011). Controlled synthesis of germanium nanowires and nanotubes with variable morphologies and sizes. *ACS Nano Lett*, 11, 1704-1709.

Liu, L., Pu, X., Zhou, Y. et al. (2020). Smart Pickering water-in-oil emulsion by manipulating interactions between nanoparticles and surfactant as potential oil-based drilling fluid. *Physicochem. And Eng, Aspect*, 586, 124246.

Liu, Y., et al. (2018). Conjugated polymer nanoparticle based fluorescent biosensor for ultrasensitive detection of hydroquinone. *Anal. Chim. Acta*, 1012, 60–65.

Lofrano, G., Carotenuto, M., Libralato, G et al. (2016). Polymer functionalized nanocomposites for metals removal from water and wastewater: An overview. *Water Res*, 92, 22–37. 10.1016/j.watres.2016.01.033.

Love, J. C., Estroff, L. A., Kriebel, J. K., Nuzzo, R. G., and Whitesides, G. M. (2005). Self- assembled monolayers of thiolates on metals as a form of nanotechnology. *Chem. Rev*, 105, 1103–1169.

Lukman, A.I., Gong, B., Marjo, C.E. et al. (2011). Facile synthesis, stabilization, and anti-bacterial performance of discrete Ag nanoparticles using *Medicago sativa* seed exudates. *J Colloid Interface Sci*, 353, 433–444.

Maham, M., Sajadi, S.M., Kharimkhani, M.M., Nasrollahzadeh, M. (2017). Biosynthesis of the CuO nanoparticles using *Euphorbia chamaesyce* leaf extract and investigation of their catalytic activity for the reduction of 4-nitrophenol. *IET Nanobiotech*, 11, 766–772.

Mahapatra, A., Mishra, B. G., and Hota, G. (2011). Synthesis of ultra-fine  $\alpha$ -Al<sub>2</sub>O<sub>3</sub> fibers via electrospinning method. *Ceram. Int*, 37, 2329–2333.

Mahato, K.K., Rathore, D.K., Dutta, K., Prusty, R.K., Ray, B.C. (2020). Effect of severely thermal shocked nano-Al<sub>2</sub>O<sub>3</sub> filled glass fiber reinforced polymeric composites: An assessment on tensile, thermal and morphological behaviour. *Mat. today: Proc*.

Maleki, A., Hajizadeh, Z., and Salehi, P. (2019). Mesoporous halloysite nanotubes modified by CuFe<sub>2</sub>O<sub>4</sub> spinel ferrite nanoparticles and study of its application as a novel and efficient heterogeneous catalyst in the synthesis of pyrazolopyridine derivatives. *Scientific reports*, 9, 5552.

Mansfield, E., Tyner, K.M., Poling, C.M., Blacklock, J.L. (2014). Determination of Nanoparticle Surface Coatings and Nanoparticle Purity Using Microscale Thermogravimetric Analysis. *Anal. Chem*, 86, 3, 1478–1484.

- Marinho, J.Z., Montes, R.H.O., Moura, A.P. de, Longo, Varela, E. J.A., Munoz, R.A.A., Lima, R.C. (2014). Rapid preparation of  $\alpha$ -FeOOH and  $\alpha$ -Fe<sub>2</sub>O<sub>3</sub> nanostructures by microwave heating and their application in electrochemical sensors. *Materials Research Bulletin*, 49, 572-576.
- Moller, M., Tarabanko, N., Wessel, C., Ellinghaus, R., Over, H., and Smarsly. (2018). Electrospinning of CeO<sub>2</sub> nanoparticle dispersions into mesoporous fibers: on the interplay of stability and activity in the HCl oxidation reaction. *RSC Adv*, 8, 132-144.
- Mukherjee, P., Ahmad, A., Mandal, D et al. (2001). Fungus-Mediated Synthesis of Silver Nanoparticles and Their Immobilization in the Mycelial Matrix: A Novel Biological Approach to Nanoparticle Synthesis. *Nano Letters*, 1, 10, 515-519.
- Nagya, A., Harrison, A., Sabbani, S., Munson, R.S. Jr., Dutta, P.K., Waldman, W.J. (2011). Silver nanoparticles embedded in zeolite membranes: release of silver ions and mechanism of antibacterial action. *Int J Nanomedicine*, 6, 1833-52.
- Nassar, N.N. (2012). Kinetics, Equilibrium and Thermodynamic Studies on the Adsorptive Removal of Nickel, Cadmium and Cobalt from Wastewater by Superparamagnetic Iron Oxide Nanoadsorbents. *Can. J. Chem. Eng*, 90, 1231-1238 (2012)
- Nath, D., and Banerjee, P. (2013). Green nanotechnology- a new hope for medical biology. *Environ. Toxicol. Pharmacol*, 36, 997 —1014.
- Oskam, G. (2006). Metal oxide nanoparticles: synthesis, characterization and application *Jour. of Sol-grl sci. and tech*, 37, 161-164. <https://doi.org/10.1007/s10971-005-6621-2>
- Pal, G., Rai, P., Pandey, A. (2019). Green synthesis of nanoparticles: a greener approach for a cleaner future. In: Shukla AK, Irvani (eds).
- Panda, P. K., Jaleel, V. A., and Devi, S. U. (2006). Hydrothermal synthesis of boehmite and  $\alpha$ - alumina from Bayer's alumina trihydrate. *J. Mater. Sci*, 41, 8386–8389.
- Perreault, F., de Faria A. F., and Elimelech, M. (2015). Environmental applications of graphene- based nanomaterials. *Chem. Soc. Rev*, 44, 5861-5896.
- Perween, S., Thakur, N.K., Beg, M., Sharma, S., Ranjan, A. (2019). Enhancing the properties of water-based drilling fluid using bismuth ferrite nanoparticles. *Physicochem. And Eng. Asp*, 561, 165-177.
- Prasad, K.S., Patra, A. (2017). Green synthesis of MnO<sub>2</sub> nanorods using *P.amarus* plant extract and their fluorescence studies. *Green Processing and Synthesis*, 1–7.
- Qu, X., Alvarez, P. J. J., and Li, Q. (2013). Applications of nanotechnology in water and wastewater treatment. *Water Res*, 47, 3931-3946.
- Rajendhiran, R., Deivasigamani, V., Palanisamy, J., Masan, S., and Pitchaiya, S. (2020). *Terminalia catappa* and *Carissa carandas* assisted synthesis of TiO<sub>2</sub> nanoparticles: A green synthesis approach. *Mat. Today: Proceedings*.

Rajput, S., Pittman, Jr., C.U. and Mohan, D. (2016). Magnetic magnetite ( $\text{Fe}_3\text{O}_4$ ) nanoparticle synthesis and applications for lead ( $\text{Pb}^{2+}$ ) and chromium ( $\text{Cr}^{6+}$ ) removal from water. *J Colloid Interface Sci*, 468, 334-346.

Ramalingam, B., Parandhaman, T., Das, S.K. (2016). Antibacterial effects of biosynthesized silver nanoparticles on surface ultrastructure and nano-mechanical properties of gram-negative bacteria viz. *Escherichia coli* and *Pseudomonas aeruginosa*. *ACS Appl Mater Interfaces*, 8, 7, 4963–4976.

Rao, C. N. R., Müller, A., Cheetham, A.K. (2005). *The chemistry of nanomaterials: Synthesis, Properties and Applications*. Wiley-VCH, ISBN: 978-3-527-30686-2, 1, 113.

Razo-Flores, E., Donlon, B., Lettinga, G., Field, J.A. (1997). Bio transformation and biodegradation of N-substituted aromatics in methanogenic granular sludge. *FEMS Microbiology Reviews*, 20, 3-4, 525-538.

Reynaud, E., Gauthier, C., Perez, C. (1999). Nanophases in polymers. *Rev. Metall*, 96, 169–176.

Rop, K., Mbui, D., Karuku, G. N., Michira, I., and Njomo, N. (2019). Characterization of water hyacinth cellulose-g-poly (ammonium acrylate-co-acrylic acid)/nano-hydroxyapatite polymer hydrogel composite for potential agricultural application. *Results in Chemistry*, 100020.

Roy, N., Saha, N., Kitano, T., Saha P. (2010). Novel Hydrogels of PVP–CMC and Their Swelling Effect on Viscoelastic Properties. *Jour. Applied Polymer Sci*, doi: 10.1002/app.32056

Saffari, H.R.M., Soltani, R., Alaei, M., and Soleymani, M. (2018). Tribological properties of water-based drilling fluids with borate nanoparticles as lubricant additives. *J. Petro. Sci. and Eng*, 171, 253-259.

Saha, S., and Bhunia, A. K. (2013). Synthesis of  $\text{Fe}_2\text{O}_3$  Nanoparticles and Study of its Structural, Optical Properties. *J. Phy. Sci*, 17, 191-195.

Sampaio, S., and Viana, J.C. (2020). Optimization of the green synthesis of Cu/Cu<sub>2</sub>O particles for maximum yield production and reduced oxidation for electronic application. *Materials Science and Eng: B*, 263, 114807.

Sathiyamoorthi, E., Moon, S.A., Alkotaini, B., Kim, B.S. Salunke, B.K. (2015). Biological synthesis of manganese dioxide nanoparticles by *Kalopanax pictus* plant extract. *IET Nanobiotech*, 9, 220–225. doi:10.1049/iet-nbt.2014.0051.

Schröfel, A., Kratošov, G., Šafařík, I., Šafaříkov, M., Raška, I., Shor, L.M. (2014). Applications of biosynthesized metallic nanoparticles – A review. *Acta Biomaterialia*, 10, 10, 4023- 4042.

- Selvarajan, E., Mohanasrinivasan, V. (2013). Biosynthesis and characterization of ZnO nanoparticles using *Lactobacillus plantarum* VITES07. *Mater Lett*, 112, 180–182. <https://doi.org/10.1016/j.matlet.2013.09.020>.
- Sen, M., Avci, E.N. (2005). Radiation synthesis of poly (N-vinyl-2-pyrrolidone)-kappa-carrageenan hydrogels and their use in wound dressing applications. I. Preliminary laboratory tests. *J Biomed Mater Res A*, 74, 2, 187-96. doi: 10.1002/jbm.a.30308.
- Sharma, B.K., Shah, D.V., Roy, D.R. (2018). Green synthesis of CuO nanoparticles using *Azadirachta indica* and its antibacterial activity for medicinal applications. *Mater. Res. Express*, 5, 9. doi: MRX-109160.R1.
- Shayegan, E., Mina, M., Ali, S., Saeid, R., Fardood, T. (2018). Plant-mediated synthesis of zinc oxide and copper oxide nanoparticles by using *Ferulago angulata* (schlecht) *boiss* extract and comparison of their photocatalytic degradation of Rhodamine B ( RhB ) under visible light irradiation. *J. Mater. Sci. Mater. Electron*, 29, 2, 1333-1340.
- Shedbalkar, U., Singh, R., Wadhvani, S., Gaidhani S., and Chopade, B. (2014). Microbial synthesis of gold nanoparticles: current status and future prospects. *Adv. Colloid Interface Sci*, 209, 40 —48.
- Shen, G., Chen, P. C., Ryu K., and Zhou, C. (2009). Devices and chemical sensing applications of metal oxide nanowires. *J. Mater. Chem*, 19, 828-839.
- Shivaji, S., Madhu, S., Singh, S. (2011). Extracellular synthesis of antibacterial silver nanoparticles using psychrophilic bacteria. *Process Biochemistry*, 46, 9, 1800-1807.
- Singh, D. P., and Ali, N. (2010). Synthesis of TiO<sub>2</sub> and CuO nanotubes and nanowires. *Sci. Adv. Mater*, 2, 295–335.
- Singh, J., Dutta, T., Kim K.H. et al. (2018). ‘Green’ synthesis of metals and their oxide nanoparticles: applications for environmental remediation. *J Nanobiotech*, 16, 84.
- Singh, P., Kim, Y. J., Zhang, D., and Yang, D. C. (2016). Biological Synthesis of Nanoparticles from Plants and Microorganisms. *Trends Biotechnol*, 34, 588 —599.
- Sone, B.T., Diallo, A., Fuku, X.G., Gurib-Fakim, A., Maaza, M. (2017). Biosynthesized CuO nano-platelets: physical properties and enhanced thermal conductivity nanofluidics. *Arab. J. Chem*, 13, 160–170.
- Sorbiun, M., Shayegan, E., Ali, M. (2018). Green Synthesis of ZnO and CuO Nanoparticles Using Aqueous Extract of Oak Fruit Hull (Jaft) and Comparing Their Photocatalytic Degradation of Basic Violet 3. *Int. J. Environ. Res*, 4.
- Stephen, J.R., Macnaughton, S.J. (1999). Developments in terrestrial bacterial remediation of metals. *Current Opinion in Biotechnology*, 10, 3, 230-233.
- Sundar, G.V., Kwon, S.J. (2018). Biosynthesis of CuO nanowires and their use for the electrochemical sensing of dopamine. *Nanomaterials*, 8, 1–17.

- Sulaiman, G.M., Tawfeeq, A.T., Jaaffer, M.D. (2017). Biogenic synthesis of CuO nanoparticles using *Olea europaea* leaf extract and evaluation of their toxicity activities : An in vivo and in vitro study. *Biotech. Prog*, 34, 1, 218-230. doi: 10.1002/btpr.2568.
- Syed, A., Saraswati, S., Kundu, G.C., Ahmad, A. (2013). Biological synthesis of silver nanoparticles using the fungus *Humicola* sp. and evaluation of their cytotoxicity using normal and cancer cell lines. *Spectrochim Acta A Mol Biomol Spectrosc*, 114, 144-147.
- Thompson, D.T. (2007). Using gold nanoparticles for catalysis. *Nanotoday*, 2, 40-43.
- Tripp, S.L., Pusztay, S.V., Ribbe, A.E., Wei, A. (2002). Self-Assembly of Cobalt Nanoparticle Rings. *J. American Chemical Society*, 124, 27, 7914-7915.
- Tripathi, R.M., and Chung, S.J. (2019). Biogenic nanomaterials: Synthesis, characterization, growth mechanism, and biomedical applications. *J. Microbiol. Methods*, 157, 65–80.
- Vayssieres, L. (2004). On the design of advanced metal oxide nanomaterials. *Int. J. of Nanotechnology*, 1, 1-40.
- Whitesides, G. M. (2005). Nanoscience, nanotechnology, and chemistry. *Small*, 1, 172-179.
- Xia, H., Zhuang, H., Zhang, T., and Xiao, D. (2008). Visible-light-activated nanocomposite photocatalyst of Fe<sub>2</sub>O<sub>3</sub>/SnO<sub>2</sub>. *Mater. Lett*, 62, 1126–1128.
- Xue, Y., Chang, Q., Hu, X., Cai, J., Yang, H. (2020). A simple strategy for selective photocatalysis degradation of organic dyes through selective adsorption enrichment by using a complex film of CdS and carboxymethyl starch. *Management*, 274,111184.
- Yallappa, S., Manjanna, J., Dhananjaya, B.L. (2015). Phytosynthesis of stable Au, Ag and Au-Ag alloy nanoparticles using *J. sambac* leaves extract, and their enhanced antimicrobial activity in presence of organic antimicrobials. *Spectrochim Acta A Mol Biomol Spectrosc*, 137, 236-43.
- Yang, M., and He, J. (2011). Fine tuning of the morphology of copper oxide nanostructures and their application in ambient degradation of methylene blue. *J. Colloid Interf. Sci*, 355, 15-22.
- Yoshimatsu, K., Ye, L., Lindberg, J., and Chronakis, I. S. (2008). Selective molecular adsorption using electrospun nanofiber affinity membranes. *Biosens. Bioelect*, 23, 1208–1215.
- Young, R.J., Kinloch, I.A., Gong, L., Novoselov, K.S. (2012). The mechanics of graphene nanocomposites: a review. *Compos. Sci. Technol*, 72, 1459–1476.
- Zhang, Y., Wu, B., Xu,H., Liu, H., M, Wang., He, Y., Pan, B. (2016). Nanomaterials-enabled water and wastewater treatment. *NanoImpact*, 3-4, 22-39.

Zhao, D., Wang Y., and Zhang, Y. (2011). High-performance Li-ion batteries and supercapacitors based on prospective 1-D nanomaterials. *Nano- Micro Lett*, 3, 62-71.

Zhu, J., Wei, S., Zhang, L., Mao, Y., Ryu, J., and Haldolaarachchige, N., Young, D. P., and Guo, Z. (2011). Electrical and dielectric properties of polyaniline–Al<sub>2</sub>O<sub>3</sub> nanocomposites derived from various Al<sub>2</sub>O<sub>3</sub> nanostructures. *J. Mater. Chem*, 21, 3952–3959.



## Chapter 2: Study of adsorption of anionic dyes over biofabricated crystalline $\alpha$ -MnO<sub>2</sub> nanoparticles

---

### 2.1 Introduction

Over the last few decades, manganese oxide has gained momentum due to its inherent physical and chemical properties. Different oxidation states of manganese are found in nature (e.g., II, III or IV) and Mn also forms oxides ranging from simple MnO, MnO<sub>2</sub> to complex compounds like Mn<sub>2</sub>O<sub>3</sub>, Mn<sub>3</sub>O<sub>4</sub> and Mn<sub>5</sub>O<sub>9</sub>. Manganese dioxide (MnO<sub>2</sub>) exhibit polymorphism and exist as  $\alpha$ ,  $\beta$ ,  $\gamma$ , and  $\delta$ -MnO<sub>2</sub>. Among all, MnO<sub>2</sub> is of much importance because of its widespread applications in different fields like catalysis [Bing et al., 2017; Andreozzi et al., 1996], water treatment processes [Fei et al., 2008], batteries [Luo et al., 2006] and energy storage [Jaganyi et al., 2012]. Various factors such as reactant concentration, temperature, reaction time etc. controls the polymorph and phase of MnO<sub>2</sub>. There are various possible methods for synthesis of these nanocrystals of different shapes and sizes [Davar et al., 2010; Anil Kumar et al., 2005; Durmus et al., 2009; Fang et al., 2007; Liu et al., 2014; Wang et al. 2007]. However, synthesis of NPs using protocols of these methods involves usage of toxic chemicals which makes it hazardous to be applied in biomedical field [Bar et al., 2009]. At present, there is a requirement to develop a method which is not only low cost, simple and rapid but also eco-friendly for synthesizing metal oxide NPs [Sharma et al., 2015; Sharma et al., 2014]. Plants are rich source of chemicals which are biologically active [Salunke et al. 2009; Patil et al., 2010]. These chemicals assist in the synthesis of various types of NPs such as gold, silver, platinum, etc. [Manjula et al., 2019; Hasnain et al., 2019; Klekotko et al., 2019]. Manganese dioxide has attracted attention of researchers due to its unique oxidative properties and also its ability to act as an adsorbent for removal of dyes from wastewater [Zhang et al., 2010]. The dyes, which are left as residual waste of different industries

such as paper and pulp, pharmaceutical, leather, etc. are released into the water bodies and need to be removed from natural water resources [Carmen et al., 1996]. Presently, there are various techniques which are applied for removal of these azo dyes such as ultrafiltration [Bouazizi et al., 2017], coagulation [Shi et al., 2007], photodegradation [Hachem et al., 2001] and reverse osmosis [Al-Bastaki et al., 2004]. Adsorption is one of the most effective techniques that is employed by various industries for the treatment of wastewater to reduce the pollutants present in it [Jain et al., 2006, Lutke et al., 2019, Silva et al., 2016]. Adsorption can be performed using membrane filtration, electrochemical method, modified clays, organic sorbents, etc. [Kausar et al., 2018; Brillas et al., 2015; Zare et al., 2018]. Several compounds have been reported to be used [Barak et al., 2019; Hu et al., 2020; Ahmad et al., 2019] for removal of these dyes, but the use of  $\alpha$ -MnO<sub>2</sub> reported here, is not only convenient and cheaper to synthesize but also an efficient adsorbent for removal of these dyes.

This study presents the development of an environment friendly and a facile method for synthesis of crystalline  $\alpha$ -MnO<sub>2</sub> nanoparticles (MNPs) using *F. retusa* (Mulberry family) leaf extract as reducing agent. *F. retusa* are evergreen plants found in Egypt, Central India, and Australia. These are cultivated as decorative plants in gardens and streets. Literature survey reveals that the aerial parts of *F. retusa* possess antimicrobial, antidiabetic, antioxidant and antiinflammatory properties [Hansson et al., 2005; Chen et al., 2008; Omar et al., 2011; Singhab et al., 2010] and also act as an astringent, refrigerant, etc. [Kumar et al., 2012]. In the present work, MNPs have been biofabricated using *F. retusa* leaves extract. The synthesis of nanomaterial was analyzed over a range of temperatures from 80 to 800°C and was found that the pure phase, well crystalline, spherical, nanostructured  $\alpha$ -MnO<sub>2</sub> particles were obtained at 800°C temperature. The performance of the synthesized material was also evaluated in terms of decolourization

during removal of certain azo dyes such as methyl orange (MO) and methyl red (MR) from their aqueous solutions.

## 2.2 Novel aspect of the work

The use of  $\alpha$ -MnO<sub>2</sub> in environmental research is quite limited. A very few studies have been reported regarding the application of MNPs for removal of MO dye. MR dye has not been targeted up till now. Some of the research articles, where MnO<sub>2</sub> has been used for removal of MO dye, are reported [Zhu et al., 2020; Pargoletti et al., 2019; Zhang et al., 2018; Zhao et al., 2014]. Pargoletti and co-workers reported the one-pot wet chemical method to synthesize ad-hoc MNPs and found to be an effective adsorbent of MO dye [Pargoletti et al., 2019]. However, no elaborated study has been carried out to determine different aspects such as kinetics of adsorption, thermodynamics, effect of various parameters such as time, concentration, etc. and isotherm study. Ultrasonic decolourisation of MO dye using MnO<sub>2</sub>/CeO<sub>2</sub> has been reported by Zhao and Zhang long with their co-workers [Zhang et al., 2018; Zhao et al., 2014]. The process of decolourization of dye using this technique is not only much more complicated than the simple method of adsorption but also it was found that 90% of the dye got decolourized within a time span of 10 min. It was also observed that there was decrease in the efficiency of adsorption when it was reused. However, in the present study, more than 95% adsorption of dye took place in a little time span of 5 min. and the efficiency of NPs remained same even after repetitive usage.

This is the first report of its kind on synthesis of MNPs using *F. retusa* leaf extract. The synthesis of NPs using this technique is not only simple but also cost effective without use of any sophisticated instrument. The novelty also lies in the fact that no analysis has ever been published for the removal of MR dye using MNPs. For MO dye, although certain analysis have been reported for its adsorption over MnO<sub>2</sub>, but the detailed study

has not been done so far. While the previously reported work is effective but in most cases, MnO<sub>2</sub> has been used as catalyst rather than adsorbent for removal of dyes. In the present research, it has been used as an adsorbent and detailed critical analyses of the results has been presented. Various other adsorbents have also been reported to be used for removal of these dyes from their aqueous solutions [Al-Ghouti et al., 2005; Hadi et al., 2010; Nhamo et al., 2016; Falaki et al., 2013; Ma et al., 2018; Kundu et al., 2017; Agcaoili et al., 2017; Zaheer et al., 2019; Saad et al., 2010; Iannou et al., 2013]. The maximum adsorption capacity of MNPs reported in this article for MO and MR dyes were found to be 116.1 and 74.02 mg g<sup>-1</sup> respectively, which is quite high as compared to other reported materials (as shown in the **table 2.7** and **2.8**).

## **2.3 Materials and method**

### **2.3.1 Materials**

The chemicals used in experiments includes potassium permanganate, methyl orange, methyl red, and nitric acid. All of these chemicals were procured from Molychem India Private Ltd. These are laboratory grade chemicals and were used directly without further purification.

### **2.3.2 Synthesis of $\alpha$ -MnO<sub>2</sub> nanoparticles**

The plant extract was prepared by boiling, thoroughly washed leaves (50 g) of *F. retusa* with 200 mL of deionized water for approximately 2 h. The extract obtained was then filtered using 0.2  $\mu$ m membrane filter to remove impurities. In the typical synthesis, the above prepared plant extract solution was slowly added to 0.1 M solution of KMnO<sub>4</sub> in the ratio of 1:2. The synthesis was carried out under constant stirring at room temperature. The prepared solution was subsequently boiled to obtain a paste which was black in colour. Later, the black coloured paste was transferred into a ceramic crucible and heated

in the muffle furnace at different temperatures viz. 80, 200, 400, 600 and 800°C for 2h to determine the suitable temperature for synthesizing MNPs.

The synthesized NPs were characterized using various analytical techniques. X-ray diffraction (XRD) analysis performed out to study the purity of the phase using PANalyticalX'pertpro MPD diffractometer which was equipped with CuK $\alpha$  radiation (1.5418 Å). Field emission scanning electron microscopy (FESEM, model no. JEOL JSM 7100F) was used to observe the surface morphology of the synthesized NPs. To prevent samples from charging, a thin gold coating was sputtered on to the samples prior to the analysis. FESEM was equipped with energy dispersive x-ray spectroscopy (EDX), which was used to determine the chemical composition and purity of the samples. Thermal stability of NPs was determined by carrying out thermogravimetric analysis (TGA, Linseis PT 1000) of the synthesized material. The TGA analysis was done in nitrogen environment (Flow rate: 50 mL min.<sup>-1</sup>) by maintaining the heating rate of 10°C min.<sup>-1</sup> from room temperature to 700°C. The hydraulic diameter of nanoparticles (NPs) along with their stability under different condition was examined using Malvern Zetasizer Nano ZS equipment at 25°C temperature. BELSORP mini X (Make – MicrotracBEL, Japan) was used to measure the surface area of biofabricated MNPs. Brunauer–Emmett–Teller (BET) method was used to calculate specific surface area using nitrogen adsorption-desorption after removing the residual impurities obstructing the pores by degassing the material at a temperature of 200°C.

#### **2.4 Removal of dyes using $\alpha$ -MnO<sub>2</sub> nanoparticles**

Adsorption experiments were conducted using two different dyes which were MO and MR. Experiments were carried out in glass beakers in which 50 mL of aqueous solution of dyes i.e., MR (20 mg L<sup>-1</sup>) and MO (10 mg L<sup>-1</sup>) were taken separately. To each of these beakers, 20 mg of synthesized NPs dispersed in 1 mL of water was added at room

temperature. Both the solutions were stirred continuously at 300 rpm for 1 h under dark condition. A sample was removed at regular interval of time and centrifuged to separate the NPs. The centrifuged dye samples were then subjected to UV-Vis spectrophotometer (Lab India UV-Vis 3200) with the objective of determining the change in concentration of dye with respect to time. The pH of solutions were adjusted using pH tutor (Eutech Instruments, Singapore).

Percentage of removal of dye was calculated using following **equation 2.1**:

$$R (\%) = \frac{C_0 - C_e}{C_0} * 100 \quad \dots\dots\dots (2.1)$$

The adsorption amount ( $q_t$ ) retained on per gram of photocatalyst in reaction time  $t$  is calculated using **equation 2.2** mentioned below.

$$q_t = \frac{C_t - C_0}{m} * V \quad \dots\dots\dots (2.2)$$

Where,  $C_0$  is initial dye concentrations ( $\text{mg L}^{-1}$ ),  $C_e$ , equilibrium dye concentration ( $\text{mg L}^{-1}$ ),  $C_t$ , dye concentration at time  $t$  ( $\text{mg L}^{-1}$ ),  $V$ , sample solution volume (L) and  $m$ , weight of NPs (g).

## 2.5 Results and discussion

### 2.5.1 Characterization of $\alpha\text{-MnO}_2$ nanoparticles

#### 2.5.1.1 FESEM analysis

The study of surface morphology was done using FESEM images. The synthesized MNPs were clean and spherical in shape [Bing et al., 2017]. The FESEM micrographs in **figure 2.1 (a-e)** depict the images of NPs synthesized over a range of temperature from 80-800°C. **Figure 2.1 (a-e)** clearly exhibit that MNPs synthesized using *F. retusa* extract were found to be well dispersed and spherical in shape. The MNPs instead of having a compressed packed structure display much open and semi-linear structure. At lower temperature (80°C), clusters of spherical NPs were observed. As the temperature of

synthesis was increased, clusters of NPs started breaking and NPs started getting separated from each other. At 800°C temperature, NPs over a range of 30-50 nm were found to be well distinguished and separated from each other.

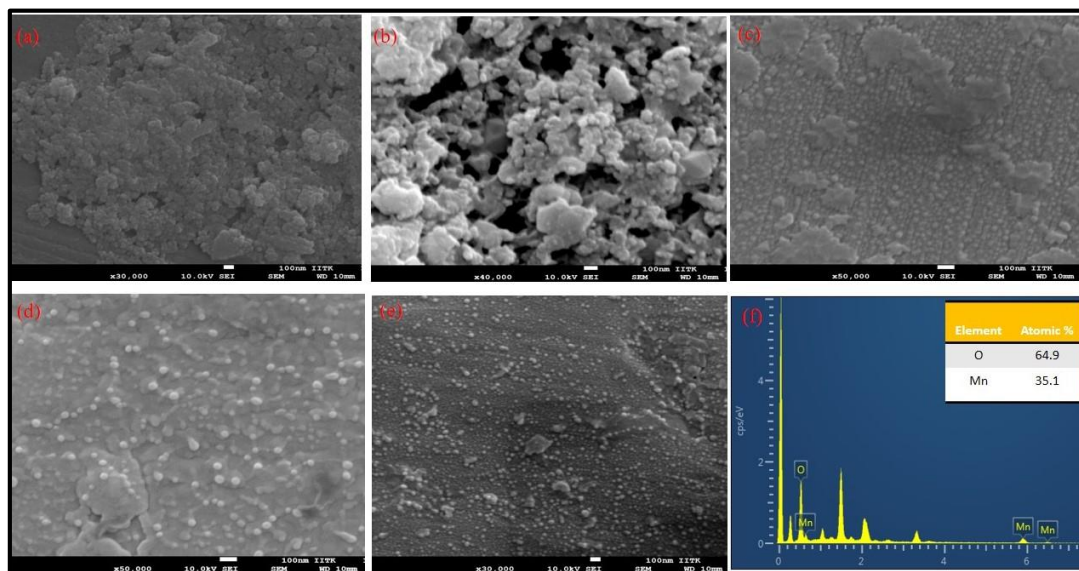


**Figure 2.1: FESEM images of synthesized MNPs at different temperatures (a) 80°C, (b) 200°C, (c) 400°C, (d) 600°C and (e) 800°C. (f) EDX analysis of  $\alpha$ -MnO<sub>2</sub> nanoparticles synthesized at 800°C temperature.**

### 2.5.1.2 EDX analysis

The presence of Mn and O in the sample was observed by the EDX analysis (**figure 2.1(f)**). The EDX analysis exhibited the atomic % of Mn and O content present in the sample of NPs which were found to be 35.1 and 64.9 % respectively. The EDX profile shows that the prepared NPs have high-purity content. These characteristics of MNPs are similar to that of same nanoparticles studied earlier [Wang et al., 2011].

### 2.5.1.3 XRD analysis

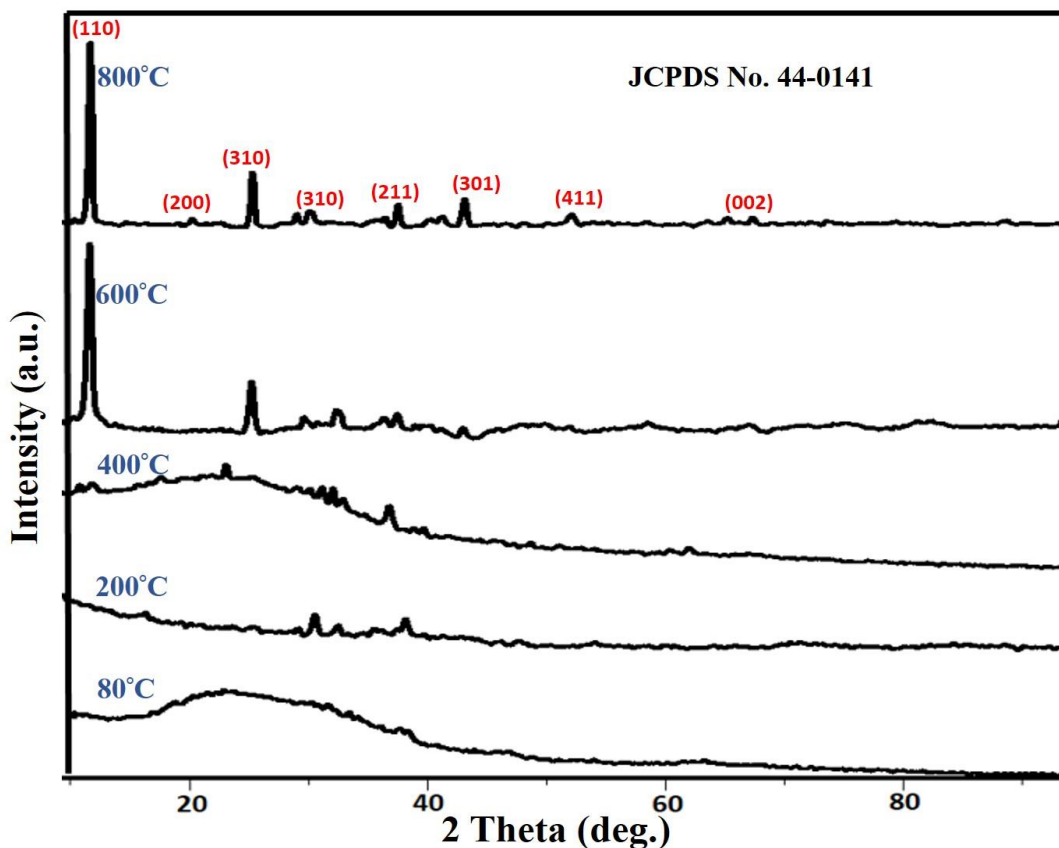


**Figure 2.2:** XRD pattern of MNPs synthesized at different temperatures.

**Figure 2.2** exhibits the XRD patterns of the MNPs synthesized at different temperatures 80, 200, 400, 600 and 800°C respectively. The diffraction peaks were observed located at  $2\theta=12.62, 18.0, 28.7, 37.15, 42.5, 49.8, 65.30^\circ$  (**figure 2.2**) owing to (110), (200), (310), (211), (301), (411), (002) planes corresponding to the tetragonal plane of  $\alpha\text{-MnO}_2$  (JCPDS No. 44-0141). The MNPs synthesized at 80°C temperature were poorly crystalline, while the films deposited at 600 and 800°C temperatures were well crystalline. The intensity of the diffraction peaks increased as the NPs got dispersed at higher temperature (800°C) as compared to diffraction peaks obtained for clustered NPs synthesized at lower temperatures indicating the improved crystallinity of the material. The sharper peak at 800°C temperature shows the crystalline nature of MNPs (**figure**

2.2). MNPs obtained at 80°C temperature were amorphous, and gradually transformed into well-crystalline  $\alpha$ -MnO<sub>2</sub> at higher temperature. No additional peaks were observed other than those corresponding to  $\alpha$ -MnO<sub>2</sub> which indicates the purity of the synthesized material. The above results showed that at 800°C temperature,  $\alpha$ -MnO<sub>2</sub> films were phase-pure and well-crystalline. The size of crystalline nanoparticles was also calculated using Debye-Scherrer equation mentioned below.

$$D = \frac{0.9\lambda}{\beta\cos\theta} \dots\dots\dots (2.3)$$

Where, D represents the mean size of crystals,  $\lambda$ , wavelength of the incident x-ray,  $\beta$ , full width half maxima (FWHM) value of the peaks in radian and  $\theta$ , Bragg angle.

Using the above **equation 2.3**, the size of nanoparticles was estimated to be approximately 13 nm.

#### 2.5.1.4 TGA analysis

TGA was employed to detect the thermal stability of MNPs synthesized at 800°C temperature (**figure 2.3**). The MNPs synthesized at 800°C temperature exhibited a continuous weight loss up till 450°C temperature, which can be credited to loss of structural water molecules [**Jia et al., 2016**]. A dramatic weight loss was then observed at about 500°C temperature, corresponding to the phase change from  $\alpha$ -MnO<sub>2</sub> to apparently Mn<sub>2</sub>O<sub>3</sub> [**Devaraj et al., 2008**]. A total weight loss of 4% was observed in the entire process.

#### 2.5.1.5 FTIR analysis

Fourier transform infrared (FTIR) spectroscopy of the laboratory synthesized nanoparticles was carried out to study the functional groups associated with MNPs through their molecular vibrations (**Sheng et al., 2013; Duan et al., 2016**). The intrinsic stretching vibrations of metal ions present in the lattice are represented by the bands detected below 1000 cm<sup>-1</sup> (**Raj et al., 2015**). The broad band located at 3170 cm<sup>-1</sup> and

the peak at  $1742\text{ cm}^{-1}$  represents the vibration modes (stretching and bending) of O-H group of moisture adsorbed at their surface (Ali et al., 2017) (Figure 2.4).

### 2.5.1.6 BET analysis

The pore structure and surface area of MNPs samples were explored by computing the nitrogen adsorption-desorption isotherm shown in figure 2.5 Brunauer–Emmett–Teller (BET) method was used to measure the surface area of sample, while the  $\text{N}_2$  adsorption-desorption isotherm and pore size was measured using Barrett–Joyner–Halenda (BJH) method at 77K temperature. As seen in figure 2.5, MNPs exhibit typical type IV form of isotherm indicating the presence of mesoporous structure (Sing et al., 2009). The average pore diameter of MNPs was calculated to be 2.7 nm and surface area was found to be  $72.4\text{ m}^2\text{ g}^{-1}$ . The pore size distribution plot shows that the maxima lies in the range of 1-3 nm. The presence of such pore size distribution validates the uniform mesoporous structure of the surface.

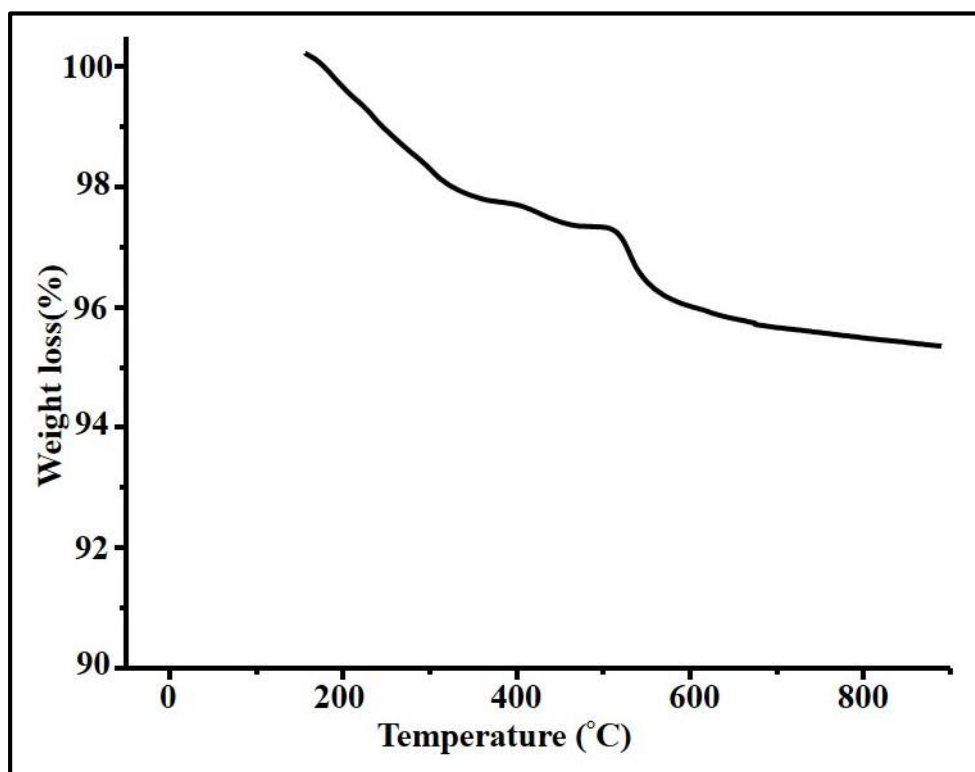


Figure 2.3: TGA of MNPs synthesized at 800°C.

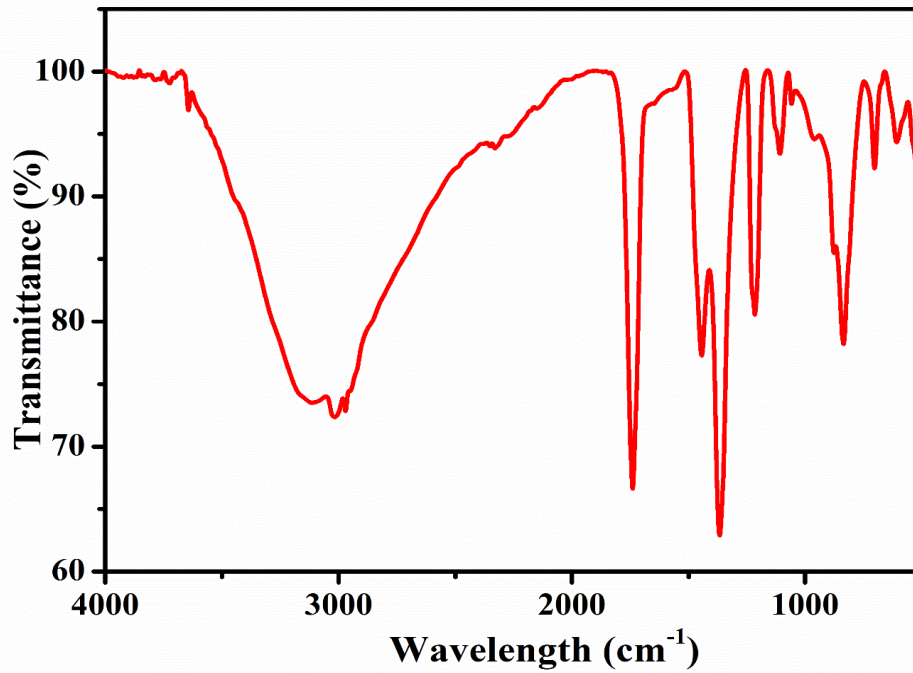


Figure 2.4: FTIR spectra of biofabricated MNPs.

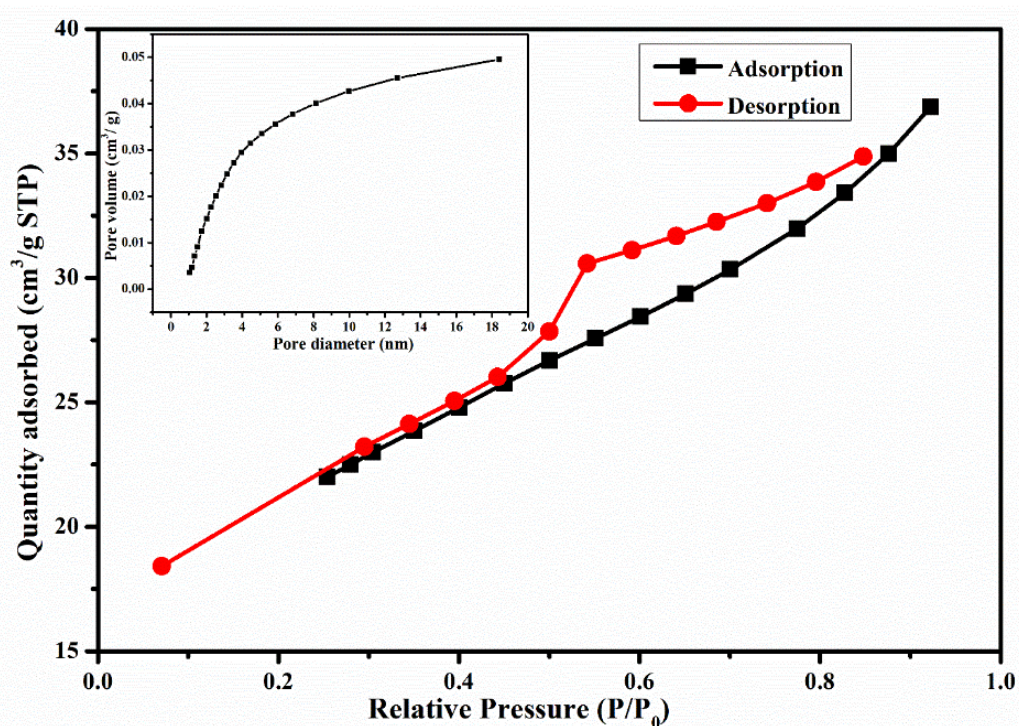


Figure 2.5: Adsorption-desorption isotherm of BET surface area analysis of MNPs.

## 2.5.2 Adsorption studies

### 2.5.2.1 Optimization of pH

The process of adsorption successfully took place only at pH 2 and 3. The adsorptive

property of adsorbate molecules was found to be greatly influenced by the pH of the system. The maximum removal of dye was observed at pH 2 [figure 2.6 (b)]. When the NPs are immersed in water, the hydrophobic nature of the NPs enables them to absorb hydrogen ions on their surface and consequently these particles become positively charged. The positively charged surface of the adsorbent molecules experience a strong electrostatic force of attraction by the negatively charged anionic dye molecules. The adsorption of dyes on to the surface of NPs occurs through a process known as surface mechanism [Stone et al., 1984]. According to this mechanism, adsorption occurs through the formation of surface-precursor complex. The transfer of electrons from organic dyes to the surface of NPs occurs via surface-precursor complex. This mechanism is being followed by several organic pollutants [Petrie et al., 2002; Zhang et al. 2005; Li et al., 2003] as well as dyes [Zhu et al., 2008]. When the pH values were kept lower, the active sites at adsorbent's surface were apparently positively charged and therefore, the negatively charged dyes were electrostatically attracted towards the surface. With increase in pH value, number of positive charges on the surface of adsorbent was deteriorated. At basic pH, there are two factors, which are supposedly responsible for the reduction in adsorption of dyes over adsorbent, the competitive dominance of OH<sup>-</sup> and the force of repulsion created between the surface of adsorbent (which acquire negative charge due to low pH) and negatively charged anions of dyes [Ai et al., 2011]. In consequence, the removal of dyes occurs only in the acidic medium.

#### **2.5.2.2 Optimization of concentration of adsorbent**

The process of adsorption was also analyzed by varying the concentration of adsorbent (NPs) from 5 mg mL<sup>-1</sup> to 30 mg mL<sup>-1</sup>. The concentration of dyes were kept constant i.e., 100 ml of MO = 10 mg L<sup>-1</sup> and MR = 20 mg L<sup>-1</sup>. On increasing the concentration of NPs, the time taken for removal of approximately 95% of dyes (MO and MR dyes) decreased

from 60 min. to 2 min. [figure 2.6 (a)]. As the concentration of adsorbent increased more number of vacant sites became available for the dye molecules to get adsorbed on their surface and therefore, the rate of reaction increased.

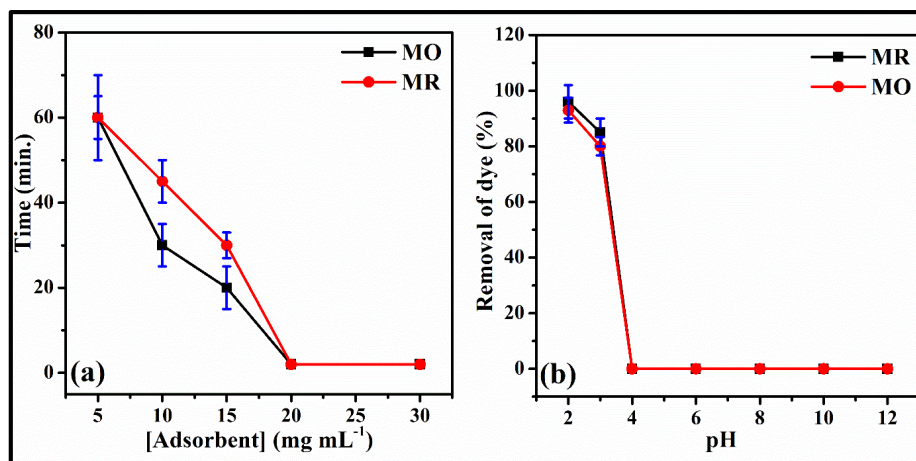


Figure 2.6: Effect of (a) pH and (b) concentration of MNPs on removal of dyes.

### 2.5.2.3 Optimization of contact time

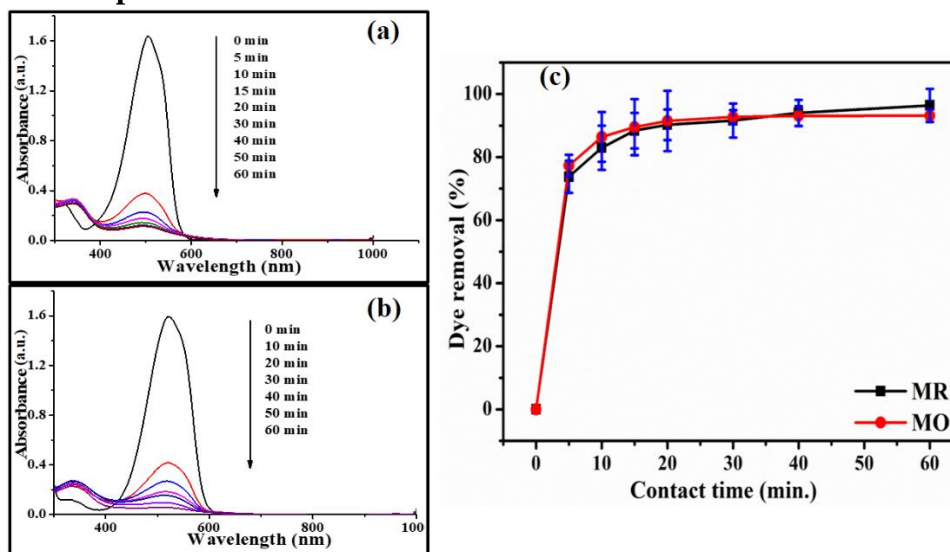


Figure 2.7: Time-dependent UV-Visible absorption spectra for the removal of (a) methyl orange and (b) methyl red dye from their aqueous media at room temperature. (c) Removal of dyes at different contact time.

The most important parameter having an influence in designing of wastewater treatment systems is the equilibrium time. The effect of contact time on the adsorption capacity of synthesized material for dyes was studied, as shown in figure 2.7 (a-c). Figure 2.7 (a) and (b) exhibit the UV-Vis adsorption spectra, which depicts the concentration of MO

and MR dye left in the solution after regular intervals of time. The adsorption of both the dyes (MR and MO dyes) was found to be rapid in the initial period (contact time < 5 min.) which may be attributed to the availability of a large number of vacant active sites on the adsorbent surface. However, with the gradual decrease in the number of vacant adsorption sites, rate of adsorption became lower. The decreased adsorption rate reveals the formation of monolayer of dyes on the surface of adsorbent [Kangralkar et al., 2019]. Although the rate of adsorption decreased after 5 min. but the process continued until almost 100% of dyes got adsorbed on the surface of adsorbent within a time span of 1h.

### 2.5.3 Adsorption kinetics

The kinetics of the adsorption of dyes was studied by analyzing the experimental data through two different kinetic models i.e., pseudo first order [Lagergren, 1898] and pseudo second order [Ho and McKay, 1999; Ho, 2006]. Both linear (coefficient of determination,  $R^2$ ) and non-linear regression analysis (Root mean square error (RMSE) and coefficient of determination,  $R^2$ ) were used to analyze the kinetic models. The linear and non-linear forms of kinetic models are represented in **table 2.1**.

In linear regression analysis, graphs are plotted between  $\log (q_e - q_t)$  vs time  $t$  and  $t/q_t$  vs  $t$  for pseudo first and pseudo second order respectively (**Figure 2.8**). The slope and intercept of the graphs gives the values of rate constants ( $k_1$  and  $k_2$ ) and  $q_e$ .

In case of non-linear regression analysis, graph is plotted between  $q_t$  vs time  $t$  (**Figure 2.9**) and the values of  $k_1$ ,  $k_2$  and  $q_e$  is determined by fitting the data to non-linear kinetic equations.

In both the analysis (linear and non-linear), the calculated value of  $q_e$  showed better compliance with the experimental value of pseudo second order kinetics (**table 2.2** and **2.3**). Moreover, higher value of  $R^2$  and lower RMSE value in case of pseudo second

order kinetics indicated that the process obeyed pseudo second order kinetics. The process following pseudo second order kinetics suggests that the considered process occurred as chemisorption. The values of kinetic parameters calculated using linear and non-linear regression are represented in **table 2.2** and **2.3** respectively.

**Table 2.1: Kinetic model equations used to study dye adsorption onto MNPs**

| Kinetic model       | Linear form  | Non-linear form                    |
|---------------------|--|------------------------------------|
| Pseudo first order  | $\log(q_e - q_t) = \log q_e - \left(\frac{k_1}{2.303}\right)t$ | $\frac{dq}{dt} = k_1(q_e - q_t)$   |
| Pseudo second order | $\frac{t}{q_t} = \frac{1}{k_2 q_e^2} + \frac{t}{q_e}$          | $\frac{dq}{dt} = k_2(q_e - q_t)^2$ |

$q_t$  and  $q_e$  ( $\text{mg g}^{-1}$ ), adsorption capacity of adsorbent at time  $t$  and equilibrium respectively.

$k_1$  ( $\text{min.}^{-1}$ ) and  $k_2$  ( $\text{g mg}^{-1} \text{min.}$ ), rate constants for pseudo first order and pseudo second order process respectively.

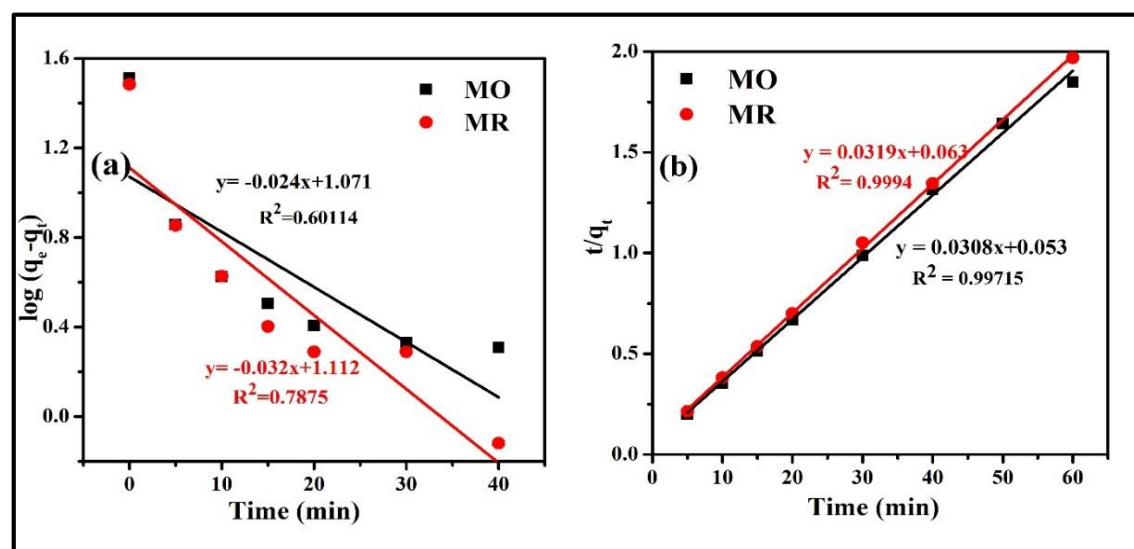


**Figure 2.8: (a) Pseudo first order and (b) Pseudo second order kinetics for adsorption of dyes over MNPs in linear regression analysis.**

**Table 2.2: Kinetic model parameters calculated using linear regression analysis of methyl orange and methyl red dye adsorption on MNPs**

| Kinetic models      | Parameter                               | Value of parameters |             |
|---------------------|---|---------------------|-------------|
|                     |   | MO dye              | MR dye      |
| Pseudo first order  | $k_1$ (min. <sup>-1</sup> )             | 0.05                | 0.07        |
|                     | $q_e$ (cal./theo.)(mg g <sup>-1</sup> ) | 11.74/32.42         | 12.82/30.47 |
|                     | $R^2$                                   | 0.601               | 0.787       |
| Pseudo second order | $k_2$ (g mg <sup>-1</sup> min.)         | 0.017               | 0.017       |
|                     | $q_e$ (cal./theo.)(mg g <sup>-1</sup> ) | 32.47/32.42         | 31.26/30.47 |
|                     | $R^2$                                   | 0.997               | 0.999       |

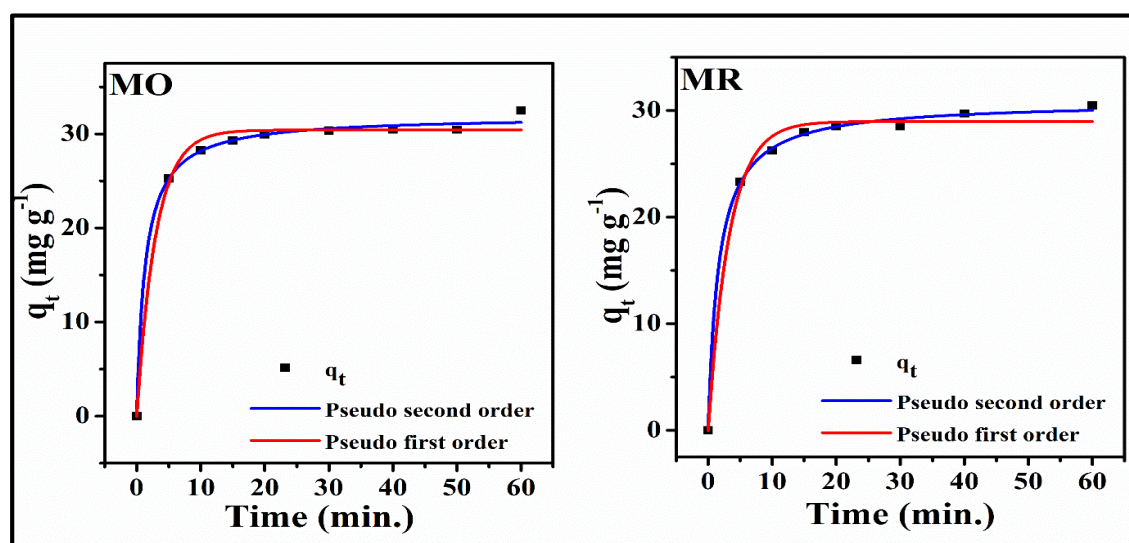


**Figure 2.9: Representation of kinetic models for adsorption of methyl orange and methyl red dyes over MNPs in non-linear regression analysis.**

**Table 2.3: Kinetic model parameters calculated using non-linear regression analysis of methyl orange and methyl red dye adsorption on MNPs**

| Kinetic models      | Parameter                                      | Value of parameters |             |
|---------------------|--|---------------------|-------------|
|                     |  | MO dye              | MR dye      |
| Pseudo first order  | $k_1$ (min. <sup>-1</sup> )                    | 0.33                | 0.30        |
|                     | $q_e$ (cal./ $q_e$ theo.)(mg g <sup>-1</sup> ) | 30.41/32.42         | 28.97/30.47 |
|                     | $R^2$  | 0.990               | 0.990       |
|                     | RMSE   | 2.01                | 0.86        |
| Pseudo second order | $k_2$ (g mg <sup>-1</sup> min.)                | 0.02                | 0.01        |
|                     | $q_e$ (cal./ $q_e$ theo.)(mg g <sup>-1</sup> ) | 31.97/32.42         | 30.84/30.47 |
|                     | $R^2$  | 0.996               | 0.998       |
|                     | RMSE   | 0.50                | 0.31        |

#### 2.5.4 Adsorption isotherm

The isotherm study has been carried out to analyse the interaction between the adsorbent and adsorbate of the system. The adsorption equilibrium of MO and MR dyes onto synthesized NPs was studied by adding 30 mg of MNPs to 50 mL of MO and MR dye solutions of concentration varying from 10-60 mg L<sup>-1</sup>.

With increasing concentration of dyes, an increase in the adsorption capacity of NPs was observed, which indicates that adsorption capacity is directly proportional to concentration of dyes (**figure 2.12**). The possible reason of this observation may be the increase in the probability of collision between the adsorption sites on the surface of NPs and dye.

Although the adsorption capacities of NPs were found to be directly proportional to the concentration of dyes but the percentage of removal of dyes exhibit an inverse relationship with its concentration (**figure 2.12**).

In this work, three isotherm models, Langmuir, Freundlich and Temkin were employed for both linear and non-linear regression analysis to interpret the equilibrium of MO and MR dyes adsorbed onto MNPs. The linear and non-linear form of isotherm models are represented in **table 2.4**.

The linear plots of the three considered isotherms for MO and MR dyes adsorption are represented in **figure 2.11**. Values of different parameters obtained from Langmuir, Freundlich and Temkin isotherms through linear regression analysis is presented in **table 2.5**. Based on the values of R<sup>2</sup>, it can be concluded that for adsorption of both MO and MR dyes, Langmuir isotherm model correlated better than Freundlich and Temkin isotherm model, suggesting the mono layer adsorption of dye over the surface of NPs. According to Langmuir isotherm, maximum adsorption capacities  $q_{\max}$  of MO and MR dyes at pH 2.0 were found to be 116.1 and 74.02 mg g<sup>-1</sup> respectively. In Freundlich isotherm model, the value of n is an important factor. The value of n being greater than 1 indicates favourable

adsorption. The value of  $n$  for MO and MR dyes is 2.96 and 1.78, indicating the good adsorption [Al-Ghouti et al., 2005]. The value of Temkin constants as presented in **table 2.5** was found to be 20.57 and 15.94 for MO and MR dye respectively. The positive value of  $B$  indicates that the adsorption process was exothermic [Hadi et al., 2010]. Although linear regression method is used to study the adsorption process but there are certain issues associated with it, such as, converting the non-linear equation into its linear form [Piccin et al., 2017]. The modification in the original equation breaches the theories on which these models are based and eventually compromises all the estimated parameters, and the consequent interpretations. Therefore, non-linear regression method is more feasible method as compared to linear regression method for estimating isotherm model parameters. Non-linear regression method uses original equations and, therefore, none of the theories of models are being violated and the parameters obtained are more relevant. The linear regression method assumes the Gaussian distribution of points around the straight line and the standard deviation at every value of  $C_e$ , which is practically impossible. These types of errors can be avoided by using non-linear regression technique for estimation of isotherm model parameters [Tvrđik et al., 2007].

For non-linear regression analysis, the isotherm models (Langmuir, Freundlich and Temkin) were described by using equations mentioned in **table 2.4**. The graph plotted between  $C_e$  vs  $q_e$  is shown in **figure 2.10**. Root mean square error (RMSE) and coefficients of determination ( $R^2$ ) were calculated for comparing the three isotherm models. The results (isotherm parameters, RMSE and  $R^2$ ) obtained for MO and MR dye adsorption on MNPs, are presented in **table 2.6**. Comparing the values obtained of RMSE and  $R^2$  for the three isotherms, the best fit model for both the dyes was found to be Langmuir model (lowest RMSE and highest  $R^2$ ).

As shown in **table 2.5** and **2.6**, the values of parameters obtained using linear and non-linear regression are in good agreement with each other. Therefore, it can be concluded that Langmuir model describes the adsorption process in the best possible manner.

**Table 2.4: Equilibrium model equations used to investigate methyl orange and methyl red dye adsorption over MNPs**

| Isotherm model    | Linear form  | Non-linear form   |
|-------------------|--|---|
| <b>Langmuir</b>   | $\frac{C_e}{q_e} = \frac{1}{q_{max}b} + \frac{C_e}{q_{max}}$ | $q_e = \frac{q_{max} \cdot b \cdot C_e}{1 + b \cdot C_e}$ |
| <b>Freundlich</b> | $\ln q_e = \ln K_f + \frac{1}{n} \ln C_e$                    | $q_e = K_f \cdot C_e^{1/n}$                               |
| <b>Temkin</b>     | $q_e = B \ln K_T + B \ln C_e$                                | $q_e = B \ln K_T \cdot C_e$                               |

$q_{max}$  ( $\text{mg g}^{-1}$ ) is the maximum monolayer adsorption capacity and  $b$  ( $\text{L mg}^{-1}$ ), Langmuir constant.

$K_f ((\text{mg g}^{-1})(\text{L mg}^{-1})^{-1/n})$  is Freundlich constant.

$B = RT/b$ , where  $b$  is the Temkin constant ( $\text{J mol}^{-1}$ ),  $R$ , universal gas constant ( $8.314 \text{ J mol}^{-1}\text{K}^{-1}$ ) and  $K_T$ , equilibrium binding constant ( $\text{L g}^{-1}$ ).

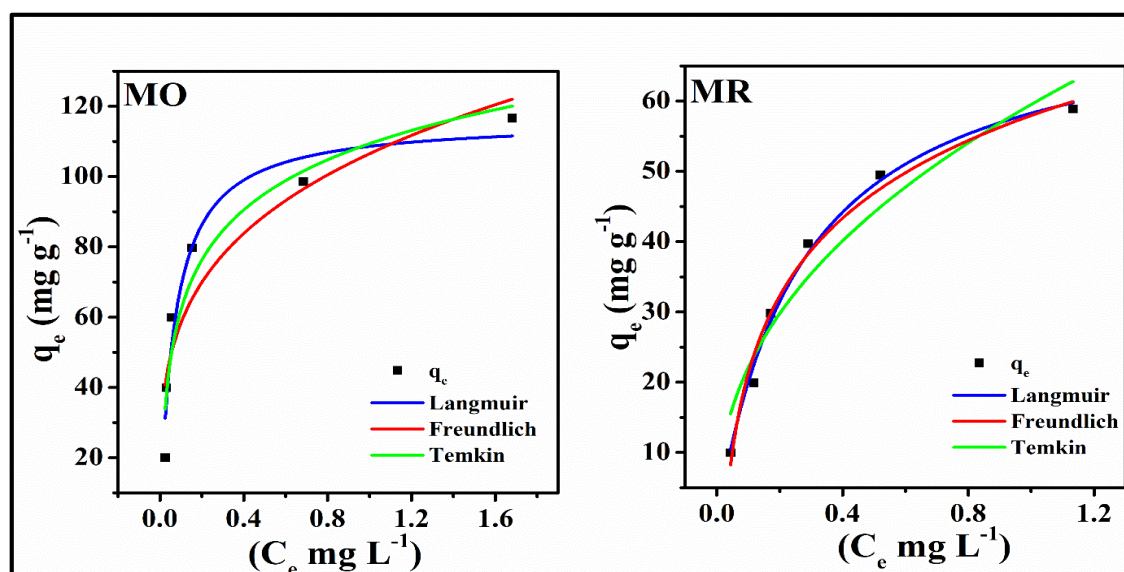


**Figure 2.10: Representation of Langmuir, Freundlich and Temkin isotherm models for MNPs in non-linear regression analysis.**

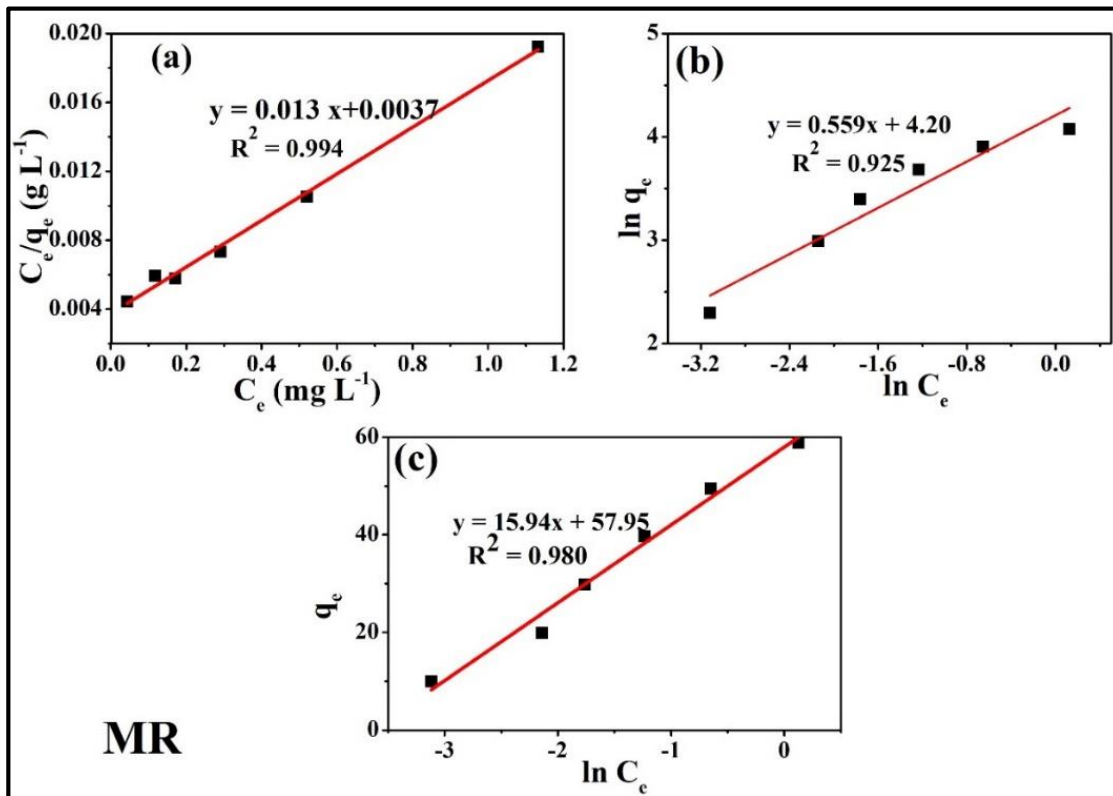
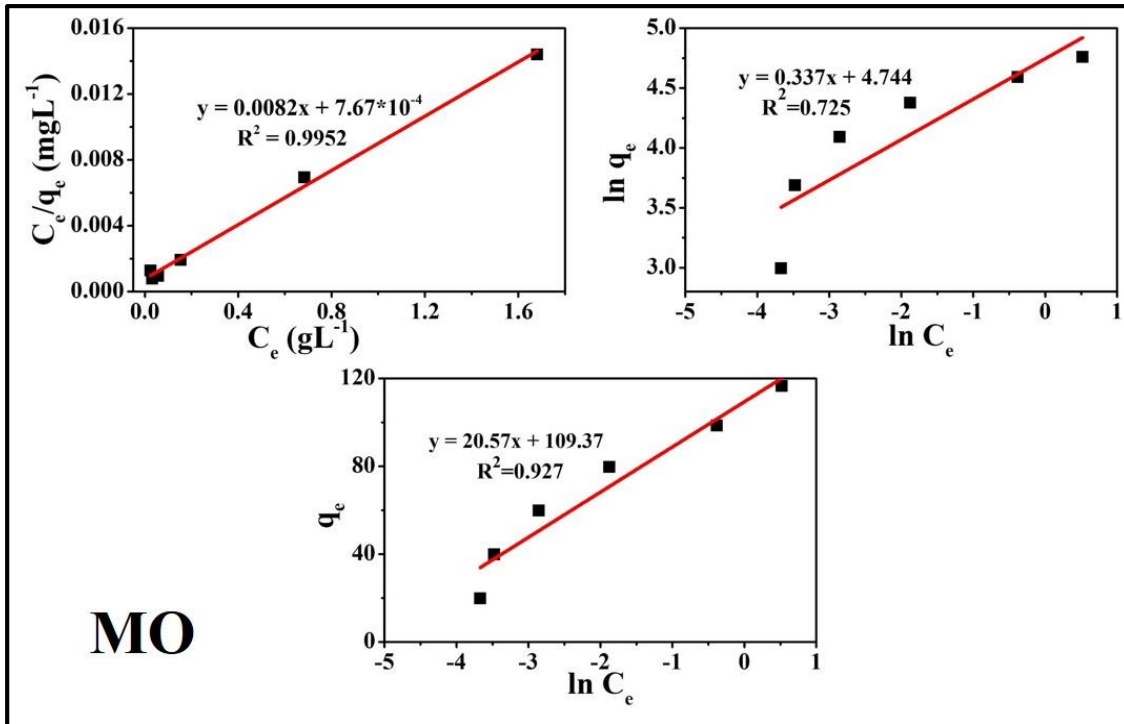


Figure 2.11: (a) Langmuir, (b) Freundlich and (c) Temkin isotherm for adsorption of methyl orange and methyl red dyes over MNPs using linear form of models.

**Table 2.5: Adsorption isotherm models and their coefficients calculated using linear regression analysis for methyl orange and methyl red dye adsorption onto MNPs**

| Isotherm model | Parameters   | Values |        |
|----------------|--|--------|--------|
|                |  | MO dye | MR dye |
| Langmuir       | $q_{\max}(\text{mg g}^{-1})$                       | 121.90 | 74.00  |
|                | $R^2$  | 0.995  | 0.994  |
| Freundlich     | $n$  | 2.96   | 1.78   |
|                | $K_f((\text{mg g}^{-1})(\text{L mg}^{-1})^{-1/n})$ | 114.80 | 67.20  |
|                | $R^2$  | 0.725  | 0.925  |
| Temkin         | $B$  | 20.57  | 15.94  |
|                | $K_T(\text{L g}^{-1})$                             | 203.50 | 37.90  |
|                | $R^2$  | 0.927  | 0.980  |

**Table 2.6: Non-linear regression analysis of adsorption isotherm models for methyl orange and methyl red dye adsorption onto MNPs**

| Isotherm models | Parameter  | Parameter values |        |
|-----------------|--|------------------|--------|
|                 |  | MO dye           | MR dye |
| Langmuir        | $q_{\max}(\text{mg g}^{-1})$                     | 116.10           | 74.02  |
|                 | $R^2$  | 0.949            | 0.991  |
|                 | RMSE   | 6.69             | 1.35   |
| Freundlich      | $n$  | 3.81             | 2.32   |
|                 | $K_f(\text{mg g}^{-1})(\text{L mg}^{-1})^{-1/n}$ | 106.50           | 59.52  |
|                 | $R^2$  | 0.852            | 0.919  |
|                 | RMSE   | 111.30           | 4.20   |
| Temkin          | $B$  | 20.56            | 15.94  |
|                 | $K_T(\text{L g}^{-1})$                           | 203.50           | 37.80  |
|                 | $R^2$  | 0.927            | 0.980  |
|                 | RMSE   | 15.80            | 2.00   |

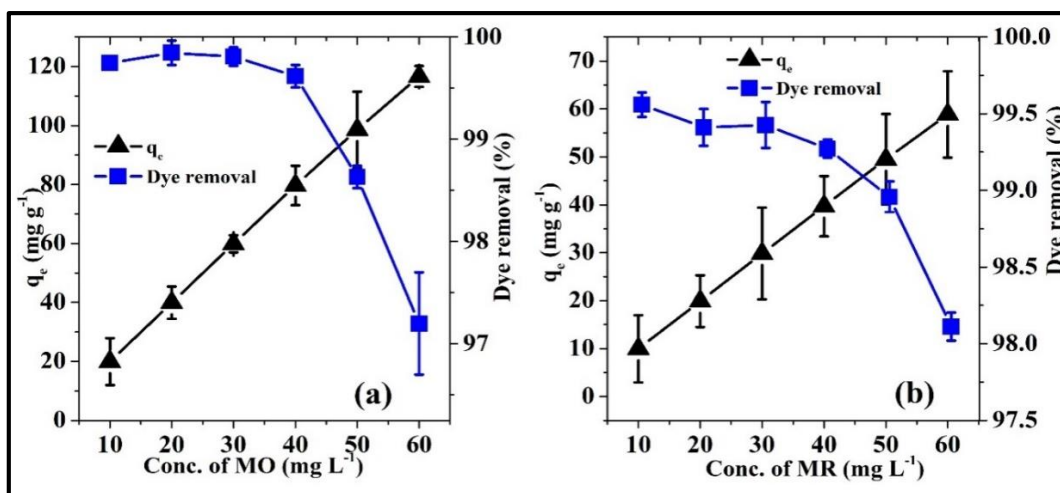


**Figure 2.12: Effect of initial concentration of dyes (methyl orange and methyl red) on dye adsorption and percentage of dye removal using 30 mg of adsorbent.**

### Comparison with other existing adsorbents

A comparative chart has been presented in **table 2.7** and **2.8**, which exhibit the list of adsorbents that have been used in the past for adsorption of MO and MR dyes. From the tables, it can be seen that the adsorption capacity of MNPs is far more superior as compared to other reported adsorbents. On the basis of these results, MNPs are green adsorbents with efficiency in removing MO and MR dyes from their aqueous solutions.

**Table 2.7: Comparison of adsorption capacity of methyl orange dye with other reported adsorbents**

| Adsorbent   | $q_{\max}$ (mg g <sup>-1</sup> ) | Reference                    |
|---|----------------------------------|------------------------------|
| Ferric oxide–biochar nanocomposites derived from pulp and paper sludge      | 16.05                            | <b>Nhamo et al., 2016</b>    |
| NiO NPs   | 11.21                            | <b>Falaki et al., 2013</b>   |
| Novel magnetic CNTs/Fe@C  | 16.53                            | <b>Ma et al., 2018</b>       |
| Hexagonal shaped nanoporous carbon  | 18.8                             | <b>Kundu et al., 2017</b>    |
| Modified ultrafine coal powder  | 18.52                            | <b>Liu et al., 2009</b>      |
| Polyacrylonitrile-coated kapok hollow microtubes                            | 34.72                            | <b>Agcaoilo et al., 2017</b> |
| Modified fly ash with Ca(OH) <sub>2</sub> /Na <sub>2</sub> FeO <sub>4</sub> | 23.8                             | <b>Zaheer et al., 2019</b>   |
| <b>MNPs</b>   | <b>116.1</b>                     | <b>Present work</b>          |

**Table 2.8: Comparison of adsorption capacity of methyl red dye with other reported adsorbents**

| Adsorbent  | q <sub>max</sub> (mg g <sup>-1</sup> ) | Reference            |
|--|--|----------------------|
| Commercially available powdered activated carbon                     | 48.42                                  | Saad et al., 2010    |
| Sugarcane bagasse (Pre-treated with phosphoric acid)                 | 10.98                                  |                      |
| Modified zeolite commercial activated charcoal                       | 7                                      | Ioannou et al., 2013 |
| Banana pseudo stem fibers  | 88.50                                  | Haris et al., 2009   |
| SiO <sub>2</sub> -coated Fe <sub>3</sub> O <sub>4</sub> magnetic NPs | 49.50                                  | Masoud et al., 2014  |
| <b>MNPs</b>  | <b>74.02</b>                           | <b>Present work</b>  |

### 2.5.5 Adsorption thermodynamics

The thermodynamic behaviour of dye adsorption has been described by evaluating various thermodynamic parameters like change in entropy ( $\Delta S^\circ$ ), enthalpy ( $\Delta H^\circ$ ), and free energy ( $\Delta G^\circ$ ) using following **equations 2.4** and **2.5**:

$$\log K_c = \frac{-\Delta H^\circ}{2.303RT} + \frac{\Delta S^\circ}{2.303R} \quad \dots\dots\dots (2.4)$$

and

$$\Delta G = -2.303 RT \log K_c \quad \dots\dots\dots (2.5)$$

Where, T is absolute temperature (in Kelvin) and R, gas constant (8.3144 J/Kmol).

The value of equilibrium constant  $K_c$  is calculated using following **equation 2.6**:

$$K_c = \frac{C_{Ae}}{C_e} \quad \dots\dots\dots (2.6)$$

Where,  $C_{Ae}$ , and  $C_e$  are the dye concentrations at equilibrium in solid phase and in solution phase respectively.

The adsorption of dyes (MO and MR) is studied over a range of temperature varying from 288 to 348 K using MNPs as an adsorbent. The experimental data show that the

adsorption capacity is inversely proportional to the temperature (**figure 2.13 a and c**). The rise in temperature decreases the ability of dye molecules to interact with the nanoparticles [**Priyadarshini et al., 2020**]. There may be two factors responsible for this behaviour (i) weakening of adsorptive forces in the adsorbent-adsorbate system and (ii) increase in the solubility of dyes with temperature.

The van't Hoff equation (**eq. 2.4**), directs the plot between  $\log K_c$  vs  $1/T$  which shows a straight line for both MO and MR in **figure 2.13 (b) and (d)**. The slope and intercept of the plot gives the values of thermodynamic parameters ( $\Delta G^\circ$ ,  $\Delta S^\circ$ , and  $\Delta H^\circ$ ) as tabulated in **table 2.9**. Negative value of  $\Delta G^\circ$  and  $\Delta H^\circ$  depicts that the adsorption processes for MO and MR dyes were spontaneous, favourable [**Li et al., 2005; Tran et al., 2017**] and exothermic in nature. The negative value of  $\Delta S^\circ$  shows the decrease in randomness of the adsorption system as MO and MR dyes were adsorbed by MNPs.

**Table 2.9: Thermodynamic parameters for adsorption of methyl orange and methyl red dye on MNPs at pH 2**

| Temperature (°C) | $-\Delta G^\circ$ (kJmol <sup>-1</sup> ) | $\Delta S^\circ$ (JK <sup>-1</sup> mol <sup>-1</sup> ) | $\Delta H^\circ$ (kJ mol <sup>-1</sup> ) | $K_c$ |
|------------------|--|--|--|-------|
| <b>MO dye</b>    |  |  |  |       |
| 15               | 10.00                                    | -93.62   | -36.43                                   | 65.23 |
| 25               | 8.15                                     |  |  | 26.87 |
| 35               | 7.19                                     |  |  | 16.60 |
| 55               | 5.20                                     |  |  | 6.76  |
| 75               | 4.37                                     |  |  | 4.52  |
| <b>MR dye</b>    |  |  |  |       |
| 15               | 9.11                                     | -58.09   | -25.67                                   | 45.02 |
| 25               | 8.19                                     |  |  | 27.30 |
| 35               | 7.93                                     |  |  | 22.17 |
| 55               | 6.12                                     |  |  | 9.45  |
| 75               | 5.80                                     |  |  | 7.43  |

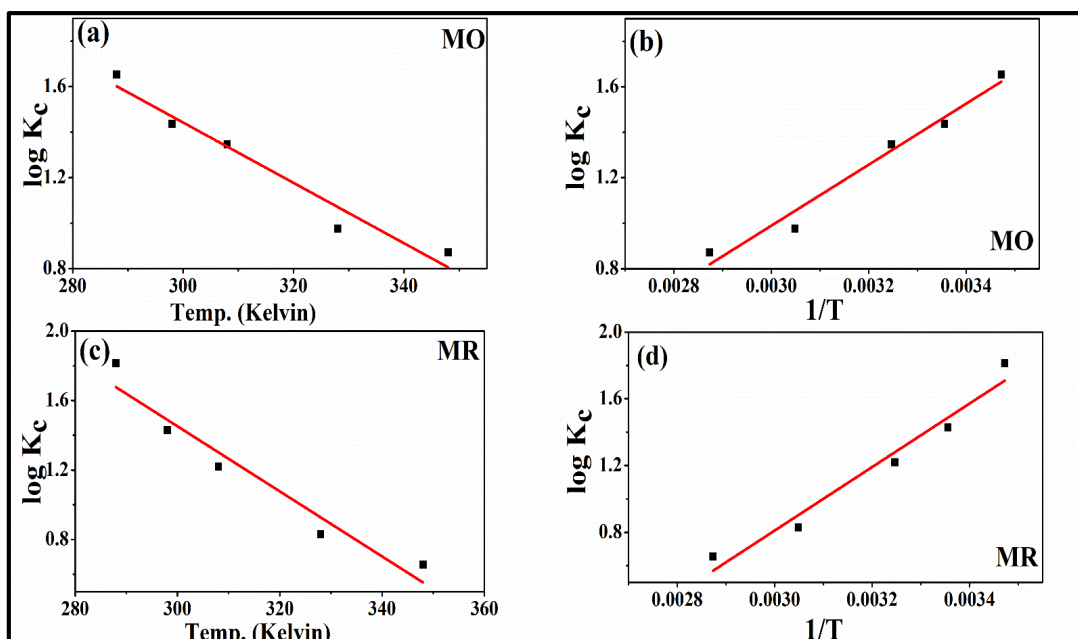


**Figure 2.13: Effect of temperature on adsorption of methyl orange and methyl red (a) Equilibrium constant for methyl orange on MNPs as function of temperature, (b) Van't Hoff plot for exchange of methyl orange with MNPs, (c) Equilibrium constant for methyl red on MNPs as function of temperature and (d) Van't Hoff plot for exchange of methyl red with MNPs.**

## 2.6 Reusability of adsorbent

When the process was completed, NPs were recovered from the solution by the process of centrifugation. The recovered adsorbent (i.e., NPs) was washed with distilled water, air dried and then subjected to another cycle of adsorption. The process was repeated six times (for both the dyes) to observe the reusability of adsorbent. As shown in **figure 2.14**, NPs were found to be reusable for six successive cycles with an efficiency of more than 95%, which depict that adsorbents are not only efficient but stable as well. The adsorptive property of the NPs remained constant even after six cycles unlike various adsorbents reported previously [Naushad et al., 2019; Banerjee et al., 2017; Istratie et al., 2016] which are although reusable but the efficiency of adsorption decreases with each repetitive cycle.

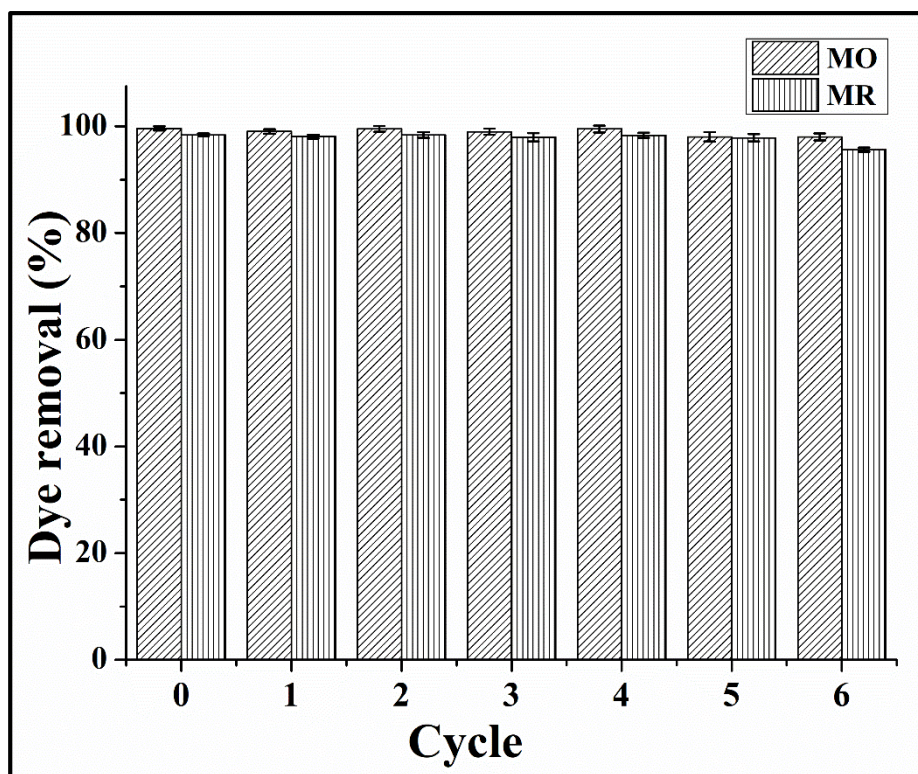


**Figure 2.14: Recyclability of MNPs in the removal of methyl red and methyl orange dyes.**

## 2.7 Conclusions

$\alpha$ -MnO<sub>2</sub> nanoparticles have been successfully synthesized through a cost effective green route by the reduction of potassium permanganate using leaf extract of *F. retusa* at 800°C temperature. XRD measurement revealed the sequence of temperature dependent phase transformation of  $\alpha$ -MnO<sub>2</sub> nanoparticles from amorphous to crystalline phase on heat treatment in the temperature range of 80-800°C. At 800°C temperature, pure phase and well crystalline spherical nanoparticles of  $\alpha$ -MnO<sub>2</sub> in the size range of 30-50 nm were obtained.

Furthermore, the synthesized nanoparticles were used as an adsorbent for removal of azo dyes such as methyl orange and methyl red. It was found that the effective removal of azo dyes was achieved in acidic medium using the nanoparticles. The degree of removal of methyl orange and methyl red using  $\alpha$ -MnO<sub>2</sub> nanoparticles reached approximately 98% within 5 min. using higher concentration of nanoparticles. The process of adsorption

obeyed Langmuir model of adsorption isotherm following pseudo second order kinetics. Thermodynamic study exhibited that the process was feasible, spontaneous and exothermic in nature. The results thereby, support the possible environment friendly application of these nanoparticles to wastewater treatment. The as-prepared nanoparticles exhibited efficient adsorption ability with good recyclability for methyl orange and methyl red dye removal.

## References

- Agcaoili, A.R., Herrera, M.U., Futralan, C.M., and Balela, M.D.L. (2017). Fabrication of polyacrylonitrile coated kapok hollow microtubes for adsorption of methyl orange and Cu (II) ions in aqueous solution. *J Taiwan Inst Chem Eng.*, 78, 359-369. doi:10.1016/j.jtice.2017.06.038.
- Ahmad, M.A., Ahmed, N.B., Adegok, K.A., and Bello, O.S. (2019). Sorption studies of methyl red dye removal using lemon grass (*Cymbopogon citratus*). *Chem Data Collections*, 22, 100249. <https://doi.org/10.1016/j.cdc.2019.100249>.
- Ai, L., Zhang, C., and Meng, L. (2011). Adsorption of Methyl Orange from Aqueous Solution on Hydrothermal Synthesized Mg À Al Layered Double Hydroxide. *J Chem.*, 56, 4217–4225. doi: 10.1021/jc200743u.
- Al-Bastaki N. (2004). Removal of methyl orange dye and Na<sub>2</sub>SO<sub>4</sub> salt from synthetic wastewater using reverse osmosis. *Chemical Engineering and Processing: Process Intensification*, 43,1561–1567. <https://doi.org/10.1016/j.cep.2004.03.001>.
- Al-Ghouthi, M., Khraisheh, M.A.M., Ahmad, M.N.M., Allen, S. (2005). Thermodynamic behaviour and the effect of temperature on the removal of dyes from aqueous solution using modified diatomite: a kinetic study. *J Colloid Interface Sci.*, 287, 6–13. <https://doi.org/10.1016/J.JCIS.2005.02.002>.
- Ali, G.A.M., Yusoff, M.M., Shaaban, E.R., Chong, K.F. (2017). High performance MnO<sub>2</sub> nanoflower supercapacitor electrode by electrochemical recycling of spent batteries. *Ceram. Int.*, 43, 8440–8448. <https://doi.org/10.1016/j.ceramint.2017.03.195>.
- Andreozzi, R., Insola, A., and Tufano, V. (1996). The use of manganese dioxide as a heterogeneous catalyst for oxalic acid ozonation in aqueous solution. *Applied Cat A: General* 138, 75–8. [https://doi.org/10.1016/0926-860X\(95\)00247-2](https://doi.org/10.1016/0926-860X(95)00247-2).
- Anil kumar, M., and Ravi, S. (2005). Synthesis of nanocrystalline Mn<sub>3</sub>O<sub>4</sub> at 100°C. *Materials Research Bulletin*, 40, 605–609. <https://doi.org/10.1016/j.materresbull.2005.01.009>.
- Bar, H., Bhui, D.K., Sahoo, G.P., Sarkar, P., De, S.P., and Misra, A. (2009). Green synthesis of silver NPs using latex of *Jatropha curcas*. *Colloids and Surfaces A: Physicochemical and Engineering Aspects*, 339, 134–139. <https://doi.org/10.1016/j.colsurfa.2009.02.008>.
- Banerjee, S., Dubey, S., Gautam, R.K., Chattopadhyaya, M.C., and Sharma, Y.C. (2017). Adsorption characteristics of alumina nanoparticles for the removal of hazardous dye, Orange G from aqueous solutions. *Arabian J Chem.* doi:10.1016/j.arabjc.2016.12.016.
- Barak, A., Goel, Y., Kumar, R., and Shukla, S.K. (2019). Removal of Methyl orange over TiO<sub>2</sub>/polyacrylamide hydrogels. *Mat Today: Proceedings*, 12, 529-535. <https://doi.org/10.1016/j.matpr.2019.03.094>.
- Bing, Y., Zhang, L., Mu, S., and Zhang, J. (2017). Facile Synthesis of α-MnO<sub>2</sub> with a 3D staghorn coral like micro structure assembled by nanorods and its application in

electrochemical supercapacitors. *Applied Sciences*, 7, 511. <https://doi.org/10.3390/app7050511>.

Bouazizi, A., Breida, M., Achiou, B., Ouammou, M., Calvo, J.I., Aaddane, A., and Younssi, S.A. (2017). Removal of dyes by a new nano-TiO<sub>2</sub> ultrafiltration membrane deposited on low-cost support prepared from natural Moroccan bentonite. *Applied Clay Science*, 149, 127–135. <https://doi.org/10.1016/j.clay.2017.08.019>.

Brillas, E., and Martínez-Huitle, C.A. (2015). Decontamination of wastewaters containing synthetic organic dyes by electrochemical methods: An updated review. *Appl Catal B: Environ.*, 166, 603-643. <https://doi.org/10.1016/j.apcatb.2014.11.016>.

Carmen, Z., and Daniela, S. (1996). Organic pollutants ten years after the environmental and analytical update, InTech, Rijeka.

Cheng, L., Abraham, N., Masakuni, T., Isao, H., and Hajime, T. (2008). Antioxidant flavonoid glycosides from the leaves of *Ficus pumila*L. *Food Chem.*, 109:415–420. <https://doi.org/10.1016/j.foodchem.2007.12.069>.

Davar, F., Salavati-niasari, M., Mir, N., Saberyan, K., and Monemzadeh, M. (2010). Thermal decomposition route for synthesis of Mn<sub>3</sub>O<sub>4</sub> NPs in presence of a novel precursor. *Polyhedron*, 29, 1747–1753. <https://doi.org/10.1016/j.poly.2010.02.026>.

Devaraj, S., and Munichandraiah, N. (2008). Effect of Crystallographic Structure of MnO<sub>2</sub> on its electrochemical capacitance properties. *J Phys Chem C*, 112, 4406-4417. <https://doi.org/10.1021/jp7108785>.

Duan, W., Vemuri, R.S., Milshtein, J.D. et al. (2016). A symmetric organic-based nonaqueous redox flow battery and its state of charge diagnostics by FTIR. *J. Mat. Chem.*, 4, 15, 5448-5456. <https://doi.org/10.1039/c6ta01177b>.

Durmus, S., Baykal, A., Kavas, H., Direkçi, M., and Toprak, M.S. (2009). Ovalbumin mediated synthesis of Mn<sub>3</sub>O<sub>4</sub>. *Polyhedron*, 28, 2119–2122. <https://doi.org/10.1016/j.poly.2009.03.026>.

Falaki, F., and Fakhri, A. (2013). Study of the adsorption of methyl orange from aqueous solution using nickel oxide NPs: Equilibrium and Kinetics Studies. *Journal of Physical and Theoretical Chemistry*, 10, 117-124.

Fang, W., Tang, K., Gao, L., and Wang, D. (2007). Facile and large-scale synthesis of single crystalline manganese oxyhydroxide/oxide nanostructures. *Mat Research Bulletin*, 42, 1761–1768. <https://doi.org/10.1016/j.materresbull.2006.11.025>.

Fei, B.J., Cui, Y., Yan, X., Qi, W., Yang, Y., Wang, K., He, Q., and Li, J. (2008). Controlled preparation of MnO<sub>2</sub> hierarchical hollow nanostructures and their application in water treatment. *Advanced Materials*, 20, 452–456. <https://doi.org/10.1002/adma.200701231>.

Hachem, C., Bocquillon, F., Zahrgaa, O., and Bouchy, M. (2001). Decolourization of textile industry wastewater by the photocatalytic degradation process. *Dyes and Pigments*, 49, 117–125. [https://doi.org/10.1016/S0143-7208\(01\)00014-6](https://doi.org/10.1016/S0143-7208(01)00014-6).

Hadi, M., Samarghandi, M.R., and McKay, G. (2010). Equilibrium two-parameter isotherms of acid dyes sorption by activated carbons: Study of residual errors. *Chem Eng J.*, 160, 408–416. <https://doi.org/10.1016/j.cej.2010.03.016>.

Hansson, A., Zelada, J.C., and Noriega, H.P. (2005). Re-evaluation of risks with the use of *Ficus insipida* latex as a traditional anthelmintic remedy in the Amazon. *J Ethno-Pharmacology*, 98, 251–257. <https://doi.org/10.1016/j.jep.2004.12.029>.

Haris, M.R.H.M., and Sathasivam, K. (2009). The removal of methyl red from aqueous solutions using banana pseudo stem fibers. *Am. J. Appl. Sci.*, 6, 1690–1700. doi: <https://doi.org/10.3844/ajassp.2009.1690.1700>.

Hasnain, M.S., Javed, N., Alam, S., and Rishishwar, P. (2019). Purple heart plant leaves extract-mediated silver nanoparticle synthesis: Optimization by Box-Behnken design. *Materials Science and Engineering C*, 99, 1105–1114. <https://doi.org/10.1016/j.msec.2019.02.061>.

Ho, Y.S. (2006). Review of second order models for adsorption systems. *J Hazard Mat.*, 136, 681.

Ho, Y.S., McKay, G. (1999). Pseudo second order model for sorption processes. *Process Biochemistry*, 34, 451.

Hu, C., Grant, D., Hou, X., and Xu, F. 2020. High Rhodamine B and methyl orange removal performance of graphene oxide/carbon nanotube nanostructure. *Mat Today: Proceedings*. <https://doi.org/10.1016/j.matpr.2020.02.711>.

Ioannou, Z., Karasavvidis, C., Dimirkou, A., and Antoniadis, V. (2013). Adsorption of methylene blue and methyl red dye from aqueous solutions onto modified zeolite. *Water Sci. Technol.*, 67, 1129–1136. doi: 10.2166/wst.2013.672.

Istratie, R., Stoia, M., Păcurariu, C., and Locovei, C. (2016). Single and simultaneous adsorption of methyl orange and phenol onto magnetic iron oxide/carbon nanocomposites. *Arabian J Chem*. doi:10.1016/j.arabjc.2015.12.012.

Jaganyi, D., Altaf, M., and Wekesa, I. (2012). Synthesis and characterization of whisker-shaped MnO<sub>2</sub> nanostructure at room temperature. *Applied Nanoscience*, 3, 329–333. <https://doi.org/10.1007/s13204-012-0135-3>.

Jain, R., and Sikarwar, S. (2006). Photocatalytic and adsorption studies on the removal of dye Congo red from wastewater. *Int J Environment and Pollution*, 27, 158–178. <http://dx.doi.org/10.1504/IJEP.2006.010460>.

Jia, J., Zhang, P., and Chen, L. (2016). The effect of morphology of  $\alpha$ -MnO<sub>2</sub> on catalytic decomposition of gaseous ozone. *Catalysis Science and Technology*, 6, 5841–5847. doi:10.1039/c6cy00301j.

Kangralkar, M.V., Kangralkar, V.A., Momin, N., and Manjanna, J. (2019). Cu<sub>2</sub>O NPs for removal of methylene blue dye from solution. *Environmental Nanotechnology Monitoring and Management*, 100265. <https://doi.org/10.1016/j.enmm.2019.100265>.

Kausar, A., Iqbal, M., Javed, A., Aftab, K., Nazli, Z., Bhatti, H.N., and Nouren, S. (2018). Dyes adsorption using clay and modified clay: A review. *J Mol Liq.*, 256, 395-407. doi:10.1016/j.molliq.2018.02.03

Klekotko, M., Brach, K., Olesiak-banska, J., and Samoc, M. (2019). Popcorn-shaped gold NPs: Plant extract-mediated synthesis, characterization and multiphoton-excited luminescence properties. *Materials Chemistry and Physics*, 229, 56–60. <https://doi.org/10.1016/j.matchemphys.2019.02.066>.

Kumar, A., Rawat, S., Tiwari, S.S., Srivastava, A., and Srivastava, S. (2012). Comparative botanical and phytochemical evaluation of medicinally important stem Bark of *Ficus* species. *Asian Pacific Journal of Tropical Disease*, 2, S33–S37. [https://doi.org/10.1016/S2222-1808\(12\)60119-4](https://doi.org/10.1016/S2222-1808(12)60119-4).

Kundu, S., Chowdhury, I.H., and Naskar, M.K. (2017). Synthesis of hexagonal shaped nanoporous carbon for efficient adsorption of methyl orange dye. *J Mol Liq.*, 234, 417-423. <http://dx.doi.org/10.1016%2Fj.molliq.2017.03.090>.

Lagergren, S. (1898). Zur theorie der sogenannten adsorption geloster stoffe. *Kungliga Svenska Vetenskaps*, 24, 1.

Li, Y.H., Di, Z., Ding, J., Wu, D., Luan, Z., and Zhu, Y. (2005). Adsorption thermodynamics, kinetic and desorption studies of Pb<sup>2+</sup> on carbon nanotubes. *Water Res.*, 39, 605–609.

Li, H., Lee, L.S., Schulze, D.G., and Guest, C.A. (2003). Role of soil manganese in the oxidation of aromatic amines. *Environ Sci Tech.*, 37, 2686–2693. <https://doi.org/https://doi.org/10.1021/es0209518>.

Liu, Y.F., Yuan, G.H., Jiang, Z.H., and Yao, Z.P. (2014). Solvothermal synthesis of Mn<sub>3</sub>O<sub>4</sub> nanoparticle/Graphene sheet composites and their supercapacitive properties. *J Nanomat.*, 2014, 1–11. <https://doi.org/10.1155/2014/190529>.

Liu, Z., Zhou, A., Wang, G., and Zhao, X. (2009). Adsorption Behaviour of Methyl Orange onto Modified Ultrafine Coal Powder. *Chinese J Chem Eng.*, 17, 942-948. doi: [https://doi.org/10.1016/S1004-9541\(08\)60300-6](https://doi.org/10.1016/S1004-9541(08)60300-6).

Luo, J.Y., Zhang, J.J., and Xia, Y.Y. (2006). Highly Electrochemical reaction of Lithium in the ordered mesoporous  $\beta$ -MnO<sub>2</sub>. *Chem Mater.*, 18, 5618–5623. <https://doi.org/10.1021/cm061458o>.

Lütke, S.F., Igansi, A.V., Pegoraro, L., Dottoa, G.L., Pinto, L.A.A., and Cadaval, T.R.S. (2019). Preparation of activated carbon from black wattle bark waste and its application for phenol adsorption. *J Env. Chem. Engineering*, 7, 103396. [10.1016/J.JECE.2019.103396](https://doi.org/10.1016/J.JECE.2019.103396).

Ma, J., Ma, Y., and Yu, F.A. (2018). Novel One-Pot Route for Large-Scale Synthesis of Novel Magnetic CNTs/Fe@C Hybrids and Their Applications for Binary Dye Removal. *Sustainable Chem Eng.*, 6, 8178-8191. doi: 10.1021/acssuschemeng.7b04668.

Manjula, R., Thenmozhi, M., Thilagavathi, S., Srinivasan, R., and Kathirvel, A. (2019). Green synthesis and characterization of manganese oxide NPs from *Gardenia resinifera* leaves. *Materials Today: Proceedings*, 7–11. <https://doi.org/10.1016/j.matpr.2019.07.396>.

Masoud, S.R., Mohsen, I., Somayyeh, A., Mostafa, F., and Fattaneh, J. (2014). Removal, preconcentration and determination of methyl red in water samples using silica coated magnetic NPs. *J. Appl. Res. Water wastewater*, 1, 6–12.

Naushad, M., Alqadami, A.A., AlOthman, Z.A., Alsohaimi, I.H., Algamdi, M.S., and Aldawsari, A.M. (2019). Adsorption kinetics, isotherm and reusability studies for the removal of cationic dye from aqueous medium using arginine modified activated carbon. *J Mol Liq.*, 293, 111442. doi:10.1016/j.molliq.2019.111442.

Nhamo, C., Edna, C.M., and Willis, G. (2016). Synthesis, characterization and methyl orange adsorption capacity of ferric oxide–biochar nano-composites derived from pulp and paper sludge. *Appl Water Sci.*, 7, 2175-2186. doi 10.1007/s13201-016-0392-5.

Omar, M.H., Mullen, W., and Crozier, A. (2011). Identification of proanthocyanidin dimers and trimers, flavone C-glycosides, and antioxidants in *Ficus deltoidea*, a Malaysian herbal tea. *J Agr and Food Chem.*, 59, 1363–1369. <https://doi.org/1369dx.doi.org/10.1021/jf1032729>.

Pargoletti, E., Pifferi, V., Falciola, L., Facchinetti, G., Re Depaolini, A., Davoli, E., Mareli, M., and Cappelletti, G. (2019). A detailed investigation of MnO<sub>2</sub> nanorods to be grown onto activated carbon, High efficiency towards aqueous methyl orange adsorption/degradation. *Applied Surface Science*, 472, 118-126. doi:10.1016/j.apsusc.2018.03.170.

Patil, S.V., Salunke, B.K., Patil, C.D., Salunkhe, R.B., Gavit, P. and Maheshwari, V.L. (2010). Potential of extracts of the tropical plant *Balanites aegyptiaca* ( L ) Del.(Balanitaceae) to control the mealy bug, *Maconellicoccus hirsutus* (Homoptera:Pseudococcidae). *Crop Protection*, 29, 1293–1296. <https://doi.org/10.1016/j.cropro.2010.05.016>.

Bonilla-Petriciolet, A., Mendoza-Castillo, D.I., Reynel-Ávila, H.E. (2017). Adsorption Processes for Water Treatment and Purification || Adsorption Isotherms in Liquid Phase: Experimental, Modeling, and Interpretations. , 10.1007/978-3-319-58136-1(Chapter 2), 19–51.

Petrie, R.A., Grossl, P.R., and Sims, R.C. (2002). Oxidation of pentachlorophenol in manganese oxide suspensions under controlled E<sub>h</sub> and ph environments. *Environ Sci Tech.*, 36, 3744–3748. <https://doi.org/https://doi.org/10.1021/es0109491>.

Piccin, J.S., Cadaval, T.R.S., Pinto, L.A.A., and Dotto, G.L. (2017). Adsorption Isotherms in Liquid Phase: Experimental, Modeling, and Interpretations. In: Bonilla.

Priyadarshini, B., Patra, T., and Sahoo, T.R. (2020). An efficient and comparative adsorption of Congo red and Trypan blue dyes on MgO nanoparticles: Kinetics, thermodynamics and isotherm studies. *J magnesium and Alloys*. <https://doi.org/10.1016/j.jma.2020.09.004>.

Raj, B.G.S., Asiri, A.M., Wu, J.J., Anandan, S. (2015). Synthesis of Mn<sub>3</sub>O<sub>4</sub> nanoparticles via chemical precipitation approach for supercapacitor application. *J. Alloys Compd.*, 636, 234–240. <https://doi.org/10.1016/j.jallcom.2015.02.164>.

Saad, S.A., Isa, K.M., and Bahari, R. (2010). Chemically modified sugarcane bagasse as a potentially low-cost biosorbent for dye removal. *Desalination*, 264, 123–128. doi: .10.1016/j.desal.2010.07.015

Salunke, B.K., Prakash, K., Vishwakarma, K.S., and Maheshwari, V.L. (2009). Plant metabolites : an alternative and sustainable approach towards post harvest pest management in pulses. *Physiol Mol Biol Plants*, 15, 185–197. <https://dx.doi.org/10.1007%2Fs12298-009-0023-9>.

Sharma, J.K., Srivastava, P., Singh, G., Akhtar, M.S. and Ameen, S. (2015). Green synthesis of Co<sub>3</sub>O<sub>4</sub>NPs and their applications in thermal decomposition of ammonium perchlorate and dye-sensitized solar cells. *Materials Science and Engineering B*, 193, 181–188. <https://doi.org/10.1016/j.mseb.2014.12.012>.

Sharma, J.K., Srivastava, P., Singh, G., Akhtar, M.S., and Ameen, S. (2014). Biosynthesized NiO NPs : Potential catalyst for ammonium perchlorate and composite solid propellants. *Ceramics International*, 41, 1573–1578. <https://doi.org/10.1016/j.ceramint.2014.09.093>.

Sheng, G., Dong, H., Shen, R., Li, Y. (2013). Microscopic insights into the temperature-dependent adsorption of Eu(III) onto titanate nanotubes studied by FTIR, XPS, XAFS and batch technique. *Chem. Eng. J.*, 217, 486–494. <https://doi.org/10.1016/j.cej.2012.10.076>.

Shi, B., Li, G., Wang, D., Feng, C., and Tang, H. (2007). Removal of direct dyes by coagulation: The performance of preformed polymeric aluminum species. *J. Haz. Mat.*, 143, 567–574. <https://doi.org/10.1016/j.jhazmat.2006.09.076>.

Singab, A.N.B., Ayoub, N.A., Ali, E.N., and Mostafa, N.M. (2010). Antioxidant and hepatoprotective activities of Egyptian moraceous plants against carbon tetrachloride-induced oxidative stress and liver damage in rats. *Pharmaceutical Biology*, 48, 1255–1264. <https://doi.org/10.3109/13880201003730659>.

Sing, K.S.W. (2009). Reporting physisorption data for gas/solid systems with special reference to the determination of surface area and porosity (Recommendations 1984), *Pure Appl. Chem.*, 57, 603–619. <https://doi.org/10.1002/9783527619474.ch11>.

Silva, J.M., Farias, B.S., Grundmann, D.D.R., Cadaval Jr., T.R.S., Moura, J.M., Dotto, G.L., and Pinto, L.A.A. (2016). Development of chitosan/Spirulina bio-blend films and

its biosorption potential for dyes. *J Applied Polymer Science*, 134, 11. 10.1002/APP.44580

Stone, A.T., and Morgan, J.J. (1984). Reduction and dissolution of Manganese (III) and Manganese (IV) Oxides by organics reaction with hydroquinone. *Env Sci and Tech.*, 18, 450–456. <https://doi.org/doi:10.1021/es00124a011>.

Tran, H.N., You, S., Chao, H. (2017). Thermodynamic parameters of cadmium adsorption onto orange peel calculated from various methods: a comparison. *Biochem. Pharmacol.*, 4, 2671–2682.

Tvrđik, J., Krivy, I., and Misik, L. (2007). Adaptive population based search: Application to estimation of non-linear regression parameters. *Comput. stat. Data Anal.*, 52, 73.

Wang, N., Guo, L., He, L., Cao, X., Chen, C., Wang, R., and Yang, S. (2007). Facile synthesis of monodisperse  $Mn_3O_4$  tetragonal NPs and their large-scale assembly into highly regular walls by a simple solution route. *Communications*, 3, 606–610. <https://doi.org/10.1002/sml.200600283>.

Wang, H.Q., Yang, G.F., Li, Q.Y., Zhong, X.X., Wang, F.P., Li, Z.S., and Li, Y.H. (2011). Porous nano  $MnO_2$ : large scale synthesis via a facile quick-redox procedure and application in a supercapacitor. *New J Chem.*, 35, 469–475. <https://doi.org/10.1039/c0nj00712a>.

Zaheer, Z., Al-Asfar, A., and Aazam, E.S. (2019). Adsorption of methyl red on biogenic  $Ag@Fe$  nanocomposite adsorbent: Isotherms, kinetics and mechanisms. *J Mol Liq.*, 283, 287–298. <https://doi.org/10.1016/j.molliq.2019.03.030>

Zare, E.N., Motahari, A., and Sillanpaa, M. (2018). Nanoadsorbents based on conducting polymer nanocomposites with main focus on polyaniline and its derivatives for removal of heavy metal ions/dyes: A review. *Environ Res.*, 162, 173–195. 10.1016/j.envres.2017.12.025.

Zhang, N., Zhang, G., Chong, S., Zhao, H., Huang, T., and Zhu, J. (2018). Ultrasonic impregnation of  $MnO_2/CeO_2$  and its application in catalytic sono-degradation of methyl orange. *J Env. Man.*, 205, 134–141. doi:10.1016/j.jenvman.2017.09.073.

Zhang, P., Zhang, Y., Cai, B., Hao, C., Wang, J., and Liu, C. (2010). Shape-controlled synthesis of  $Mn_3O_4$  nanocrystals and their catalysis of the degradation of methylene blue. *Nano Res.*, 3, 235–243. <https://doi.org/10.1007/s12274-010-1026-0>.

Zhang, H., and Huang, C.H. (2005). Oxidative transformation of fluoroquinolone antibacterial agents and structurally related amines by  $MnO_2$ . *Environ. Sci. Tech.*, 39, 4474–4483. <https://doi.org/10.1021/es048166d>.

Zhao, H., Zhang, G., and Zhang, Q. (2014).  $MnO_2/CeO_2$  for catalytic ultrasonic degradation of methyl orange. *Ultrasonics Sonochemistry*, 21, 991–996. doi:10.1016/j.ultsonch.2013.12.002

Zhu, L., Cheng, H., Ma, J., Kong, Y., Qin, Y., and Komarneni, S. (2020). Decolorization of methyl orange by MnO<sub>2</sub>/organic acid system: The role of Mn(III). *Materials Research Bulletin*, 122, 110670. doi:10.1016/j.materresbull.2019.110670.

Zhu, M., Wang, Z., and Zhou, L.Y. (2008). Oxidative decolorization of methylene blue using pelagite. *J Hazardous Mat.*, 150, 37–45. <https://doi.org/https://doi.org/10.1016/j.jhazmat.2007.04.042>.



## **Chapter 3: Novel PVA/Chitosan composite membrane modified using biofabricated $\alpha$ -MnO<sub>2</sub> nanoparticles for photocatalytic degradation of cationic dyes**

---

### **3.1 Introduction**

From last several decades, water pollution has become a threat to environment. It is majorly due to the presence of heavy metal ions, toxic dyes and pigments used in various industries. It has been reported that approximately 1.6 million tons of these dyes are produced per year, out of which, 10-15% of dyes are being discharged into the water bodies [Hunger, 2003]. The degradation of these dyes discharged into water streams is very difficult, therefore, these dyes remain as such in the water bodies for a very long time and creates problem for the environment [Carmen and Daniela, 2012; Srinivasan and Viraraghavan, 2010]. The presence of dyes in aquatic habitat hinders the sunlight and oxygen to penetrate the water surface and thereby reduces the normal rate of photosynthesis as a repercussion of which the aquatic ecosystem deteriorates [Crini, 2006]. Not only is the aquatic environment being effected but the exposure of these dyes also has a fatal impact on human health. Several diseases like cancer, heart diseases, mutation, allergies, tumours and many more are the outcomes of consumption of wastewater [Alver and Metin, 2012; Vakili et al., 2014]. Based on their chemical structure, dyes can be classified into three types: anionic (acid dyes), cationic (basic dyes), and non-ionic (disperse dyes) [Srinivasan and Viraraghavan, 2010]. Several methods have been reported for removal of these dyes from their aqueous solution such as oxidation technique, flocculation and biological treatment [Yao et al., 2015; Jayanthi and Suja, 2016; Zhou et al., 2016; Tian et al., 2016; Gupta and Suhas, 2009; Demirbas, 2009]. Although these techniques are being used for dye removal but there

are certain drawbacks associated with all of these methods such as lesser efficiency, higher energy requirements and production of toxic by-products such as aromatic amines (including benzidine) which are carcinogenic in nature **[Fishbein, 1979]**.

On this account, there is an urgent requirement to explore a method which should not only be efficient but also environment friendly and cost effective. For these reasons, photocatalytic degradation of dyes has become the latest area of interest for researchers. The literature survey reveals that researchers have reported several metal oxide semiconductor nanoparticles such as TiO<sub>2</sub>, SiO<sub>2</sub>, Al<sub>2</sub>O<sub>3</sub>, MnO<sub>2</sub>, ZrO<sub>2</sub>, etc. as photocatalyst **[Jayanthi and Suja, 2016; Pina-Perez et al., 2017; Reddy et al., 2018]** for the purpose.

Among all these transition metal oxides, manganese dioxide is one of the most significant section of materials used as photocatalyst. Nanostructured manganese dioxide has the ability to attain structural flexibility which makes it suitable to be used in the field of catalysis **[Djurisic et al., 2014; Espinal et al., 2004]**, biosensors **[Ou et al., 2017; Yuan et al., 2014]**, energy storage **[Zhang et al., 2015; Lang et al., 2011]**, ion exchange **[Liu et al., 2016]** and as electrode materials used in batteries **[Truong et al., 2012; Wang and Li, 2002]**. The role of MnO<sub>2</sub> as catalyst for degradation of organic compounds helps in environmental remediation.  $\alpha$ -MnO<sub>2</sub> is a semi-conductor having a band gap of 1.3 eV and therefore, can effectively be used as a photocatalyst.

Over the past few years, the investigation of organic-inorganic nanocomposite is being carried out extensively to merge the benefits of inorganic materials such as photocatalytic property and stability with organic polymers having advantages like processibility and ductility **[Elsayed et al., 2011]**.

Therefore, the use of polymers such as polyvinyl alcohol (PVA), polyvinyl pyrrolidone (PVP), chitosan (CS), cellulose etc. with metal oxide nanomaterials is a recent and

suitable approach for removing these toxic dyes from water bodies. These polymers are used as matrix for semiconductor materials [Alexandre and Dubois, 2000; Tao et al., 2009; Vicentini et al., 2010; Zhang et al., 2011]. The role of these polymers is to provide an interface for transfer of charge and obstruct leakage of ions in water. Among several polymers, the most extensively used polymer is chitosan because its non-toxic and biodegradable polymer nature [Synowiecki et al., 2003; Fong et al., 2015; Yaroslavov et al., 2021].

CS is basically a natural polysaccharide which is constituted of glucosamine and N-acetyl glucosamine [Nghah et al., 2011; Lim et al., 2021; Munide et al., 2020]. Although CS possesses certain properties like solubility in acid, tendency to attract negatively charged species etc. [Martinova and Lubasova, 2008] but it has certain limitations as well.

The blend of CS with an appropriate polymer (such as cellulose acetate, polyvinyl pyrrolidone and polyvinyl alcohol) results in the formation of highly reactive and mechanically stable film [Jayakumar et al., 2011; Shawky, 2009]. The mechanical stability of the membrane is also enhanced by incorporating nanoparticles into it [Ashori and Bahrami, 2014; Delavar and Shojaei, 2017; Ghaee et al., 2010; Khabashesku et al., 2005; Khan et al., 2017; Vatanpour et al., 2012].

In this study, laboratory synthesized MnO<sub>2</sub> nanoparticles (MNPs) are used, for the first time, to alter the property of PVA/CS membrane. The synthesized membrane is biodegradable in nature and can be easily separated from water after treatment and then can be reused for several times after washing. The PVA-CS/MNPs film was used to remove cationic azo dyes such as eosin yellow (EY) and methylene blue (MB) and the kinetics of reaction along with its mechanism are also investigated.

## 3.2 Materials and method

### 3.2.1 Materials

Chitosan and sodium hydroxide were procured from Molychem India Pvt. Ltd. Polyvinyl alcohol (PVA) was provided by LOBA Chemie., India. Acetic acid was supplied by Merck Life Science Private Ltd, India. Dyes, eosin yellow (Molecular weight = 691.86 g/mol) and methylene blue (Molecular weight = 373.9 g/mol) were obtained from Fisher Scientific and Finar Chemicals respectively.

### 3.2.2 Fabrication of membrane

MNPs were synthesized by reduction of potassium permanganate ( $\text{KMnO}_4$ ) using leaf extract of *Ficus retusa* as mentioned in chapter 2.

The fabrication of membrane was carried out by preparing two solutions: Solution A and Solution B. Solution A was comprised of 4.3 g CS flakes and MNPs (varying concentrations) dissolved in 200 mL of 2% v/v acetic acid solution kept in a water bath at 90 °C temperature for 3 h and stirred for 2 h at 600 rpm using magnetic stirrer at a temperature of 60 °C. Solution B was prepared by dissolving 8 g of PVA in 100 mL distilled water and this solution was stirred at 600 rpm for 5 h at a temperature of 60 °C. The two solutions (Solution A and B) were then mixed and agitated at 600 rpm overnight to prepare a homogenous solution. The blend prepared, at the end, was then poured evenly in a petri dish and dried at 40 °C temperature for 24 h. The prepared membrane was then separated by pouring 1 M solution of NaOH in the petri dish and keeping it aside for 1 h. The PVA/CS-MNPs membrane was then washed several times with distilled water and then finally used for further experimentations. The amount of nanoparticles used for preparation of membranes is shown in the table given below (Table 3.1).

**Table 3.1: Amount of nanoparticles in the studied PVA/CS-MNPs membrane with corresponding designations**

| Sl. No. | Quantity of MNPs (g) | Percentage of MNPs | Membrane sample code |
|---------|----------------------|--------------------|----------------------|
| 1       | 0.1                  | 0.80               | Composite 1          |
| 2       | 0.5                  | 4.0                | Composite 2          |
| 3       | 1.0                  | 8.0                | Composite 3          |

### 3.2.3 Characterization

The PVA-CS/MNPs membranes were characterized using following analytical tools:

Fourier transform infrared (FTIR) spectroscopy was used to determine the functional groups coupled with the nanopolymer composite membrane. This study was conducted using Spectrum 2-FTIR Spectroscopy, Perkin Elmer within the wavelength range of 400 to 4000  $\text{cm}^{-1}$ . Mechanical properties of the fabricated membrane was determined using Universal testing machine (Tinius Olsen H5KL). FESEM (Field emission scanning electron microscopy) images of the membranes were taken using Nova NanoSEM 450 instrument to examine the surface morphology of the membranes.

### 3.3 Photocatalytic activities

The photocatalytic activity of PVA/CS-MNPs membrane was studied by carrying out the degradation of cationic dyes viz. MB and EY dyes. Dye solutions of varying concentrations were degraded using membranes incorporated with different concentration of nanoparticles (Composite 1, 2 and 3). 0.50 g of catalyst was separately added to 25 mL solution of MB and EY dyes at 25 °C temperature and initial pH of 8.0. The concentrations of MB dye solutions used for degradation were 10, 20, 30 and 40 mg/L while EY dye of concentrations 10, 25, 50 and 100 mg/L were considered for the study. The suspensions were first kept in dark for about half an hour. These suspensions were then irradiated with sunlight under continuous stirring until the solutions turned into colourless. The mixture was stirred to prevent the catalyst from settling and also for

providing continuous exposure of catalyst to sunlight. The progression of the reactions was registered by quantifying the absorbance obtained through UV-Vis spectrophotometer (Lab India 3200). The course of reaction was also monitored using Carry Eclipse fluorescence spectrometer (MY 14270004). Electrospray ionization mass spectrometry (ESI-MS) was conducted using Waters UPLC-TQD mass spectrometer to validate the fact that dyes were completely degraded at the end of the reaction. The details of parameters for ESI-MS studies are given below.

ESI-MS was done in positive mode maintaining flow rate of drying gas of 7.01 mL/min. at 325°C temperature and 30 psi pressure. The product was investigated in the range of 100-800 m/z.

The photocatalytic degradation efficiency of the composites was calculated using following equation:

$$\text{Dye removal (\%)} = \frac{C_0 - C_e}{C_0} * 100 \quad \dots\dots\dots (3.1)$$

Where,  $C_0$  represents initial concentration of dyes and  $C_e$ , concentration of dye at equilibrium.

### **3.4 Results and discussion**

#### **3.4.1 Characterization of PVA/CS-MNPs membrane**

##### **3.4.1.1 FTIR analysis**

FTIR analysis is a non-destructive technique which was used to obtain the details of inorganic and organic components of the membrane fabricated in this work. FTIR-ATR of PVA, PVA/CS and PVA/CS-MNPs membrane was performed as shown in **figure 3.1**. For pure PVA membrane, the band at 3301  $\text{cm}^{-1}$  corresponds to –OH stretching vibration. The sharp peak at 2925  $\text{cm}^{-1}$  is attributed to asymmetric  $\text{CH}_2$  group stretching vibration. The peak obtained in the range of 1650-1430  $\text{cm}^{-1}$  is due to the  $\text{C}=\text{C}$  stretching vibration

of PVA. The peak at  $1078\text{ cm}^{-1}$  and  $835\text{ cm}^{-1}$  is because of the C-O and C-C stretching vibration respectively [Bonilla et al., 2014; El Miri et al., 2015].

In case of PVA/CS membrane, the incorporation of CS into the pure PVA membrane brought certain changes in the structure of PVA membrane. A peak at  $1583\text{ cm}^{-1}$  was observed in case of PVA-CS membrane, which was not observed in pure PVA corresponding to the N-H functional group of CS.

For PVA/CS-MNPs membrane, bands at  $3305$ ,  $2944$  and  $2122\text{ cm}^{-1}$  correspond to O-H, C-H symmetric and asymmetric stretching respectively. C=O and C=C stretching vibrations are assigned to the bands obtained at  $1739\text{ cm}^{-1}$  and  $1640\text{ cm}^{-1}$ . The bands at  $1428\text{ cm}^{-1}$  and  $1369\text{ cm}^{-1}$  are ascribed to the vibration of C-H bending and C-H wagging. The next set of bands are located at  $1218$  and  $1081\text{ cm}^{-1}$  owing to C-O stretching and C-H wagging acetate residue vibrations. The band located at  $896\text{ cm}^{-1}$  is because of the rocking vibration of  $\text{CH}_2$  group.

It was found that the intensity of peak at  $2925\text{ cm}^{-1}$  became weaker on incorporation of chitosan into PVA and further reduced with addition of MNPs into the matrix, which is probably due to crosslinking between PVA and MNPs. The peak obtained at  $1078\text{ cm}^{-1}$  representing the C-O-C group got weaker, which indicates that MNPs could increase the degree of crosslinking of the composite membrane.

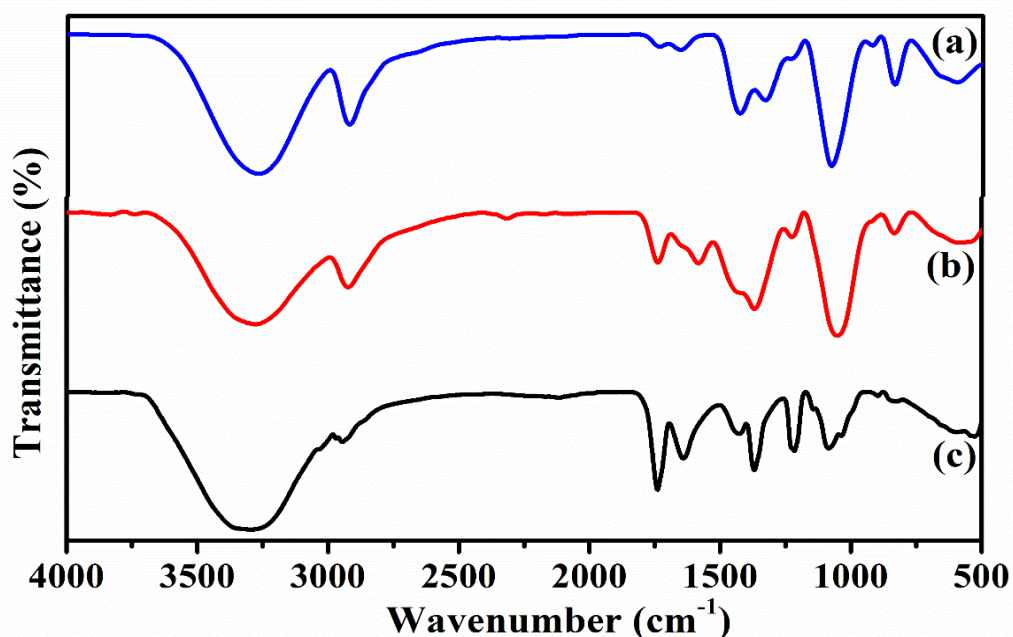


**Figure 3.1:** FTIR spectra of membrane of (a) PVA, (b) PVA-CS and (c) PVA-CS/MNPs.

#### 3.4.1.2 Mechanical properties of the fabricated membranes

**Figure 3.2** exhibits that the mechanical properties of PVA membrane are noticeably enhanced by the incorporation of CS, which is then furthermore improved by incorporation of MNPs into the matrix of PVA/CS membrane. The improvement in the tensile strength, toughness and strain was observed for lower concentration of nanoparticles being added to the membrane. On increasing the concentration of nanoparticles into the matrix of PVA/CS membrane, a downfall in the mechanical properties of membrane was observed. Therefore, it can be concluded that the optimum concentration for fabrication of membrane with good tensile strength is 0.1g, which is approximately 0.8 w/w%. Composite 1 exhibited an excellent tensile strength of 21.5 MPa, strain of approximately 21% and toughness of 133.13 kJ/m<sup>3</sup>. **Figure 3.3** shows the photographs of membranes of varying concentrations of nanoparticles within the membrane. The excellence achieved in the mechanical properties of membrane may be attributed to the homogeneous dispersion of MNPs within the matrix of polymer along

with the suitable interfacial interactions among them as validated by FESEM and FTIR [Yang et al., 2010].

### 3.4.1.3 FESEM analysis of membranes

Figure 3.4 exhibits the FESEM images of PVS/CS blend as well as PVA/CS-MNPs membranes containing different concentrations of MNPs. From FESEM data, it is revealed that the surface of PVA/CS blend without nanoparticles is homogenous while on incorporating nanoparticles into the membrane, heterogeneous surface appeared and the heterogeneity increased with the increase in the loadings of MNPs. It is clearly visible in the images that the higher concentration leads to aggregation of nanoparticles and blocked the surface of PVA/CS membrane. The blocking of the surface of PVA/CS membrane does not allow the light to interact with the catalyst and hence, reduces the photoactivated volume and alters the rate of reaction.

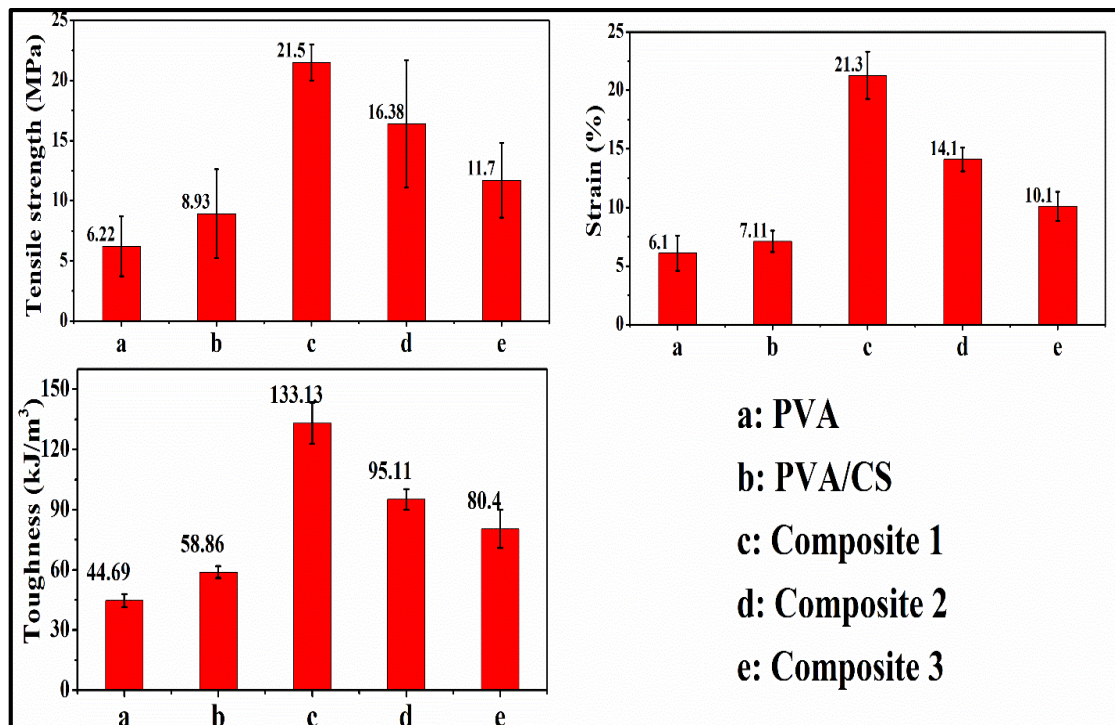
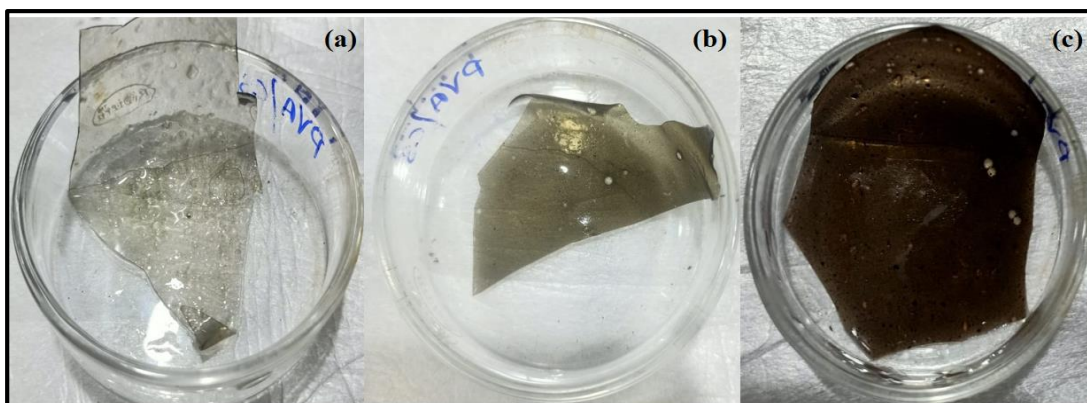
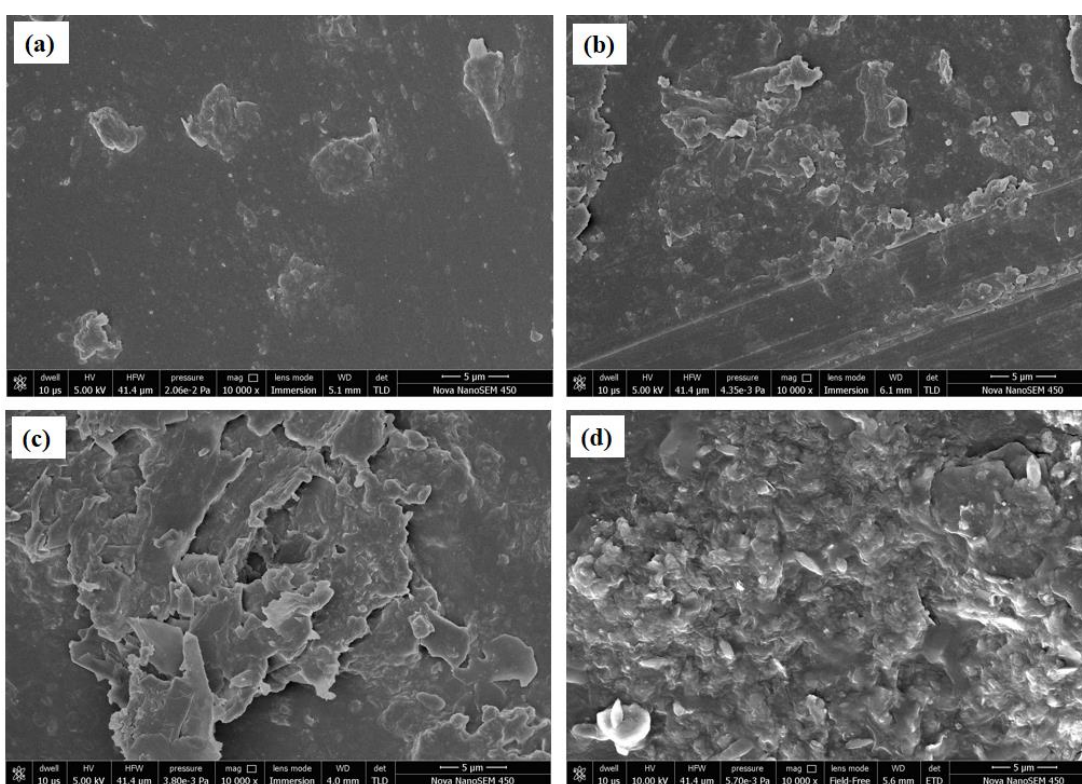


Figure 3.2: Comparison of (a) tensile strength, (b) strain, and (c) toughness of pure PVA, PVA/CS and PVA/CS-MNPs membrane of varying concentrations.



**Figure 3.3: Photographs of PVA/CS-MNPs membrane (a) Composite 1, (b) Composite 2 and (c) Composite 3.**



**Figure 3.4: FESEM images (a) PVA/CS membrane (without MNPs), (b) Composite 1, (c) Composite 2 and (d) Composite 3.**

### 3.4.2 Removal of dyes

#### 3.4.2.1 Decolourization of dyes

The photocatalytic activity of PVA/CS-MNPs membrane was evaluated for degrading dyes such as EY and MB by subjecting the aqueous solution of dyes along with the prepared membrane to sunlight for certain time. The ability of the prepared membrane to decolourize the dye solutions (EY and MB) was studied at fixed concentration of 10 mg

$L^{-1}$  of dye solutions (EY and MB) using composite 1. The elementary observation of the process was the progressive change in the colour of dyes with time. It was found that at the end of 2 h, both EY and MB dye solutions turned into colourless from their respective orange and deep blue colours. The decrease in the concentration of dyes with time was calculated by examining the adsorption spectra of decolourization of EY and MB at different irradiation time using UV-Vis spectrometer. **Figure 3.5** shows that the characteristic absorption band of EY and MB dyes at 524 and 664 nm respectively decreased gradually and completely vanished after certain time interval, which indicates the degradation of high molecular weight organic dyes are to simpler products.

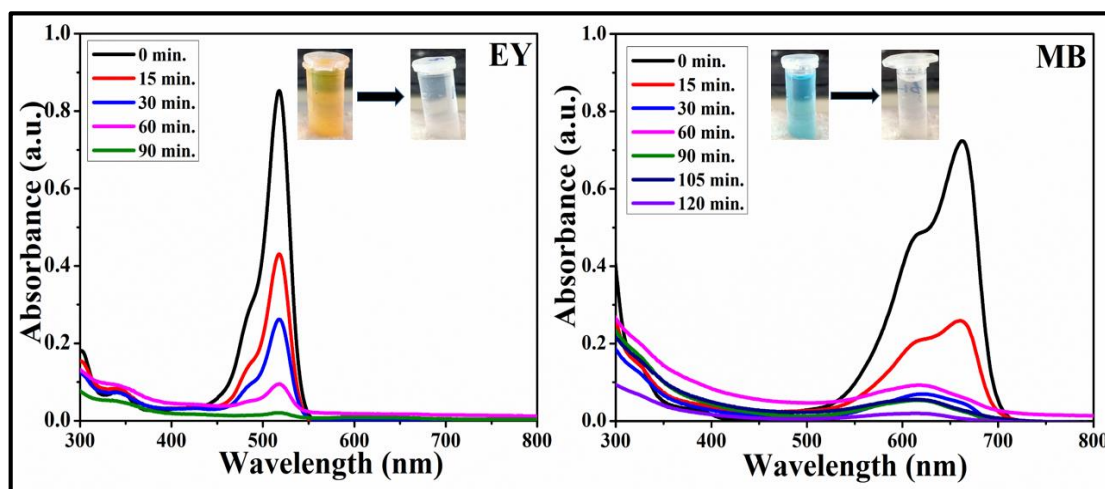


**Figure 3.5: UV-Vis spectra of degradation of eosin yellow and methylene blue dyes at different time interval.**

### 3.4.2.2 Degradation of dyes

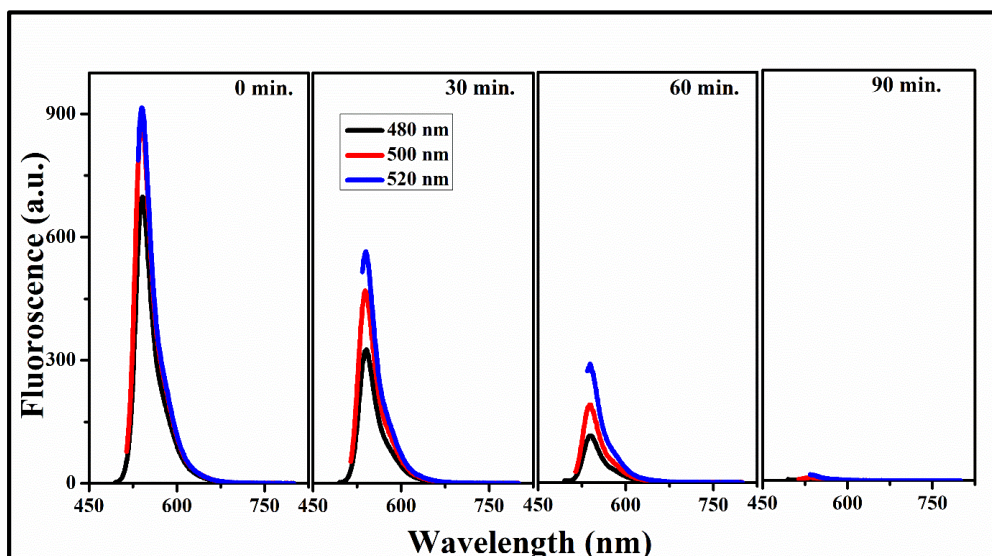


**Figure 3.6:** Eosin yellow dye fluorescence spectra (at  $\lambda_{\text{ex}}$ : 520, 500 and 480 nm) at different time intervals of 0, 30, 60 and 90 min.

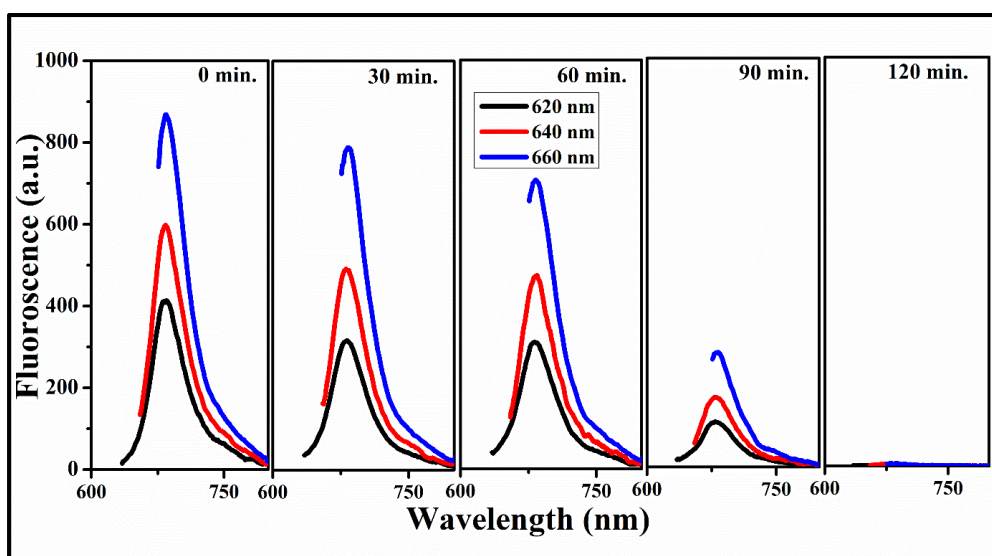


**Figure 3.7:** Methylene blue dye fluorescence spectra (at  $\lambda_{\text{ex}}$ : 660, 640 and 620 nm) at different time intervals of 0, 30, 60, 90 and 120 min.

Until now, the decolourization of dyes using PVA/CS-MNPs membrane triggered by visible light has been discussed. To validate this observation and further investigate the process, fluorescence spectroscopy was carried out at different excitation wavelength corresponding to the compound detected through adsorption maxima spectra obtained from UV-Vis spectroscopy data (**figure 3.5**). Fluorescence spectroscopy is an effective tool for monitoring of the mechanism involved in different chemical reactions [**Lopez et**

al., 2013; Russo et al., 2009; Giustini et al., 2013; Carstea et al., 2016; Travaglini et al., 2014].

Figure 3.6 and 3.7 highlights the fluorescence spectra of degradation of EY and MB dyes respectively mediated through the membrane composite 1. With this approach, it was ascertained that no intermediate product was formed during the degradation of EY dye. By exciting the solution of EY at three different wavelengths viz. 520, 500 and 480 nm, only a single specie is identified that emits at 540 nm. The peak corresponding to 540 nm completely disappeared in a time span of 90 min. of exposure to sunlight in the presence of PVA/CS-MNPs membrane.

Similar to EY, MB dye solution was also excited at three different wavelength such as 660, 640 and 620 nm for which emission was obtained at 680 nm. The intensity of emission peak reduced with time and disappeared at the end of 2 h. No other peak was found at any point of time during the degradation process.

### 3.4.2.3 ESI-MS analysis

#### i. Identification of end product of degradation of MB dye by ESI-MS

ESI-MS of MB dye was recorded at the beginning and end of reaction (table 3.2). The mass spectral analysis of reaction at 0 min. shows a peak at  $m/z$  (mass-to-charge ratio) 284, which corresponds to MB dye [Mahamallik et al., 2016]. The mass spectral analysis of the solution obtained at the end of reaction did not show the peak for parent MB dye molecule at  $m/z$  value of 284 which indicates that no MB dye was left in the solution and was completely degraded on to PVA-CS/MNPs membrane. However, a peak at 226  $m/z$  ratio is most probably due to loss of methyl groups and oxidative degradation of MB. A peak at  $m/z$  301 may be attributed to hydroxylation of MB. A sharp peak is seen at 183  $m/z$  value, which is in good agreement with the previously reported work [Rashid et al., 2018; Rauf et al., 2010]. In the lower region, of spectrum,

various peaks have been recorded at m/z values of 102,110, and 159. These peaks clearly validate the degradation of MB dye due to the attack of OH radical.

#### ii. Identification of end product of degradation of EY by ESI-MS

The ESI-MS of EY was also recorded at the beginning and the end of the reaction. Results found were similar as that of MB dye degradation. At the beginning of reaction, a peak at m/z ratio of 648 is observed which disappears at the end of reaction showing the degradation of dye. At the end of reaction, peaks are seen at m/z values of 100, 126, and 148 indicating the complete degradation of dye using fabricated membrane as photocatalyst.

**Table 3.2: ESI-MS of dye solutions before and after the removal of dyes**

| Sl. No. | Sample                          | m/z ratio |
|---------|---------------------------------|-----------|
| 1       | MB dye solution before reaction | 284       |
| 2       | MB dye solution after reaction  | 102       |
| 3       | EY dye solution before reaction | 648       |
| 4       | EY dye solution after reaction  | 100       |

#### 3.4.3 Mechanism of degradation

**Figure 3.8** represents the scheme of mechanism of degradation of dyes (MB and EY) on exposing the aqueous solution of these dyes under sunlight in presence of PVA/CS-MNPs membrane. An important aspect of the entire photodegradation process is concerned with the surface charge of MNPs [Venditti et al., 2015]. On irradiating the membrane to sunlight, firstly  $\alpha$ -MnO<sub>2</sub> nanoparticles embedded into the matrix of membrane, experience a charge separation phenomenon, which kicks the electrons from valence band (VB) to conduction band (CB) and ultimately creates a hole in the VB. The development of heterojunction, causes transfer of photo generated electrons and holes from CB to VB and VB to CB respectively. During this transfer, electrons are captured by the PVA/CS membrane through semiconductor  $\alpha$ -MnO<sub>2</sub> heterojunction, which

amplified the efficiency of charge separation dramatically. The photogenerated electrons and holes react with water and oxygen dissolved in water and produce highly reactive superoxide ( $\cdot\text{O}_2^-$ ) and hydroxyl radicals ( $\cdot\text{OH}$ ). These radicals are highly reactive in nature and react with dye molecules and convert them to simple molecules of  $\text{CO}_2$ ,  $\text{H}_2\text{O}$ , etc.

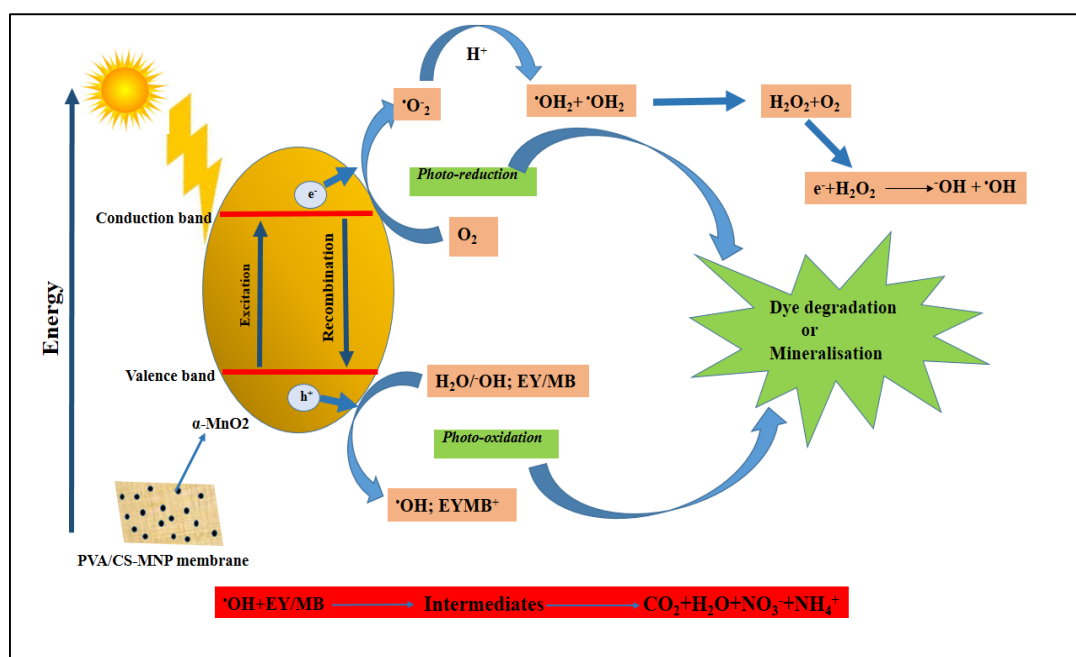


**Figure 3.8: Schematic diagram showing the possible charge separation and transfer during photocatalytic degradation of eosin yellow/methylene blue dyes.**

### 3.4.4 Effect of pH

pH of the solution has an influence on the process of photocatalysis, making it necessary to optimize the pH for efficient degradation of dyes as well as for commercializing the fabricated material. The ionization state of the catalyst surface affects the optimization of pH. In case of PVA-CS/ MNP membrane, the surface of  $\text{MnO}_2$  is positively charged in acidic medium while negatively charged in the basic medium. The optimal pH for degradation of MB and EY dyes was studied by varying the pH of reaction mixture from 2 to 12 using MB and EY dye concentration ( $10 \text{ mg L}^{-1}$ ) and 0.5 g of composite 1 membrane. The normal pH of MB and EY dye aqueous solution was approximately 8. It

was observed that the reaction was feasible only at pH above 7 and the rate of reaction increased tremendously on increasing the pH from 7 to 12. The enhanced activity of photocatalyst at higher pH is due to the cationic nature of dyes. These dyes are very easily ionized in basic medium to its cationic form. In addition, electrons are also available at higher pH to attract the positively charged dye molecule through electrostatic force of attraction. Therefore, at higher pH (in the range of 8-12), MB and EY cations are adsorbed on to the surface of PVA-CS-MNP membrane having negatively charged surface. Moreover, at higher pH, cationic form of MB and EY dyes are reduced directly by highly reactive superoxide radical. The summary of optimization of pH is mentioned in **table 3.3**

**Table 3.3: Effect of pH on photocatalytic degradation of dyes**

| pH | Feasibility of reaction |              | Time taken (min.) |        |
|----|-------------------------|--------------|-------------------|--------|
|    | EY dye                  | MB dye       | EY dye            | MB dye |
| 2  | Not feasible            | Not feasible | -                 | -      |
| 4  |                         |              |                   |        |
| 8  | Feasible                | Feasible     | 90                | 120    |
| 12 |                         |              | 50                | 60     |

#### **3.4.5 Effect of concentration of $\alpha$ -MnO<sub>2</sub> nanoparticles within membrane**

With the objective of studying effect of concentration of nanoparticles on the efficiency of membrane to degrade dye solutions, three sets of nanopolymer composite (PVA/CS-MNP) membranes were prepared. It was found that, on increasing the concentration of nanoparticles incorporated into the membrane, the rate of reaction became slower (**figure 3.9 and 3.10**). The reason for it may be attributed to the agglomeration of nanoparticles on increasing the concentration within the matrix of membrane. The agglomeration of nanoparticles not only decreases the surface area but also reduces the penetration of light, which lessens the photoactivated volume and ultimately lowers the rate of reaction.

### 3.4.6 Effect of initial dye concentration

The effect of initial concentration of dyes (MB and EY) on photocatalytic degradation efficiency of PVA/CS-MNPs membrane was studied by varying the concentration of dyes. The concentration of dye solutions used for study was 10, 20, 30 and 40 mg L<sup>-1</sup> for MB dye and 10, 25, 50 and 100 mgL<sup>-1</sup> for EY dye solutions. It was observed that percentage of removal of dye was higher in case of lowest concentration in a lesser span of time (**figure 3.9** and **3.10**). The lowest dye concentration (10 mgL<sup>-1</sup>) completely degraded at a higher pace. As the concentration of dyes (MB and EY) increased, the efficiency and rate of degradation decreased. The decrease in efficiency took place because at higher concentrations, the deep colour of dyes reduced the excitation of electrons in catalyst. The deep colour of dyes got adsorbed onto the surface of catalyst and hence, a major portion of sunlight was taken up by the dark solution instead of reaching the catalyst. This observation is in accordance with the facts reported earlier [**Gnanaprakasam et al., 2015**]. Although more than 95% of dyes of all concentration degraded but the degradation of lesser concentrated dye solutions occurred faster as compared to high concentration dyes.

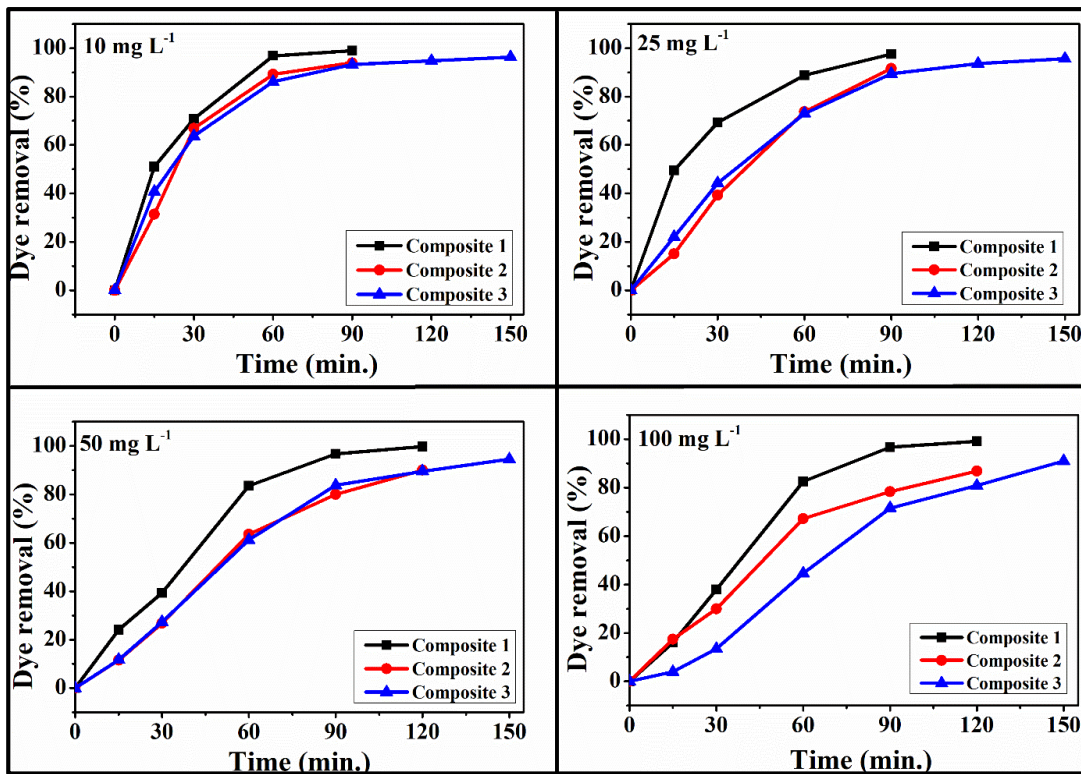


Figure 3.9: Percentage of removal of eosin yellow dye on varying its initial concentration.

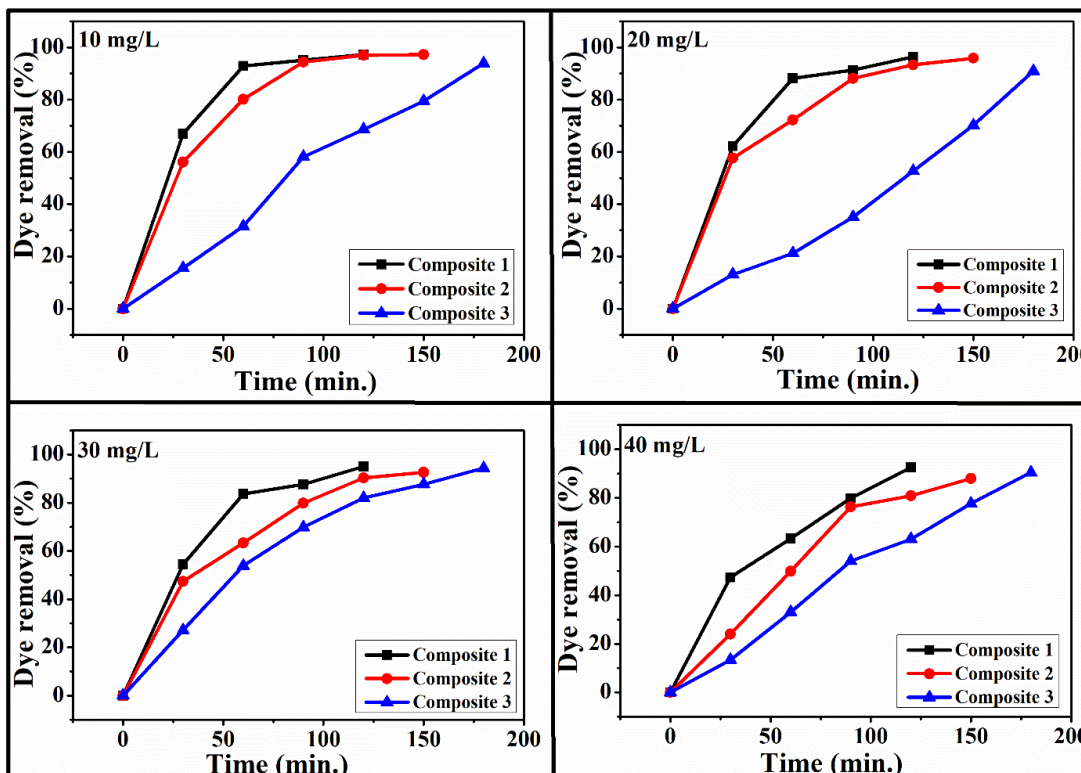


Figure 3.10: Percentage of removal of methylene blue dye on varying its initial concentration.

### 3.4.7 Kinetics of photocatalytic reaction

The photocatalytic degradation of dyes is expressed by pseudo first order kinetic model, which is illustrated by a plot between  $\ln (C_0/C_t)$  and irradiation time for all the synthesized materials used for degrading varying concentrations of dyes. A straight line was obtained as shown in **figure 3.11** and **3.12**, which highlights that the reaction process followed pseudo first order kinetics. **Figure 3.9** and **3.10** also exhibit the percentage of removal of dye with time and it was found that the percentage of removal of dyes increased progressively with time. As mentioned above, composite 1 is the most effective PVA/CS-MNPs membrane for degradation of dyes. The time required by composite 1 for degradation of dyes was found to be approximately 90 min. for EY dye and 2 h for MB dye at pH 8. More than 95% of dyes got degraded within this time span.

**Table 3.4** shows the rate constant for the prepared membranes with respect to the concentrations of dyes (both EY and MB). Value of rate constant was calculated using equation mentioned below (**eq. 3.2**).

$$\ln \frac{C_0}{C_t} = -kt \quad \dots\dots\dots (3.2)$$

Where,  $C_0$  is the initial concentration of dye,  $C_t$ , concentration of dye after time  $t$  and  $k$ , rate constant.

It was found that the rate constant was decreasing with increase in the concentration of MNPs incorporated into the PVA/CS-MNPs membrane. The maximum values of rate constant were observed for the reactions involving composite 1 as catalyst (**table 3.4**). The value of rate constant also varied with initial concentration of dyes as depicted in **table 3.4**. The increase in concentration of dyes leads to reduction in the value of rate constant.

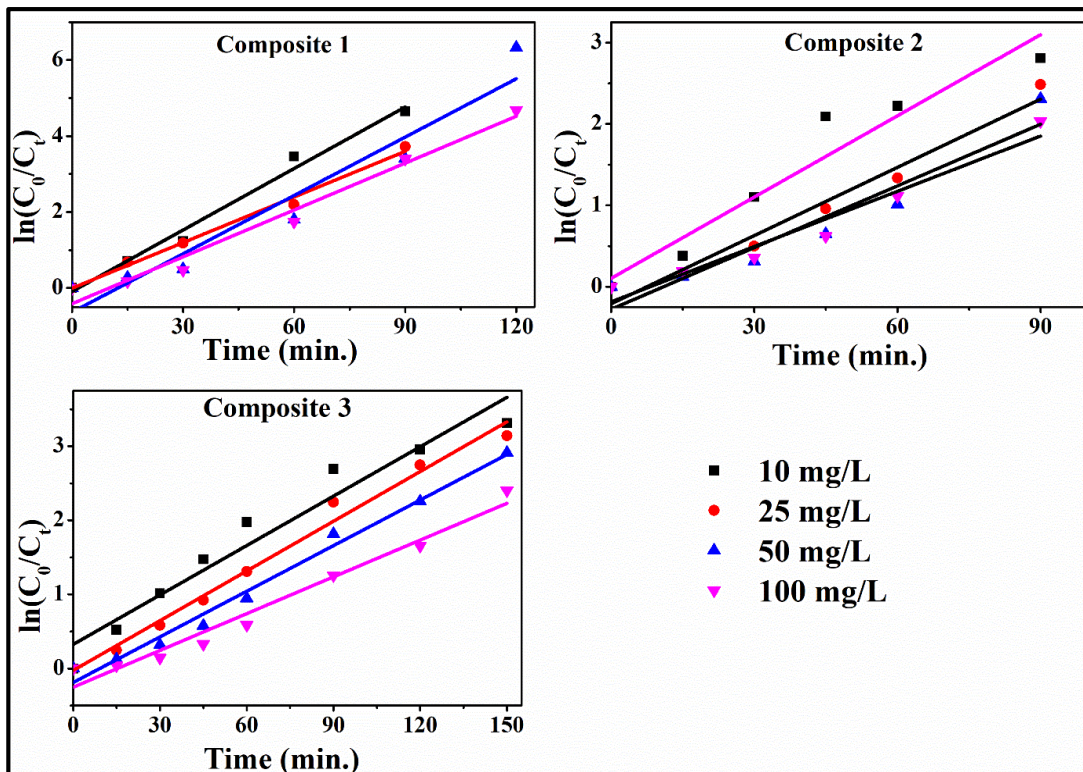


Figure 3.11: Pseudo first order kinetics for the degradation of eosin yellow dye using different composites of PVA/CS-MNPs membrane.

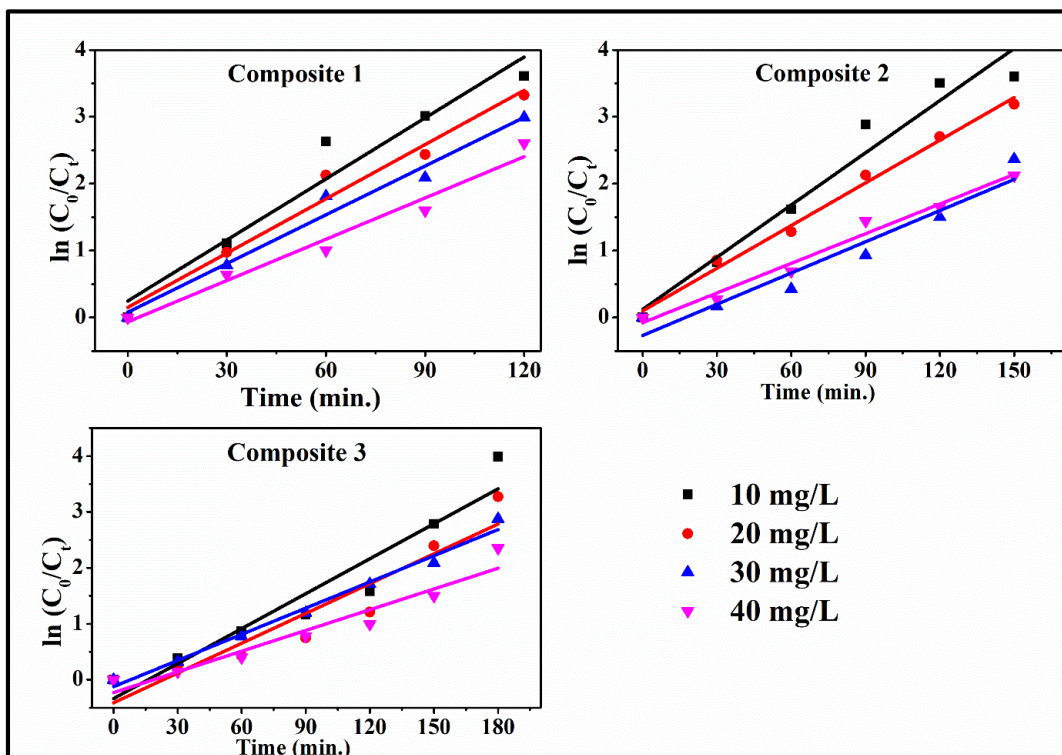


Figure 3.12: Pseudo first order kinetics for the degradation of methylene blue dye using different composites of PVA/CS-MNPs membrane.

**Table 3.4: Rate constant for photodegradation of eosin yellow and methylene blue dyes using varying composition of membrane and initial concentration of dyes**

| PVA/CS-MNPs membrane | Conc. of EY dye (mg L <sup>-1</sup> ) | Rate constant for EY (min. <sup>-1</sup> ) | Conc. of MB dye (mg L <sup>-1</sup> ) | Rate constant for MB (min. <sup>-1</sup> ) |
|----------------------|---------------------------------------|--|---------------------------------------|--|
| <b>Composite 1</b>   | 10                                    | 0.117                                      | 10                                    | 0.069                                      |
|                      | 25                                    | 0.100                                      | 20                                    | 0.062                                      |
|                      | 50                                    | 0.094                                      | 30                                    | 0.055                                      |
|                      | 100                                   | 0.078                                      | 40                                    | 0.047                                      |
| <b>Composite 2</b>   | 10                                    | 0.076                                      | 10                                    | 0.059                                      |
|                      | 25                                    | 0.072                                      | 20                                    | 0.048                                      |
|                      | 50                                    | 0.068                                      | 30                                    | 0.035                                      |
|                      | 100                                   | 0.063                                      | 40                                    | 0.034                                      |
| <b>Composite 3</b>   | 10                                    | 0.044                                      | 10                                    | 0.047                                      |
|                      | 25                                    | 0.043                                      | 20                                    | 0.040                                      |
|                      | 50                                    | 0.040                                      | 30                                    | 0.035                                      |
|                      | 100                                   | 0.033                                      | 40                                    | 0.028                                      |

### 3.5 Recyclability of catalyst

For practical utilization, stability of catalyst is a significant parameter in the catalysis domain. To evaluate the stability of the fabricated membrane used as catalyst, the membrane was recycled five times for photocatalytic degradation of dyes (MB and EY) at pH 8. The membrane can be easily recovered as such at the end of the reaction and therefore, there is no loss of catalyst amount after each cycle. It is shown in **figure 3.13** that the removal of MB and EY dyes through the process of photocatalysis using PVA/CS-MNPs membrane was successful even after five cycles of reuse. The removal efficiency could still reach up to 99% for both the dyes, which indicates the good stability of the fabricated membrane.

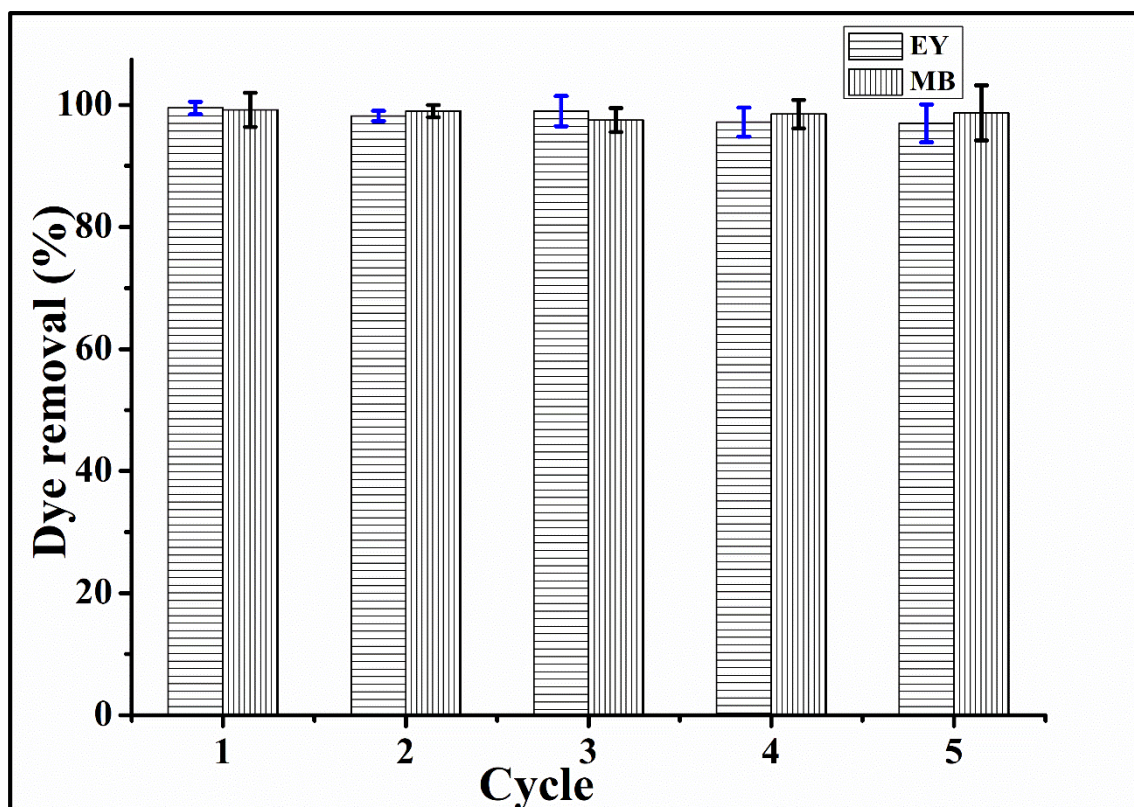


**Figure 3.13: Percentage degradation of eosin yellow and methylene blue dyes at different cycles.**

### 3.6 Comparison of PVA/CS-MNPs membrane with other photocatalysts

A comparison of efficiency of previously reported photocatalysts with the membrane presented in this work for degradation of EY and MB dyes is shown in **table 3.5** and **3.6**. PVA/CS-MNPs membrane degraded 99% of EY dye in a time span of 50 min. As shown in **table 3.5**, similar to PVA/CS-MNPs membrane materials reported previously could successfully degrade EY dye upto 99% but the rate of reaction using the material reported in this work is much faster as compared to previously reported materials.

The synthesised membrane was equally effective for degrading MB dye as well. PVA/CS- MNP membrane has the ability to remove approximately 99 % of MB dye which is way too higher than other materials.

**Table 3.5: Photocatalytic degradation of methylene blue dye using different photocatalysts**

| Photocatalyst  | Degradation (%) | Reference                                     |
|--|-----------------|---|
| Sodium titanate nanotube   | -85             | <b>Kiatkittipong and Assabumrungrat, 2017</b> |
| Hydrogen titanate nanotubes  | -80             |   |
| $\alpha$ -Bi <sub>2</sub> O <sub>3</sub>                           | 50.0            | <b>Jalah et al., 2015</b>                     |
| $\alpha$ -Fe <sub>2</sub> O <sub>3</sub>                           | 51.0            | <b>Tan et al., 2013</b>                       |
| ZnS:CdS  | 65.0            | <b>Soltani et al., 2012</b>                   |
| Fe <sub>3</sub> O <sub>4</sub> /SiO <sub>2</sub> /TiO <sub>2</sub> | 90.0            | <b>Alzahrani et al., 2017</b>                 |
| <b>PVA/CS-MNPs membrane</b>  | <b>99.0</b>     | <b>Present work</b>                           |

**Table 3.6: Photocatalytic degradation of eosin yellow dye using different photocatalysts**

| Photocatalyst   | Degradation (%) | Conversion time (min.) | Reference                   |
|---|-----------------|------------------------|-----------------------------|
| EG-TiO <sub>2</sub>   | 46.0            | 180                    | <b>Ndlovu et al., 2014</b>  |
| La-ZnO-GO   | 92              | 210                    | <b>Oppong et al., 2018</b>  |
| Zn <sub>2</sub> SnO <sub>4</sub> -V <sub>2</sub> O <sub>5</sub> | 92              | 180                    | <b>Raja et al., 2018</b>    |
| Cadmium vanadate  | 57              | 200                    | <b>Mazloom et al., 2016</b> |
| <b>PVA/CS-MNPs membrane</b>                                     | <b>99.0</b>     | 50                     | <b>Present work</b>         |

### 3.7 Conclusions

$\alpha$ -MnO<sub>2</sub> nanoparticles were successfully fabricated in the laboratory via green route and the synthesized nanoparticles were incorporated into polymer membrane prepared using polyvinyl alcohol along with chitosan. The as synthesized nanocomposite membrane was investigated for its ability to act as photocatalyst for degradation of cationic dyes such as methylene blue and eosin yellow. The photocatalytic degradation of dyes was carried out under sunlight. On carrying out a detailed study on the process of removal of these dyes using the PVA/CS-MNPs membrane, it was found that the membrane completely degraded the targeted dyes. It was observed that the process of degradation of dyes was feasible only in basic medium, lowering the pH hinders the reaction process. The increase in concentration of nanoparticles within the matrix of membrane decreases the effectiveness of reaction and increase in concentration of dye also reduces the rate of

photocatalytic degradation. Therefore, it can be concluded that maximum removal of dyes at faster pace was obtained using composite 1 membrane at pH 12. The recycling efficiency of nanophotocatalyst was also explored and found that the photocatalyst was successful in removing approximately 99% of dyes even after reusing it for 5 times. The novel composite membrane is an ideal catalyst with excellent efficiency and reusability in various industrial reactions and wastewater treatment.

## References

- Alexandre, M., Dubois, P. (2000). Polymer-layered silicate nanocomposites: preparation, properties and uses of a new class of materials. *Materials Science and Engineering: R: Reports*, 28, 1, 1–63.
- Alver, E., Metin, A.U. (2012). Anionic dye removal from aqueous solutions using modified zeolite: Adsorption kinetics and isotherm studies. *Chem. Eng. J*, 200, 59-67.
- Alzahrani, E. (2017). Photodegradation of binary azo dyes using core-shell  $\text{Fe}_3\text{O}_4/\text{SiO}_2/\text{TiO}_2$  nanospheres. *Am. J. Anal. Chem*, 8, 95.
- Ashori, A., Bahrami, R. (2014). Modification of physico-mechanical properties of chitosan-tapioca starch blend films using nano graphene. *Polym. Plast. Technol. Eng*, 53, 3, 312–318. doi:10.1080/03602559.2013.866246.
- Bonilla, J., Fortunati, E., Atarés, L., Chiralt, A., Kenny, J.M. (2014). Physical, structural and antimicrobial properties of polyvinyl alcohol-chitosan biodegradable films. *Food Hydrocoll*, 35, 463–470.
- Carmen, Z., Daniela, S. (2012). Textile organic dyes—characteristics, polluting effects and separation/elimination procedures from industrial effluents—a critical overview. [ISBN: 978-953-307-917-2].
- Carstea, E.M., Bridgeman, J., Baker, A., and Reynolds, D.M. (2016). Fluorescence spectroscopy for wastewater monitoring: a review. *Water Res*, 95, 205–219.
- Crini, G. (2006). Non-conventional low-cost adsorbents for dye removal: A review. *Biores. Tech*, 97, 1061–1085. doi:10.1016/J.BIORTECH.2005.05.001.
- Delavar, Z., and Shojaei, A. (2017). Enhanced mechanical properties of chitosan/nanodiamond composites by improving interphase using thermal oxidation of nanodiamond. *Carbohydr. Polym*, 167, 219– 228.
- Demirbas, A. (2009). Agricultural based activated carbons for the removal of dyes from aqueous solutions: A review. *J. Hazard. Mater*, 167, 1–9. doi:10.1016/j.jhazmat.2008.12.114.
- Djurisic, A. B., Leung, Y. H., and Ng, A.M.C. (2014). Strategies for Improving the Efficiency of Semiconductor Metal Oxide Photocatalysis. *Mater. Horiz*, 1, 400–410.
- El Miri, N., Abdelouahdi, K., Zahouily, M., Fihri, A., Barakat, A., Solhy, A., and El Achaby, M. (2015). Bio-nanocomposite films based on cellulose nanocrystals filled polyvinyl alcohol/chitosan polymer blend. *J. Appl. Polym. Sci*, 132.
- Elsayed, A.H., Mohy Eldin, M.S., Elsyed, A.M., Abo Elazm, A.H., Younes, E.M., Motaweh, H.A. (2011). Synthesis and Properties of Polyaniline/ferrites Nanocomposites. *Int. J. Electrochem. Sci*, 6 206 – 221.

Espinal, L., Suib, S. L., and Rusling, J.F. (2004). Electrochemical Catalysis of Styrene Epoxidation with Films of MnO<sub>2</sub> Nanoparticles and H<sub>2</sub>O<sub>2</sub>. *J. Am. Chem. Soc.*, 126, 7676–7682.

Fishbein, L. (1979). Aromatic Amines and Azo Dyes, in: L. Fishbein (Ed.), *Studies in Environmental Science*, Elsevier. Amsterdam, 356–416. doi:10.1016/S0166-1116(08)71329.

Fong, D., Marianne, B.A., Joel, G-L., Caroline, D.H. (2015). Biodegradable chitosan microparticles induce delayed STAT-1 activation and lead to distinct cytokine responses in differentially polarized human macrophages in vitro. *Acta Biomaterialia*, 12, 183-194. <https://doi.org/10.1016/j.actbio.2014.10.026>.

Gnanaprakasam, A., Sivakumar, V., and Thirumarimurugan, M. (2015). Influencing parameters in the photocatalytic degradation of organic effluent via nanometal oxide catalyst: a review. *Indian J. Eng. Mater. S.*, 2015, 1-16.

Ghaee, A., Shariaty Niassar, M., Barzin, J., and Matsuura, T. (2010). Effects of chitosan membrane morphology on copper ion adsorption. *Chem. Eng. J.*, 165, 1, 46–55.

Giustini, M., Angelone, D., Parente, M., Dini, D., Decker, F., Lanuti, A., Reale, A., Brown, T., and Di Carlo, A. (2013). Emission spectra and transient photovoltage in dye-sensitized solar cells under stress tests. *J. Appl. Electrochem.* 43, 209–215.

Gupta, V.K., Suhas. (2009). Application of low-cost adsorbents for dye removal-A review. *Journal of Environmental Management*, 90, 2313–2342. doi:10.1016/j.jenvman.2008.11.017.

Hunger, K. (2003). Dyes, General Survey, in: *Industrial Dyes: Chemistry, Properties, Applications*. Wiley Subscription Services, Inc., A Wiley Company, Frankfurt. 1–10. doi:10.1021/ja0335418.

Jalalah, M., Faisal, M., Bouzid, H., Park, J.G., Al-Sayari, S., and Ismail, A.A. (2015). Comparative study on photocatalytic performances of crystalline a-and b-Bi<sub>2</sub>O<sub>3</sub> nanoparticles under visible light. *J. Ind. Eng. Chem*, 30, 183-189.

Jayakumar, R., Tamura, H., Prabakaran, M., Kumar, P.T.S., Nair, S.V., and Furuike, T. (2011). Novel chitin and chitosan materials in wound dressing. In: *Biomedical Engineering. Trends in Materials Science*, 1–22.

Jayanthi K.G., and Suja, S.K. (2016). TiO<sub>2</sub> (rutile) embedded inulin a versatile bio-nanocomposite for photocatalytic degradation of methylene blue. *Carbohydrate Polymers*, 143, 51–60.

Khabashesku, V., Margrave, J., and Barrera, E. (2005). Functionalized carbon nanotubes and nanodiamonds for engineering and biomedical applications. *Diam. Relat. Mater.*, 14, 3, 859–866.

- Khan, A., Begum, S., Ali, N., Khan, S., Hussain, S., and Sotomayora, M.D.P.T. (2017). Preparation of cross linked chitosan magnetic membrane for cations sorption from aqueous solution. *Water Sci. Technol*, 75, 2034–2046.
- Kiatkittipong, K., and Assabumrungrat, S. (2017). A comparative study of sodium/hydrogen titanate nanotubes/nanoribbons on destruction of recalcitrant compounds and sedimentation. *J. Clean. Prod*, 148, 905-914.
- Lang, X.Y., Hirata, A., Fujita, T., and Chen, M.W. (2011). Nanoporous Metal/Oxide Hybrid Electrodes for Electrochemical Supercapacitors. *Nat. Nanotechnol*, 6, 232–236.
- Lim, C., Dong, S.H., Dong, W.L., (2021). Intermolecular interactions of chitosan: Degree of acetylation and molecular weight. *Carbohydrate Polymers*, 259, 117782. <https://doi.org/10.1016/j.carbpol.2021.117782>.
- Liu, J. T., Ge, X., Ye, X. X., Wang, G. Z., Zhang, H. M., Zhou, H. J., Zhang, Y.X., and Zhao, H.J. (2016). 3D Graphene/ $\delta$ -MnO<sub>2</sub> Aerogels for Highly Efficient and Reversible Removal of Heavy Metal Ions. *J. Mater. Chem. A*, 4, 1970–1979.
- Lopez, F., Cuomo, F., Lo Nostro, P., and Ceglie, A. (2013). Effects of solvent and alkaline earth metals on the heat-induced precipitation process of sodium caseinate. *Food Chem*, 136, 266–272.
- Martinová, L., and Lubasová, D. (2008). Electrospun chitosan based nanofibers. *Research Journal of Textile and Apparel*, 12, 72–79.
- Mazloom, F., Masjedi-Arani, M., and Salavati-Niasari, M. (2016). Controllable synthesis, characterization and photocatalytic studies on cadmium vanadate nanostructures. *Journal of Molecular Liquids*, 220, 566–572. doi:10.1016/j.molliq.2016.05.003
- Mahamallik, P., Pal, A. (2016). Photo-Fenton process in a Co (II)–adsorbed micellar softtemplate on an alumina support for rapid methylene blue degradation. *RSC Adv*, 6, 100876–100890.
- Muinde, V.M., Onyari, J.M., Wamalwa, B., Wabomba, J.N. (2020). Adsorption of malachite green dye from aqueous solutions using mesoporous chitosan–zinc oxide composite material. *Environmental Chemistry and Ecotoxicology*, 2, 115–125. doi:10.1016/j.enceco.2020.07.005.
- Ndlovu, T., Kuvarega, A.T., Arotiba, O.A., Sampath, S., Krause, R.W., Mamba, B.B. (2014). Exfoliated graphite/titanium dioxide nanocomposites for photodegradation of eosin yellow. *Applied Surface Science*, 300, 159–164.
- Ngah, W.W., Teong, L., Hanafiah, M. (2011). Adsorption of dyes and heavy metal ions by chitosan composites: a review. *Carbohydrate Polymers*, 83, 4, 1446–1456.
- Opping, S.O.B., Anku, W.W., Opoku, F., Shukla, S.K., and Govender, P.P. (2018). Photodegradation of eosin yellow dye in water under simulated solar light irradiation

using La-doped ZnO nanostructure decorated on graphene oxide as an advanced photocatalyst. *Chem. Select*, 3, 1180–1188.

Ou, M., Huang, J., Yang, X., Quan, K., Yang, Y., Xie, N., and Wang, K. 2017. MnO<sub>2</sub> Nanosheet Mediated “DD–A” FRET Binary Probes for Sensitive Detection of Intracellular mRNA. *Chem. Sci*, 8, 668– 673.

Pina-Pérez, Y., Tzompantzi-Morales, F., Pérez-Hernández, R., Arroyo-Murillo, R., Acevedo-Peña, R., and Gómez-Romero, R. (2017). Photo catalytic activity of Al<sub>2</sub>O<sub>3</sub> improved by the addition of Ce<sup>3+</sup>/Ce<sup>4+</sup> synthesized by the sol gel method. *Fuel*, 198, 11-21.

Raja, V.R., Rosaline, D.R., Suganthi, A., and Rajarajan, M. (2018). Facile sonochemical synthesis of Zn<sub>2</sub>SnO<sub>4</sub>-V<sub>2</sub>O<sub>5</sub> nanocomposite as an effective photocatalyst for degradation of eosin yellow. *Ultrason. Sonochem*, 44, 310–318.

Rashid, J., Saleem, S., Awan, S.U., Iqbal, A., Kumar, R., Barakat, M.A., Arshad, M., Zaheer, M., Rafique, M., Awad, M. (2018). Stabilized fabrication of anatase-TiO<sub>2</sub>/FeS<sub>2</sub> (pyrite) semiconductor composite nanocrystals for enhanced solar light-mediated photocatalytic degradation of methylene blue. *RSC Adv*, 8, 11935–11945.

Rauf, M.A., Meetani, M.A., Khaleel, A., Ahmad, A. (2010). Photocatalytic degradation of Methylene Blue using a mixed catalyst and product analysis by LC/MS. *Chem. Eng. J*, 157, 373–378.

Reddy, C. V., Babu, B., Reddy, I. N., and Shim, J. (2018). Synthesis and characterization of pure tetragonal ZrO<sub>2</sub> nanoparticles with enhanced photocatalytic activity. *Ceramics International*, 44, 6, 6940–6948.

Russo, M.V., Avino, P., Notardonato, I., and Cinelli, G. (2009). Cyanopropyl bonded-phase cartridges for trace enrichment of dioxins and chlorinated pesticides from water samples. *Chromatographia*, 69, 709–7017.

Shawky, H.A. (2009). Synthesis of ion-imprinting chitosan/PVA crosslinked membrane for selective removal of Ag (I). *App. Poymer Sci*, 114, 2608-2615. <https://doi.org/10.1002/app.30816>.

Soltani, N., Saion, E., Hussein, M.Z., Erfani, M., Abedini, A., Bahmanrokh, G., Navasery, M., and Vaziri, P. (2012). Visible light-induced degradation of methylene blue in the presence of photocatalytic ZnS and CdS nanoparticles. *Int. J. Mol. Sci*, 13, 10, 12242-12258.

Srinivasan, A., and Viraraghavan, T. (2010). Decolorization of dye wastewaters by biosorbents: A review. *J. Environ. Manage*, 91, 1915–1929. doi:10.1016/j.jenvman.2010.05.003.

Synowiecki, J., and Al-Khateeb, N.A. (2003). Production, Properties, and Some New Applications of Chitin and Its Derivatives. *Crit. Rev. Food Sci. Nutr*, 43, 145–171. doi: 10.1080/10408690390826473.

- Tao, Y., Ye, L., Pan, J., Wang, Y., and Tang, B. (2009). Removal of Pb (II) from aqueous solution on chitosan/TiO<sub>2</sub> hybrid film. *Journal of Hazardous Materials*, 161, 2, 718–722.
- Tan, W.F., Yu, Y.T., Wang, M.X., Liu, F., and Koopal, L.K. (2013). Shape evolution synthesis of monodisperse spherical, ellipsoidal, and elongated hematite ( $\alpha$ -Fe<sub>2</sub>O<sub>3</sub>) nanoparticles using ascorbic acid. *Cryst. Growth Des*, 14, 1, 157-164.
- Tian, Y., Ju, B., Zhang, S., and Hou, L. (2016). Thermo responsive cellulose ether and its flocculation behaviour for organic dye removal. *Carbohydrate Polymers*, 136, 1209–1217.
- Travaglini, L., Gubitosi, M., Di Gregorio, M.C., Pavel, N.V., D'Annibale, A., Giustini, M., Tellini, V.H.S., Tato, J.V., Obiols-Rabasa, M., Bayati, S., and Galantini, L. (2014). On the self-assembly of a tryptophan labeled deoxycholic acid. *Phys. Chem. Chem. Phys*, 16, 19492–19504.
- Truong, T.T., Liu, Y., Ren, Y., Trahey, L., and Sun, Y. (2012). Morphological and Crystalline Evolution of Nanostructured MnO<sub>2</sub> and Its Application in Lithium-Air Batteries. *ACS Nano*, 6, 8067–8077.
- Vakili, M., Rafatullah, M., Salamatinia, B., Abdullah, A.Z., Ibrahim, M.H., Tan, K.B., Gholami, Z., and Amouzgar, P. (2014). Application of chitosan and its derivatives as adsorbents for dye removal from water and wastewater: A review. *Carbohydr. Polym*, 113, 115–130. doi:10.1016/j.carbpol.2014.07.007.
- Vatanpour, V., Madaeni, S.S., Rajabi, L., Zinadini, S., and Derakhshan, A.A. (2012). Boehmite nanoparticles as a new nanofiller for preparation of antifouling mixed matrix membranes. *J. Membr. Sci*, 401, 132–143.
- Venditti, F., Cuomo, F., Ceglie, A., Avino, P., Russo, M.V., and Lopez, F. (2015). Visible light caffeic acid degradation by carbon-doped titanium dioxide. *Langmuir*, 31, 3627–3634.
- Vicentini, D.S., Smania, A., and Laranjeira, M. (2010). Chitosan/poly (vinyl alcohol) films containing ZnO nanoparticles and plasticizers. *Materials Science and Engineering: C*, 30, 4, 503–508.
- Wang, X., and Li, Y. (2002). Selected-Control Hydrothermal Synthesis of  $\alpha$  and  $\beta$ -MnO<sub>2</sub> Single Crystal Nanowires. *J. Am. Chem. Soc*, 124, 2880–2881.
- Yang, X., Li, I., Shang, S., and Tao, X. (2010). Synthesis and characterization of layer aligned poly (vinyl alcohol)/ graphene nanocomposites. *Polymer*, 51, 15, 3431-3435.
- Yao, T., Guo, S., Zeng, C., Wang, C., and Zhang, L. (2015). Investigation on efficient adsorption of cationic dyes on porous magnetic polyacrylamide microspheres. *Journal of Hazardous Materials*, 292, 90–97.
- Yaroslavov, A.A., Efimova, A.A., Krasnikov, E.A., Trosheva, K.S., Popov, A.S., Melik-Nubarov, N.S., Krivtsov, G.G., (2021). Chitosan-based multi-liposomal complexes:

Synthesis, biodegradability and cytotoxicity. *International Journal of Biological Macromolecules*. <https://doi.org/10.1016/j.ijbiomac.2021.02.169>

Yuan, Y., Wu, S., Shu, F., and Liu, Z. (2014). A MnO<sub>2</sub> Nanosheet as a Label-Free Nanoplatfom for Homogeneous Biosensing. *Chem. Commun*, 50, 1095–1097.

Zhang, K., Han, X., Hu, Z., Zhang, X., Tao, Z., and Chen, J. (2015). Nanostructured Mn-based Oxides for Electrochemical Energy Storage and Conversion. *Chem. Soc. Rev*, 44, 699–728.

Zhang, M., Yuan, R., Chai, Y., Li, W., Zhong, H., and Wang, C. (2011). Glucose biosensor based on titanium dioxide-multiwall carbon nanotubes-chitosan composite and functionalized gold nanoparticles. *Bioprocess and Biosystems Engineering*, 34, 9, 1143-1150.

Zhou, Z., Peng, X., Zhong, L., Wu, L., Cao, X., and Sun, R.C., (2016). Electrospun cellulose acetate supported Ag@AgCl composites with facet-dependent photocatalytic properties on degradation of organic dyes under visible-light irradiation. *Carbohydrate Polymers*, 136, 322–328.

## **Chapter 4: Application of manganese dioxide nanoparticles synthesized via green route for improved performance of water-based drilling fluids**

---

### **4.1 Introduction**

The planetary rise in the demand of energy and reduction in the production of oil from available resources has created a need to investigate unconventional hydrocarbon reservoirs such as shale formations and reservoirs which are difficult to access due to severe drilling conditions. Oil is produced from reservoirs through wellbore after performing a series of operations including drilling operation where drilling fluid is a key component of this operation. The composition and properties of drilling fluids enable these operations to be performed effectively. Drilling fluid has a role to play in different activities such as averting drill cuttings, cooling of drilling pipes, minimizing formation damage, and stabilization of wellbore [Abdo et al., 2012; Dardir et al., 2014; Sami et al., 2016; Kelessidis et al., 2011; Caenn et al., 2011]. The drilling operation can be carried out successfully in the shortest duration of time by carefully selecting and designing drilling fluids. Drilling fluids alternatively known as drilling muds are mainly classified into three types, which are oil-based mud (OBM), water-based mud (WBM) and synthetic drilling mud (SBM). Although the operational efficiency of OBM and SBM is higher as compared to WBM but these muds have significantly higher costs and possesses serious environmental threats, which restrict its usage in drilling operation [Riley et al., 2012; Sharma et al., 2012; Al-Arfaj et al., 2014; Dejtardon et al., 2019]. Therefore, out of the three, WBMs are preferred choice of muds despite of its reduced performance. Moreover, WBMs also have an advantage of lower average costs and lesser environmental restrictions [Davoodi et al., 2019]. The performance of WBM is improving with the advent of newer technologies and the mud chemists and engineers

across the globe are working tirelessly to make WBM performance at par with that of OBM with development of newer additives and techniques [**Hanyi et al., 2013; Kosynkin et al., 2012; Pakdaman et al., 2019**].

Rheological and filtration characteristics of drilling fluids are two most important mud properties for hydraulic designing of drilling fluid that need to be controlled with great caution. Mud rheology parameters such as apparent viscosity (AV), plastic viscosity (PV), yield point (YP) and gel strength (GS) are important factors in rate of penetration, cuttings holding in static conditions, cuttings removal and hole cleaning. Control of filtration rate is very critical in case of water-based drilling fluids. Filtration causes loss of water from drilling fluids into the formation and higher fluid loss values will result in increase of mud additives concentration that will alter the rheological parameters dramatically and ultimately affecting the whole drilling operation [**Abdou et al., 2014; Beg et al., 2019; Kelessidis et al., 2011**]. Another major issue associated with high fluid loss values of mud is the problem of shale instability of formations with high clay content because water interacts with clays present in shale formation and depending on the type of clay present in formation, it may cause swelling, which will destabilize the uncased well section [**Li et al., 2016**]. Higher fluid loss values also result in deposition of a thick mud cake which ultimately causes excessive drag and torque, stuck pipe, high pressures of swab and surge and formation damage [**Davoodi et al., 2019**]. In high pressure and high temperature (HPHT) conditions, there may be a dramatic increase in the fluid loss, which makes drilling fluids unsuitable to be used for drilling operations. Thus, to develop an effective drilling fluid, the two most important properties which need to be controlled are filtration and rheological properties [**Caenn et al., 2017a; Perween et al., 2018; Li et al., 2015; Li et al., 2015**]. An important consideration in designing a water-based drilling fluid is to perform the hot rolling experiment. The conditions of severe

temperatures and continuous circulation while sustaining heat, as experienced by a drilling fluid while drilling a well bore can be simulated by subjecting the drilling fluid to hot rolling in a roller oven for certain duration. The hot rolling of mud is carried out to determine the effect of continuous shear and thermal ageing on the properties of drilling fluid [Beg et al., 2019; Beg et al., 2018; Liu et al., 2016; Jain et al., 2015; Pakdaman et al., 2019]. After the exposure to higher temperatures, it is difficult to predict the rheology of drilling fluid owing to the physical, chemical and electrochemical changes in the composition of mud [Caenn et al., 2011]. Therefore, testing of each mud sample certifies respective rheological and filtration parameters.

Several experimental analyses have been carried out with the objective of formulating water-based drilling fluids impregnated with various additives to enhance the rheological properties and simultaneously reduce the filtration loss of drilling fluid. These studies reported polymers, nanomaterials, modified cellulose, polymer nanocomposites and most recently some ionic liquids as effective additives for rheology and fluid loss control in water-based drilling fluid [Davoodi et al., 2019; Perween et al., 2019; Parizad et al., 2016; Li et al., 2015; Ofei et al., 2017; Luo et al., 2017; Salih et al., 2016]. Commonly available polymeric additives are prone to thermal degradation in high temperature drilling operations due to their limited thermal stability. Therefore, it is necessary to either increase the thermal resistance of polymers suitable for drilling fluid applications or some other additives must be explored for the purpose. Here comes the advent of nanotechnology into play.

Recently, nanotechnology has found its potential application areas in oil and gas industry and has been introduced for modification of drilling fluid properties [Ramasamy et al., 2020; Perween et al., 2019; Rafati et al., 2018]. Different nanoparticles are used to amend the properties of the drilling fluid to enhance their functionalities. Some of the

recent studies reported the use of metal oxides [Dejtaradon et al., 2019; Bayat and Shams, 2019; Barry et al., 2015; Bayat et al., 2018; Beg et al., 2019; Salehnezhad et al., 2019, William et al., 2014], bimetallic oxides [Perween et al., 2018; Perween et al., 2019], magnesium aluminium silicate [Wang et al., 2018], cellulose nanomaterials [Li et al., 2015; Li et al., 2016; Song et al., 2016; Liet al., 2018] and polymer nanocomposites [Aftab et al., 2017; Jain et al., 2015b, Betiha et al., 2020; Jain et al., 2015b] in water-based drilling fluids. These modified drilling fluids are referred to as nano-enhanced drilling fluids or smart fluids, which possess improved rheological properties, high temperature resistance, and reduction in filtration losses, ability to maintain the stability of wellbore and eradicate harmful gases such as hydrogen sulphide. The incorporation of nanomaterial additives into drilling fluids is responsible for their distinguished thermo-physical properties [William et al., 2014]. Despite of various nanomaterials proposed for drilling fluids application, there is a need for further investigation on use of nanoparticles in water-based drilling fluids. With ever evolving nanotechnology and emphasis to further improve the mud properties for high performances. The requirement of exploration and investigation of new additives is an ongoing process. Nanoparticles impart desired properties to the drilling fluid owing to their smaller size in the range of 1-100 nm. The incorporation of nanoparticles in drilling fluid results in high surface area to volume ratio of the nanofluids in comparison to the conventional additives [El-Diasty et al., 2013].

In the present research work, a novel nanomaterial additive for water-based drilling fluid,  $\alpha$ -MnO<sub>2</sub> nanoparticles (MNPs), is studied for its effect on the filtration and rheological properties of a typical water-based drilling fluid. Manganese dioxide nanoparticles used for the preparation of nano-enhanced drilling fluids were synthesized through green route using the plant extract of *Ficus retusa*. The concentration of laboratory synthesized

MNPs was varied in a typical clay and polymer containing base mud (BM), and effect on rheology and filtration characteristics was considered. Then optimum concentration was fixed and further investigations were performed to identify the suitability and effectiveness of these nanoparticles in water-based drilling fluids. Effect of MNP on HPHT filtration loss and thermal stabilization of mud during the high temperature hot rolling was also investigated.

## **4.2 Experimental**

This study is the extension of the research work shown in the previous chapter discussing the application of nanoparticles synthesized by green route in development of water-based drilling fluids for drilling operation. The process of synthesis of manganese dioxide nanoparticles along with their characterization is mentioned in detail in chapter 2. Synthesized MNPs were used for enhancing the rheological properties of water-based drilling fluid. Following experiments were conducted to establish the application of MNPs in the development of water-based drilling fluid.

### **4.2.1 Drilling fluids preparation**

#### **4.2.2.1 Materials**

Bentonite powder (Bt), xanthan gum (XG) and potassium chloride (KCl) were procured from Molychem, India and used as obtained without any further modifications. Polyanionic cellulose regular grade (PAC) was provided by Oil and Natural Gas Corporation (ONGC) Ltd, India for research purpose and was used without any chemical treatment.

#### **4.2.2.2 Method**

20.00 g bentonite was taken and mixed in 400 mL of tap water using Hamilton beach (HB) mixer at speed I for 20 min. and then left overnight (for 16 hours) for complete hydration of clay. This prehydrated bentonite slurry (PHBS) was first mixed at speed I of Hamilton beach mixer. MnO<sub>2</sub> nanoparticles (MNPs) were then added into PHBS and

mixed at speed I. The PHBS-MNPs system was ultrasonicated for 30 min. before adding XG and PAC to the system. At the end, mud was mixed at the highest shear rate in HB mixer using speed III and kept for cooling down to room temperature in a water bath for 15-20 min. Finally, mud was homogenized for 3 min. at a speed of 15000 rpm using tool HT 1025 in Homogenizer HG-15D (Daihan Scientific Co. Ltd.). Same procedure was followed for preparation of all the drilling fluid formulations studied. The concentration of XG and PAC was fixed to be 0.25 w/v % each i.e., 1.00 g of XG and 1.00 g of PAC for the preparation of 400 mL mud sample. Following concentrations of nanoparticles were used for the preparation of mud samples:

**Table 4.1: Concentration of nanoparticles in the studied drilling fluids with corresponding codes**

| Sl. No. | MNPs conc. (w/v %) | MNPs mass for 400 mL mud sample (g) | Mud sample code |
|---------|--------------------|-------------------------------------|-----------------|
| 1       | 0.00               | 0                                   | BM              |
| 2       | 0.01               | 0.04                                | BM01            |
| 3       | 0.05               | 0.20                                | BM05            |
| 4       | 0.10               | 0.40                                | BM10            |
| 5       | 0.20               | 0.80                                | BM20            |
| 6       | 0.30               | 1.20                                | BM30            |
| 7       | 0.40               | 1.60                                | BM40            |
| 8       | 0.50               | 2.00                                | BM50            |
| 9       | 0.60               | 2.40                                | BM60            |

#### 4.2.2 Drilling fluids testing before and after hot rolling

Drilling mud formulations as mentioned in **table 4.1** were subjected to a roller oven at 30 rpm and temperature of 100°C temperature for 16 h after placing the mud samples inside an ageing cell of 500 mL capacity and then pressurizing the cell to 100 psi. The conditions of pressure, high temperature and continuous rotation of fluid are used to simulate the well bore condition and to study the effect of high temperature exposure for long durations. Thermally unstable mud formulation will undergo dramatic degradation where the rheological and filtration properties are altered too much to be used for

practical applications. However, these degradation in properties of polymer containing water-based drilling fluid should not be too large to ascertain the applicability of mud sample in the oilfields. The schematic of hot rolling process is represented in **figure 4.1**.

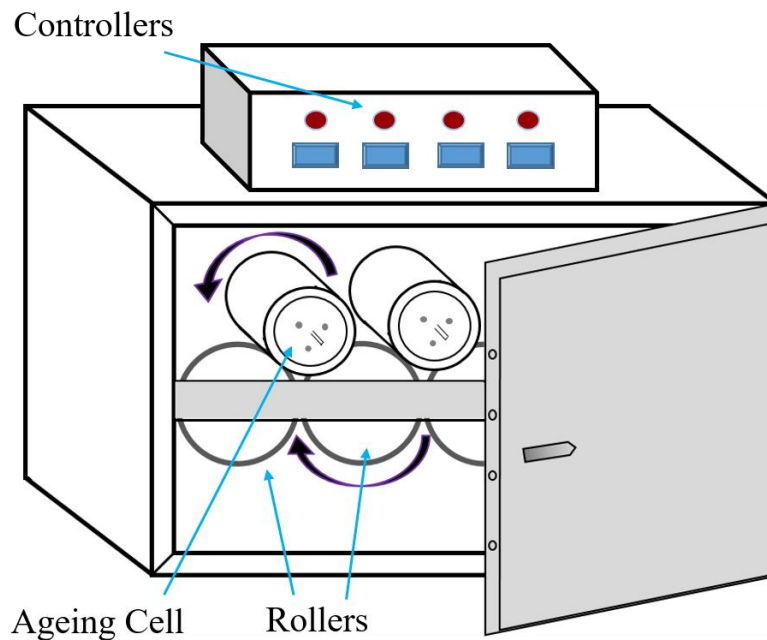


**Figure 4.1: Schematic of hot rolling process.**

**4.2.3 Evaluation of rheological parameters**

FANN Viscometer Model 35 was used for determination of viscosity and other rheological parameters of WBM formulations for freshly prepared mud as well as after hot rolling (AHR). This equipment is a direct indicating type viscometer in which the fluid is sheared inside the annular space between the two cylinders, namely bob and rotor and the deflection of the bob is indicated by a dial. The dial reading at rotational speed ‘n’ rpm can be denoted by  $\phi_n$ . The properties of drilling fluid can be obtained by Bingham plastic model by using following equations:

$$\text{Apparent viscosity (AV)} = \phi_{600}/2 \quad \dots\dots\dots (4.1)$$

$$\text{Plastic viscosity (PV)} = \phi_{600} - \phi_{300} \quad \dots\dots\dots (4.2)$$

$$\text{Yield point (YP)} = \phi_{300} - PV \quad \dots\dots\dots (4.3)$$

However, the initial gel strength can be directly obtained as the maximum dial deflection on switching on the motor at 3 rpm after the fluid has been at rest for 10 seconds. The similar procedure is used to obtain the final gel strength except the time for which fluid has been at rest will be 10 min. The units of AV and PV are cP and those of rest of the three properties is same, which is lb/100ft<sup>2</sup>.

### **Rheological analysis of drilling fluids**

After hot rolling of drilling fluids, five different mud samples were tested for rheology analysis by Anton Paar MCR-52 in cone and plate arrangement. A varying shear rate in the range of 0.1 to 1000 s<sup>-1</sup> was applied for the analysis. Temperature was maintained at 25°C for all the measurements. This was done to see the effect of varying shear rate on drilling mud samples.

#### **4.2.4 Filtration testing**

Filtration testing was performed as per the API recommended procedure for fluid loss testing of water-based drilling fluids. Low pressure - low temperature (LPLT) filter press was used for the determination of API fluid loss, which is the filtrate volume collected in 30 min. time maintaining 100 psi pressure at room temperature. High pressure – high temperature (HPHT) fluid loss was determined at a differential pressure of 500 psi and a temperature of 150°C in FANN HPHT filter press having 175 mL cell capacity. Filter cake formed due to the solids deposition on filter paper during LPLT filtration testing was taken out carefully after the test. It was washed using tap water with a gentle stream of water and mud cake was allowed to be dried. After drying, the surface of mud cake was analyzed with field emission scanning electron microscopy (FESEM) technique for investigating the effect of nanoparticles on its morphology.

### 4.3 Results and discussion

#### 4.3.1 DLS study of water-based drilling fluid

**Table 4.2** depicts the zeta potential values of xanthum gum,  $\alpha$ -MnO<sub>2</sub> nanoparticles and their blend. Each of the samples were dispersed in de-ionized water. It was found that the zeta potential value of MNPs is -28.4 mV. Zeta potential values in the range of 30-60 mV show upright stability and good dispersion of nanoparticles in distilled water [Wissing et al., 2004; Ravichandran et al., 2014]. The value of zeta potential below 20 mV shows short term stability while values above 60 mV is for excellent stability [Honary et al., 2013]. Therefore, it can be concluded that the biofabricated MNPs are on the borderline stability of colloidal systems. However, the zeta potential value of XG was found to be -43.5 mV, which indicates the dispersion stability in colloidal state. On preparing a blend of MNPs with XG, dispersed in de-ionized water, the zeta potential value increased from -28.4 mV to -40.4 mV. The increase in the stability of colloidal dispersion of MNPs on addition of XG can be attributed to the interaction of electronegative functional groups present in the polymer chain network of XG.

The particle size distribution of the abovementioned systems was investigated using DLS analysis. The DLS study exhibits that the size of MNPs in powder form is very less as compared to their hydraulic size in distilled water, which validates the aggregation of NPs in distilled water (**table 4.2**). The average particle size of nanoparticles dispersed in water was found to be 172.0 nm, which increased to 271.0 nm on adding XG to the solution. This observation further validates the theory of interaction between the molecules of XG and MNPs, which lead to the modification in zeta potential and size distribution of nanoparticles.

**Table 4.2: Zeta potential (at room temperature) of xanthun gum (0.05 w/v %), MNPs (0.05 w/v %), and a combination of xanthan gum (0.05 w/v %) and MNPs (0.05 w/v %); each dispersed in deionized water**

| Sl. No. | Sample  | Average particle size (nm) | Zeta potential (mV) |
|---------|---------|----------------------------|---------------------|
| 1       | MNPs    | 83.1                       | -28.4               |
| 2       | XG      | 172.0                      | -43.5               |
| 3       | XG+MNPs | 201.5                      | -40.4               |

#### 4.3.2 Rheological parameters of $\alpha$ -MnO<sub>2</sub> nanoparticles containing mud formulations

Mud formulations with varying quantities of MNPs (as shown in **table 4.1**) were subjected to hot rolling for 16 hours at 100°C temperature. The rheological parameters of various muds before and after hot rolling (AHR and BHR) are shown in **figure 4.2**. In case of freshly prepared mud samples (before hot rolling), it was observed that the AV, PV, YP and GS (both GS-0 and GS-10) all increased with the concentration of NPs. Addition of 0.6 w/v % of MNPs into BM increased AV, PV, YP, GS-0 and GS-10 by ~71, ~43, ~90, ~154 and ~103 percent respectively at before hot rolling (BHR) condition. It shows that the minimum impact of the presence of nanoparticles was on plastic viscosity, while GS-0 was affected by highest margin. Increase in the value of apparent viscosity is desirable for the better hole cleaning since the lifting capacity of cuttings is also dependent on the apparent viscosity of the drilling fluids [Dejtaradon et al., 2019]. Plastic viscosity of drilling fluids should be lower for the faster rate of penetration but this parameter is also dependent on to other rheological parameters. In general, an increase in apparent viscosity increases the plastic viscosity. In case of present mud formulations, the increase in apparent viscosity (and other rheological parameters as shown in **figure 4.2a** and **4.2c**) can be achieved by addition of nanoparticles that will have minimal effect on plastic viscosity as the plot for plastic viscosity is almost flat as compared to that for other parameters. Yield point is an important parameter for cutting carrying capacity of drilling fluid and higher values of yield point helps in carrying

heavier cutting with ease. Here the effect of nanoparticles on yield point is such that it will help in improving the cuttings carrying capacity. Addition of just 0.01 w/v % of MNPs increases AV, PV and YP of base mud by ~6, 0 and ~10 % respectively and the corresponding values for 0.05 w/v % of MNPs in mud (i.e., for mud formulation BNM05) were found to be ~10, ~7 and ~13%. Above data show that even at very low concentration of nanoparticles, significant improvement in drilling fluid rheology can be achieved by MNPs with an additional advantage of less increment in PV to keep up faster rate of penetration. Gel strength of drilling fluid is important for holding the cutting in suspension while there is a halt in drilling operation. If sufficient gel strength is not there, the cuttings will start settling to the bottom and may choke the drill string. MNPs enhanced both initial and final gel strength with increase in nanoparticles concentration.

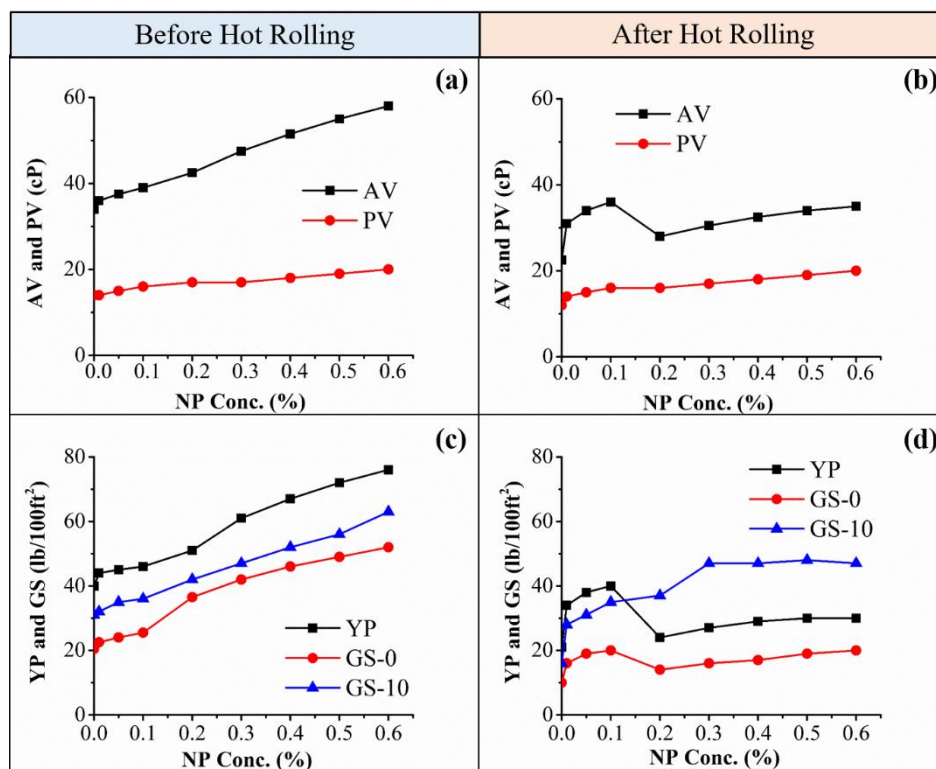


**Figure 4.2: Rheological parameters of drilling fluids before and after hot rolling at 100°C temperature for 16 hours (AV = Apparent viscosity, PV = Plastic viscosity, YP = Yield point, GS = Gel strength, GS-0 = Initial GS and GS-10= 10 minutes or final GS).**

The effect of ageing process on a typical polymer containing mud system is that rheological properties are diminished due to the degradation of biopolymers (such as XG and PAC) to some extent, depending upon the temperature [Beg et al., 2018]. In present case, base mud has xanthan gum and polyanionic cellulose present in it, and ageing caused reduction in its rheological properties as can be observed in **figure 4.2**. However, the addition of small amount of nanoparticles decreases the extent by which this reduction happened due to ageing. In absence of nanoparticles, AV and YP of base mud reduced by ~34% and ~48% due to ageing at 100°C temperature and the corresponding figures (reduction in AV and YP) for BMN01, BMN05 and BMN10 were (~14 and ~23%), (~9 and ~16%) and (~8 and ~13%) respectively. Experimental data indicated that the increase in MNPs concentration is improving the thermal stability of polymer containing mud system, which is essential for using polymer-based drilling fluids at high temperatures. At the MNPs concentration higher than 0.1 w/v %, AV, YP and GS-0 reduced dramatically and further addition of nanoparticles gradually improved rheological properties after hot rolling (**figure 4.2b** and **4.2d**). This strange behaviour may be due to the aggregation of nanoparticles at higher concentrations. When MNPs concentration reached the concentration of 0.2 w/v %, the population of MNPs in the mud system became so high that they interacted with each other more frequently during the 16 hours of hot rolling and started aggregating inside the mud system, which reduced the rheological properties by a higher fraction than anticipated. Further increase in MNPs concentration increases the number of MNPs aggregates and rheological properties increase (**figure 4.2b** and **4.2d**). Another factor to promote aggregation is the ferromagnetic nature of  $\alpha$ -MnO<sub>2</sub> in presence of K<sup>+</sup> ions, which are present in the mud system [Tseng et al., 2015]. At higher concentrations, these factors overcome the zeta potential of MnO<sub>2</sub> nanoparticles in polymer matrix and thus, resulting in formation of

nanoparticle clusters. Ultimately, due to the presence of less scattering of nanoparticles in the drilling fluid formulations, AHR properties beyond 0.1 w/v % are showing unusual trend. To further investigate the rheological behaviour of after hot rolling mud formulations, rheology was performed for five after hot rolling drilling fluid samples namely BM, BMN05, BMN10, BMN20 and BMN30 using Anton Paar MCR52 and results are shown in **figure 4.3** given below. It was found that the viscosity of base mud remains lowest among the tested mud samples and the viscosity of BMN10 was found to be higher than that of BMN20 and BMN30. Viscosity of all mud samples decreased with shear rate, which shows the drilling fluid samples are shear thinning and this will be helpful for effective hole cleaning and low pressure losses through the drill bit nozzles.

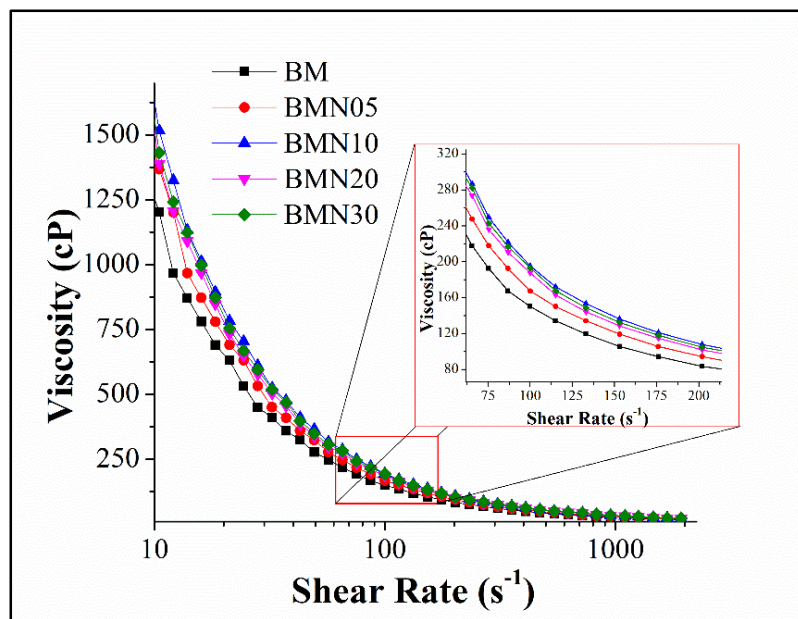


**Figure 4.3: Viscosity vs shear stress curves of drilling fluid samples after hot rolling.**

#### 4.3.3 Low pressure-low temperature filtration

LPLT fluid loss of the mud formulations (before and after hot rolling) is shown in **figure 4.4**. It can be seen in the plot that the addition of nanoparticles is reducing the API fluid loss, which is the filtrate volume collected in 30 min. maintaining 100 psi pressure at room temperature. Ageing at 100°C temperature resulted in an increase in filtrate loss of BM and API filtrate increased from 9.0 to 10.2 mL due to hot rolling. For BMN01, the

fluid loss increased from 8.1 to 9.1 mL, an increase of 3.4%, which is very small as compared to 13.3% increase for BM. For BMN05 and BMN10, percentage increase in API fluid loss was 3.4 and 3.5% respectively. At higher concentrations, the fluid loss further decreased with nanoparticle concentration but the percent increase due to ageing was higher than 15% or more for MNPs concentrations more than 0.2 w/v %. Therefore, it can be suggested that the optimum MNPs concentration for the studied mud system is ~0.1 w/v %. The nanoparticles help in reducing the fluid loss by plugging the micro pores of mud filter cake formed by the deposition of solids left behind during the filtration. Small nanoparticles, their aggregates and polymer chains combined with small clusters of nanoparticles choke the nano-scale and sub micro-scale permeable gaps and reduce the rate of filtration [Bayat et al., 2019]. Nanoparticles also help in forming a compact filter cake with low permeability, which results in minimizing the fluid loss along with mitigating other problems such as pipe stuck and friction between drill string and wellbore [Parizad et al., 2016].

FESEM analysis of dried filter cakes, which were formed during LPLT filtration of BM and BMN10 (mud containing 0.1 w/v % of MNPs) were analysed and have been shown in **figure 4.5**. It was found that the filter cake formed by filtration test of BM has some cracks on the surface of mud cake, which gets minimized in case of BMN10 due to the presence of nanoparticles. EDX analysis of both filter cakes was performed to detect the presence of MNPs on the surface of filter cake and it was confirmed that MNPs are present on the mud cake surface, which are responsible for better binding of solids in mud cake to reduce the permeability and thus lowering the fluid loss. **Figure 4.6** shows the photograph of filter cakes with and without nanoparticles.

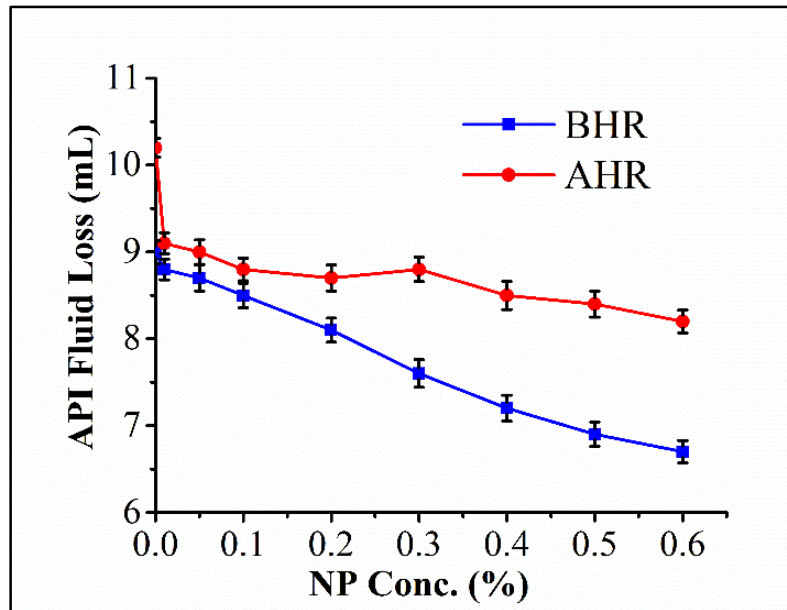


Figure 4.4: Low pressure-low temperature fluid loss of drilling base mud and nanoparticles containing mud formulations before and after hot rolling at 100°C temperature.

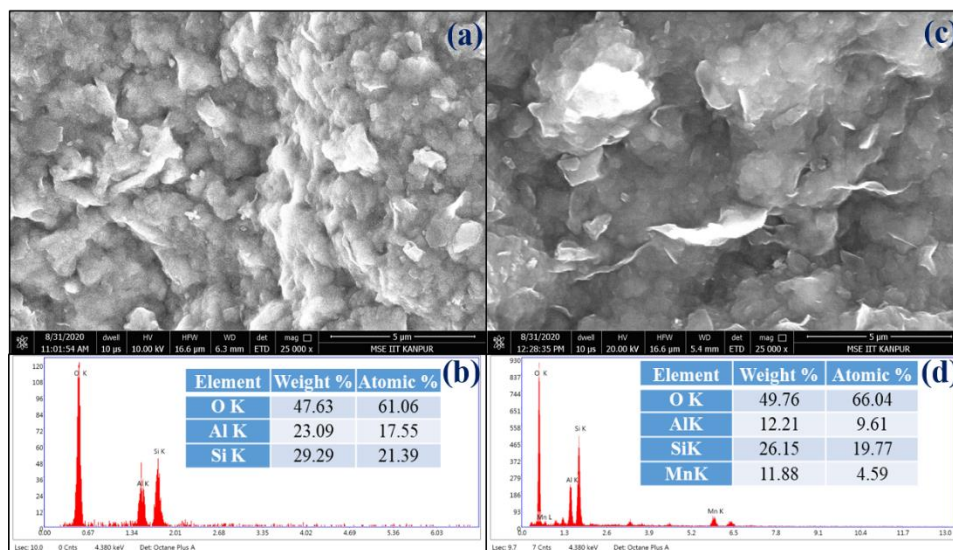
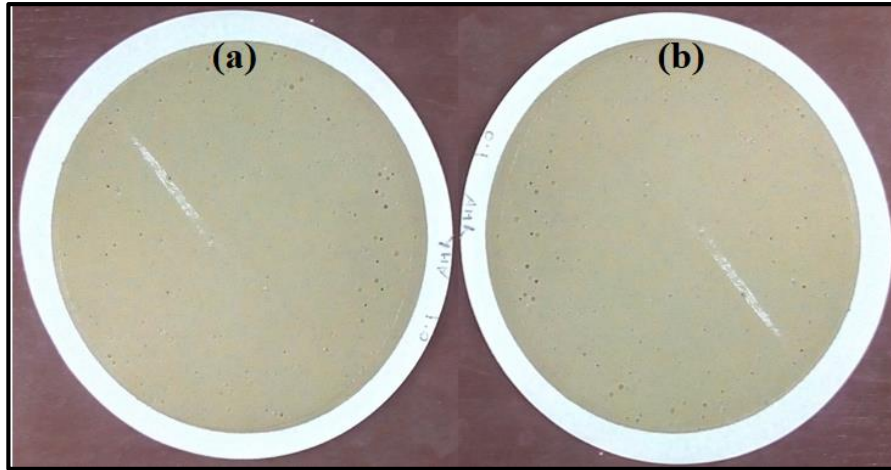
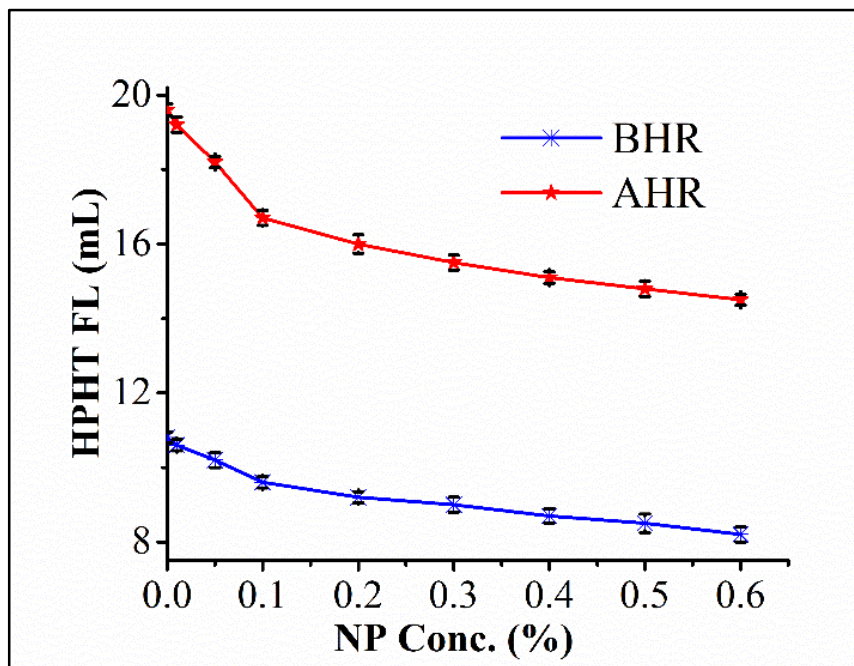


Figure 4.5: FESEM and EDX analysis of filter cake formed by low pressure-low temperature filtration test of base mud (a and b) and mud with 0.10 w/v % of MNPs (c and d).



**Figure 4.6:** Filter cake obtained by API filtration test (a) base mud and (b) mud with 0.20 w/v % of MNPs.

#### 4.3.4 High pressure-high temperature fluid loss



**Figure 4.7:** High pressure-high temperature fluid loss of nanoparticles containing mud formulations before and after hot rolling.

HPHT fluid loss of drilling fluids was at a temperature of 150°C and the results obtained are shown in **figure 4.7**. Similar to the LPLT fluid loss, the filtration loss at HPHT conditions also reduced due to the addition of MNPs but the filtration rates per unit area were more than twice than those for LPLT conditions as the filtration area for HPHT filter press was about half the area for LPLT filter press. Next notable observation is the

change in filtration rate after hot rolling is about ~82% for BM, which reduced to ~74% for mud formulation containing 0.1 w/v % of MNPs. The effect of 0.1 w/v % of MNPs before hot rolling was to reduce HPHT fluid loss by ~11%, which attained a value of ~15% after the hot rolling. At higher concentration, the effectiveness of MNPs remained similar to that by 0.1 w/v % on reducing the hot rolling effect on HPHT filtration. Reduction in HPHT filtration loss is evident that the MNPs are helpful in reducing the fluid loss effectively.

#### 4.3.5 Effect of concentration of $\alpha$ -MnO<sub>2</sub> nanoparticles on pH and electrical conductivity

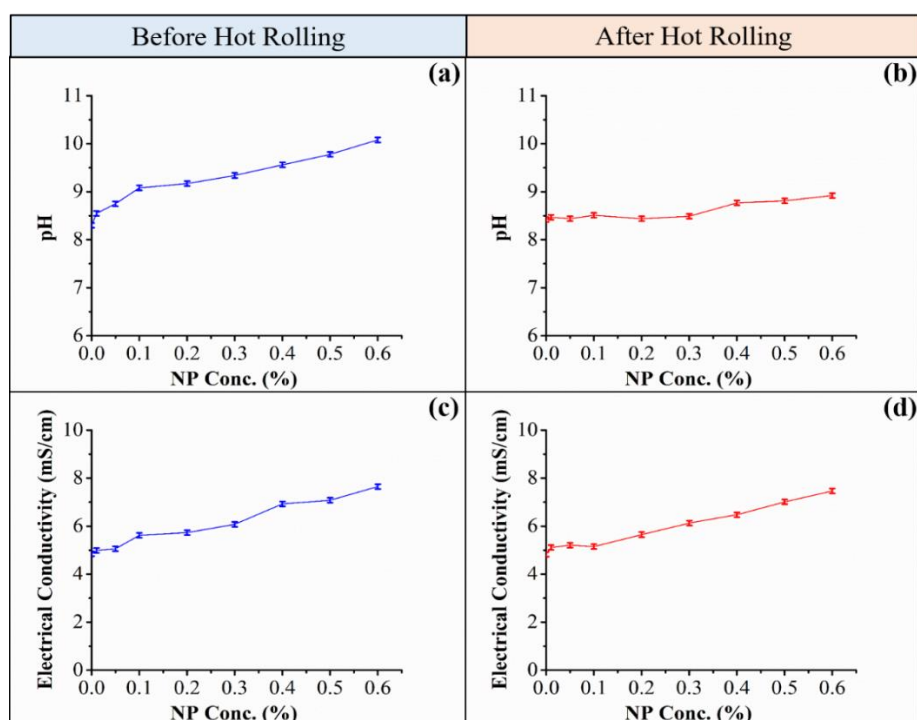


**Figure 4.8: pH and electrical conductivity of drilling fluids before hot rolling (a and b) and after hot rolling (c and d) at 100°C temperature (both measured at room temperature i.e., 25°C).**

MNPs affected both pH of the drilling fluid and its electrical conductivity. The increase in concentration of MNPs concentration increased the pH of the mud formulation for freshly prepared samples (before hot rolling) (figure 4.8a and 4.8b) and even after ageing (after hot rolling) of mud samples (figure 4.8c and 4.8d). The increase in pH of the mud

due to the addition of nanoparticles can be attributed to the mildly basic nature of MNPs since it is a metal oxide. pH of BM increased to 9.08 on addition of 0.1 w/v % of MNPs and further addition gradually increased mud pH to 10.08 at highest concentration. After ageing, maximum pH of 8.92 was obtained for 0.6 w/v % of MNPs containing mud (BMN60) and that for BMN10 was 8.51. Electrical conductivity of mud samples before and after hot rolling also increased gradually due to the addition of nanoparticles and it remained in the range of 4.99 – 7.65 mS/cm for freshly prepared samples and 5.11 – 7.47 mS/cm after hot rolling of mud. Base mud showed the electrical conductivity values 4.85 and 4.83 mS/cm for before and after hot rolling respectively. It is clear that the nanoparticles are effective in enhancing the electrical conductivity of drilling fluids that is advantageous for well logging for formation evaluation [Parizad et al., 2018]. At 0.1 w/v % of MNPs concentration, electrical conductivity of BM increased by 16%, which shows a significant improvement.

#### **4.4 Conclusions**

The study aimed at investigating the effect of laboratory synthesized biofabricated  $\alpha$ -MnO<sub>2</sub> nanoparticles on the rheological properties along with fluid loss of water-based drilling fluid. The drilling fluid system was also subjected to ageing with the objective of studying the effect of hot rolling on the abovementioned properties. On the basis of abovementioned study, it was observed that

- The biofabricated nanoparticles are effective in aiding water-based drilling fluid to refine the rheological and filtration properties.
- The nanoparticles were capable of improving the rheological properties of base fluid even at the lowest concentration of 0.01 w/v % and increasing the concentration further enhances the properties.

- $\alpha$ -MnO<sub>2</sub> nanoparticles-based nanoenhanced drilling fluid were found to be effective in reducing both LPLT and HPHT filtrate loss of mud samples aged at 100°C temperature.
- The presence of  $\alpha$ -MnO<sub>2</sub> nanoparticles over the surface of mud cakes seal up the cracks present on cakes' surface and thereby reducing the filtrate loss.
- Mud formulation containing  $\alpha$ -MnO<sub>2</sub> nanoparticles showed improved electrical conductivity, which is helpful in mud logging.

Therefore, it can be concluded that the  $\alpha$ -MnO<sub>2</sub> nanoparticles synthesized via green route can be used as an additive to water-based drilling fluids to upgrade their properties and the enhanced nano-drilling fluids can be helpful in providing more efficiency to drilling operations of oil and gas industries.

## References

Abdo, J., Haneef, M.D. (2012). Nano-Enhanced Drilling Fluids: Pioneering Approach to Overcome Uncompromising Drilling Problems. *J. Energy Resour. Technol*, 134, 1–6. <https://doi.org/10.1115/1.4005244>.

Abdou, M.I., Abuseda, H. (2014.) Improving the performance of clay from Gabal Um Kumar as drilling mud. *Egypt. J. Pet*, 23, 213–220. <https://doi.org/10.1016/j.ejpe.2014.05.008>.

Aftab, A., Ismail, A.R., Ibupoto, Z.H., Akeiber, H., Malghani, M.G.K. (2017). Nanoparticles based drilling muds a solution to drill elevated temperature wells: A review. *Renew. Sustain. Energy Rev*, 76, 1301–1313. <https://doi.org/10.1016/j.rser.2017.03.050>.

Al-Arfaj, M.K., Amanullah, M., Sultan, A.S., Hossain, E., Abdurraheem, A. (2014). Chemical and mechanical aspects of wellbore stability in shale formations: A literature review, in: Abu Dhabi Int. Pet. Exhib. Conf., Abu Dhabi. <https://doi.org/10.2118/171682-ms>.

Ali, G.A.M., Yusoff, M.M., Shaaban, E.R., Chong, K.F. (2017). High performance MnO<sub>2</sub> nanoflower supercapacitor electrode by electrochemical recycling of spent batteries. *Ceram. Int*, 43, 8440–8448. <https://doi.org/10.1016/j.ceramint.2017.03.195>.

Barry, M.M., Jung, Y., Lee, J.K., Phuoc, T.X., Chyu, M.K. (2015). Fluid filtration and rheological properties of nanoparticle additive and intercalated clay hybrid bentonite drilling fluids. *J. Pet. Sci. Eng*, 127, 338–346. <https://doi.org/10.1016/j.petrol.2015.01.012>.

Bayat, A.E., Jalalat Moghanloo, P., Piroozian, A., Rafati, R. (2018). Experimental investigation of rheological and filtration properties of water-based drilling fluids in presence of various nanoparticles. *Colloids Surfaces A Physicochem. Eng. Asp*, 555, 256–263. <https://doi.org/10.1016/j.colsurfa.2018.07.001>.

Bayat, A.E., Shams, R. (2019). Appraising the impacts of SiO<sub>2</sub>, ZnO and TiO<sub>2</sub> nanoparticles on rheological properties and shale inhibition of water-based drilling muds. *Colloids Surfaces A Physicochem. Eng. Asp*, 581, 123792. <https://doi.org/10.1016/j.colsurfa.2019.123792>.

Beg, M., Kesarwani, H., Sharma, S., Gandhi, R. (2019). SPE-197703-MS Effect of CuO and ZnO Nanoparticles on Efficacy of Poly 4-Styrenesulfonic Acid-Co-Maleic Acid Sodium Salt for Controlling HPHT Filtration.

Beg, M., Kesarwani, H., Sharma, S. Effect of CuO and ZnO Nanoparticles on Efficacy of Poly 4-Styrenesulfonic Acid-Co-Maleic Acid Sodium Salt for Controlling HPHT Filtration, in: Abu Dhabi Int. Pet. Exhib. Conf., SPE, Abu Dhabi, 2019: pp. 1–11. <https://doi.org/10.2118/197703-ms>.

Beg, M., Singh, P., Sharma, S., Ojha, U. (2019). Shale inhibition by low-molecular-weight cationic polymer in water-based mud. *J. Pet. Explor. Prod. Technol*, 9, 1995–2007. <https://doi.org/10.1007/s13202-018-0592-7>.

Beg, M., Sharma, S., Ojha, U. (2018a). Effect of cationic copolyelectrolyte additives on drilling fluids for shales. *J. Pet. Sci. Eng*, 161, 506–514. <https://doi.org/10.1016/j.petrol.2017.12.009>.

Beg, M., Sharma, S., Ojha, U. (2018b). Effect of cationic copolyelectrolyte additives on drilling fluids for shales. *J. Pet. Sci. Eng*, 161, 506–514. <https://doi.org/10.1016/j.petrol.2017.12.009>.

Betiha, M.A., Mohamed, G.G., Negm, N.A., Hussein, M.F., Ahmed, H.E. (2020). Fabrication of ionic liquid-cellulose-silica hydrogels with appropriate thermal stability and good salt tolerance as potential drilling fluid. *Arab. J. Chem*, 13, 6201–6220. <https://doi.org/10.1016/j.arabjc.2020.05.027>.

Caenn, R., Darley, H.C.H., Gray, G.R. (2011). *Composition and properties of drilling and completion fluids*. Seventh Ed, Gulf Professional Publishing.

Caenn, R., Darley, H.C.H., Gray, G.R. (2017a). *The Filtration Properties of Drilling Fluids*. <https://doi.org/10.1016/b978-0-12-804751-4.00007-9>.

Caenn, R., Darley, H.C.H., Gray, G.R. (2017b). *Drilling Problems Related to Drilling Fluids*. <https://doi.org/10.1016/b978-0-12-804751-4.00010-9>.

Dardir, M.M., Ibrahime, S., Soliman, M., Desouky, S.D., Hafiz, A.A. (2014). Preparation and evaluation of some esteramides as synthetic based drilling fluids. *Egypt. J. Pet*, 23, 35–43. <https://doi.org/10.1016/j.ejpe.2014.02.006>.

Davoodi, S., Ramazani S.A., Soleimanian, A., Fella Jahromi, A. (2019). Application of a novel acrylamide copolymer containing highly hydrophobic comonomer as filtration control and rheology modifier additive in water-based drilling mud. *J. Pet. Sci. Eng*, 180, 747–755. <https://doi.org/10.1016/j.petrol.2019.04.069>.

Dejtaradon, P., Hamidi, H., Chuks, M.H., Wilkinson, D., Rafati, R. (2019). Impact of ZnO and CuO nanoparticles on the rheological and filtration properties of water-based drilling fluid. *Colloids Surfaces A Physicochem. Eng. Asp*, 570, 354–367. <https://doi.org/10.1016/j.colsurfa.2019.03.050>.

Duan, W., Vemuri, R.S., Milshtein, A. et al. (2016). Symmetric organic-based nonaqueous redox flow battery and its state of charge diagnostics by FTIR. <https://doi.org/10.1039/c6ta01177b>.

El-Diasty, A.I., Salem Ragab, A.M. (2013). Applications of nanotechnology in the Oil and Gas industry: Latest trends worldwide and future challenges in Egypt, in: *North Africa Tech. Conf. Exhib.*, Cairo, <https://doi.org/10.2118/164716-ms>.

Hanyi, Z., Zhengsong, Q., Weian, H., Caojie., Daquan, H., Haibin, L. (2013). Successful Application of Unique Polyamine High Performance Water- Based Drilling Fluid in Bohai Bay Shale Formations. in: *Int. Pet. Technol. Conf.*, Beijing.

Honary, S., Zahir, F. (2013). Effect of zeta potential on the properties of nano-drug

delivery systems - A review (Part 1). *Trop. J. Pharm. Res*, 12, 255–264.

Jain, R., Mahto, V., Sharma, V.P. (2015). Evaluation of polyacrylamide-grafted-polyethylene glycol/silica nanocomposite as potential additive in water-based drilling mud for reactive shale formation. *J. Nat. Gas Sci. Eng*, 26, 526–537. <https://doi.org/10.1016/j.jngse.2015.06.051>.

Jain, R., Mahto, V. (2015). Evaluation of polyacrylamide/clay composite as a potential drilling fluid additive in inhibitive water-based drilling fluid system. *J. Pet. Sci. Eng*.

Jain, R., Mahto, V., Sharma, V.P. (2015). Evaluation of polyacrylamide-grafted-polyethylene glycol/silica nanocomposite as potential additive in water-based drilling mud for reactive shale formation. *J. Nat. Gas Sci., Eng*, 26, 526–537. <https://doi.org/10.1016/j.jngse.2015.06.051>.

Jia, J., Zhang, P., Chen, L. (2016). The effect of morphology of  $\alpha$ -MnO<sub>2</sub> on catalytic decomposition of gaseous ozone. *Catal. Sci. Technol*, 6, 5841–5847. <https://doi.org/10.1039/c6cy00301j>.

Kelessidis, V.C., Poulakakis, E., Chatzistamou, V. (2011). Use of Carbopol 980 and carboxymethyl cellulose polymers as rheology modifiers of sodium-bentonite water dispersions. *Appl. Clay Sci*, 54, 63–69. <https://doi.org/10.1016/j.clay.2011.07.013>.

Kosynkin, D.V., Ceriotti, G., Wilson, K.C., Lomeda, J.R., Scorsone, J.T., Patel, A.D., Friedheim, J.E., Tour, J.M. (2012). Graphene Oxide as a High-Performance Fluid-Loss-Control Additive in Water-Based Drilling Fluids. *ACS Appl. Mater. Interfaces*, 4, 222–227. <https://doi.org/10.1021/am2012799>.

Li, M.C., Wu, Q., Song, K., Lee, S., Jin, C., Ren, S., Lei, T. (2015). Soy Protein Isolate As Fluid Loss Additive in Bentonite–Water-Based Drilling Fluids. <https://doi.org/10.1021/acsami.5b07883>.

Li, M.C., Wu, Q., Song, K., Qing, Y., Wu, Y. (2015). Cellulose nanoparticles as modifiers for rheology and fluid loss in bentonite water-based fluids. *ACS Appl. Mater. Interfaces*, 7, 5006–5016. <https://doi.org/10.1021/acsami.5b00498>.

Li, M.C., Wu, Q., Song, K., De Hoop, C.F., Lee, S., Qing, Y., Wu, Y. (2016). Cellulose Nanocrystals and Polyanionic Cellulose as Additives in Bentonite Water-Based Drilling Fluids: Rheological Modeling and Filtration Mechanisms, *Ind. Eng. Chem. Res*, 55, 133–143. <https://doi.org/10.1021/acs.iecr.5b03510>.

Li, M.C., Wu, Q., Song, K., French, A.D., Mei, C., Lei, T. (2018). Ph Responsive Water-Based Drilling Fluids Containing Bentonite and Chitin Nanocrystals. *ACS Sustain. Chem. Eng*, 6, 3783–3795. <https://doi.org/10.1021/acssuschemeng.7b04156>.

Li, M.C., Ren, S., Zhang, X., Dong, L., Lei, T., Lee, S., Wu, Q. (2018). Surface-Chemistry-Tuned Cellulose Nanocrystals in a Bentonite Suspension for Water-Based Drilling Fluids. *ACS Appl. Nano Mater*, 1, 7039–7051. <https://doi.org/10.1021/acsanm.8b01830>.

Liu, F., Jiang, G., Peng, S., He, Y., Wang, J. (2016). Amphoteric Polymer as an Anti-calcium Contamination Fluid-Loss Additive in Water-Based Drilling Fluids. *Energy and Fuels*, 30, 7221–7228. <https://doi.org/10.1021/acs.energyfuels.6b01567>.

Luo, Z., Pei, J., Wang, L., Yu, P., Chen, Z. (2017). Influence of an ionic liquid on rheological and filtration properties of water-based drilling fluids at high temperatures. *Appl. Clay Sci*, 136, 96–102. <https://doi.org/10.1016/j.clay.2016.11.015>.

Ofei, T.N., Bavoh, C.B., Rashidi, A.B. (2017). Insight into ionic liquid as potential drilling mud additive for high temperature wells. *J. Mol. Liq*, 242, 931–939. <https://doi.org/10.1016/j.molliq.2017.07.113>.

Pakdaman, E., Osfouri, S., Azin, R., Niknam, K., Roohi, A. (2019). Improving the rheology, lubricity, and differential sticking properties of water-based drilling muds at high temperatures using hydrophilic Gilsonite nanoparticles. *Colloids Surfaces A Physicochem. Eng. Asp*, 582, 123930. <https://doi.org/10.1016/j.colsurfa.2019.123930>.

Pakdaman, E., Osfouri, S., Azin, R., Niknam, K., Roohi, A. (2019). Synthesis and characterization of hydrophilic gilsonite fine particles for improving water-based drilling mud properties. *J. Dispers. Sci. Technol*, 41, 1633–1642. <https://doi.org/10.1080/01932691.2019.1634582>.

Parizad, A., Shahbazi, K. (2016). Experimental investigation of the effects of SnO<sub>2</sub> nanoparticles and KCl salt on a water base drilling fluid properties. *Can. J. Chem. Eng*, 94, 1924–1938. <https://doi.org/10.1002/cjce.22575>.

Parizad, A., Shahbazi, K., Ayatizadeh Tanha, A. (2018). Enhancement of polymeric water-based drilling fluid properties using nanoparticles. *J. Pet. Sci. Eng*, 170, 813–828. <https://doi.org/10.1016/j.petrol.2018.06.081>.

Perween, S., Beg, M., Shankar, R., Sharma, S., Ranjan, A. (2018). Effect of zinc titanate nanoparticles on rheological and filtration properties of water-based drilling fluids. *J. Pet. Sci. Eng*, 170, 844–857. <https://doi.org/10.1016/j.petrol.2018.07.006>.

Perween, S., Thakur, N.K., Beg, M., Sharma, S., Ranjan, A. (2019). Enhancing the properties of water-based drilling fluid using bismuth ferrite nanoparticles. *Colloids Surfaces A Physicochem. Eng. Asp*, 561, 165–177. <https://doi.org/10.1016/j.colsurfa.2018.10.060>.

Perween, S., Beg, M., Shankar, R., Sharma, S., Ranjan, A. (2018). Effect of zinc titanate nanoparticles on rheological and filtration properties of water-based drilling fluids. *J. Pet. Sci. Eng*, 170, 844–857. <https://doi.org/10.1016/J.PETROL.2018.07.006>.

Perween, S., Thakur, N.K., Beg, M., Sharma, S., Ranjan, A. (2019). Enhancing the properties of water-based drilling fluid using bismuth ferrite nanoparticles. *Colloids Surfaces A Physicochem. Eng. Asp*, 561, 165–177. <https://doi.org/10.1016/j.colsurfa.2018.10.060>.

Rafati, R., Smith, S.R., Sharifi Haddad, A., Novara, R., Hamidi, H. (2018). Effect of nanoparticles on the modifications of drilling fluids properties: A review of recent

- advances. *J. Pet. Sci. Eng.*, 161, 61–76. <https://doi.org/10.1016/j.petrol.2017.11.067>.
- Raj, G.S., Asiri, A.M., Wu, J.J., Anandan, S. (2015). Synthesis of Mn<sub>3</sub>O<sub>4</sub> nanoparticles via chemical precipitation approach for supercapacitor application. *J. Alloys Compd.*, 636, 234–240. <https://doi.org/10.1016/j.jallcom.2015.02.164>.
- Ramasamy, J., Amanullah, M. (2020). Nanocellulose for oil and gas field drilling and cementing applications. *J. Pet. Sci. Eng.*, 184. <https://doi.org/10.1016/j.petrol.2019.106292>.
- Ravichandran, K., Palaniraj, R., Saw, N.M.M.T., Gabr, A.M.M., Ahmed, A.R., Knorr, D., Smetanska, I. (2014). Effects of different encapsulation agents and drying process on stability of betalains extract. *J. Food Sci. Technol.*, 51, 2216–2221. <https://doi.org/10.1007/s13197-012-0728-6>.
- Riley, M., Young, S., Stamatakis, M.E., Guo, Q., Ji, L., De Stefano, G., Price, K., Friedheim, J. (2012). Wellbore Stability in Unconventional Shales - The Design of a Nano-Particle Fluid, in: *SPE Oil Gas India Conf. Exhib.*, Mumbai. <https://doi.org/10.2118/153729-ms>.
- Salehnezhad, L., Heydari, A., Fattahi, M. (2019). Experimental investigation and rheological behaviors of water-based drilling mud contained starch-ZnO nanofluids through response surface methodology. *J. Mol. Liq.*, 276, 417–430. <https://doi.org/10.1016/j.molliq.2018.11.142>.
- Salih, A.H., Elshehabi, T.A., Bilgesu, H.I. (2016). Impact of nanomaterials on the rheological and filtration properties of water-based drilling fluids, *SPE East. Reg. Meet. 2016-Janua*. <https://doi.org/10.2118/184067-MS>.
- Sami, N.A. (2016). Effect of magnesium salt contamination on the behavior of drilling fluids. *Egypt. J. Pet.*, 25, 453–458. <https://doi.org/10.1016/j.ejpe.2015.10.011>.
- Sharma, M.M., Zhang, R., Chenevert, M.E., Ji, L., Guo, Q., Friedheim, J. (2012). A New Family of Nanoparticle Based Drilling Fluids, in: *SPE Annu. Tech. Conf. Exhib. San Antonio*. <https://doi.org/10.2118/160045-ms>.
- Sheng, G., Dong, H., Shen, R., Li, Y. (2013). Microscopic insights into the temperature-dependent adsorption of Eu(III) onto titanate nanotubes studied by FTIR, XPS, XAFS and batch technique. *Chem. Eng. J.*, 217, 486–494. <https://doi.org/10.1016/j.cej.2012.10.076>.
- Sing, K.S.W. (2009). Reporting physisorption data for gas/solid systems with special reference to the determination of surface area and porosity (Recommendations 1984). *Pure Appl. Chem.*, 57, 603–619. <https://doi.org/10.1002/9783527619474.ch11>.
- Song, K., Wu, Q., Li, M.M., Wojtanowicz, A.K., Dong, L., Zhang, X., Ren, S., Lei, T. (2016). Performance of low solid bentonite drilling fluids modified by cellulose nanoparticles. *J. Nat. Gas Sci. Eng.*, 34, 1403–1411. <https://doi.org/10.1016/j.jngse.2016.08.036>.

Tseng, L.T., Lu, Y., Fan, H.M., Wang, Y., Luo, X., Liu, T., Munroe, P., Li, S., Yi, J. (2015). Magnetic properties in  $\alpha$ -MnO<sub>2</sub> doped with alkaline elements. *Sci. Rep*, 5, 9094. <https://doi.org/10.1038/srep09094>.

Wang, K., Jiang, G., Liu, F., Yang, L., Ni, X., Wang, J. (2018). Magnesium aluminum silicate nanoparticles as a high-performance rheological modifier in water-based drilling fluids. *Appl. Clay Sci*, 161, 427–435. <https://doi.org/10.1016/j.clay.2018.05.012>.

Wang, H.Q., Yang, G.F., Li, Q.Y., Zhong, X.X., Wang, F.P., Li, Z.S., Li, Y.H. (2011). Porous nano-MnO<sub>2</sub>: Large scale synthesis via a facile quick-redox procedure and application in a supercapacitor. *New J. Chem*, 35, 469–475. <https://doi.org/10.1039/c0nj00712a>.

William, J.K.M., Ponmani, S., Samuel, R., Nagarajan, R., Sangwai, J.S. (2014). Effect of CuO and ZnO nanofluids in xanthan gum on thermal, electrical and high pressure rheology of water-based drilling fluids. *J. Pet. Sci. Eng*, 117, 15–27. <https://doi.org/10.1016/j.petrol.2014.03.005>.

Wissing, S.A., Kayser, O., Müller, R.H. (2004). Solid lipid nanoparticles for parenteral drug delivery. *Adv. Drug Deliv. Rev*, 56, 1257–1272. <https://doi.org/10.1016/j.addr.2003.12.002>.



## **Chapter 5: Investigation on enhancement of adsorptive property of pure chitosan beads by immobilization of biofabricated CuO nanoparticles for wastewater treatment**

---

### **5.1 Introduction**

The continuous increase in the industrial activities has greatly pushed the quantities of liquid waste to a threatening level. These wastes need removal from water bodies to protect the ecosystem. The major source of water pollution is considered to be the organic pollutants such as dyes, nitro phenols, etc. Dyes released into the water bodies from the industries are mostly synthetic dyes, which are classified into different groups such as acid, basic, reactive, direct and azoic dyes [Yagub et al., 2014]. Among these synthetic dyes, the most important ones are reactive dyes which constitute approximately 12% of the total production all over the world [Zhou et al., 2010]. There are several known techniques such as oxidation, electrocoagulation, membrane separation and adsorption implemented by different researchers to remove these dyes from water bodies [Abbeglen et al., 2009; Kochany et al., 2008; Wang et al., 2009; Tan et al., 2007; Altindag et al., 2015]. One of the most convenient methods for removing these organic dyes is adsorption of these pollutants over different surfaces. Various materials such as metal/metal oxides, clay, fly ash etc. have been studied earlier as an adsorbent for removal of organic and inorganic pollutants discharged into the water bodies [Li et al., 2009; Adamczuk et al., 2015; Zhou et al., 2015; Reddy et al., 2013]. Lately, hydrogels such as starch, sodium alginate, chitosan, etc. have also been evaluated for their adsorptive properties [Bhatnagar et al., 2010; Gong et al., 2015; Eser et al., 2012]. On the basis of these studies, it was found that these hydrogels have the ability to be used as an alternative to previously reported adsorbents for removal of unwanted organic compounds.

In recent years, number of articles have been reported in which chitosan (CS) or chitosan based adsorbents have been used for removal of dyes from their aqueous solutions [**da Rosa Schio et al., 2019; Cestari et al., 2008; Zhang et al., 2014; Salzano de Luna et al., 2017a, b; Salzano de Luna et al., 2019; Dotto et al., 2013; Dotto et al., 2015; Sellaoui et al., 2016; Banerjee et al., 2017**]. Chitosan (CS) is basically a natural biopolymer, which is cationic in nature and is derived from chitin through the process of N-deacetylation [**Khawar et al., 2019; Tahira et al., 2019**]. CS possesses the ability to act as an adsorbent, which makes it suitable to use as an agent for removal of harmful dyes discharged into water bodies. Nanotechnology is currently applied in every possible fields such as catalysis, wastewater treatment, engineering applications, etc. Nanomaterials are gaining importance owing to their porous structures and multidimensional phases in the nano range of 1-100 nm [**Tian et al., 2013**]. These nanosized materials possess novel properties, which can be employed to enhance the properties of existing ones.

CuO is a p-type semiconductor possessing notable characteristics that makes it suitable to be used effectively as a photocatalyst and as an adsorbent. It is reported that CuO nanoparticles (NPs) loaded on nanoporous activated carbon acts as an effective adsorbent for removal of methylene blue dye [**Prajapati et al., 2020**].

Different methods like thermal oxidation [**Manmeet et al., 2011**], quick precipitation [**Rujun et al., 2010; Zhu et al., 2004**], sonochemical [**Narongdet et al., 2011**] and combustion [**Yamukyan, 2008**] have been reported for synthesis of CuO NPs with desired morphological qualities. Other than these methods, biosynthesis of NPs is also an effective alternative method involving usage of plant extracts, micro-organisms as raw materials [**Hebbalalu et al., 2013**]. Laboratory synthesis of NPs has been widely reported in the recent times [**Saratale et al., 2018**]. Plant extract acts as a reservoir of alkaloids

and flavonoids which assists the synthesis of NPs [Nadagouda and Varma, 2008; Nadagouda et al., 2014]

In the present work, laboratory synthesized CuO NPs were immobilized on to the surface of pure chitosan beads. The NPs were fabricated using plant extract of *Ficus retusa* as reducing as well as capping agent. These CS/CuO nano-beads were used to remove anionic dyes such as eriochrome Black-T (EBT) and congo red (CR) from their aqueous solutions by batch adsorption system. The adsorptive property of CS beads was compared with that of CS/CuO nano-beads and laboratory synthesized CuO NPs.

## 5.2 Materials and method

### 5.2.1 Chemicals used

The chemicals used in experiments include copper sulphate pentahydrate, sodium hydroxide and congo red dye (molecular weight = 696.65 g mol<sup>-1</sup>) procured from Molychem India Private Ltd. Eriochrome Black T dye (molecular weight = 461.38 g mol<sup>-1</sup>). Glacial acetic acid were from Fisher Scientific. High molecular weight chitosan was obtained from Tokyo Chemical Industry Co. Ltd., Japan.

### 5.2.2 Plant material and extraction

*Ficus retusa* (*F. retusa*) leaves were collected from Rajiv Gandhi Institute of Petroleum Technology campus, Uttar Pradesh. Leaves of the plant were picked up and washed thoroughly, firstly with tap water and then twice using double distilled water. The leaves were air dried in dark at room temperature. Dried leaves were then grounded to fine powder. 10 g of powder was boiled well with 200 mL of distilled water for 2 h at a temperature of 80°C. At the end of 2 h, a dark brown solution was obtained. The solution was then filtered using Whatmann filter paper no. 1. The filtrate was stored in an air tight vessel. It was further used for synthesis of NPs.

### 5.2.3 Green synthesis of CuO nanoparticles

CuO NPs were biofabricated by following the procedure mentioned below:

80 mL of copper (II) nitrate trihydrate solution (0.1 M) was stirred for 15 min. to obtain a clear homogeneous solution. 20 mL of leaves extract of *F. retusa* was then mixed in homogeneous solution of copper metal precursor with vigorous stirring at 80°C temperature for 4 h. A greenish blue coloured paste was obtained, which was then cooled to attain room temperature. The obtained paste like product was scratched from the surface of beaker and transferred into silica crucible, calcinated in muffle furnace at 800°C temperature for 2 h, subsequently black colour nanopowder was achieved.

### 5.2.4 Preparation of CS/CuO nano-beads

CS/CuO nano-beads were prepared by immobilizing the laboratory synthesized CuO NPs into the matrix of CS beads. CuO NPs solution was prepared by dissolving 100 mg of NPs in 25 mL of distilled water. This solution was added to another solution prepared by dissolving 0.5 g of CS in 25 mL of 2% acetic acid solution. Stirring of mixture was done until a homogenous solution was obtained devoid of air bubbles. Spherical beads of this solution were dropped through a syringe needle into a chilled solution of aqueous NaOH (4% w/v). These beads were allowed to rest for an hour in NaOH solution and were then filtered. The spherical beads were washed twice with double deionized water. The scheme of synthesis is represented in **figure 5.1**

CS beads were synthesized using same procedure as mentioned above without incorporating NPs into the solution.

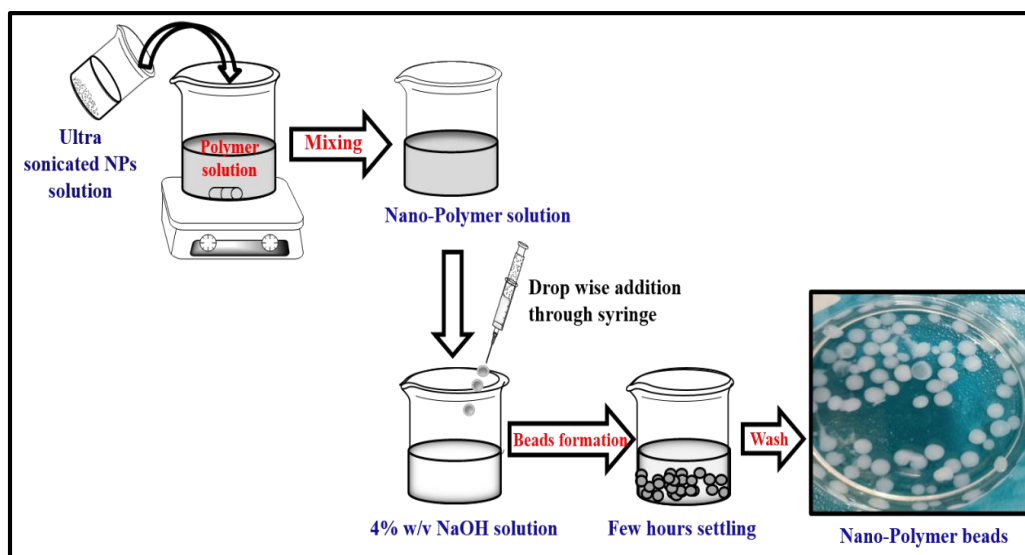


**Figure 5.1: Preparation of CS/CuO nano-beads.**

### 5.2.5 Material characterization

The CuO NPs were characterized by recording x-ray diffraction (XRD) patterns using PANalytical X'pertpro MPD diffractometer equipped with CuK $\alpha$  radiation (1.5418 Å). The surface morphology of the samples was obtained through field emission scanning electron microscopy (FESEM, model no. JEOL JSM 7100F). The FESEM instrument was furnished with energy dispersive x-ray (EDX) analysis which determines the purity of samples. Thermogravimetric analysis (TGA) was carried out using TGA, Linseis PT 1000 to evaluate the effect of immobilizing CuO NPs into the matrix of CS beads. Fourier transform infrared (FTIR) spectroscopy of CuO NPs, pure CS beads and CS/CuO nano-beads was recorded on Spectrum 2-FTIR Spectroscopy, Perkin Elmer in the range of 4000-400  $\text{cm}^{-1}$ . Brunauer–Emmett–Teller (BET) analysis of the hydrogel beads (Both CS and CS/CuO nano-beads) was carried out to determine the surface area, pore size and pore volume using Autosorb iQ Station 1 instrument.

### 5.3 Adsorption experiments

Batch technique was used to carry out the adsorption experiments. 1.0 g of CS/CuO nano-beads were put separately in beakers containing 10 mL of 50  $\text{mg L}^{-1}$  of congo red and

eriochrome black–T dye solutions. The experiments were conducted in dark under constant stirring at pH 7 and room temperature. After certain time intervals, the dye solutions were decanted and the concentration of dye solutions were evaluated using UV-Vis spectrophotometer (Lab India UV-Vis 3200).

The contact time was kept to be 2 h for CR and 4 h for EBT dye. The impact of contact time was also observed for the process of adsorption. Isotherm studies were performed keeping the weight of adsorbent to be constant and varying the initial concentrations of dye solutions i.e., in the range of 10-50 mg L<sup>-1</sup>. Other than isotherm, kinetics of the adsorption process was also studied in detail.

The adsorption capacity of adsorbent for both the dyes at any point of time t was calculated using following equation (eq. 5.1):

$$q_t = \frac{(C_0 - C_t) * V}{m} \dots\dots\dots (5.1)$$

Where, q<sub>t</sub> is the amount (mg g<sup>-1</sup>) of EBT/CR dye adsorbed over adsorbent at time t, C<sub>0</sub>, initial concentration of EBT/CR dye in solution (in mg L<sup>-1</sup>), C<sub>t</sub>, concentration of dye in solution at time t (in mg L<sup>-1</sup>), V, volume (L) of the solution and m, mass (g) of adsorbent used.

The percentage of removal of dye is calculated using **equation 5.2** mentioned below.

$$\text{Dye removal (\%)} = \frac{C_0 - C_e}{C_0} \dots\dots\dots (5.2)$$

C<sub>e</sub> represents concentration of dye at equilibrium.

The change in concentration of dyes was obtained using UV-Vis spectroscopy. The adsorptive property of CS/CuO nano-beads was compared with that of pure CS beads (without immobilizing NPs).

### **5.3.1 Effect of pH**

The prepared CS/CuO nano-beads were evaluated to determine the effect of initial pH of dye solutions on the percentage removal of CR and EBT dyes from their aqueous solutions. The experiments were performed by adding 1.0 g of beads in 10 mL of CR and EBT (50 mg L<sup>-1</sup>) dye solutions. The pH of solutions was varied from 2-12 and adjusted by adding dilute aqueous solutions of HCl or NaOH (0.1 M). The pH of the solutions was measured using Eutech instruments pH tutor.

### **5.3.2 Effect of dyes' initial concentration**

The effect of dyes' initial concentration was studied by varying the initial concentration of dye solutions in the range of 10-50 mg L<sup>-1</sup> (pH 7). The concentration of adsorbent was kept constant. The solution was stirred in a beaker at 25°C temperature.

### **5.3.3 Effect of dosage concentration**

To study the effect of concentration of adsorbent, 10 mL of aqueous dye solutions (CR and EBT dyes) with initial dye concentration of 50 mg L<sup>-1</sup> (pH 7) and an adsorbent dosage equal to 50, 100, 250, 500, and 1000 mg were placed in a beaker and stirred at 25°C temperature.

### **5.3.4 Effect of contact time**

The effect of contact time was also observed for adsorption of these dyes (CR and EBT) over the surface of CS beads and CS/CuO nano-beads. The concentration of CR and EBT dyes used for this study was 10 mg L<sup>-1</sup>. The adsorption of CR dye was analysed from 0 to 2 h while the adsorption of EBT dye was observed from 0 to 4 h.

## **5.4 Results and discussion**

### **5.4.1 Characterization of CuO nanoparticles and CS/CuO nano-beads**

The x-ray diffraction pattern of the laboratory synthesized CuO NPs is represented in **figure 5.2a**. All the peaks shown in the XRD pattern are well in agreement with JCPDS data (48-1548) of the monoclinic phase of CuO. Other than the peaks responsible for

monoclinic phase of CuO, no other peaks of impurities such as Cu(OH)<sub>2</sub> (used as precursor), Cu<sub>2</sub>O, were observed, which indicate the synthesis of pure phase CuO. The average crystallite size of CuO NPs is also calculated by putting the values obtained from XRD data in Debye Scherrer formula represented by **equation 5.3** [Amal et al., 2018].

$$D = \frac{K\lambda}{B\cos\theta} \dots\dots\dots (5.3)$$

Where, D represents the size of CuO NPs (nm), λ, x-ray wavelength, B, full width at half maxima (FWHM) of the diffraction peak and θ, measured Bragg angle.

The average crystallite size of nanoparticles obtained using **equation 5.3** is 14.59 nm.

TGA measurements were done to estimate the thermal behaviour of laboratory synthesized CuO NPs (shown in **figure 5.2b**). As seen from **figure 5.2b**, CuO NPs did not show any weight loss except for the loss of water molecules present on their surface.

There are two main stages which were seen in thermal decomposition profile of CS beads and CS/CuO nano-beads. The thermal decomposition started at around 210 °C temperature and then occurred at a temperature of 300 °C. Out of the two stages, maximum loss of mass was observed at 300 °C temperature. At higher temperature, the loss of CS beads' mass was higher as compared to CS/CuO nano-beads, which shows that the incorporation of CuO NPs into the matrix of CS beads enhanced the thermal stability of CS beads and made them even more resistant to degradation [Celabi et al., 2015].

FTIR spectra of CuO NPs, CS beads and CS/CuO nano-beads are shown in **figure 5.3**. FTIR spectrum of CuO fabricated using plant extract shows a broad band at 3425 cm<sup>-1</sup>, which is a characteristic band of CuO NPs and may be attributed to N-H stretching for Cu compound. The band observed at 2970 cm<sup>-1</sup> is due to the symmetric stretching of C-H bond. The carbonyl group present in the plant extract also exhibits its band at 1739 cm<sup>-1</sup>. Bands at 1437 and 1367 cm<sup>-1</sup> represent the asymmetric C-H bending and O-H bending respectively. The O-H bonding is due to the aqueous phase synthesis of NPs. Bands at

1213, 1087 and 904  $\text{cm}^{-1}$  are attributed to C-H bending (aromatic in plane), C-C vibrations and C-H bending (out of plane) respectively. The FTIR spectra of pure CS beads shows bands at 3297, 1064 and 1027  $\text{cm}^{-1}$  which are because of the stretching vibration mode of OH groups, 3'-OH, and 5'-OH groups respectively [Moradi Dehaghi et al., 2014]. The peak at 2970  $\text{cm}^{-1}$  corresponds to C-H stretching. The peaks obtained at 1645 and 1580  $\text{cm}^{-1}$  represent stretching vibration of C=O and scissoring vibration of  $\text{NH}_2$  group respectively [Pearson et al., 1960; Brugnerotto et al., 2001]. In case of CS/CuO nano-beads, a stronger peak obtained at 3453  $\text{cm}^{-1}$  represents the strong attachment of CuO NPs with the amide group of CS molecules. The presence of peaks at 1064 and 1027  $\text{cm}^{-1}$  represent stretching vibration mode of 3'-OH, and 5'-OH groups respectively as in case of pure CS beads. Other than the peak at 3453  $\text{cm}^{-1}$ , peaks at 1738, 1443, 1369 and 1216  $\text{cm}^{-1}$  are also observed, which were also seen in case of CuO NPs showing the presence of CuO NPs within the beads.

FESEM images of CuO NPs, CS and CS/CuO nano-beads are shown in **figure 5.4 a, b** and **c** respectively. The CuO NPs were found to be spherical in shape and were well separated from each other. The average size of NPs is in the range of 10-15 nm, which validates the average value of crystal size obtained from XRD data. The comparison of images in **figure 5.4 b** and **c** provides an evidence of the immobilization of CuO NPs into the matrix of CS beads. The surface of CS beads was found to be rough and wrinkled (**figure 5.4b**). The dots present on the surface of CS beads depict the CuO NPs (**figure 5.4c**).

EDX spectra of CuO NPs (**figure 5.4d**) demonstrate the presence of Cu and O approximately in the ratio of 1:1, which indicates the presence of Cu in the form of oxide. Presence of other elements were detected in negligible amount due to the interaction of

Cu salt with the extract during bioprocessing. EDX spectra of CS and CS/CuO nano-beads (**figure 5.4 e and f**) shows the immobilization of Cu into the matrix of CS beads.

The BET analysis of CS beads and CS/CuO nano-beads was carried out to compare the two materials for its adsorptive properties. **Table 5.1** lists the BET surface area, pore volume and pore size of CS and CS/CuO nano-beads used as an adsorbent. The surface area and pore volumes of CS beads and CS/CuO nano-beads increased from 15.844 m<sup>2</sup>/g and 0.024 cm<sup>3</sup>/g to 25.303 m<sup>2</sup>/g and 0.33 cm<sup>3</sup>/g respectively. The incorporation of CuO nanoparticles into the matrix of hydrogel beads lead to increase in the surface area of these beads, which enhances the adsorptive properties of these beads.

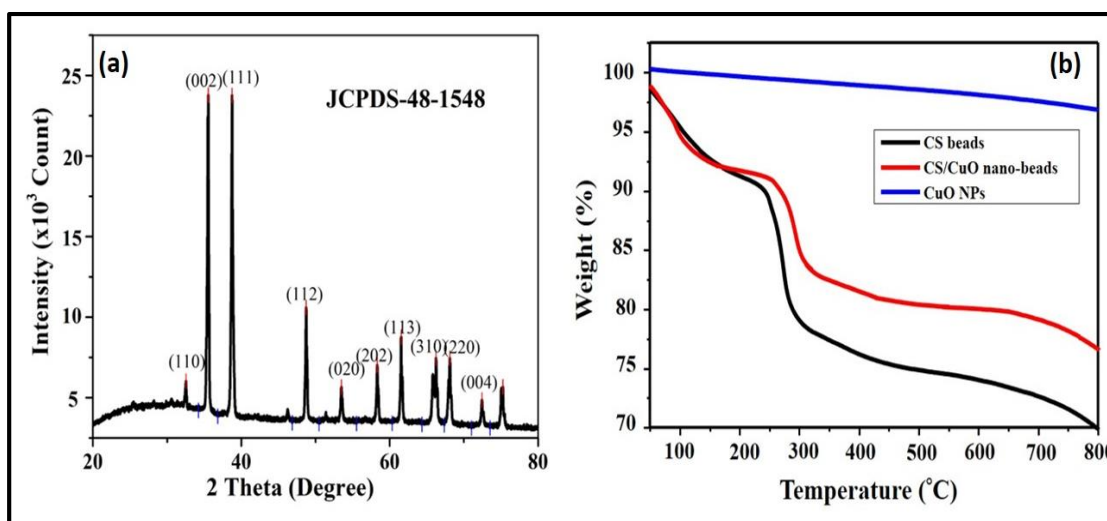


**Figure 5.2:** (a) XRD of CuO nanoparticles and (b) TGA of of CuO nanoparticles, pure chitosan beads and CS/CuO nano-beads.

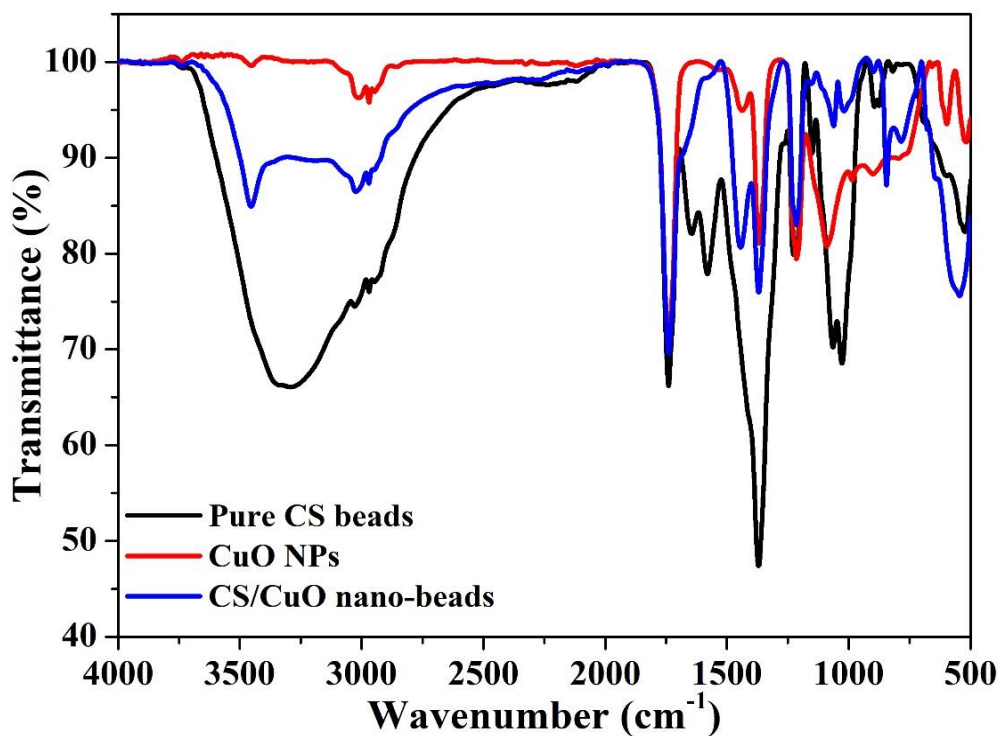


Figure 5.3: FTIR spectra of pure chitosan beads, CuO nanoparticles and CS/CuO nano-beads.

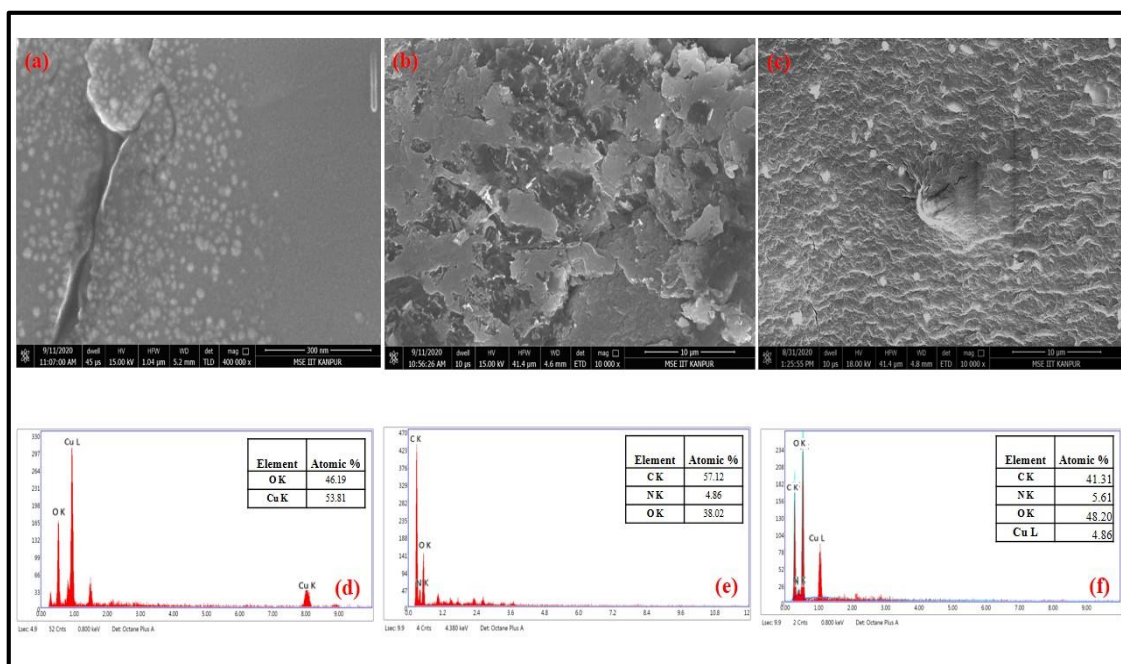


Figure 5.4: FESEM images of (a) CuO nanoparticles, (b) chitosan beads and (c) CS/CuO nano-beads. EDX of (d) CuO nanoparticles, (e) chitosan beads and (f) CS/CuO nano-beads.

**Table 5.1: BET analysis of pure chitosan beads and CS/CuO nano-beads**

| <b>Material</b>          | <b>Pore volume<br/>(cm<sup>3</sup> g<sup>-1</sup>)</b> | <b>Pore size<br/>(nm)</b> | <b>Surface are<br/>(m<sup>2</sup>/g)</b> |
|--------------------------|--|---------------------------|--|
| <b>CS beads</b>          | 0.024  | 2.3100                    | 15.84                                    |
| <b>CS/CuO nano-beads</b> | 0.033  | 1.2267                    | 25.30                                    |

#### **5.4.2 Mechanism of adsorption of dyes**

The prominent aim of the present work is the removal of toxic, carcinogenic dyes from aqueous solution. The interactions, which are possible to exist between the beads (CS and CS/CuO nano-beads) and CR and/or EBT dye molecules are demonstrated in **figure 5.5**. The adsorption of dye molecule over the adsorbent may be influenced by several factors such as adsorbents' surface property, structure as well as charge of dye molecule, electrostatic interactions, hydrophobic/hydrophilic nature of adsorbate and adsorbent, vander waals' forces and hydrogen bonding [Liu et al., 2015; Sorlier et al., 2001]. The dye molecules adsorb over the surface of adsorbent due to the physical forces as well as electrostatic interactions. Firstly, the negatively charged dye molecules interact with the positively charged surface of adsorbent through electrostatic attraction. Other than electrostatic interaction, there is a strong hydrogen bonding between  $\equiv\text{N}$  group of dyes and OH group of the chitosan molecule [Monash et al., 2009; Chari et al., 2019; Nguyen-Le et al. 2015]. The structure of both the dyes assist the attachment of their molecules onto the beads' surface. In addition to the the strong hydrogen bond, other physical forces such as van der Waals force are also responsible for the adsorption of dyes.

On comparing the adsorptive property of CS beads with that of CS/CuO nano-beads a drastic improvement in the adsorption rate and percentage of removal of dyes was observed. The enhancement in adsorptive property suggests that the composition of CuO increases the dye removal capacity of CS beads. The difference in the adsorptive capacity of pure CS beads and CS/CuO nano beads is due to the lower mass density of CS, which

makes it difficult for the adsorbate to settle. The CuO NPs in the composite act as a supporting medium and allow the dyes to settle on adsorbent. The incorporation of CuO NPs into the matrix of CS beads add to the strength of electrostatic interaction as well as hydrogen bond responsible for binding the dye molecules to the adsorbents' surface. The electronegative O atom of CuO provides an additional possibility of hydrogen bonding between the hydroxyl group of CuO and amine group of dyes.

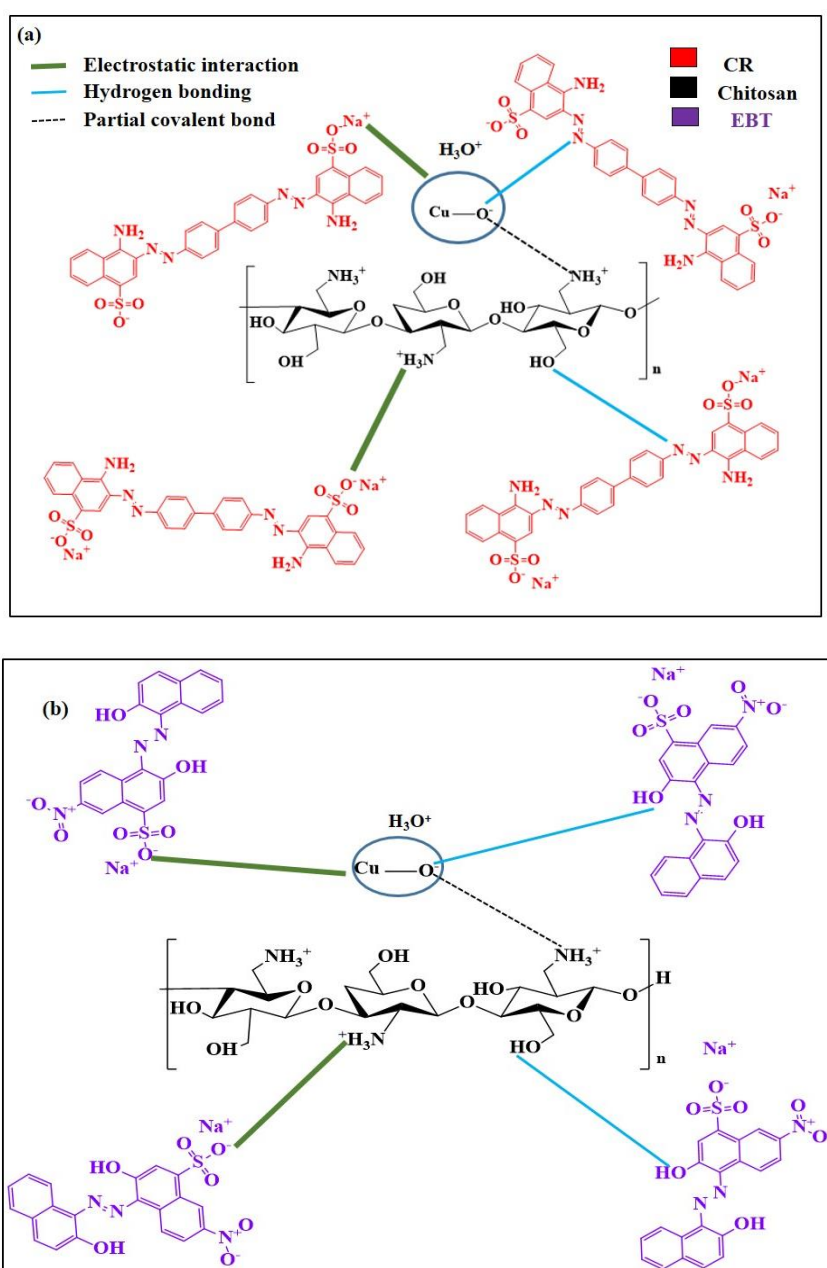


**Figure 5.5: Mechanism of adsorption of (a) congo red and (b) eriochrome black T dyes over CS/CuO nano-beads.**

### 5.4.3 Effect of pH

The adsorptive removal of dye from its aqueous solution is influenced significantly by the initial pH of the solution. The effect of pH on removal of dyes is shown in **figure 5.6**. The CS beads synthesized in this work are formed through precipitation in NaOH, therefore, these CS beads eventually get dissolved in acidic media [**Pillai et al., 2009**]. It was observed that at lower pH, the beads began to deform and became soft and translucent after sometime and finally started dissolving in the acidic dye solution. This deformation and dissolution of beads did not allow the adsorption of dyes over their surface in acidic medium. As the pH of solution decreases, the dissolution of beads in the acidic media get faster and the instability of beads increases. Therefore, no adsorption of dyes occurs in the acidic media. The zero point charge ( $\text{pH}_{\text{pzc}}$ ) of chitosan and CuO NPs is 6.3 and 6.21 respectively, therefore, with increase in pH the surface of beads becomes less positive, which hinder their interaction with negatively charged dye molecules. On increasing the pH above 7, the surface of adsorbent acquires both positive and negative charges which lead to comparable degree of adsorption. On further increasing the pH above 10, the surface of adsorbent becomes negatively charged that lead to electrostatic repulsion of anionic dye molecules. Therefore, the optimum pH for adsorption of dyes is 7. The adsorption of dyes was observed even at pH 12, which is attributed to the strong hydrogen bonding present between the functional groups of dye molecules and adsorbents' surface.

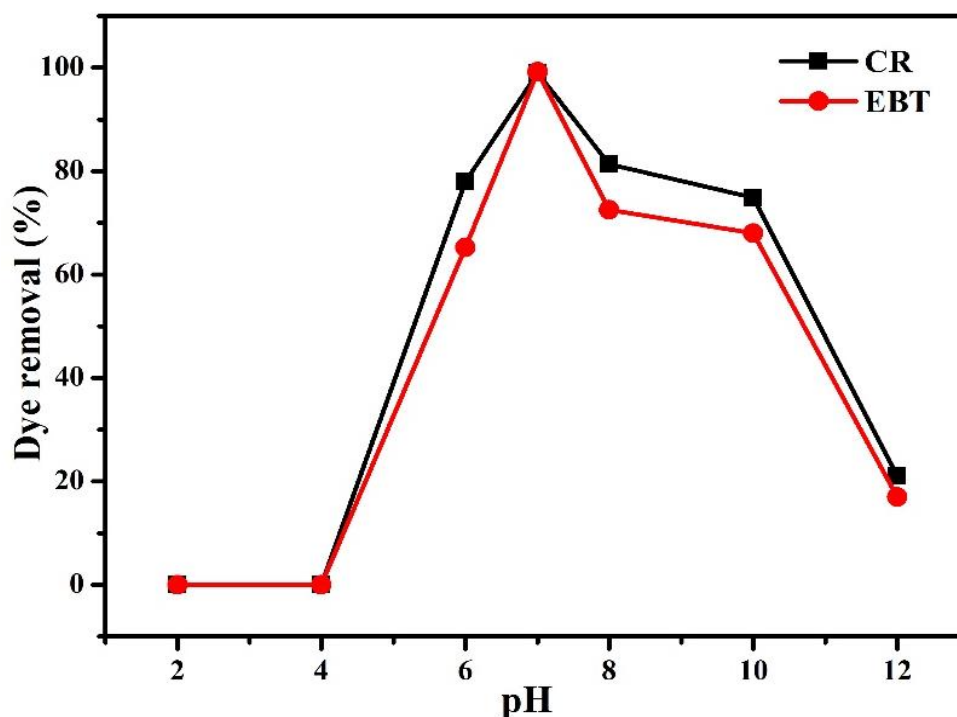


**Figure 5.6: Effect of initial pH of solution on removal of dyes.**

#### **5.4.4 Effect of dosage concentration**

The effect of varying the concentration of CS and CS/CuO nano-beads (in the range of 0.05–1.0 g) on the removal of the CR and EBT dyes is shown in **figure 5.7**. The percentage of removal of dyes increased on increasing the quantity of adsorbents. On increasing the dosage of CS/CuO nano-beads from 0.05 to 1.0 g, the percentage of removal of dyes increased from 49 to 98% for CR dye while for EBT dye, increase in percentage of removal of dye was from 24 to 97.7% in 2 h of time span. A similar trend was obtained when CS beads were used as adsorbent for removal of these dyes. But, it was seen that even after 24 h of contact time, the percentage of removal of dyes using CS beads was unsubstantial as compared to percentage of removal obtained using CS/CuO nano-bead (**table 5.2**). An increase in percentage of removal of dyes may be attributed to the increase in surface area of adsorbent and therefore, more number of vacant sites were available for adsorption of dye molecules on the surface of adsorbent [**Sheshmani, Ashori et al., 2014**]. Although, the percentage of removal of dyes is directly proportional to the amount of adsorbent but the adsorption capacity decreased by increasing

adsorbent's concentration (**figure 5.7**). The reason for reduced adsorption capacity may be either the presence of adsorption sites, which are unsaturated during the process or the aggregation of particles due to higher mass of adsorbent. The aggregation of these particles leads to reduction in total surface area of the adsorbent and eventually increases the diffusional path length [**Hamzeh et al., 2012**].

On comparing the dye adsorbed over CS beads with CS/CuO nano-beads, it was found that the adsorption capacity of CS/CuO nano-beads is much higher as compared to CS beads. Therefore, it can be concluded that, on using CS/CuO nano-beads, higher percentage of dyes were removed in a shorter span of time as shown in **figure 5.9**.

**Table 5.2: Comparison of percentage of dye removal over varying concentration of adsorbents**

| Sl. No. | Conc. of dye<br>(mg L <sup>-1</sup> ) | Conc. of<br>adsorbent<br>(g) | Removal of dye<br>(%) |              |                       |              |
|---------|---------------------------------------|------------------------------|-----------------------|--------------|-----------------------|--------------|
|         |                                       |                              | CS beads              |              | CS/CuO nano-<br>beads |              |
|         |                                       |                              | CR dye                | EBT dye      | CR dye                | EBT dye      |
| 1       | 50                                    | 0.05                         | 8.04                  | <b>3.07</b>  | 49.36                 | <b>24.91</b> |
| 2       | 50                                    | 0.10                         | 14.30                 | <b>5.48</b>  | 66.5                  | <b>47.03</b> |
| 3       | 50                                    | 0.25                         | 27.88                 | <b>12.90</b> | 82.84                 | <b>79.01</b> |
| 4       | 50                                    | 0.50                         | 52.15                 | <b>20.69</b> | 97.00                 | <b>96.53</b> |
| 5       | 50                                    | 1.0                          | 72.17                 | <b>36.66</b> | 98.00                 | <b>97.70</b> |

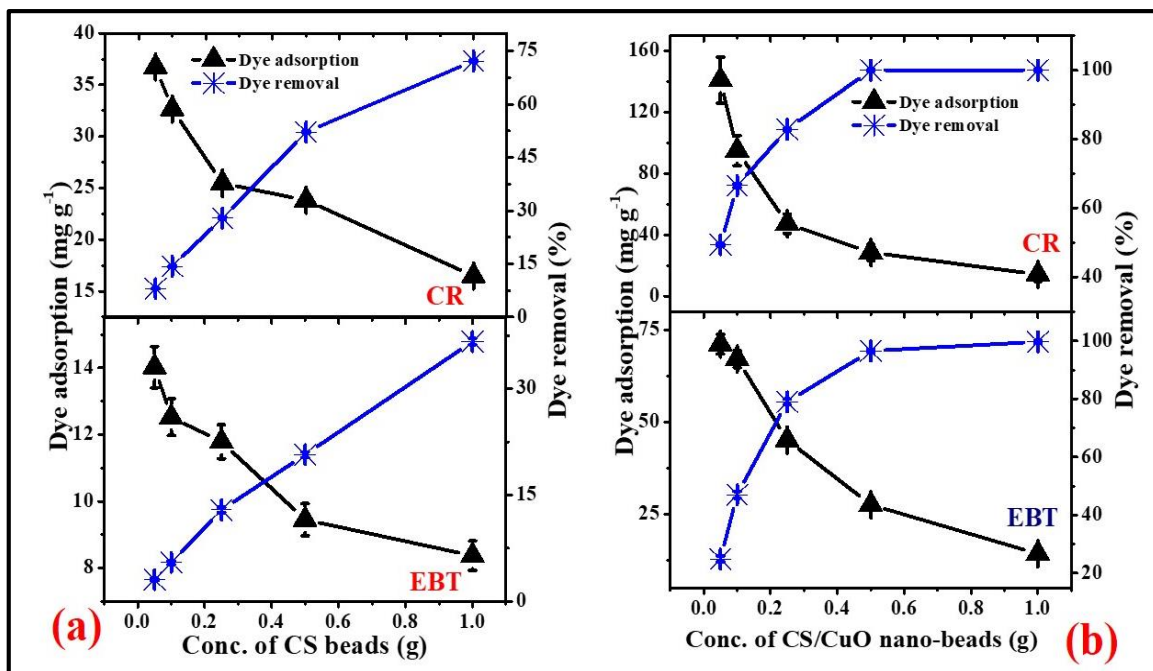


**Figure 5.7:** Effect of adsorbent dosage on the removal of congo red and eriochrome black T dyes using (a) chitosan beads and (b) CS/CuO nano-beads (for 50 mg L<sup>-1</sup> dyes concentration).

#### 5.4.5 Effect of initial dye concentration

The initial concentration of dye is inversely proportional to the percentage of its removal while directly proportional to the adsorption capacity. The adsorption of dyes over any of the adsorbents (CS beads or CS/CuO nano-beads) exhibit the abovementioned trend. When the concentration of dye is low, the adsorption sites are unoccupied. On the other hand, when the concentration of dye is higher, all the adsorption sites over adsorbent gets saturated and therefore, number of adsorption sites are reduced [Boukoussa et al., 2018; Abid et al., 2019; Medjdoubi, et al., 2019]. On comparing the amount of dyes adsorbed over adsorbents, it was found that the adsorption capacity of CS beads is unsubstantial as compared to CS/CuO nano-beads (figure 5.8).

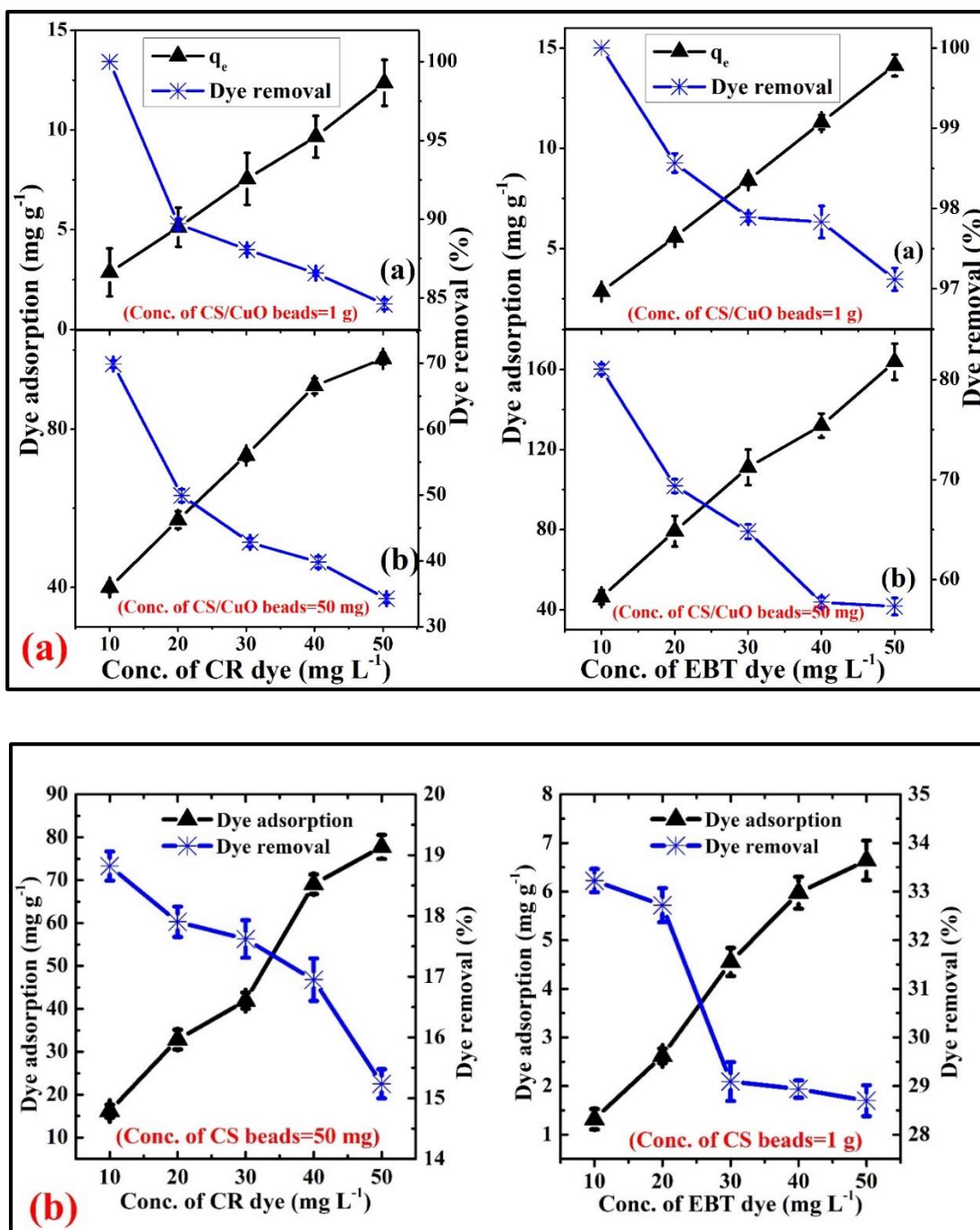


Figure 5.8: Effect of initial concentration of dyes (congo red and eriochrome black T) on its removal using (a) CS/CuO nano-beads and (b) chitosan beads.

**Table 5.3: Comparison of percentage of dye removal on varying the initial concentration of dyes**

| Sl. No. | Conc. of dyes (mg L <sup>-1</sup> ) | Conc. of adsorbent (g) |             | Removal of dye (%) |              |                   |              |
|---------|-------------------------------------|------------------------|-------------|--------------------|--------------|-------------------|--------------|
|         |                                     |                        |             | CS beads           |              | CS-CuO nano-beads |              |
|         |                                     |                        |             | CR dye             | EBT dye      | CR dye            | EBT dye      |
| 1       | 10                                  | 0.05                   | <b>1.00</b> | 17.62              | <b>33.22</b> | 69.86             | <b>98.01</b> |
| 2       | 20                                  | 0.05                   | <b>1.00</b> | 14.06              | <b>32.72</b> | 49.88             | <b>98.88</b> |
| 3       | 30                                  | 0.05                   | <b>1.00</b> | 12.66              | <b>29.09</b> | 42.78             | <b>98.83</b> |
| 4       | 40                                  | 0.05                   | <b>1.00</b> | 10.94              | <b>28.93</b> | 39.78             | <b>98.11</b> |
| 5       | 50                                  | 0.05                   | <b>1.00</b> | 9.11               | <b>28.69</b> | 34.23             | <b>97.56</b> |

#### 5.4.6 Effect of contact time

Although both the adsorbents (CS beads and CS/CuO nano-beads) were effective to remove the dyes from their aqueous solutions but the efficiency of CS/CuO nano-beads was far better than CS beads. The percentage of removal of CR using CS and CS/CuO nano-beads maintaining a contact time of 2 h was found to be 72 and 98% respectively. In case of EBT dye, on maintaining a contact time of 4 h, the percentage of dye removal was found to be 36 and 97.70 % respectively over CS and CS/CuO nano-beads adsorbent. Hence, it can be concluded that a drastic reduction in the time taken for removal of dyes (CR and EBT) was observed on immobilizing the pure CS beads with laboratory synthesized CuO NPs. The process of adsorption completed in much shorter span of time.

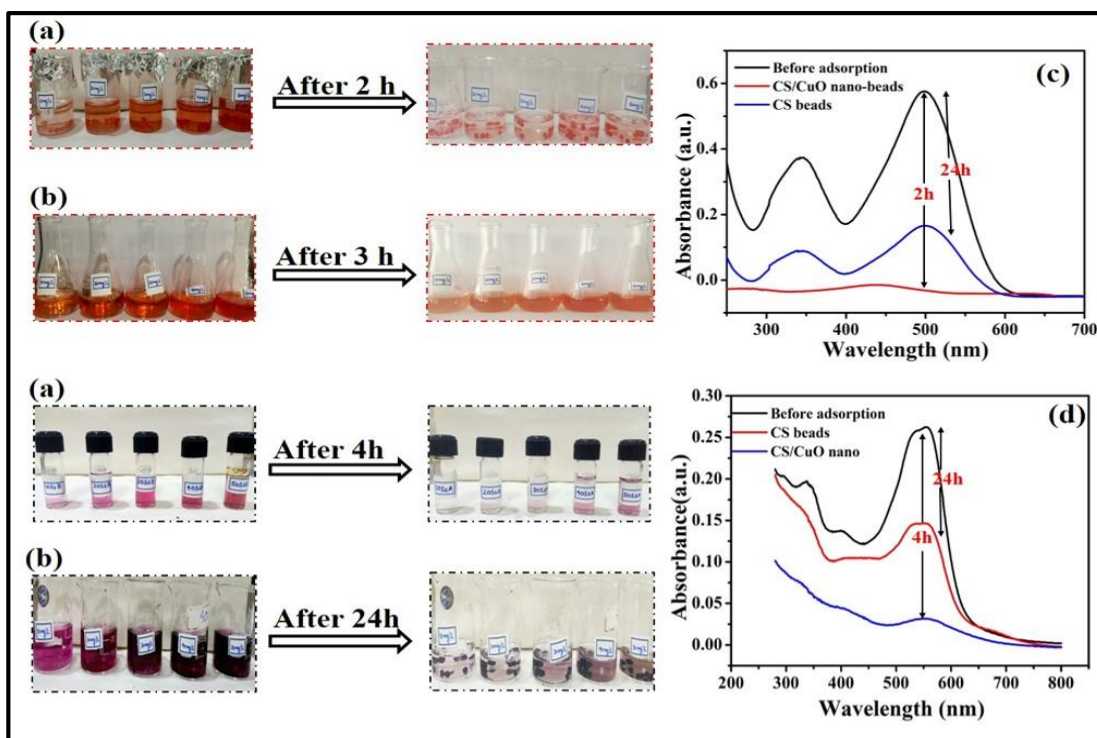


**Figure 5.9:** Images showing adsorption of congo red and eriochrome black T dye solutions of varying concentrations over (a) CS/CuO nano-beads and (b) chitosan beads respectively. UV-Vis spectra of removal of (c) congo red and (d) eriochrome black T dye ( $10 \text{ mg L}^{-1}$ ) using  $1.0 \text{ g}$  of adsorbents.

#### 5.4.7 Adsorption isotherm

The mechanism of the adsorption can be understood by studying its adsorption isotherm. The study of adsorption isotherm gives an insight into the distribution of adsorbate molecules between the liquid and solid phase. The adsorption isotherm experiments were carried out by varying the initial concentration of dyes (CR and EBT) from  $10\text{-}50 \text{ mgL}^{-1}$  at pH 7. The concentration of adsorbent was kept to be  $50 \text{ mg}/10 \text{ mL}$ . The experimental data of removal of dyes on CS/CuO nano-beads were simulated using Langmuir, Freundlich and Temkin adsorption models. The adsorption equilibrium was analyzed by making an attempt to fit the data in both linear and non-linear form of three isotherm models mentioned below.

The non-linear and linear form of Langmuir equation is expressed by the following equations (eq. 5.4 and 5.5):

$$q_e = \frac{q_{max} \cdot b \cdot C_e}{1 + b \cdot C_e} \quad \text{(Non-linear form)} \quad \dots\dots\dots (5.4)$$

$$\frac{C_e}{q_e} = \frac{1}{q_{max} \cdot b} + \frac{C_e}{q_{max}} \quad \text{(Linear form)} \quad \dots\dots\dots (5.5)$$

Where,  $C_e$  is the equilibrium concentration of dyes in solution ( $\text{mg L}^{-1}$ ),  $q_e$ , adsorption capacity at equilibrium ( $\text{mg g}^{-1}$ ),  $q_{max}$ , maximum adsorption capacity of dye on the adsorbent and  $k$ , Langmuir adsorption constant ( $\text{L mg}^{-1}$ ) defining the free energy of adsorption. Langmuir isotherm represents the monolayer adsorption of dye on the surface of adsorbent.

The heterogeneous nature of the surface of adsorbent is denoted by Freundlich isotherm model. Following equations represents the non linearized and linearized form of Freundlich equation (**eq. 5.6 and 5.7**):

$$q_e = K_f \cdot C_e^{1/n} \quad \text{(Non-linear form)} \quad \dots\dots\dots (5.6)$$

$$\ln q_e = \ln K_f + \frac{1}{n} \ln C_e \quad \text{(Linear form)} \quad \dots\dots\dots (5.7)$$

In the above equation,  $q_e$  is the amount of adsorbate adsorbed at equilibrium ( $\text{mg g}^{-1}$ ) and  $C_e$ , concentration of adsorbate in solution at equilibrium ( $\text{mg L}^{-1}$ ).  $K_f$  and  $1/n$  are characteristic constants where  $K_f \{(\text{mg g}^{-1})(\text{L mg}^{-1})^{1/n}\}$  depicts the adsorption capacity while  $1/n$  represents the adsorption intensity of the system.

The interaction between adsorbent and adsorbate is taken into consideration in Temkin isotherm model. The Temkin relationship can be given as (**eq. 5.8 and 5.9**)

$$q_e = B \ln K_T \cdot C_e \quad \text{(Non-linear form)} \quad \dots\dots\dots (5.8)$$

$$q_e = B \ln K_T + B \ln C_e \quad \text{(Linear form)} \quad \dots\dots\dots (5.9)$$

Where,  $q_e$  is the amount of adsorbate adsorbed at equilibrium ( $\text{mg g}^{-1}$ ) and  $C_e$ , concentration of adsorbate in solution at equilibrium ( $\text{mg L}^{-1}$ ).  $B$  is a constant associated with the heat of adsorption and is expressed as

$$B = RT/b \quad \dots\dots\dots (5.10)$$

b is the Temkin constant (J mol<sup>-1</sup>), T, absolute temperature (K), R, gas constant (8.314 J mol<sup>-1</sup>K<sup>-1</sup>) and K<sub>T</sub>, Temkin isotherm constant (L g<sup>-1</sup>).

It was found that Freundlich model is more appropriate for simulation of CR and EBT dyes adsorption as compared to Langmuir and Temkin model. The plots for all three models using linear as well as non-linear regression analysis are given in **figure 5.10** and **5.11** respectively. The value of different parameters derived using linear regression analysis are listed in **table 5.4** where the maximum adsorption capacities of CR and EBT dyes are reported as 121.95 and 217 mg L<sup>-1</sup> respectively. The values of correlation coefficient of the Freundlich model for CR and EBT dyes are 0.9739 and 0.9902 respectively, which are consistent with the simulations in **figure 5.10**. Value of n for CR and EBT dyes are 2.58 and 1.96 respectively, which indicates the favourable adsorption of dyes [Al-Ghouti et al., 2005]. Temkin constants are shown in **table 5.4**.

Non-linear regression analysis of the models was also being carried out. The graph is plotted between C<sub>e</sub> and q<sub>e</sub> as represented in **figure 5.11**. The data was studied by calculating root mean square error (RMSE) and correlation coefficient (R<sup>2</sup>) to compare three isotherm models. On comparing these values, it was found that the best fit model for removal of dyes (both CR and EBT) is Freundlich model (highest R<sup>2</sup> and lowest RMSE) (**table 5.5**). These results confirm the efficient removal of CR and EBT dyes from aqueous solution.

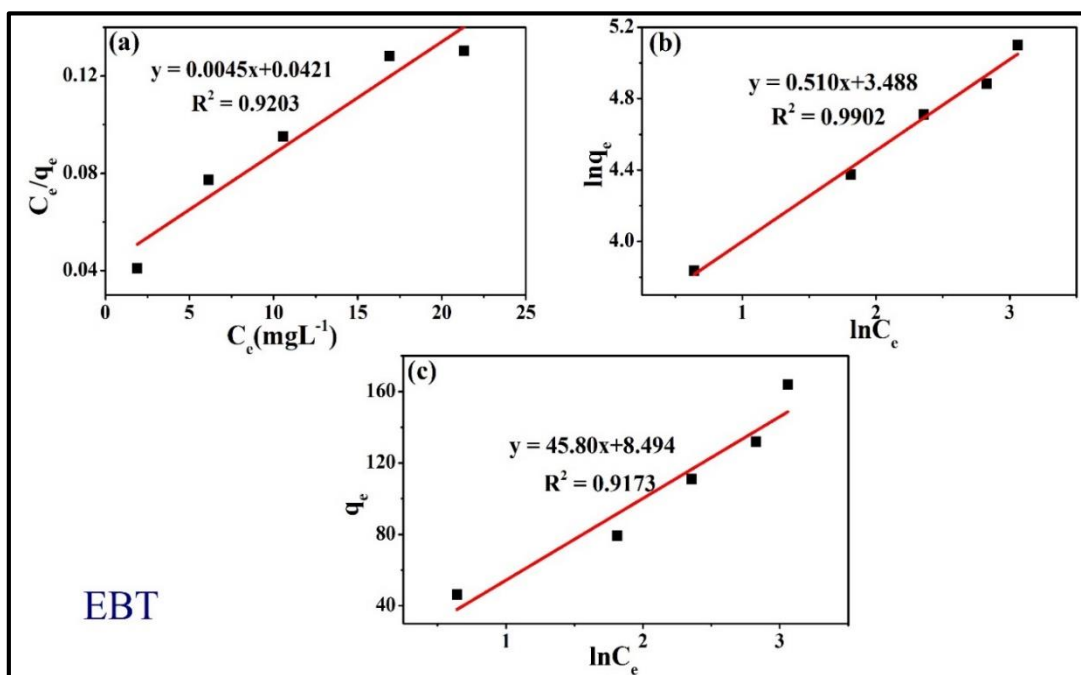
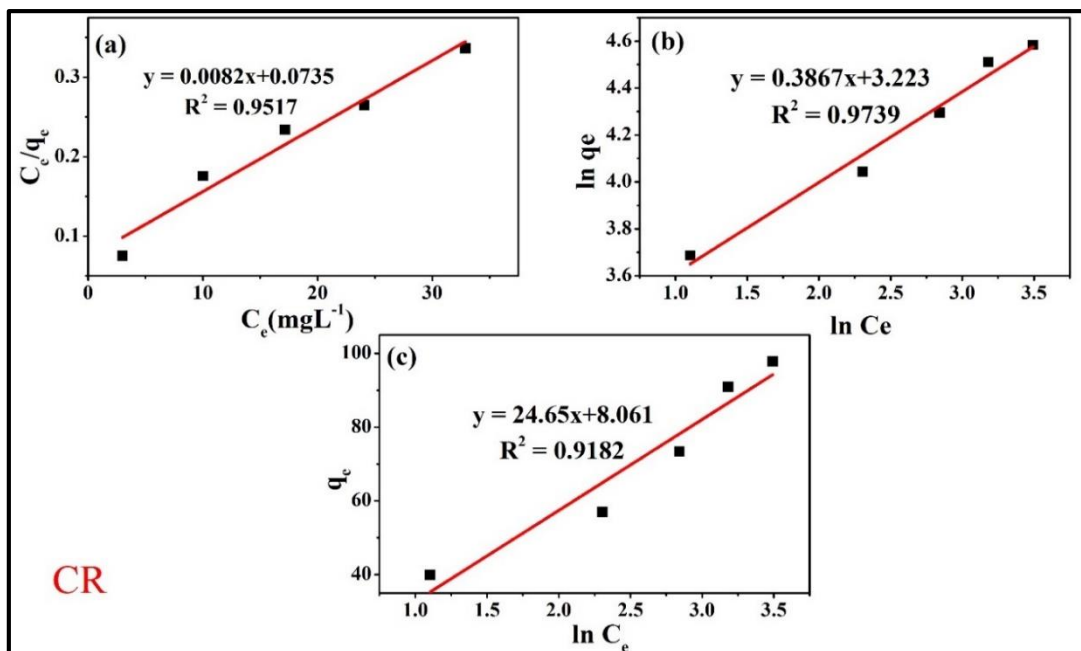


Figure 5.10: (a) Langmuir, (b) Freundlich and (c) Temkin isotherm for adsorption of congo red and eriochrome black T dye over CS/CuO nano-beads.

**Table 5.4: Linear regression analysis of adsorption isothermal models for congo red and eriochrome black T dye adsorption over CS/CuO nano-beads**

| Isotherm model | Parameters   | Values |         |
|----------------|--|--------|---------|
|                |  | CR dye | EBT dye |
| Langmuir       | $q_{\max}$ (mg g <sup>-1</sup> )                     | 121.95 | 217     |
|                | $R^2$  | 0.951  | 0.920   |
| Freundlich     | n  | 2.58   | 1.96    |
|                | $K_f \{(\text{mg g}^{-1})(\text{L mg}^{-1})^{1/n}\}$ | 25.10  | 32.72   |
|                | $R^2$  | 0.973  | 0.990   |
| Temkin         | B  | 24.60  | 45.80   |
|                | $K_T$ (L g <sup>-1</sup> )                           | 1.38   | 1.20    |
|                | $R^2$  | 0.918  | 0.917   |

**Table 5.5: Interpretation of adsorption isotherm models using non-linear regression analysis for congo red and eriochrome black T dye adsorption over CS/CuO nano-beads**

| Isotherm model | Parameters   | Values |         |
|----------------|--|--------|---------|
|                |  | CR dye | EBT dye |
| Langmuir       | $q_{\max}$ (mg g <sup>-1</sup> )                     | 119.70 | 235.70  |
|                | $R^2$  | 0.889  | 0.943   |
|                | RMSE   | 13.74  | 18.83   |
| Freundlich     | n  | 2.43   | 1.876   |
|                | $K_f \{(\text{mg g}^{-1})(\text{L mg}^{-1})^{1/n}\}$ | 23.56  | 30.97   |
|                | $R^2$  | 0.974  | 0.9825  |
|                | RMSE   | 6.62   | 10.44   |
| Temkin         | B  | 100.40 | 54.03   |
|                | $K_T$ (L g <sup>-1</sup> )                           | 1.38   | 1.20    |
|                | $R^2$  | 0.918  | 0.917   |
|                | RMSE   | 11.82  | 22.70   |

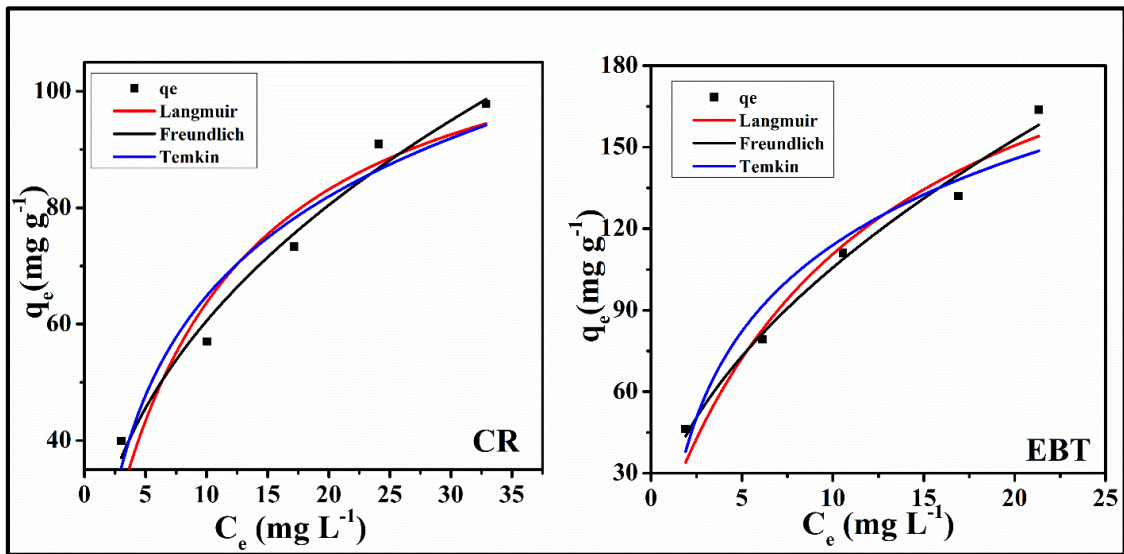


**Figure 5.11: Representation of Langmuir, Freundlich and Temkin isotherm models for CS/CuO nano-beads in non-linear regression analysis.**

**5.4.8 Adsorption kinetics**

The adsorption of dyes over the surface of CS/CuO nano-beads was analyzed for their kinetics. The kinetics of adsorption has been determined by fitting the experimental data into two different kinetic models such as pseudo first order [Lin and Wang, 2009] and pseudo second order [Ho and McKay, 1998]. Kinetic models were analyzed using both linear and non-linear regression analysis. These models give the values of different kinetic parameters and correlation coefficient which help in determining the kinetics of reaction.

Pseudo first order model can be represented in the form of equations mentioned below (eq. 5.11 and 5.12) [Lin and Wang, 2009].

$$\frac{dq}{dt} = k_1(q_e - q_t) \quad (\text{Non-linear}) \quad \dots\dots\dots (5.11)$$

$$(q_e - q_t) = \log q_e - \left(\frac{k_1}{2.3033}\right) t \quad (\text{Linear}) \quad \dots\dots\dots (5.12)$$

Where,  $q_e$  ( $\text{mg g}^{-1}$ ) represents the adsorption capacity of adsorbent at equilibrium,  $q_t$ , amount of dyes adsorbed ( $\text{mg g}^{-1}$ ) in time  $t$  (min.) and  $k_1$ , rate constant of the pseudo

first order kinetic model (min.<sup>-1</sup>).

Pseudo second order kinetics is represented by following equations (eq. 5.13 and 5.14)[Ho and Ofomaja, 2006]:

$$\frac{dq}{dt} = k_1(q_e - q_t)^2 \quad (\text{Non-linear}) \quad \dots\dots\dots (5.13)$$

$$\frac{t}{q_t} = \frac{1}{k_2 q_e^2} + \frac{t}{q_e} \quad (\text{Linear}) \quad \dots\dots\dots (5.14)$$

Where,  $q_e$  (mg g<sup>-1</sup>) represents the adsorption capacity of adsorbent at equilibrium,  $q_t$ , amount of dyes adsorbed (mg g<sup>-1</sup>) in time  $t$  (min.) and  $k_2$ , rate constant (g mg<sup>-1</sup> min.<sup>-1</sup>) of the pseudo second-order kinetic model for adsorption.

Values of various parameters obtained by using abovementioned equations are mentioned in **table 5.6** and **5.7**. The linear regression analysis shows that the process followed pseudo first order kinetics as the value of correlation coefficient was higher for pseudo first order kinetic model (**figure 5.12**). The theoretical and calculated value of adsorption capacity were also found to be coordinated in case of pseudo first order kinetic model, which confirms that process of adsorption follows pseudo first order kinetics (**table 5.6**).

In case of interpretation of data through non-linear regression analysis (**figure 5.13**), higher values of correlation coefficient and lower value of RMSE was obtained for EBT dye while for CR dye both these values were almost equal (**table 5.7**). But, the theoretical and calculated value of  $q_e$  for both the dyes were well in agreement in case of pseudo first order kinetic model. Hence, it can be concluded that the process of adsorption followed pseudo first order kinetics.

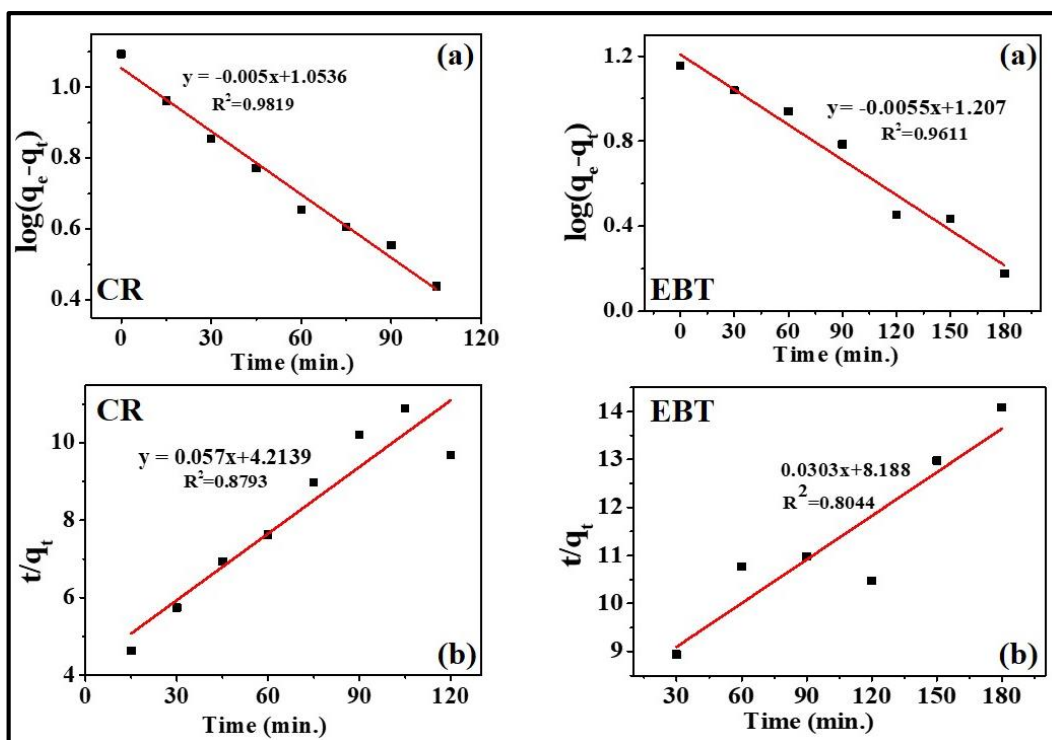


Figure 5.12: (a) Pseudo first order kinetics and (b) Pseudo second order kinetics of adsorption of congo red and eriochrome black T dyes over CS/CuO nano-beads.

Table 5.6: Kinetic models parameter study of congo red and eriochrome black T dyes on CS/CuO nano-beads using linear regression analysis

| Kinetic models      | Parameter                       | Value of parameters   |                       |
|---------------------|---------------------------------|-----------------------|-----------------------|
|                     |                                 | CR dye                | EBT dye               |
| Pseudo first order  | $k_1$ (min. <sup>-1</sup> )     | 0.013                 | 0.012                 |
|                     | $q_e$ (cal/theo)                | 11.29/12.39           | 16.10/16.36           |
|                     | $R^2$                           | 0.981                 | 0.961                 |
| Pseudo second order | $k_2$ (g mg <sup>-1</sup> min.) | $7.72 \times 10^{-4}$ | $9.08 \times 10^{-5}$ |
|                     | $q_e$ (cal/theo)                | 17.54/12.39           | 33.33/16.36           |
|                     | $R^2$                           | 0.879                 | 0.804                 |

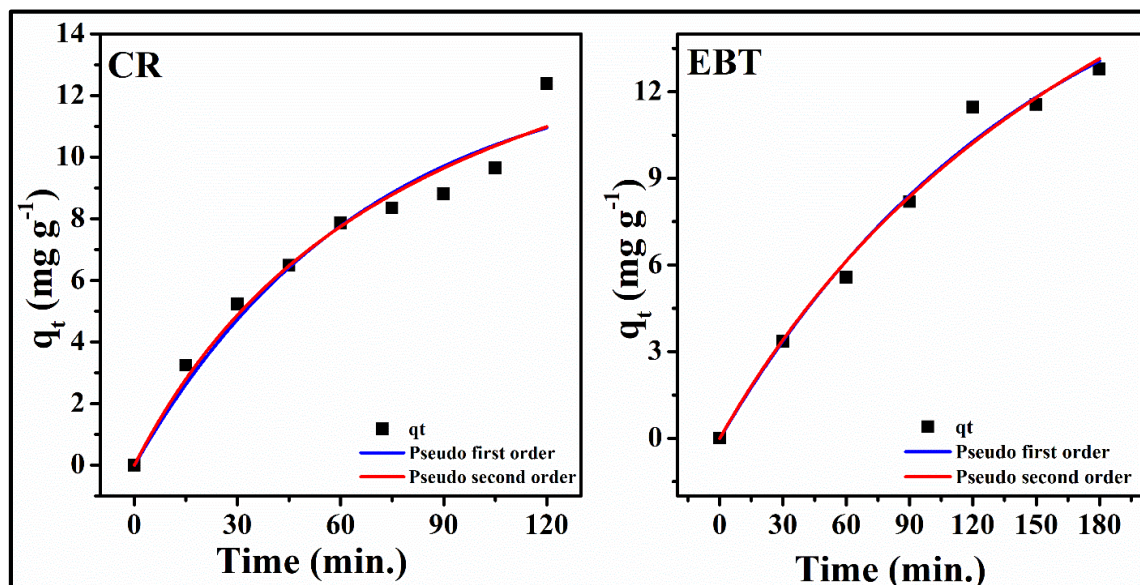


Figure 5.13: Representation of kinetic models for adsorption of congo red and eriochrome black T dyes over CS/CuO nano-beads through non-linear regression analysis.

Table 5.7: Kinetic models parameter study of congo red and eriochrome black T dyes adsorption on CS/CuO nano-beads using non-linear regression analysis

| Kinetic models      | Parameter                       | Value of parameters   |                       |
|---------------------|---------------------------------|-----------------------|-----------------------|
|                     |                                 | CR dye                | EBT dye               |
| Pseudo first order  | $k_1$ (min. <sup>-1</sup> )     | 0.014                 | 0.0066                |
|                     | $q_e$ (cal/theo)                | 13.17/12.39           | 18.80/16.36           |
|                     | $R^2$                           | 0.954                 | 0.983                 |
|                     | RMSE                            | 2.07                  | 2.18                  |
| Pseudo second order | $k_2$ (g mg <sup>-1</sup> min.) | $6.15 \times 10^{-4}$ | $1.36 \times 10^{-4}$ |
|                     | $q_e$ (cal/theo)                | 18.88/12.39           | 30.61/16.36           |
|                     | $R^2$                           | 0.960                 | 0.982                 |
|                     | RMSE                            | 1.92                  | 9.90                  |

## 5.5 Conclusions

CuO nanoparticles were successfully synthesized using the plant extract of *F. retusa* as reducing agent. These nanoparticles were incorporated into the matrix of pure CS beads. The laboratory synthesized nanoparticles, pure CS beads and CS/CuO nano-beads were characterized using BET, FESEM, EDX, FTIR TGA, and XRD techniques. The adsorptive property of pure chitosan beads for anionic dyes was compared with that of

CS beads immobilized with CuO nanoparticles (CS/CuO nano-beads). It was found that the adsorptive capacity of CS/CuO nano-beads was far better than that of pure chitosan beads. The resultant CS/CuO nano-beads demonstrate a huge enhancement in the adsorption capacity and removal efficiencies of two anionic dyes (congo red and eriochrome black T) as compared to pure chitosan beads. On using CS/CuO nano-beads as an adsorbent for removal of dyes (congo red and eriochrome black T) from their aqueous solutions, it was observed that approximately 97% dyes were removed in a very short span of time. On the other hand, on using pure chitosan beads as an adsorbent the percentage of removal of dyes within the same time span was unsubstantial.

The adsorption of dyes over the surface of modified chitosan beads follows the Freundlich isotherm model. The maximum adsorption capacity of CS/CuO nano-beads was estimated to be 121.95 and 217 mg g<sup>-1</sup> for congo red and eriochrome black T dyes respectively. The kinetics of adsorption process followed Lagergren pseudo-first-order kinetic model. The aforementioned results indicate that the CS/CuO nano-beads developed in this present work are anticipated to be a favourable adsorbent for highly efficient removal of organic dyes from aqueous solutions due to their high separation efficiency in a shorter span of time and low production cost.

## References

- Abegglen, C., Joss, A., Boehler, M., Buetzer, S., Siegrist, H. (2009). Reducing the natural color of membrane bioreactor permeate with activated carbon or ozone. *Water Sci. Technol*, 60, 155–165.
- Abid, Z., Hakiki, A. et al. (2019). Preparation of highly hydrophilic PVA/SBA-15 composite materials and their adsorption behaviour toward cationic dye: effect of PVA content. *J. Mat. Sci*, 54, 7679-7691.
- Adamczuk, A., Kołodynska, D. (2015). Equilibrium thermodynamic and kinetic studies on removal of chromium, copper, zinc and arsenic from aqueous solutions onto fly ash coated by CS. *Chem. Eng. J*, 274, 200–212.
- Al-Ghouti, M., Khraisheh, M.A.M., Ahmad, M.N.M., Allen, S. (2005). Thermodynamic behaviour and the effect of temperature on the removal of dyes from aqueous solution using modified diatomite: a kinetic study. *J. Colloid Interface Sci*, 287, 6-13.
- Altındag, I.G., Dincer, A., Becerik, S., Eser, A., Aydemir, T. (2015). Poly (methyl methacrylate-ethylene glycol dimethacrylate) copolymer for adsorptive removal of erythrosine dye from aqueous solution. *Des. Water*, 54, 1717–1726.
- Amal, M.I., Ghaida, H.M., Laila, M. (2018). A Copper (II) oxide nanocatalyst preparation and characterization: green chemistry route. *Bull. Natl. Res. Cent*, 42, 6.
- Banerjee, P., Barman, S.R., Mukhopadhyay, A., Das, P. (2017). Ultrasound assisted mixed azo dye adsorption by CS–graphene oxide nanocomposite. *Chem. Eng. Res. Des*, 117, 43–56.
- Bhatnagar, A., Sillanp, M. (2010). Utilization of agro-industrial and municipal waste materials as potential adsorbents for water treatment a review. *Chem. Eng. J*, 157, 277–296.
- Boukoussa, B., Hakiki, A. et al. (2018). Adsorption behaviours of cationic and anionic dyes from aqueous solution on nanocomposite polypyrrole/SBA-15. *J. Mat. Sci*, 53, 7372-7386.
- Brugnerotto, J., Lizardi, J., Goycoolea, F.M., Argüelles-Monal, W., Desbrières, J., Rinaudo, M. (2001). An infrared investigation in relation with chitin and chitosan characterization. *Polymer*, 42, 3569–3580.
- Chaari, I., E. Fakhfakh., Mounir, M., Fakher, J. (2019). Comparative study on adsorption of cationic and anionic dyes by smectite rich natural clays. *Journal of Molecular Structure*, 1179, 672-677.
- Celebi, H., Kurt, A. (2015). Effects of processing on the properties of chitosan/cellulose nanocrystal films. *Carbohydr. Polym*, 133, 284-293.
- Cestari, A.R., Vieira, E.F.S., Tavares, A.M.G., Bruns, R.E. (2008). The removal of the indigo carmine dye from aqueous solutions using cross-linked CS-Evaluation of adsorption thermodynamics using a full factorial design. *J. Hazard Mater*, 153, 1–2, 566–574.
- da Rosa Schio, R., da Rosa, B.C., Gonçalves, J.O., Pinto, L.A.A., Mallmann, E.S., Dotto, G. L. (2019). Synthesis of a bio-based polyurethane/CS composite foam using ricinoleic acid for the adsorption of Food Red 17 dye. *Int. J. Biol. Macromol*, 121, 373–380.

- Dotto, G.L., Moura, J.M., Cadaval, T.R.S., Pinto, L.A.A. (2013). Application of CS films for the removal of food dyes from aqueous solutions by adsorption. *Chem. Eng. J.*, 214, 8–16.
- Dotto, G.L., Pinto, L.A.A., Hachicha, M.A., Knani, S. (2015). New physicochemical interpretations for the adsorption of food dyes on CS films using statistical physics treatment. *Food Chem*, 171, 1–7.
- Eser, A., Tirtom, V.N., Aydemir, T., Becerik, S., Dinc, A. (2012). Removal of nickel (II) ions by histidine modified CS beads. *Chem. Eng. J.*, 210, 590–596.
- Hamzeh, Y., Ashori, A., Azadeh, E., Abdulkhani, A. (2012). Removal of Acid Orange 7 and Remazol Black 5 reactive dyes from aqueous solutions using a novel biosorbent. *Mater. Sci. Eng. C*, 32, 1394–1400.
- Gong, G., Zhang, F., Cheng, Z., Zhou, L. (2015). Facile fabrication of magnetic carboxymethyl starch/poly (vinyl alcohol) composite gel for methylene blue removal. *Int. J. Biol. Macromol*, 81, 205–211.
- Hebbalalu, D., Lalley, J., Nadagouda, M.N., Varma, R.S. (2013). Greener techniques for the synthesis of silver nanoparticles using plant extracts, enzymes, bacteria, biodegradable polymers, and microwaves. *ACS Sustain. Chem. Eng.*, 1, 703–712.
- Ho, Y.S., and McKay, G. (1998). Kinetic models for the sorption of dye from aqueous solution by wood. *Process Safety and Environmental Protection*, 76, 183-191.
- Ho, Y.S., and Ofomaja A. E. (2006). Pseudo-second-order model for lead ion sorption from aqueous solutions onto palm kernel fiber. *J. Haz. Mat*, 129, 137-142.
- Khawar, A., Aslam, Z., Zahir, A., Akbar, I., Abbas, A. (2019). Synthesis of Femur extracted hydroxyapatite reinforced nanocomposite and its application for Pb (II) ions abatement from aqueous phase. *Int. J. Biol. Macromol*, 122, 667–676.
- Kochany, E., Kochany, J. (2008). Effect of humic substances on the Fenton treatment of wastewater at acidic and neutral pH. *Chemosphere*, 73, 745–750.
- Li, Y., Gao, B., Wu, T., Wang, B., Li, X. (2009). Adsorption properties of aluminum magnesium mixed hydroxide for the model anionic dye Reactive Brilliant Red K-2BP. *J. Hazard. Mater*, 164, 1098–1104.
- Lin, J., and L. Wang. (2009). Comparison between linear and non-linear forms of pseudo-first-order and pseudo-second-order adsorption kinetic models for the removal of methylene blue by activated carbon. *Frontiers of Environmental Science and Engineering in China*, 3, 320-324.
- Liu, L., Gao, Z. Y., Su, X. P., Chen, X., Jiang L., Yao, J. M. (2015). Adsorption Removal of Dyes from Single and Binary Solutions Using a Cellulose-based Bioadsorbent. *ACS Sustainable Chem. Eng.* 2015, 3, 432-442.
- Manmeet, K., Muthea, K.P., Despande, S.K., Shipra, C., Singh, J.B., Neetika, V., Gupta, S.K., Yakhmi, J.V. (2011). Growth and branching of CuO nanowires by thermal oxidation of copper. *J Cryst Growth*, 289, 670-675.
- Medjdoubi, Z., Hachemaoui, M. et al. (2019). Adsorption behaviour of Janus Green B dye on Algerian diatomite. *Mat. Research Exp.*

- Monash, P., and G. Pugazhenth. (2009). Adsorption of crystal violet dye from aqueous solution using mesoporous materials synthesized at room temperature. *Adsorption*, 15, 390-405.
- Moradi Dehaghi, S., Rahmanifar, B., Moradi, A.M., and Azar, P.A. (2014). Removal of permethrin pesticide from water by chitosan–zinc oxide nanoparticles composite as an adsorbent. *Journal of Saudi Chemical Society*, 18, 4, 348–355. doi:10.1016/j.jscs.2014.01.004.
- Nadagouda, M.N., Varma, R.S. (2008). Green synthesis of silver and palladium nanoparticles at room temperature using coffee and tea extract. *Green Chem*, 10, 859–862.
- Nadagouda, M.N., Iyanna, N., Lalley, J., Han, C., Dionysiou, D.D., Varma, R.S. (2014). Synthesis of silver and gold nanoparticles using antioxidants from blackberry, blueberry, pomegranate and turmeric extracts. *ACS Sustain. Chem. Eng*, 2, 1717–1723.
- Narongdet, W., Piyanut, C., Naratip, V., Wisanu, P. (2011). Sonochemical Synthesis and Characterization of Copper Oxide Nanoparticles. *Energy Procedia*, 29, 404-409.
- Nguyen-Le, M.T., Lee, B.K. (2015). Enhanced adsorption capacity of polypyrrole/TiO<sub>2</sub> composite modified by carboxylic acid with hydroxyl group. *Chum Eng J*, 281, 20-33.
- Pearson, F.G., Marchessault, R.H., Liang, C.Y.J. (1960). Infrared spectra of polysaccharides. V. chitin. *Polym. Sci*, 43, 101–116.
- Pillai, C.K.S.; Paul, W.; Sharma, C.P. (2009). Chitosan and chitosan polymers: Chemistry, solubility and fiber formation. *Prog. Polym. Sci*, 34, 641–678.
- Prajapati A.K., Mondal M.K. (2020). Comprehensive kinetic and mass transfer modelling for methylene blue dye adsorption onto CuO nanoparticles loaded on nanoporous activated carbon prepared from waste coconut shell. *J. Mol. Liq*, 307, 112949.
- Reddy, D.H.K., Lee, S. (2013). Application of magnetic CS composites for the removal of toxic metal and dyes from aqueous solutions. *Adv. Colloid Interface Sci*, 201–202, 68–93.
- Rujun, W., Zhenye, M., Zhenggui, G., Yan, Y. (2010). Preparation and characterization of CuO nanoparticles with different morphology through a simple quick-precipitation method in DMAC water mixed solvent. *J Alloy Comp*, 504, 45-49.
- Salzano de Luna, M. et al. (2017a). Role of polymer network and gelation kinetics on the mechanical properties and adsorption capacity of CS hydrogels for dye removal. *J. Polym. Sci. Part B: Polym. Phys*, 55, 24, 1843–1849.
- Salzano de Luna, M. et al. (2017b). CS hydrogels embedding hyper-crosslinked polymer particles as reusable broad-spectrum adsorbents for dye removal. *Carbohydr. Polym*, 177, 347–354.
- Salzano de Luna, M. et al. (2019). Optimization of dye adsorption capacity and mechanical strength of CS aerogels through crosslinking strategy and graphene oxide addition. *Carbohydr. Polym*, 211, 195–203.

- Saratale, R.G. et al. (2018). A comprehensive review on green nanomaterials using biological systems: recent perception and their future applications. *Colloids Surf. B Biointerfaces*, 170, 20–35.
- Sellaoui, L., Dotto, G.L., Gonçalves, J.O., Pinto, L.A.A., Knani, S., Ben Lamine, A. (2016). Equilibrium modeling of single and binary adsorption of Food Yellow 4 and Food Blue 2 on modified CS using a statistical physics theory: new microscopic interpretations. *J. Mol. Liq*, 222, 151–158.
- Sheshmani, S., A. Ashori, Hasanzadeh, S. (2014). Removal of Acid Orange 7 from aqueous solution using magnetic graphene/chitosan: a promising nano-adsorbent. *Int. J. Bio. Macromolecules*, 68, 218-224
- Sorlier, P., Denuziere, A., Viton, C., Domard, A. (2001). Relation between the degree of acetylation and the electrostatic properties of chitin and chitosan. *Bio macromolecules*, 2, 765–772.
- Tahira, I., Aslam, Z., Abbas, A., Monim-ul-Mehboob, M., Ali, S., Asghar, A. (2019). Adsorptive removal of acidic dye onto grafted CS: a plausible grafting and adsorption mechanism. *Int. J. Biol. Macromol*, 136, 1209–1218.
- Tan, Y., Kilduff, J.E. (2007). Factors affecting selectivity during dissolved organic matter removal by anion-exchange resins. *Water Res*, 41, 4211–4221.
- Tian, J., Xu, J., Zhu, F., Lu, T., Su, C., Ouyang, G. (2013). Application of nanomaterials in sample preparation (Review). *J. Chromatogr. A*, 1300, 2–16.
- Wang, K., Guo, J., Yang, M., Junji, H., Deng, R. (2009). Decomposition of two haloacetic acids in water using UV radiation, ozone and advanced oxidation processes. *J. Hazard. Mater*, 162, 1243–1248.
- Yagub, M.T., Sen, T.K., Afroze, S., Ang, H.M. (2014). Dye and its removal from aqueous solution by adsorption: a review. *Adv. Colloid Interface Sci*, 209, 172–184.
- Yamukyan, M.H., Manukyan, K.V., Kharatyan, S.L. (2008). Copper oxide reduction by combined reducers under the combustion mode. *Chem*, 137, 636 642.
- Zhang, L., Cheng, Z., Guo, X., Jiang, X., Liu, R. (2014). Process optimization, kinetics and equilibrium of orange G and acid orange 7 adsorptions onto CS/surfactant. *J. Mol. Liq*, 197, 353–367.
- Zhou, L., Gao, C., Xu, W. (2010). Magnetic dendritic materials for highly efficient adsorption of dyes and drugs. *ACS Appl. Mater. Interfaces*, 2, 1483–1491.
- Zhou, Q., Gao, Q., Luo, W., Yan, C., Ji, Z., Duan, P. (2015). One-step synthesis of amino-functionalized attapulgite clay nanoparticles adsorbent by hydrothermal carbonization of CS for removal of methylene blue from wastewater. *Colloid Surf. A*, 470, 248–257.
- Zhu, J., Li, D., Chen, H., Yang, X., Lu, L., Wang, X. (2004). Highly dispersed CuO nanoparticles prepared by a novel quick-precipitation method. *Mater Letter*, 58, 3324-3327.



## Chapter 6: Green synthesis of biogenic silver particles, process parameter optimization and application as photocatalyst in dye degradation

---

### 6.1 Introduction

Recently, nanoparticles have gained momentum due to their various beneficial applications in various fields. The unique feature of the nanoparticles is that their properties such as optical, magnetic and electronic vary from their bulk material [Ibrahim et al., 2017]. The specific properties of nanomaterials have been attributed to the fact that these particles have characteristic size, shape, area and surface chemistry. Nanoparticles can be synthesized using a variety of methods such as laser ablation, photochemical reduction, sono chemical method, etc [Li et al., 2010; Boutinguiza et al., 2014; Kempa et al., 2006; Sen et al., 2003]. Though, there are several processes available for synthesis of these particles, the processes using chemicals are not eco-friendly and relatively expensive. An alternative way needs to be searched, which should be environment friendly and cheaper. The most efficient and cost effective method for synthesis of metal nanoparticles is synthesis using natural resources like plant or fruit or fruit peel extract as stabilizing and reducing agent [Goswami and Ghosh, 2013; Pirtarighat et al., 2018]. Recent literature revealed the enthusiasm of green route to synthesize nano-structures silver particles (AgNPs) using banana peel extract [Gopi et al., 2014], *Azadirachta indica* leaf [Roy, 2017], *Garcinia mangostana* leaf [Veerasingam, 2011], *Terminalia arjuna* leaf [Ahmed and Ikram, 2015], *Murraya koenigii* leaf [Sajesh et al., 2015], *Punica granatum* peel [Ahmad et al., 2012] and *Cinnamomum zeylanicum* leaf [Gauthami et al., 2015]. Therefore, this green process can be used for production of nanoparticles at large scale as well. Biogenic methods of synthesis of nanoparticles

have several advantages over physiochemical methods. Besides being environment friendly and non-toxic in nature, this method leads to production of nanoparticles having well defined morphology and size [Ibrahim et al., 2017]. In the proposed work, *Citrus sinensis* has been employed for the synthesis of nanoparticles. *Citrus sinensis* (Orange) belonging to a family rutaceae is mainly found in dry and arid regions of tropical and sub-tropical areas.

Metal nanoparticles have got vital role in various areas such as pharmaceutical, biotechnological and industrial. In particular, silver nanoparticles possesses antibacterial, antifungal and larvicidal properties as reported earlier [Yeo et al., 2003; Kennedy et al., 2017; Mocanu et al., 2019]. In fact, silver has the lowest toxicity to animal cells and is found to be most effective against bacterial action. Besides their antimicrobial property, silver nanoparticles also exhibit photocatalytic properties in the field of dye detoxification and its removal [Varadavenkatesan et al., 2019; Rafique et al., 2019, Bonnia et al., 2016]. Dyes used in different industries are directly discharged into the water bodies without any treatment. These dyes, which are non-biodegradable and potentially hazardous, can cause serious damage to ecology [Kant, 2012; Hossain et al., 2018]. Various other methods are also being practiced for treatment of wastewater such as UV-light degradation, redox treatment, carbon sorption and flocculation. However, these techniques are not that effective and, therefore, needs better approach [Awual, 2019a; Awual, 2019b; Awual et al., 2016; Awual et al., 2017].

The objective of present study is to yield relatively stable dispersion of AgNPs in a simple and cheap manner by reducing the silver salt solution using orange peel extract. Peel extract has been used as both reducing and stabilizing agent. Optimal condition to obtain stable dispersion of AgNPs is obtained by evaluating different parameters such as pH, temperature and concentration of reducing agent. The synthesized nanoparticles have

been evaluated for their antimicrobial property and finally these AgNPs were also used as photocatalyst for the removal of an azo dye i.e., congo red (CR) present in wastewater. Further, the kinetic study of degradation has also been reported.

## **6.2 Experimental**

### **6.2.1 Materials**

Silver nitrate ( $\text{AgNO}_3$ , Extra pure, 99%) and sodium borohydride of Molychem India Pvt Ltd. were being used for different purposes. *Citrus sinensis* peels were collected from the local market in Jais, India. A total of two bacterial strains namely *Pseudomonas aeruginosa* and *Pseudomonas syringae* and a fungal strain, *Alternaria brassicicola* were used in the study. The bacterial and fungal strains were obtained from CSIR-National Botanical Research Institute, Lucknow, India. For preparation of solutions, double distilled water was used.

### **6.2.2 Synthesis of Ag nanoparticles**

Extracted component of orange peel was used as stabilising and reducing agent for the synthesis of AgNPs. 10 g of orange peel was dried in sunlight for 4-5 days. The dried peel was grounded into fine powder in a grinder. It was taken in a round bottom flask where 200 mL methanol/water solution was added to it in the ratio of 4:1 (v/v). The resulting solution was placed on a heating mantle with stirrer and refluxed for 4-5 h. The solvent was removed from the solution using rotary evaporator (Heidolph Laborota 4001 Rotary Evaporator). The extract was dried and further converted into powdered form. The powdered form of the extract was used for further experimentation. A required amount of this powdered extract was mixed with known amount of double distilled water to achieve the desired concentration and final volume of 15 mL. The preparation of AgNPs was carried out by adding 25 mL of 600 ppm silver nitrate solution to 15 mL of prepared extract solution while stirring (~1000 rpm). Four solutions of AgNPs were

prepared and in each of the solutions, the concentration of silver nitrate was kept 600 ppm while the concentration of peel extracts were kept 0, 300, 1500, 3000 ppm respectively. In this method,  $K_{Ext/Ag}$  depicts the ratio of extracted component to silver ion concentration. **Table 6.1** presents the value of this ratio for all the samples. Once the formation of nanoparticles was completed, nanoparticles were washed by ultracentrifugation at 14000 rpm for 20 min. The liquid was removed and the powder obtained at the bottom of the centrifuge tubes was suspended in deionized water. The suspension was again centrifuged at 14000 rpm for 20 min. and the process was repeated thrice. Finally, the powder obtained was suspended in water and sonicated using Q Sonica Sonicator at room temperature. Variation in the pH of extract solution has an effect on synthesis reaction and to avoid this, pH of the peel extract was adjusted to 7 in all the cases before mixing.

**Table 6.1: Composition of sample solutions**

| Sample | $K_{Ext/Ag}$ | [Extract](ppm) | [Ag <sup>+</sup> ](ppm) | [NaBH <sub>4</sub> ](ppm) |
|--------|--------------|----------------|-------------------------|---------------------------|
| 1      | 0.0          | 0              | 600                     | 300                       |
| 2      | 0.5          | 300            | 600                     | 0.0                       |
| 3      | 2.5          | 1500           | 600                     | 0.0                       |
| 4      | 5.0          | 3000           | 600                     | 0.0                       |

### 2.3. Characterization of AgNPs

At initial stage, the synthesis of AgNPs was monitored using LAB India UV-Vis 3200 spectrophotometer in a wavelength range of 300-700 nm. A glass cuvette having optical path of 1 cm was used. The stability of colloidal AgNPs was studied by taking the UV-Vis absorption spectra of all samples after 30 min. of synthesis and were compared with spectra taken after 7 days and then after 20 days. The UV-Vis absorption spectra for different samples were taken at room temperature. PANalytical X'pert Pro MPD diffractometer was used to perform powder x-ray diffraction analysis (XRD) to obtain

the diffraction pattern from the sample. The AgNPs were further characterized by dynamic light scattering (DLS) study using a Nano Brook 90 plus PALS at 25°C temperature. The hydrodynamic diameter (Z-average), PDI (Poly dispersity index) and width distribution of particles were also determined through DLS study. Morphology and size of the nanoparticles was determined using field emission scanning electron microscopy (FESEM). FESEM images of the nanoparticles were taken by using ZEISS microscope (accelerating voltage ranged from 5 to 20 kV). FESEM samples were prepared by placing 2 µL of AgNPs on thin aluminium foil. The chemical composition was verified using elemental analysis on a ZEISS electron microscope equipped with an energy dispersive x-ray (EDX) analyser. To prevent samples from charging, a thin gold coating was sputtered onto the samples prior to the analysis. Coating the sample with a layer of metal resists charging, prevents thermal damage and improves the secondary electron signals, which is required for topographical examination of the sample.

### **6.3 Stability of Ag nanoparticles at different pH and temperature**

The colloidal stability of synthesized AgNPs was screened at different pH and temperature. The hydrodynamic diameter and PDI of the nanoparticles were measured over a pH range of 2-10 and temperature range of 25-75°C using NanoBrook 90 plus PALS. 0.1 M aqueous NaOH solution and 0.1 M HCl were used to adjust the desired pH environment.

### **6.4 Antimicrobial assay of Ag nanoparticles**

#### **6.4.1 Antibacterial activity assessment**

Antibacterial potential of biogenic AgNPs of different  $K_{Ext/Ag}$  were tested against *P. aeruginosa* and *P. syringae* (Gram negative bacteria) by disk diffusion method [Kumari et al., 2016]. To study the effect of AgNPs on pathogens, 100 µl of cultures, which were

allowed to grow overnight were spread on nutrient agar plates in a uniform manner. Pre-sterilized cotton of 1cm<sup>2</sup> was placed on the centre of the plates and 50 µL of desired nanoparticles were added to it and dried in air. The plates were incubated at 27°C temperature for 24 h. After 24 h, zone of inhibition was measured. Peel extract (3000 ppm) was used as control in the process.

#### **6.4.2 Antifungal activity evaluation**

Antifungal assay of the synthesized nanoparticles against *A. brassicicola* was conducted to evaluate the effect of AgNPs on the mycelial growth of the fungi. Three plates of autoclaved potato dextrose agar (PDA) were prepared in which nanoparticles synthesized using different  $K_{Ext/Ag}$  ratio were added to each of these plates. The other plate was kept as control containing only Milli-Q Water (without AgNPs). A disc of mycelia was withdrawn from the fungal culture and was placed at the centre of the plate containing silver nanoparticles assimilated in PDA Medium. The plates were then incubated at 25°C temperature for 7 days. The efficiency of the synthesized nanoparticles was evaluated by measuring the diameter of the fungal colony growth.

#### **6.5 Photocatalysis**

The photocatalytic activity of the AgNPs was studied by employing an aqueous solution of an azo dye i.e., congo red (20 mg L<sup>-1</sup>). Thereafter, the photocatalytic reaction was conducted outdoor under the sunlight as main energy source. The experiment was set up by suspending 5 mL of AgNPs solution in 50 mL of dye solution. The mixture was kept in dark under continuous stirring for 30 min. to bring the AgNPs to constant equilibrium in the mixture. The mixture was then kept under sunlight for 4-5 h. Degradation of congo red dye was analysed using UV-Vis spectroscopy by collecting the samples at regular time interval. The kinetics of the reaction has also been studied.

## 6.6 Results and discussion

### 6.6.1 Characterization of Ag nanoparticles

#### 6.6.1.1 Visual change

The preliminary analysis, which indicates the synthesis of nanoparticles, is the visible change in the colour on addition of peel extract to the silver nitrate solution. On adding different concentrations of peel extract to silver nitrate, a significant change in colour was observed. The colour of the solution turned from colourless to orange when the extract ratio was 0.5 and on increasing the extract ratio to 2.5, brown colour was observed, which turned to dark brown on further increasing the extract ratio to 5.0. The reason for the change in colour is excitation in the surface plasmon resonance (SPR). The SPR is a distinctive optical property, which is exhibited when all the electrons present in conduction band vibrate in resonance, which in turn, is responsible for the absorption ranging between 380 and 500 nm in UV-Vis spectra for the synthesized silver nanoparticles. Thus, the colour change confirmed the synthesis of silver nanoparticle, which was further confirmed using UV-Vis spectrometer.

#### 6.6.1.2 UV-Vis results

A UV-Vis absorption spectra of the prepared samples at different concentration of peel extract is presented in **figure 6.1** and **6.2**. **Figure 6.1** shows the UV-Vis spectra of nanoparticles at various extract concentrations immediately after their synthesis. The concentration of peel extract influenced the intensity of extinction peak. With increase in concentration of peel extract, the probability of aggregation of nanoparticles decreased and the rate of nucleation increased, which result in the synthesis of large number of nanoparticles [Barani et al., 2010; Barani et al., 2014]. The functional group of the stabilizer reacted with the nanoparticles and did not allow the collision of these nanoparticles, therefore, the aggregation of nanoparticles did not occur. The appearance

of peak in the range of 400-420 nm confirms the synthesis of AgNPs [Barani et al., 2011].

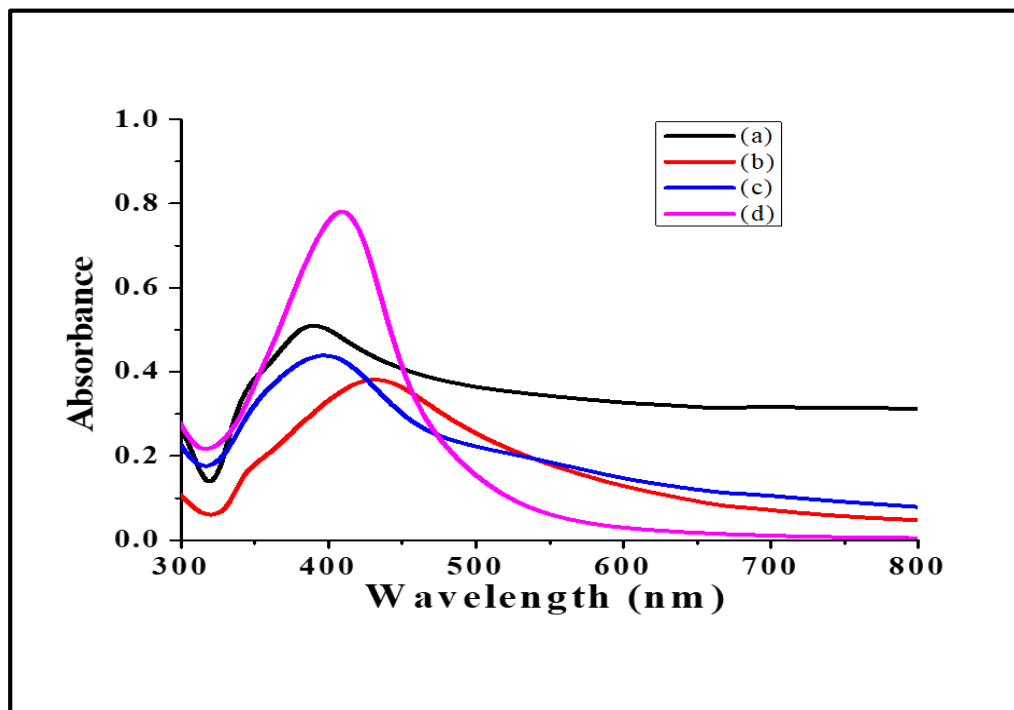


**Figure 6.1:** UV-Vis absorption spectra of AgNPs synthesized after 30 minutes in solution (a) without extract, (b)  $K_{Ext/Ag} = 0.5$ , (c)  $K_{Ext/Ag} = 2.5$  and (d)  $K_{Ext/Ag} = 5.0$ .

UV-Vis absorption spectrum of the synthesized nanoparticles using sodium borohydride as reducing agent and without adding peel extract (stabilizing agent) is depicted in **figure 6.2a**. The UV-Vis spectrum taken immediately after synthesizing AgNPs showed peak at 390 nm, which indicated the formation of spherical AgNPs but the spectrum taken after 1 day did not show any peak. The peak at 390 nm disappeared, which illustrated the instability of synthesized nanoparticles while spectrum of the nanoparticles obtained in the presence of peel showed no changes even after a week time. The UV-Vis absorption spectrum for nanoparticles having  $K_{Ext/Ag} = 0.5$  and 2.5 was stable even after a week but the stability of nanoparticles obtained from  $K_{Ext/Ag} = 5.0$  was even higher (**figure 6.2 b, c and d**). There are two factors, which determine the stability of nanoparticles. These are (a) changes in the maximum absorption wavelength, and (b) sharpness of the peak.

AgNPs having lowest change in the absorption and also sharpest peak has the highest stability [Chen et al., 2007]. Based on these results, the solution of nanoparticles with  $K_{Ext/Ag} = 5.0$  has the highest stability. This shows that peel extract acts as a stabilizer and increase in its concentration increased the stability of nanoparticles. Even slight change in the shape, size and distribution of the solution has an influence on the UV-Vis extinction characteristics such as shifting of the peak, intensity and full width half maxima (FWHM) [Barani et al., 2014].

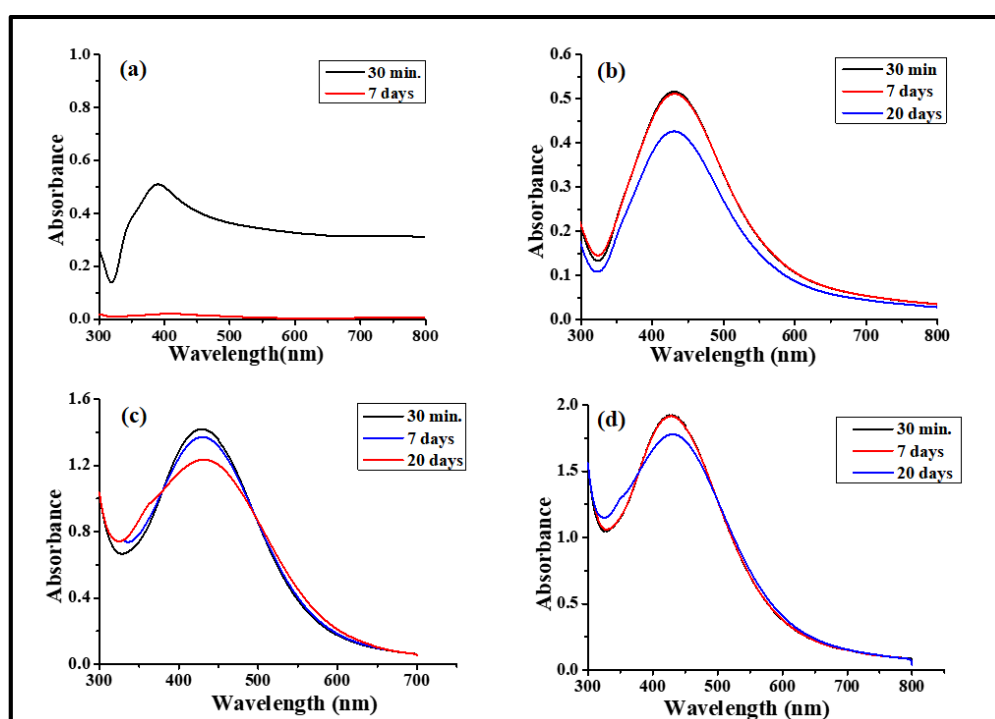


**Figure 6.2:** UV-Vis absorption spectra of AgNPs synthesized over a period of time (a) [Extract] = 0 ppm, NaBH<sub>4</sub> was used as reducing agent, (b)  $K_{Ext/Ag} = 0.5$ , (c)  $K_{Ext/Ag} = 2.5$  and (d)  $K_{Ext/Ag} = 5.0$ .

### 6.6.1.3 XRD analysis

**Figure 6.3** represents the XRD pattern of the nanoparticles synthesized at 45°C temperature and pH 10. The peaks at 35.6, 42.79, 48.16, 57.10, 64.33 are assigned to diffraction from [111], [220], [200], [222] and [220] planes of face centred cubic silver nanoparticles. The peaks have been matched with the standard data file (The JCPDS Card no. 04-0784).

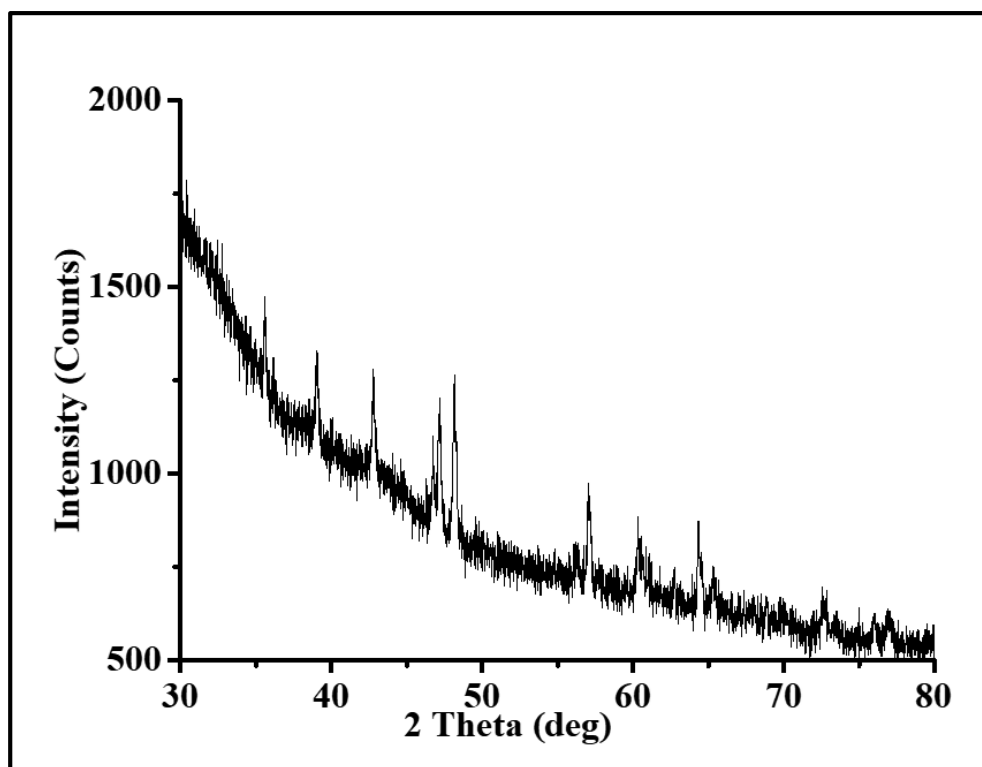


Figure 6.3: XRD pattern of AgNPs synthesized using  $K_{Ext/Ag}$  ratio = 5.0.

#### 6.6.1.4 DLS results

The effect of different amount of peel extract on Z-average of AgNPs is demonstrated in **table 6.2** given below. An increase of the extract concentration resulted in decrease in the size of AgNPs. **Figure 6.4** depicts the size of nanoparticles obtained from different  $K_{Ext/Ag}$  ratio. These trends can be explained by the fact that an increase in concentration of extract controls the growth of nanoparticles as a result of which the size of nanoparticles decreases. The sample having  $K_{Ext/Ag} = 5.0$  exhibited the lowest PDI value. All the four samples having PDI value lower than  $\sim 0.3$  indicate narrow particle size distribution [Barani et al., 2014].

**Table 6.2: Effect of different concentrations of peel extract on Z-average and zeta potential of AgNPs**

| $K_{Ext/Ag}$ | Z-average (nm) | Zeta potential (mV) | PDI  |
|--------------|----------------|---------------------|------|
| 0            | Precipitated   | Precipitated        | 1.00 |
| 0.5          | 149.0          | -25.79              | 0.32 |
| 2.5          | 58.5           | -28.06              | 0.32 |
| 5.0          | 46.6           | -26.97              | 0.25 |

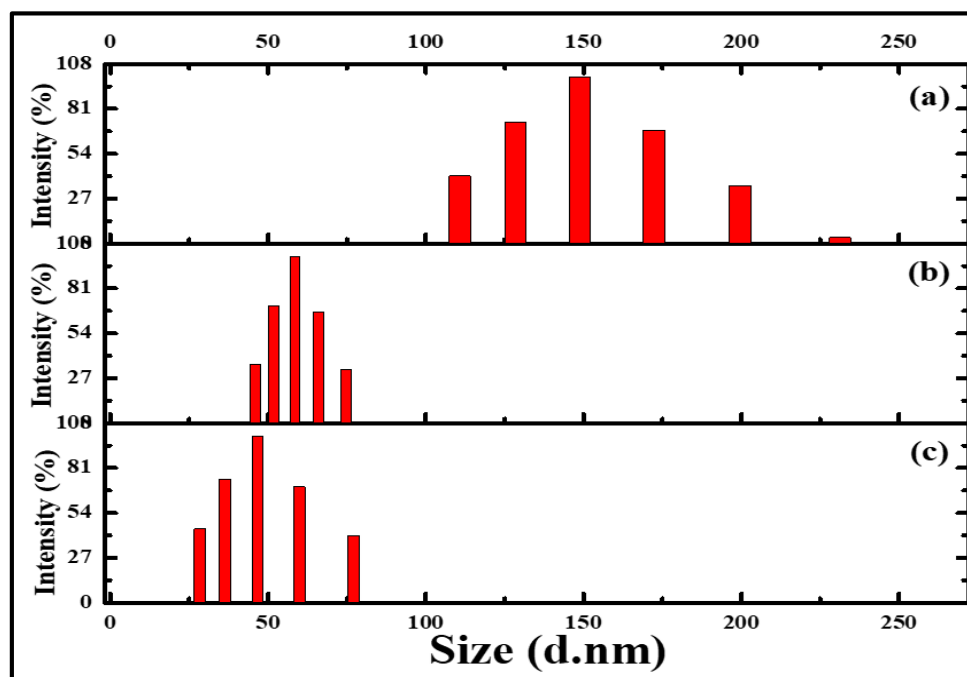


**Figure 6.4: Hydrodynamic diameter of AgNPs (a)  $K_{Ext/Ag} = 0.5$ , (b)  $K_{Ext/Ag} = 2.5$  and (c)  $K_{Ext/Ag} = 5.0$ .**

#### 6.6.1.5 FESEM results

FESEM images of synthesized AgNPs are presented in **figure 6.5**. The micrographs were taken at  $1\mu\text{m}$  (low resolution) and  $100\text{ nm}$  (high resolution). FESEM images show that synthesized nanoparticles are uniformly spherical in shape. The AgNPs, which were not stabilized by extract solution, were easily agglomerated and linked created large particles. The size of nanoparticles reduced with increasing  $K_{Ext/Ag}$  ratio.

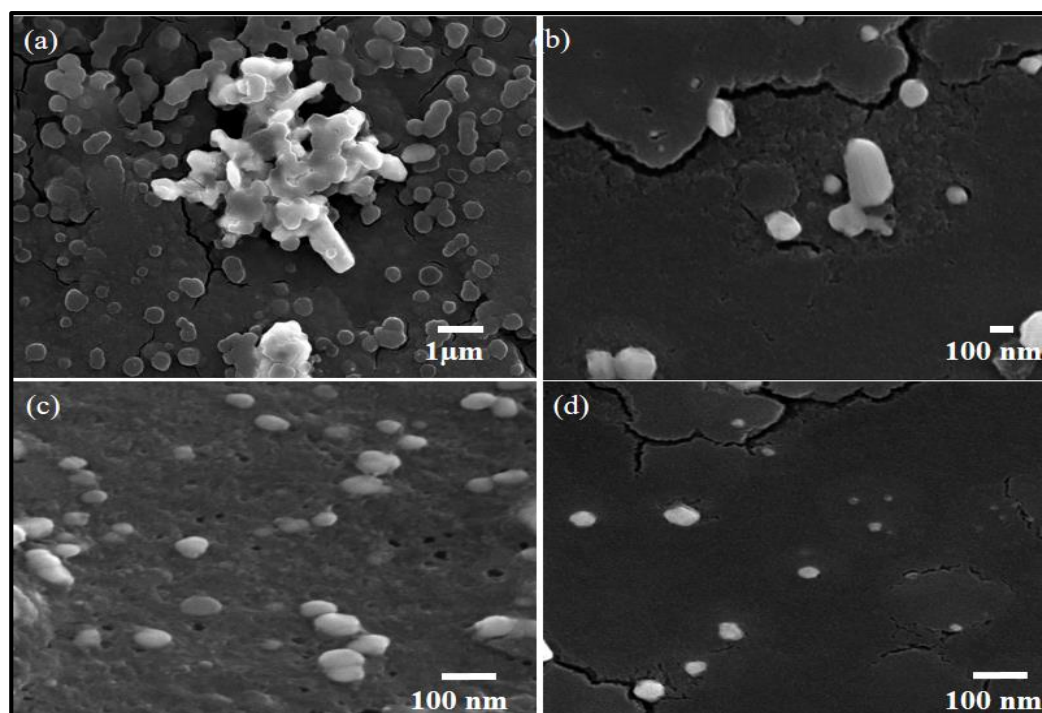


**Figure 6.5:** SEM images of synthesized AgNPs (a) without extract, (b)  $K_{Ext/Ag} = 0.5$ , (c)  $K_{Ext/Ag} = 2.5$  and (d)  $K_{Ext/Ag} = 5.0$ .

#### 6.6.1.6 EDX analysis

EDX spectra recorded from the silver nanoparticles are shown in **figure 6.6**. The EDX spectra show the presence of Ag and O. The strong signal of Ag confirms the synthesis of AgNPs while O may have originated from the biomolecules, which are capped on to the silver nanoparticles. A typical optical absorption peak at 3 keV is generally shown by silver nanoparticles due to SPR. The variation in the intensity of O peak with the size of capping molecule depicts that AgNPs are in metallic form with no formation of  $Ag_2O$  in them and free from any other impurities. Other weaker signals from Cl, P, Na and Ca atoms have also been observed due to the presence of impurities in plant extract. Al was also observed as the sample was drop-casted on Al foil [Bar et al., 2009; Magudapathy et al., 2001].

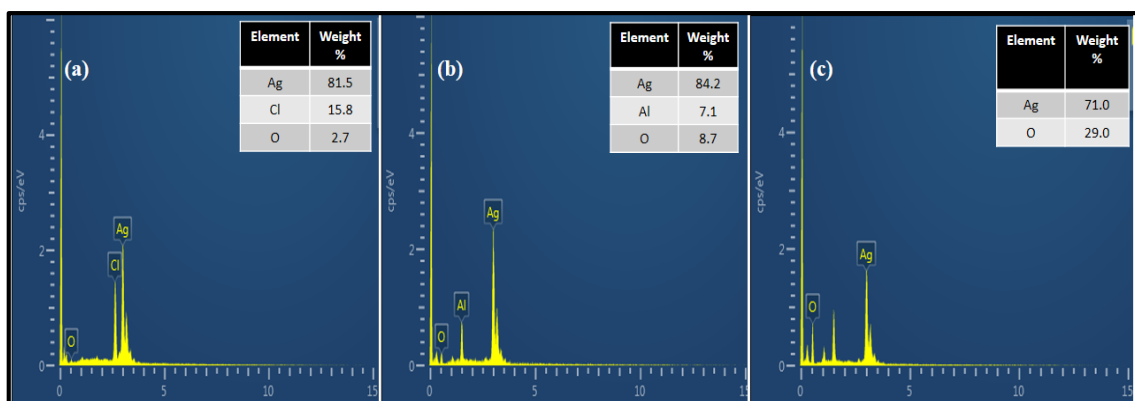


**Figure 6.6:** EDX spectrum of AgNPs (a)  $K_{Ext/Ag} = 0.5$ , (b)  $K_{Ext/Ag} = 2.5$  and (c)  $K_{Ext/Ag} = 5.0$ .

### 6.6.2 Effect of pH on the stability of Ag nanoparticles

The colloidal stability of synthesized nanoparticles with  $K_{Ext/Ag} = 0.5$  was evaluated using particle size analyser in a pH range of 2-10. The size and the PDI of the nanoparticles remained almost the same over the wide range of pH (**figure 6.7a**). There was not a significant variation in the size of nanoparticle in the pH range of 2-8. The size of the particles in the pH range 2-8 varied from 198 to 186 nm. In contrast, a further increase in pH resulted in considerable decrease in the size of the nanoparticle (139.0 nm). The PDI of the nanoparticles remained almost the same in the pH range of 2-10. The lower value of PDI (0.212-0.286) indicates the homogeneity of nanoparticles which means particles have narrow particle size distribution.

### 6.6.3 Stability of nanoparticles at different temperatures

The stability of nanoparticles was studied over a temperature range 25-75 °C. The particle size and PDI of synthesized nanoparticles using  $K_{Ext/Ag} = 0.5$  with varying temperature is shown in **figure 6.7b**. The size of the nanoparticles increased from 51 to 72 nm on increasing the temperature from 25 °C to 75 °C. The PDI of synthesized nanoparticles decreased till 45 °C (from 0.415 to 0.204) then increased at 55 °C temperature and then further decreased. The PDI presents the homogeneity of the size distribution in a dispersion of colloidal AgNPs. A lower PDI indicates the presence of more homogeneous

particles. Therefore, the most optimum temperature for the stability of nanoparticles was found to be 45°C at which the particles were smaller in size and homogenous in nature.

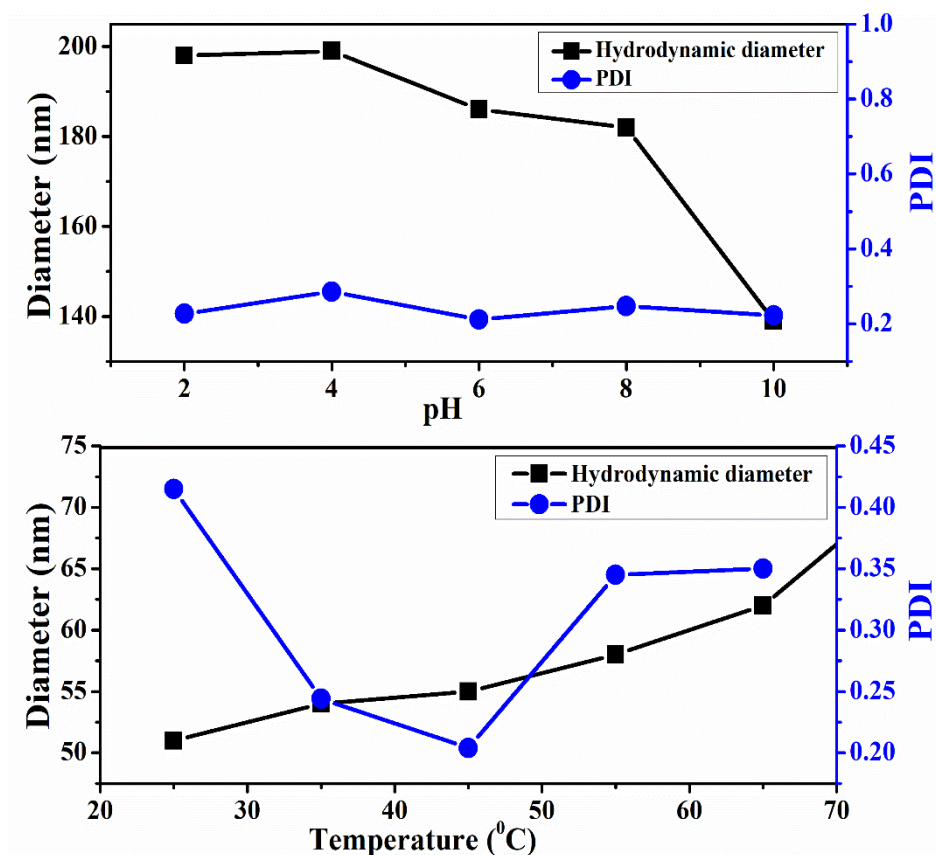


Figure 6.7: Hydrodynamic diameter and polydispersity index of AgNPs with changing (a) pH and (b) temperature.

#### 6.6.4 Antibacterial assay result

The antibacterial activity of AgNPs was determined by zone inhibition method with gram negative bacteria *P. syringae* and *P. aeruginosa*. AgNPs synthesized using orange peel extract showed inhibitory activity against both of them. AgNPs synthesized using three different  $K_{Ext/Ag}$  ratio were used for the analysis of antibacterial activity. **Figure 6.8A (1)** and **6.8B (1)** represents the antibacterial activity of peel extract. Orange peel extract did not show any zone of inhibition confirming itself having no antibacterial property [Kaviya et al., 2011]. The diameter of inhibition zone against *P. syringae* and *P. aeruginosa* is given in **table 6.3**. The inhibition zone varies from one bacterial species to

another due to variation in the composition of their cell wall [Keshavamurthy et al., 2017; Rajesh kumar et al., 2016].

The highest  $K_{Ext/Ag}$  ratio of 5.0 exhibited maximum antibacterial activity as compared to other counterparts. As observed in **figure 6.8**, the diameter of zone of inhibition increased with the increase in  $K_{Ext/Ag}$  ratio, which reflects that synthesized AgNPs using higher concentration of extract exhibited higher bactericidal properties as compared to others.

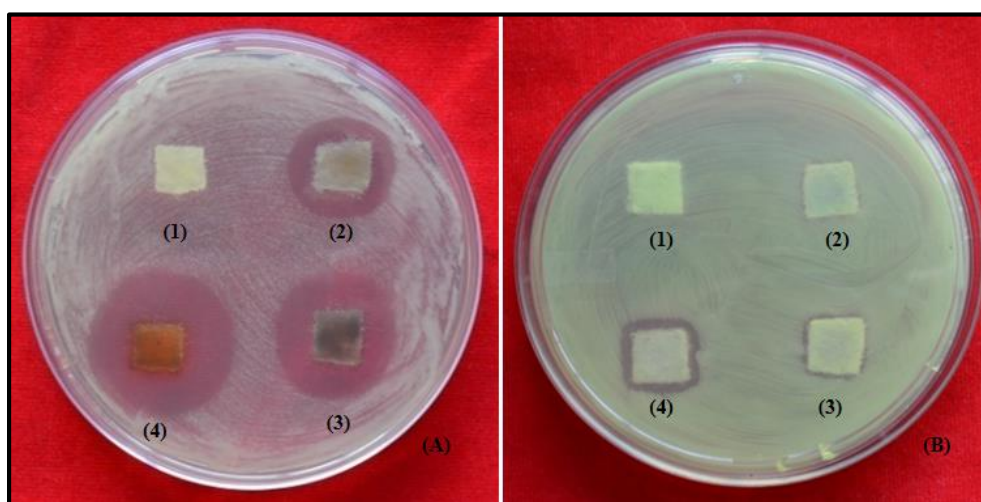


**Figure 6.8: Antibacterial activity of biogenic AgNPs against (A) *P. syringae*, and (B) *P. aeruginosa* (1) peel extract, (2)  $K_{Ext/Ag} = 0.5$ , (3)  $K_{Ext/Ag} = 2.5$  and (4)  $K_{Ext/Ag} = 5.0$  (in both the cases).**

The increase in the antibacterial activity is because of the fact that with increase in the concentration of peel extract, small sized nanoparticles were obtained (**table 6.2**) due to which larger surface area became available for the interaction and hence, bactericidal activities increased as compared to large sized particles and killed the microorganism [Carlson et al., 2008; Kaviya et al., 2011].

When nanoparticles interacted with the bacterial membrane, certain changes occurred on bacterial surface. The changes produced on the surface of bacterial membrane lead to increase in its permeability, which ultimately affected the transport through plasma membrane. The disturbance in the transportation through plasma membrane consequently caused cell death [Dibrov et al., 2002; Sondi et al., 2004]. The silver

nanoparticles, which penetrated the bacterial surface, interacted with compounds containing sulphur and phosphorous [Feng et al., 2000] and disturbed the regular cycle leading to ultimate demise of the cell. In case of *P. syringae*, an increase in the  $K_{Extact/Ag}$  ratio resulted in increase in the killing rate of bacteria. *P. aeruginosa* also exhibited the same trend but the zone of inhibition exhibited by it was comparatively smaller as compared to *P. syringae* (as shown in table 6.3). Similar kind of results have been reported when AgNPs were used to kill *E.coli* and *S.aureus* [Ren et al., 2019].

**Table 6.3: Zone of inhibition (Mean± SD) exhibited by AgNPs against gram negative bacteria (*P. syringae* and *P. aeruginosa*)**

| $K_{Ext/Ag}$ | Zone of inhibition (mm) |                      |
|--------------|-------------------------|----------------------|
|              | <i>P. syringae</i>      | <i>P. aeruginosa</i> |
| 0.5          | 20.83 ± 0.84            | 0.00 ± 0.00          |
| 2.5          | 24.83 ± 0.62            | 12.16 ± 0.23         |
| 5.0          | 26.33 ± 0.62            | 14.33 ± 0.23         |

### 6.6.5 Antifungal assay result

The effect of AgNPs on the mycelial growth of fungi, *A. brassicicola* was observed after 7 days. The diameter of the mycelial growth decreased with increase in the  $K_{Ext/Ag}$  ratio (table 6.4). Although the growth of fungi was not completely inhibited by the nanoparticles but spore growth was affected by it. A change in colour from dark green to light yellow and then finally white indicates the inhibition in the spore growth (figure 6.9).

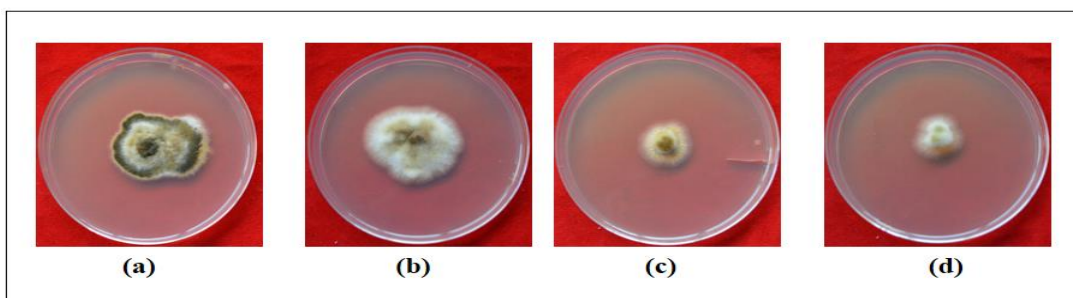


**Figure 6.9:** Images showing mycelial growth of *A. brassicicola* on PDA medium containing nanoparticles synthesized using (a)  $K_{Ext/Ag} = 0$  (peel extract), (b)  $K_{Ext/Ag} = 0.5$ , (c)  $K_{Ext/Ag} = 2.5$  and (d)  $K_{Ext/Ag} = 5.0$ .

AgNPs synthesized from the maximum  $K_{Ext/Ag}$  ratio i.e., 5.0 exhibited maximum percentage of inhibition of fungal growth and hence, maximum antifungal activity (**figure 6.10**). The inhibition of the spore growth occurred because of the generation of reactive oxygen species (ROS), which interacted with the fungal biomolecule and induced oxidative stress that hindered the cell from performing its normal physiological functions and caused cell death [Fu et al., 2014].

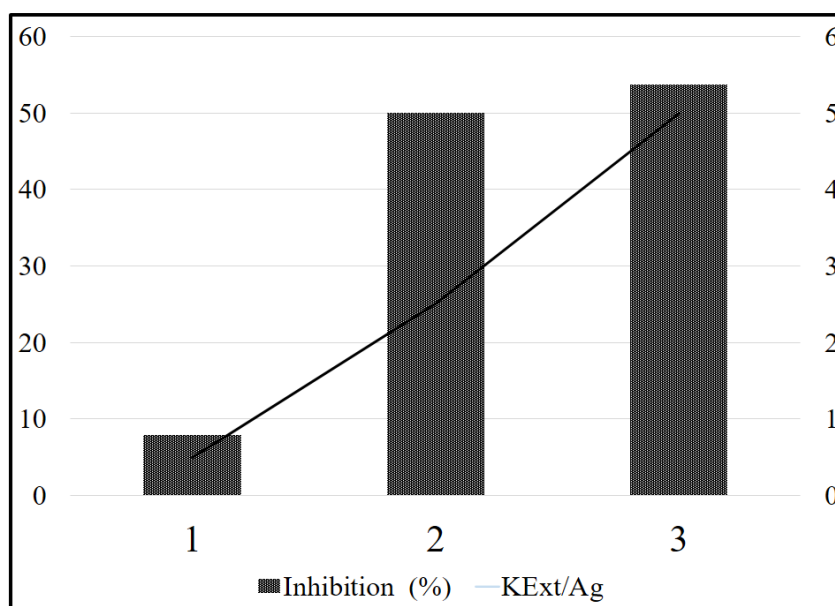


**Figure 6.10:** Percentage of inhibition of fungal (*A. brassicicola*) growth using AgNPs having (1)  $K_{Ext/Ag} = 0.5$ , (2)  $K_{Ext/Ag} = 2.5$  and (3)  $K_{Ext/Ag} = 5.0$ .

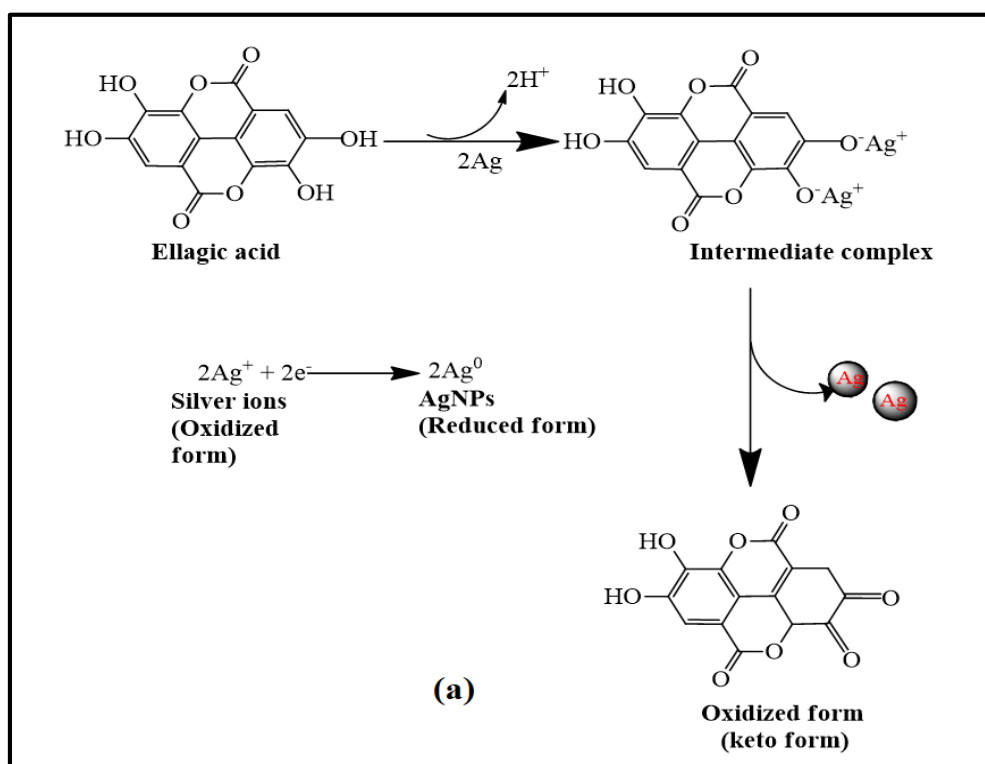
**Table 6.4: Fungal growth (colony diameter, mm) in presence of AgNPs synthesized using variable  $K_{Ext/Ag}$**

| $K_{Ext./Ag}$ | Diameter of fungal growth (mm) |
|---------------|--------------------------------|
| 0.5           | 55.5±1.0                       |
| 2.5           | 30.0±1.0                       |
| 5.0           | 27.7±0.7                       |

#### **6.6.6 Mechanism of synthesis of silver nanoparticles using orange peel**

The orange peel extract is composed of various polyphenolic compounds such as tannins flavonoids, alkaloids, saponins, quinines, steroids, etc. These chemical compounds are responsible for the instantaneous reduction of the silver ions in the reaction mixture [Makarov et al., 2014]. Extract was prepared using methanol/water solution because of the fact that although the phytochemicals present in the plant extract are soluble in water but the maximum extraction of these compounds occurs in presence of methanol. Several researchers have reported the potential of solvents for phytochemical extraction [Daneshfar et al., 2008; Dhawan and Gupta, 2016]. Among various active constituents present in the peel extract, one of them is ellagic acid, which is an antioxidant and has the ability to scavenge the free radicals. Ellagic acid possesses hydroxyl and carboxyl groups, which has strong tendency to bind the heavy metal ion ([Silvert et al., 1997]. Polyphenols and phenolic derivatives have strong nature to form chelated compound [Hider et al., 2001] and, therefore, inactivate the metal ion [Ky et al., 2014]. The inactivation of metal ions and formation of chelated compounds plays an important role in the formation of metal nanoparticles ([Jacob, 2008]. When silver nitrate comes in contact with the peel extract, the hydroxyl group present in the plant extract gets esterified as a result of elimination of reactive unpaired electrons in oxygen radicals. The eliminated electrons are transferred to hydroxyl group. This causes the reduction of  $Ag^+$  ions to atomic Ag. The esterification of the hydroxyl and carbonyl present in ellagic acid makes easier for the hydrogen atom to leave ortho-phenolic hydroxyl group, thus the

phenolic group is oxidized. The oxidation of phenolic group results in the formation of quinone or quinoid (**figure 6.11a**). The reduction of  $\text{Ag}^+$  ions to Ag is facilitated by the higher total phenolic content of the orange peel extract. The electron donating tendency of the phenolic group makes it suitable for reducing silver ion to nano size silver atoms. The quinoid compounds, which are synthesized by the oxidation of phenolic group, get adsorbed on the surface of synthesized nanoparticles and hence, get stabilized (**figure 6.11b**). By this way, the orange peels extract acts as both reducing as well as stabilizing agent.



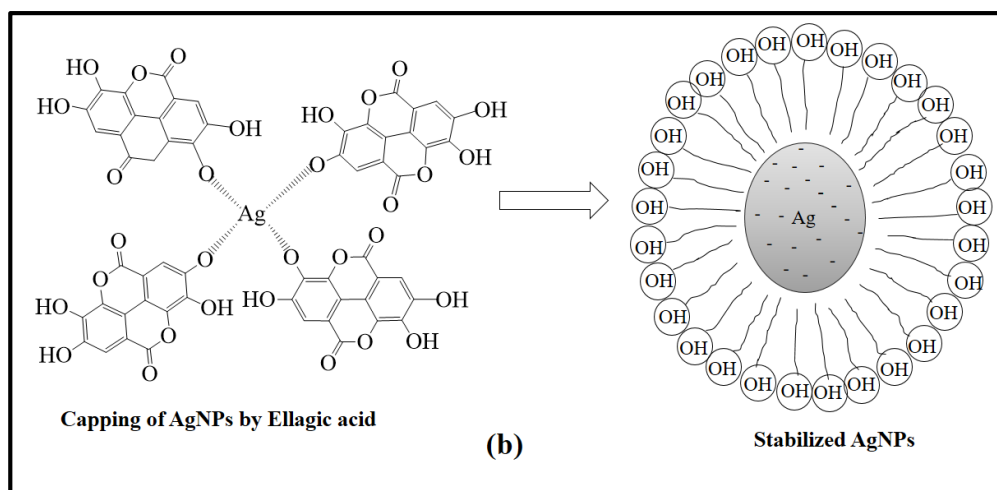


**Figure 6.11:** A schematic illustration of the mechanism for formation and stabilization of AgNPs using orange peel (a) Redox reaction showing mechanism of reduction of  $\text{Ag}^+$  ions to  $\text{Ag}^0$  by ellagic acid and (b) Capping and stabilization of AgNPs.

### 6.6.7 Photocatalysis

Firstly, the catalytic degradation of CR dye in presence of AgNPs was observed by visual change in the colour. The intensity of the colour of dye gradually decreased with time from red to light yellow in presence of AgNPs under sunlight. Congo red is a secondary diazo dye and a carcinogenic metabolite, which is used in many industries. It is a coloured dye and has high amount of dissolved solid along with high chemical oxygen demand [Maiti et al., 2008]. The degradation of the dye solution using AgNPs in presence of sunlight was confirmed using UV-Vis spectrophotometer (figure 6.12 b). Figure 6.12a exhibits the change in intensity of peak of the dye solution in absence of sunlight, which reveals that although a small shift in the intensity occurred in a time span of 2 h but at extremely slow pace. The characteristic peaks for congo red was obtained at 507 nm and 355 nm, which correspond to  $\pi-\pi^*$  transitions of azo group ( $-\text{N}=\text{N}-$ ) and naphthalene rings of the dye respectively ([Yokoyama et al., 2010]. After the addition of AgNPs, the solution was stirred in absence of light for 30 min. to attain the adsorption-desorption equilibria. The removal of dye at the initial stage reflects the capability of dye molecules to get adsorbed on the surface of nanoparticles [Movahedi and Mahjoub, 2009]. The

dye molecules were adsorbed on to the active sites of the surface of nanoparticle through the oxygen atoms of the sulphonate group present in congo red dye. After sometime, the active sites of AgNPs was saturated with the dye molecules being adsorbed on its surface. Consequently, there was no space left for further adsorption and the process of adsorption was then followed by photodegradation. The gradual decrease in the peak intensity confirmed the degradation of dye. There was complete change in the colour of the dye from bright red to light yellow at the end of 4 h.

On exposing the congo red solution to the solar radiation, the peak observed at 507 nm suppressed significantly, which depicts the mineralization of azo bonds by the attack of hydroxyl radicals. On the other hand, the peak centred at 355 nm which was attributed to naphthalene ring, exhibited a lesser suppression. Thus, it can be concluded that azo bonds are more susceptible to degradation by hydroxyl radicals as compared to the aromatic rings.

#### **6.6.7.1 Mechanism of degradation of dye**

Several studies have reported the increased degradation percentage with increase in time of exposure of dye and AgNPs complex in sunlight [Roshmi et al., 2016; Vanaja et al., 2014]. The reaction did not occur in the absence of AgNPs and even in the presence of nanoparticles in dark [Roy et al., 2014]. The reaction in the absence of sunlight confirmed the importance of sunlight in the catalytic activity of synthesized nanoparticles. There are two processes, which are involved in the photocatalytic decomposition of dyes i.e., adsorption and decomposition. The mechanism of degradation of dye could probably be attributed to the SPR effect. The excitation of SPR occurs due to oscillating charge density propagating at the interface between nanoparticles and dielectric medium [Gracia, 2011]. The mechanism is similar to the one proposed in the study [Nasir, 2018]. Ag<sup>+</sup> also shows the similar activity as Cd ions. When nanoparticles are exposed to sunlight, the photons hits the surface and electrons get

excited. The oxygen molecule dissolved in the reaction medium accepts the electrons released from the particle surface and get converted into oxygen anion radicals. These radicals break the organic dye into simple organic molecules, which result in the degradation of dye [Edison et al., 2016]. Since the process of photocatalysis takes place on the surface of AgNPs, therefore, enhancing the surface area available for photocatalysis can have crucial impact on its ability to catalyse the process. The photocatalytic degradation mechanism occurring on the catalyst surface can be explained through the following set of reactions (eq. 6.1-6.9):



#### 6.6.7.2 Kinetics of degradation of dye

The kinetics of the sunlight assisted photocatalytic degradation of dye was studied with the help of Langmuir-Hinshelwood model. The linear form of the model is expressed in the form of **equation 6.10**.

$$\ln (A_0/A_t) = kt \dots\dots\dots (6.10)$$

Where,  $A_0$  is the initial concentration of dye,  $A_t$ , concentration of dye at time  $t$ , slope ( $k$ ), rate constant of the reaction and  $t$ , irradiation time.

The rate of reaction was determined by giving a plot between  $\ln(A_0/A_t)$  versus reduction and slope of the graph depicts the rate of reaction. The order of the reaction was found to be of pseudo first order and the rate constant calculated from the slope of the graph was found to be  $0.20 \text{ h}^{-1}$  (figure 6.12c).

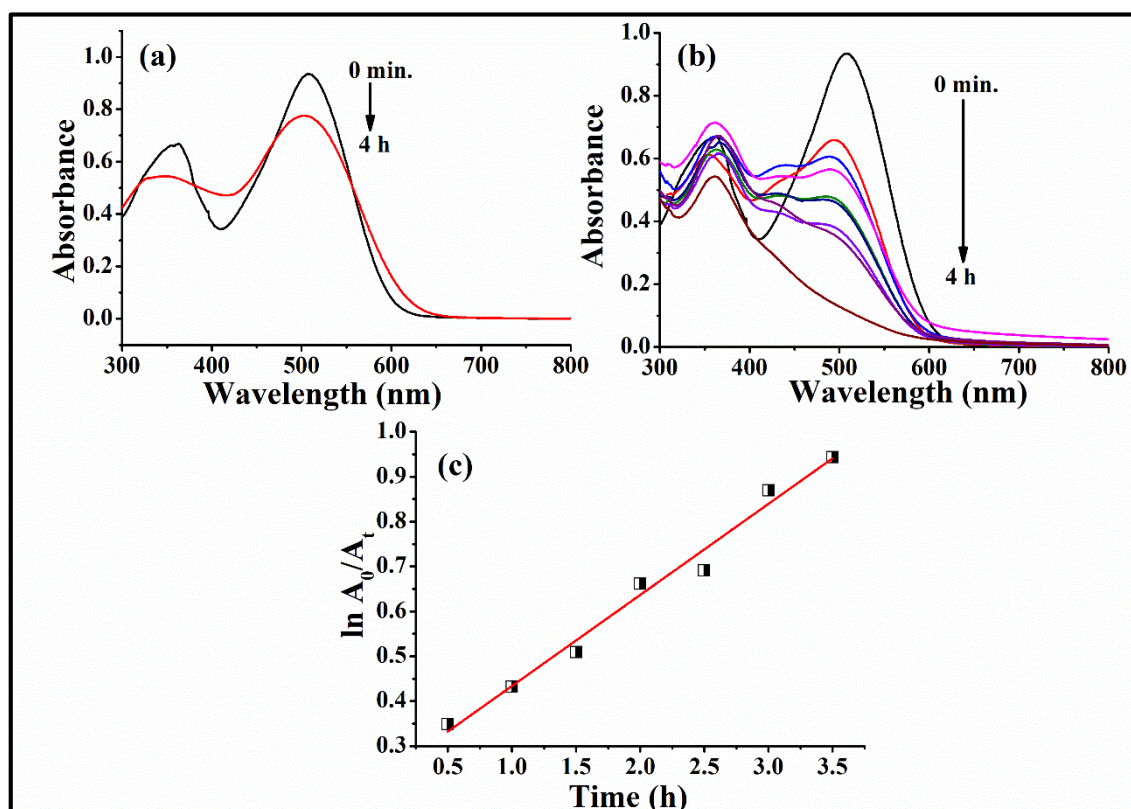


**Figure 6.12: Time dependent UV-Vis spectra for the photocatalytic degradation of congo red dye using silver nanoparticles (a) in absence and (b) in presence of sunlight. (c) The plot of  $\ln A_0/A_t$  versus time for the degradation of congo red.**

## 6.7 Conclusions

In the study, silver nanoparticles were prepared using green route and stabilized in the presence of orange peel extract. The concentration of peel extract influenced not only the size, PDI and FWHM but also had an effect on colloidal stability of nanoparticles. According to the UV-Vis data obtained,  $K_{Ex/Ag} = 5.0$  is the most optimum concentration for obtaining nanoparticles of higher stability. A considerable increase in the intensity of

the UV-Vis spectrum peak was observed in the presence of extract, which indicates synthesis of large number of nanoparticles. FESEM images confirmed the role of peel extract in the synthesis of silver nanoparticles. The morphology and composition of silver nanoparticles are in good agreement with those reported earlier. The hydrodynamic diameter of the silver nanoparticles was found to be smallest at pH 10 and 45°C temperature and, therefore, it was concluded that the optimum condition for the maximum stability of nanoparticles was found to be at pH 10 and 45°C temperature. Orange peel is not only cost effective but is also readily available and hence, provides a cheap and easy method to synthesize stable silver nanoparticles, which can be further used for various applications. Synthesized and stabilized silver nanoparticles silver nanoparticles exhibited good antimicrobial activity against bacteria *P. syringae* and *P. aeruginosa* and fungi *A. brassicicola*. The silver nanoparticles were also capable of degrading congo red dye efficiently and exhibited higher catalytic activity. Thus, greener route for synthesis of nanoparticles could be used for making comparatively better antimicrobial and catalytic agent for various purposes.

## References

Ahmad, N., Sharma, S., Rai, R. (2012). Rapid green synthesis of silver and gold nanoparticles using peels of *Punica granatum*. *Advanced Materials Letters*, 3, 376–380. <http://dx.doi.org/10.5185/amlett.2012.6357>.

Ahmed, S., Ikram, S. (2015). Silver Nanoparticles : One Pot Green Synthesis Using *Terminalia arjuna* Extract for Biological Application. *Journal of Nanomedicine and Nanotechnology*, 6. 10.4172/2157-7439.1000309

Awual, R. (2019a). Innovative composite material for efficient and highly selective Pb(II) ion capturing from wastewater. *Journal of Molecular Liquids*, 284, 502–510. <https://doi.org/10.1016/j.molliq.2019.03.157>

Awual, R. (2019b). Novel conjugated hybrid material for efficient lead(II) capturing from contaminated wastewater. *Materials Science and Engineering C*, 101, 686–695. <https://doi.org/10.1016/j.msec.2019.04.015>

Awual, R. et al. (2017). Inorganic-organic based novel nano-conjugate material for effective cobalt(II) ions capturing from wastewater. *Chemical Engineering Journal*, 324, 130–139. <http://dx.doi.org/10.1016/j.cej.2017.05.026>

Awual, R., Miyazaki, Y., Taguchi, T., Shiwaku, H., Yaita, T. (2016). Encapsulation of cesium from contaminated water with highly selective facial organic-inorganic mesoporous hybrid adsorbent. *Chemical Engineering Journal*, 291, 128–137. <http://dx.doi.org/10.1016/j.cej.2016.01.109>.

Mocanu, A. et al. (2019). Antimicrobial properties of polysulfone membranes modified with carbon nanofibers and silver nanoparticles. *Materials Chemistry and Physics*, 223, 39–45. <https://doi.org/10.1016/j.matchemphys.2018.10.002>.

Bar, H., Bhui, D.K., Sahoo, G.P., Sarkar, P., De, S.P., Misra, A. (2009). Green synthesis of silver nanoparticles using latex of *Jatropha curcas*. *Colloids and Surfaces A: Physicochemical and Engineering Aspects*, 339, 134–139.

Barani, H., Montazer, M., Braun, H., Dutschk, V. (2014). Stability of colloidal silver nanoparticles trapped in lipid bilayer: effect of lecithin concentration and applied temperature. *IET Nanobiotechnology*, 8, 282–289. <https://doi.org/10.1049/iet-nbt.2013.0048>

Barani, H., Montazer, M., Toliyat, T., Samadi, N. (2010). Synthesis of Ag-liposome nanocomposites. *Journal of Liposome Research*, 20, 323–329. <https://doi.org/10.3109/08982100903544177>

Barani, H., Montazer, M., Samadi, N., Toliyat, T. (2011). Nano silver entrapped in phospholipids membrane: Synthesis, characteristics and antibacterial kinetics. *Molecular Membrane Biology*, 28, 206–215. <https://doi.org/10.3109/09687688.2011.565484>

Bonnia, N.N. et al. (2016). Green Biosynthesis of Silver Nanoparticles Using ‘ Polygonum Hydropiper’ And Study Its Catalytic Degradation of Methylene Blue. *Procedia Chemistry*, 19, 594–602. <https://doi.org/10.1016/j.proche.2016.03.058>

Boutinguiza, M., Comesaña, R., Lusquiños, F., Riveiro, A., Val, J., Pou, J. (2014). Production Of Silver Nanoparticles By Laser Ablation In Open Air. *Applied Surface Science*, 336, 108–111. <http://dx.doi.org/10.1016/j.apsusc.2014.09.193>.

Carlson, C., Hussain, S.M., Schrand, A.M., Hess, K.L., Jones, R.L., Schlager, J.J. (2008). Unique Cellular Interaction of Silver Nanoparticles: Size-Dependent Generation of Reactive Oxygen Species. *J. Phys. Chem.*, 112, 13608–13619. doi: 10.1021/jp712087m.

Chen, M., Feng, Y.G., Wang, X., Li, T.C., Zhang, J.Y., Qian, D.J. (2007). Silver Nanoparticles Capped by Oleylamine: Formation, Growth, and Self-Organization. *Langmuir*, 23, 5296–5304. <https://doi.org/10.1021/la700553d>.

Daneshfar, A., Ghaziaskar, H.S., Homayoun, N. (2008). Solubility of Gallic Acid in Methanol, Ethanol, Water, and Ethyl Acetate. *Journal of Chem., Eng* 53, 776–778. <https://doi.org/10.1021/je700633w>.

Dhawan, D., Gupta, J. (2016). Comparison of Different Solvents for Phytochemical Extraction Potential from Datura metel Plant Leaves. *International Journal of Biological Chemistry*, 11, 17–22. <http://dx.doi.org/10.3923/ijbc.2017.17.22>

Dibrov, P. et al. (2002). Chemiosmotic Mechanism of Antimicrobial Activity of Ag<sup>+</sup> in *Vibrio cholerae*. *Antimicrobial agents and Chemotherapy*, 46, 8–11. <https://dx.doi.org/10.1128%2FAAC.46.8.2668-2670.2002>.

Edison, T.N.J.I., Atchudan, R., Sethuraman, M.G., Lee, Y.R. (2016). Reductive-degradation of carcinogenic azo dyes using *Anacardium occidentale* testa derived silver nanoparticles. *Journal of Photochemistry and Photobiology B : Biology*, 162, 604–610. <https://doi.org/10.1016/j.jphotobiol.2016.07.040>.

Feng, Q.L., Wu, J., Chen, G.Q., Cui, F.Z., Kim, T.N., Kim, J.O. (2000). A mechanistic study of the antibacterial effect of silver ions on *Escherichia coli* and *Staphylococcus aureus*. *Journal of Biomedical Materials Research*, 52, 662–668. [https://doi.org/10.1002/1097-4636\(20001215\)52:4%3C662::aid-jbm10%3E3.0.co;2-3](https://doi.org/10.1002/1097-4636(20001215)52:4%3C662::aid-jbm10%3E3.0.co;2-3).

Fu, P.P., Xia, Q., Hwang, H.M., Ray, P.C., Yu, H. (2014). Mechanisms of nanotoxicity: Generation of reactive oxygen species. *Journal of Food and Drug Analysis*, 22, 64–75. doi: 10.1016/j.jfda.2014.01.005.

Gauthami, M., Srinivasan, N., Goud, N.M. (2015). Synthesis of Silver Nanoparticles using *Cinnamomum zeylanicum* Bark Extract and its Antioxidant Activity. *Nanoscience and Nanotechnology-Asia*, 5, 2–7. <https://doi.org/10.2174/221068120501150728103209>.

Gopi, D., Kanimozhi, K., Bhuvaneshwari, N., Indira, J., Kavitha, L. (2014). Novel banana peel pectin mediated green route for the synthesis of hydroxyapatite nanoparticles and their spectral characterization. *Spectrochimica Acta Part A: Molecular and*

- Biomolecular Spectroscopy, 118, 589–597. <https://doi.org/10.1016/j.saa.2013.09.034>.
- Goswami, A.M., Ghosh, S. (2013). Biological Synthesis of Colloidal Gold Nanoprisms Using *Penicillium citrinum* MTCC9999. *Journal of Biomaterials and Nanobiotechnology*, 4, 20–27. <http://dx.doi.org/10.4236/jbnb.2013.42A003>.
- Gracia, M.A. (2011). Surface plasmons in metallic nanoparticles:fundamentals. *Journal of Physics D:Applied Physics*, 44, 283001. <https://doi.org/10.1088/0022-3727/44/28/283001>
- Hider, R.C., Liu, Z.D., Khodr, H.H. (2001). Metal chelation of polyphenols. *Methods in Enzymology*, 335, 190–203. [https://doi.org/10.1016/s0076-6879\(01\)35243-6](https://doi.org/10.1016/s0076-6879(01)35243-6)
- Hossain, L., Sarker, S.K., Khan, M.S. (2018). Evaluation of Present and Future Wastewater Impacts of Textile Dyeing Industries in Bangladesh. *Environmental Development*, 26, 23–33. <https://doi.org/10.1016/j.envdev.2018.03.005>.
- Ibrahim, K., Khalid, S., and Idrees, K. (2017). Nanoparticles : Properties , applications and toxicities. *Arabian Journal of Chemistry*, 12, 908-931. <https://doi.org/10.1016/j.arabjc.2017.05.011>.
- Jacob, J.A. et al. (2008). Role of Phenol Derivatives in the Formation of Silver Nanoparticles. *Langmuir*, 24, 528–533. <https://doi.org/10.1021/la702073r>
- Kant, R. (2012). Textile dyeing industry an environmental hazard. *Natural Science*, 4, 22–26. <http://dx.doi.org/10.4236/ns.2012.41004>.
- Kaviya, S., Santhanalakshmi, J., Viswanathan, B., Muthumary, J., Srinivasan, K. (2011). Biosynthesis of silver nanoparticles using citrus sinensis peel extract and its antibacterial activity. *Spectrochimica Acta - Part A: Molecular and Biomolecular Spectroscopy*, 79, 594–598. doi: 10.1016/j.saa.2011.03.040.
- Kempa, T.J., Farrer, R.A., Giersig, M. (2006). Photochemical synthesis and multiphoton luminescence of monodisperse silver nanocrystals. *Plasmonics*, 1, 45–51. [10.1007/s11468-006-9008-5](https://doi.org/10.1007/s11468-006-9008-5).
- Kennedy, J. et al. (2017). Bioreduction potentials of dried root of *Zingiber officinale* for a simple green synthesis of silver nanoparticles: Antibacterial studies. *Journal of Photochemistry and Photobiology, B: Biology*, 177, 62–68. [10.1016/j.jphotobiol.2017.10.007](https://doi.org/10.1016/j.jphotobiol.2017.10.007).
- Keshavamurthy, M., Srinath, B.S., Rai, V.R. (2017). Phytochemicals Mediated Green Synthesis of Gold Nanoparticles Using *Pterocarpus Santalinus* L. ( Red Sanders ) Bark Extract and Their Antimicrobial Properties. *Particulate Science and Technology*, 36, 785–790. <https://doi.org/10.1080/02726351.2017.1302533>
- Kumari, M. et al. (2016). Tailoring shape and size of biogenic silver nanoparticles to enhance antimicrobial efficacy against MDR bacteria. *Microbial Pathogenesis*, 105, 346–355. <https://doi.org/10.1016/j.micpath.2016.11.012>

Ky, I., Lorrain, B., Kolbas, N., Crozier, A., Teissedre, P.L. (2014). Wine by-Products: Phenolic characterization and antioxidant activity evaluation of grapes and grape pomaces from six different French grape varieties. *Molecules*, 19, 482–506. doi: 10.3390/molecules19010482.

Li, Z., Wang, Y., Yu, Q. (2010). Significant Parameters in the Optimization of Synthesis of Silver Nanoparticles by Chemical Reduction Method. *J. of Materi Eng and Perform*, 19, 252–256. <http://dx.doi.org/10.1007/s11665-009-9486-7>.

Magudapathy, P., Gangopadhyay, P., Panigrahi, B.K., Nair, K.G.M., Dhara, S. (2001). Electrical transport studies of Ag nanoclusters embedded in glass matrix. *Physica B*, 299, 142–146. doi:10.106/s0921-4526(00)00580-9

Maiti, S., Purakayastha, S., Ghosh, B. (2008). Production of low-cost carbon adsorbents from agricultural wastes and their impact on dye adsorption. *Chemical Engineering Communications*, 195, 386–403. <https://doi.org/10.1080/00986440701707917>

Makarov, V.V., Love, A.J., Sinitsyna, O.V., Makarova, S.S., Yaminsky, I.V. (2014). Green Nanotechnologies : Synthesis of Metal Nanoparticles Using Plants. *Acta Naturae*, 6, 35–44.

Mocanu, A. et al. (2019). Antimicrobial properties of polysulfone membranes modified with carbon nanofibers and silver nanoparticles. *Materials Chemistry and Physics*, 223, 39–45. <https://doi.org/10.1016/j.matchemphys.2018.10.002>

Movahedi, M., Mahjoub, A.R. (2009). Photodegradation of Congo Red in Aqueous Solution on ZnO as an Alternative Catalyst to TiO<sub>2</sub>. *Iranian Chemical Society*, 6, 70–577. <http://dx.doi.org/10.1007/BF03246536>.

Nasir, J.A. et al. (2018). Efficient Solar Light Driven Photocatalytic Degradation of Congo Red Dye on CdS Nanostructures Derived from Single Source Precursor. *Journal of Nanoscience and Nanotechnology*, 18, 7405–7413. <https://doi.org/10.1166/jnn.2018.16038>

Pirtarighat, S., Ghannadnia, M., Baghshahi, S. (2018). Biosynthesis of silver nanoparticles using *Ocimum basilicum* cultured under controlled conditions for bactericidal application. *Materials Science and Engineering: C*, 98, 250–255. 10.1016/j.msec.2018.12.090.

Rafique, M. et al. (2019). Novel and facile synthesis of silver nanoparticles using *Albizia procera* leaf extract for dye degradation and antibacterial applications. *Materials Science and Engineering C*, 99, 1313-1324. <https://doi.org/10.1016/j.msec.2019.02.059>

Rajeshkumar, S. (2016). Synthesis of silver nanoparticles using fresh bark of *Pongamia pinnata* and characterization of its antibacterial activity against gram positive and gram negative pathogens. *Resource-Efficient Technologies*, 2, 30–35. <https://doi.org/10.1016/j.refit.2016.06.003>

Ren, Y., Yang, H., Wang, T., Wang, C. (2019). Bio-synthesis of silver nanoparticles with antibacterial activity. *Materials Chemistry and Physics*, 235, 121746.

<https://doi.org/10.1016/j.matchemphys.2019.121746>

Roshmi, T., Jishma, P., Radhakrishnan, E.K. (2016). Photocatalytic and antibacterial effects of silver nanoparticles fabricated by *Bacillus subtilis* SJ 15. *Inorganic and Nanometal Chemistry*, 3174, 901–908. <https://doi.org/10.1080/15533174.2016.1228668>

Roy, K., Sarkar, C.K., Ghosh, C.K. (2014). Photocatalytic activity of biogenic silver nanoparticles synthesized using yeast (*Saccharomyces cerevisiae*) extract. *Applied Nanoscience*, 5, 953–959. <https://doi.org/10.1007/s13204-014-0392-4>

Roy, P. (2017). Green synthesis of silver nanoparticles using *Azadirachta indica* leaf extract and its antimicrobial study. *Applied Nanoscience*, 7, 843–850. <https://doi.org/10.1007/s13204-017-0621-8>.

Sajeshkumar, N.K., Vazhacharickal, P.J., Mathew, J.J., Sebastin, A. (2015). Synthesis of silver nanoparticles from curry leaf (*Murraya koenigii*) extract and its antibacterial activity. *Journal of Pharmaceutical Sciences*, 4, 15–25.

Sen, P., Ghosh, J., Abdullah, A., Kumar, P., Vandana. (2003). Preparation of Cu, Ag, Fe and Al nanoparticles by the exploding. *Journal of Chemical Sciences*, 115, 99–508. <https://doi.org/10.1007/BF02708241>.

Silvert, P.Y., Herrera-Urbina, R., Tekaiia-Elhsissen, K. (1997). Preparation of colloidal silver dispersions by the polyol process. *Journal of Materials Chemistry*, 7, 293–299.

Sondi, I., Salopek-sondi, B. (2004). Silver nanoparticles as antimicrobial agent : a case study on *E. coli* as a model for Gram-negative bacteria. *Journal of Colloid and Interface science*, 275, 177–182. <https://doi.org/10.1016/j.jcis.2004.02.012>

Vanaja, M. et al. (2014). Degradation of Methylene Blue Using Biologically Synthesized Silver Nanoparticles. *Bioinorganic Chemistry and Applications*, 2014, 1-8. <http://dx.doi.org/10.1155/2014/742346>

Varadavenkatesan, T., Vinayagam, R., Selvaraj, R. (2019). Green synthesis and structural characterization of silver nanoparticles synthesized using the pod extract of *Clitoria ternatea* and its application towards dye degradation. *Materials Today*, 4–6. <http://doi.org/10.1016/j.matpr.2019.04.216>

Veerasamy, R. et al. (2011). Biosynthesis of silver nanoparticles using mangosteen leaf extract and evaluation of their antimicrobial activities. *Journal of Saudi Chemical Society*, 15, 113–120. <https://doi.org/10.1016/j.jscs.2010.06.004>

Yeo, S.Y., Lee, H.J., Jeong, S.H. (2003). Preparation of nanocomposite fibers for permanent antibacterial effect. *Journal of Materials Science*, 38, 2143–2147. <https://doi.org/10.1023/A:1023767828656>

Yokoyama, K., Fisher, A.D., Amori, A.R., Welchons, D.R., Mcknight, R.E. (2010). Spectroscopic and calorimetric studies of congo red dye-amyloid B peptide complexes. *Journal of Biophysical Chemistry*, 1, 153–163. <http://dx.doi.org/10.4236/jbpc.2010.13018>.



## **Chapter 7: Kinetic and isothermal study of effect of transition metal doping on adsorptive property of zinc oxide nanoparticles synthesized via green route using *Moringa oleifera* leaf extract**

---

### **7.1 Introduction**

Nanotechnology is one of the most dynamic fields which has got applications in diverse areas such as electronics, agriculture, energy, pharmaceutical, wastewater treatment, etc. Variety of organic compounds and synthetic dyes are used in various industries like food, pulp and paper, leather, textile, printing and cosmetic industries. The bright colored dyes, which are very useful in these industries, are toxic and carcinogenic in nature. These are released into the water bodies as effluent from those industries. Therefore, these dyes are considered as undesirable materials from environmental point of view [Lachheb et al., 2002]. These dyes are posing serious health hazards to living organisms. The efficient removal of congo red (CR) dye has always been challenging for researchers [Tanwar et al., 2017; Rekha et al., 2015; Yagub et al., 2014]. Congo red dye is mainly discharged into the water bodies from paper, plastic and textile industries [Zare et al., 2015; Chen et al., 2013]. After usage, the dyes are directly released into the water bodies. For reducing these dyes some nanoparticles have been developed to degrade such toxic dyes into non-toxic compounds [Chamjangali et al., 2015; Kumar et al., 2013; Tripathi et al., 2014; Tian et al., 2015]. Among all the developed methods, adsorption is one such method which is used to remove dyes and various heavy metal ions from the wastewater. This method is advantageous because it is not only economical but is also easy to execute. It has simple design and is effective against toxic pollutants and harmful substances [Sharma et al., 2010]. While working on adsorption, researchers have used different

adsorbents such as sawdust [Malik et al., 2004], activated carbon [Rodríguez et al., 2009], carbon nanotubes [Gupta et al., 2013], swelling clays [Li et al., 2011] etc. to remove dyes from the wastewater from aqueous solution. Although these adsorbents have been found to be useful for the removal of dyes from the wastewater but there are many disadvantages associated with those materials. These adsorbents are costly, have long adsorption time and also inconvenient to separate, which creates a need to find other alternatives. Nanomaterials possess specific chemical properties, which are completely dependent on their composition, shape and size. The unique physical and chemical properties of nanomaterials make them suitable to be used as adsorbent. The nanometre size of particles enables it to disperse easily in the solution and provides high surface contact with the pollutants. The present work concerns green route synthesis of nanoparticles using plant extract derived from *Moringa oleifera*. Different methods have been reported for synthesis of zinc oxide nanoparticles (ZNPs), which include solvothermal and hydrothermal synthesis [Chen et al., 2013], sol gel method [Ba-Abbad et al., 2013], polymerization method, and precipitation method. These methods have several issues associated with them such as stability of nanoparticles, heterogeneity, aggregation which results in broadening of particle size distribution [Chandra et al., 2019]. Green route synthesis is the simple, cost effective, ecofriendly method for the synthesis of nanoparticles [Kharissova et al., 2013; Bansal et al., 2006]. Natural products such as plant extract and microbial surfactants containing different organic compounds have been used as reductants and as capping agents during synthesis [Singh et al., 2012; Agarwal et al., 2019]. According to Raveendran and co-workers, nanoparticles synthesized using biosynthetic routes have better defined sizes as well as morphology as compared to other methods [Raveendran et al., 2003]. The natural compounds present in biological system play a vital role not only in the synthesis of

nanoparticles but also acts as reducing and capping agent. The literature survey exhibits that as compared to other biological systems plant extract offers additive advantages. Plants are easily accessible, safe to handle and also produce highly stable nanoparticles [Agarwal et al., 2019; Kharissova et al., 2013]. ZNPs and Cu doped ZNPs (Cu-ZNPs) were synthesized using plant extract and then used as adsorbent for degradation of CR dye in aqueous solution. Most of the literature have reported the degradation of dyes using nanoparticles as photocatalyst [Chamjangali et al., 2015; Tripathi et al., 2014; Chidambaram et al., 2016; Huang et al., 2015].

The aim of this study is to depollute the water from dye using synthesized nanomaterials as adsorbent. As per literature survey, no study has been carried out which uses Cu-ZNPs as adsorbent, for dye removal. The objective of this work is also to compare the efficiency of adsorption of the pure and doped ZNPs. The process of adsorption was studied as a function of pH, contact time, adsorbent dose, and concentration of dye for maximum adsorption. The adsorption data obtained for different time and concentration was fitted to kinetics and isotherm models to analyse the adsorption process.

## **7.2 Materials and method**

### **7.2.1 Materials**

Zinc acetate dehydrate, zinc sulphate heptahydrate and copper sulphate pentahydrate were procured from S D Fine-Chemicals Ltd, India. Sodium hydroxide pellets and congo red (CR) dye were supplied by Molychem, India. All chemicals used in this study were of LR grade.

### **7.2.2 Synthesis of plant extract**

The extract was prepared by using leaves of a plant called *Moringa oleifera*. The leaves of the plant were collected from the fields in Jais, India. Leaves were properly washed by using tap water and then twice using double distilled water. They were then kept in

sunlight, dried for 2-3 days and finally crushed into powdered form. Crushed leaves were used to prepare plant extract by heating 10 g of leaves powder with 200 mL of distilled water at 100°C temperature for around 2 h. The resulting solution was then cooled at room temperature. After cooling, the solution was filtered using Whatmann filter paper no. 1. The filtrate was then stored at 4°C temperature in an amber bottle for further experimentations.

### **7.2.3 Biosynthesis of pure ZnO nanoparticles and Cu doped ZnO nanoparticles**

15 mL of leaf extract was added to 35 mL of 200 mM zinc acetate dihydrate (prepared by dissolving 1.536 g of zinc acetate dihydrate in 35 mL of distilled water). The reaction mixture was thoroughly stirred on a magnetic stirrer for about 6 h. After 6 h, the pH of the solution was adjusted at 12 (pH of the solution was maintained using 0.1 M aqueous NaOH solution) to make it basic and the reaction mixture was heated at a temperature of 90°C overnight with magnetic stirring. After heating the solution overnight, the white powder dispersed in solution was centrifuged at 13500 rpm for 15 min. The powder obtained was washed three times using distilled water and then thrice with ethanol. It was eventually dried overnight at 90°C temperature and was crushed into fine powder using mortar and pestle.

For Cu-ZNPs, 5 g of zinc sulphate heptahydrate was added to 50 mL of plant extract and 50 mg of copper sulphate pentahydrate. The solution was stirred for an hour. The final solution was then treated in the same way as that of undoped ZNPs. The possible mechanism for the synthesis of these nanoparticles is possibly similar to the one reported by Singh and co-workers [Singh et al., 2014]. The synthesized powders were characterized using different analytical tools such as UV-Visible spectroscopy (UV-Vis), fourier transform infrared spectroscopy (FTIR), x-ray diffraction analysis (XRD), thermogravimetric analysis (TGA), transmission electron microscopy (TEM) and field

emission scanning electron microscopy (FESEM) with energy dispersive x-ray (EDX) analysis. The plant extract obtained from *Moringa oleifera* consists of various organic compounds such as polyphenols, flavonoids, carotenoids, fatty acids, etc. [Saini et al., 2016]. The synthesis reaction follows the similar mechanism as mentioned in [Ahmed et al., 2017; Khalifi et al., 2019].

#### 7.2.4 Adsorption experiments

The adsorption experiments were carried out for the removal of CR dye. The reaction was carried out using 50 mL of CR dye (20 mg/L) and 0.1 g of synthesized material solution was added to it. The temperature of the reaction was maintained at 28°C and the stirring speed was kept 200 rpm under dark condition. The pH of the dye solution was analysed using pH tutor (Eutech Instruments, Singapore). The concentration of the dye was recorded using UV-Vis spectrophotometer (Lab India UV-Vis 3200). The adsorption experiments were conducted to optimize process parameters viz., pH, time, temperature, etc. Dye removal (D) in percent was calculated using following **equation 7.1**:

$$D = \frac{C_0 - C_e}{C_0} * 100 \quad \dots\dots\dots (7.1)$$

In the above **equation 7.1**,  $C_0$  represents the initial concentration and  $C_e$ , equilibrium dye concentration in  $\text{mg L}^{-1}$ . The amount of dye adsorbed per unit of the adsorbent at equilibrium was calculated in terms of  $q_e$  ( $\text{mg g}^{-1}$ ) using **equation 7.2** given below.

$$q_e = \frac{C_0 - C_e}{m} * V \quad \dots\dots\dots (7.2)$$

Where,  $q_e$  is adsorption capacity,  $V$ , volume of dye solution (L) and  $m$ , mass of the adsorbent (g).

## 7.3 Results and discussion

### 7.3.1 Characterization of biosynthesized ZnO nanoparticles

#### 7.3.1.1 UV-Vis spectroscopy

The synthesis of nanoparticles (NPs) and the adsorption study was carried out using UV-Vis spectroscopy (Lab India UV-Vis 3200 spectrophotometer). The spectrum was recorded in the range of 300-800 nm with a 10 mm path length quartz cuvette. The UV-Vis spectrum revealed a characteristic absorption peak of ZNPs at wavelength of 358 nm and the peak for Cu-ZNPs was obtained at 366 nm (**figure 7.1**).

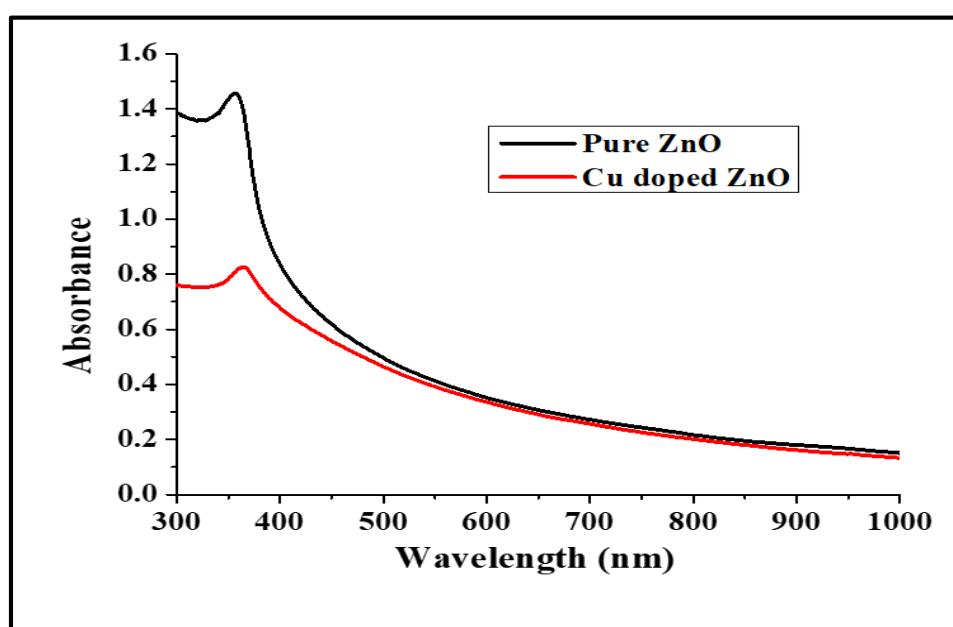


**Figure 7.1: FTIR spectra of pure ZNPs and Cu doped ZNPs.**

#### 7.3.1.2 XRD analysis

The purity of the phase was studied by using PANalyticalX'pertpro MPD diffractometer. x- ray diffraction spectrometry technique helps to investigate the formation and quality of synthesized NPs. Scanning of the samples was done in the range of  $2\theta$  from 20 to  $80^\circ$  with monochromatic radiation ( $\text{CuK}\alpha$ ).

XRD technique was used for identification of crystal structure and for getting various lattice parameters. The XRD spectra of pure and Cu-ZNPs are shown in the **figure 7.2** below. The data revealed a series of characteristic peaks with  $2\theta$  values of  $31.774^\circ$ ,

34.4268°, 47.5965°, 56.6433° and 62.9327° (**figure 7.2**). These peaks were indexed to (1 0 0), (0 0 2), (1 0 2), (1 1 0) and (1 0 3) planes of ZNPs hexagonal phase structure respectively. The peaks and Miller Indices obtained are related to the standard hexagonal wurtzite crystal structure. The data are in accordance with the standard JCPDS card (36-1451). The data not only confirm the synthesis of ZNPs but also the absence of other impurities.

When the Cu is doped into the ZnO lattice, much significant shift in the peaks was not observed. Small intensity peaks were observed for copper which indicates that copper has been incorporated well inside the crystal lattice of synthesized ZNPs.

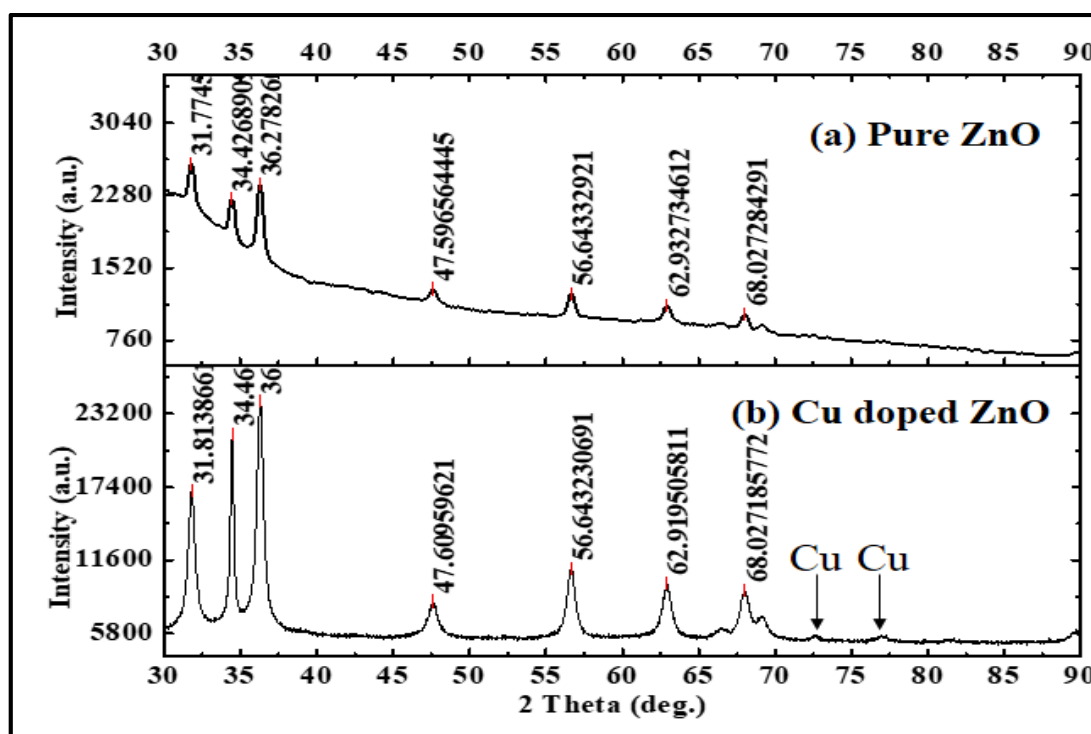


**Figure 7.2:** XRD spectra of (a) pure ZNPs and (b) Cu doped ZNPs.

### 7.3.1.3 FESEM analysis with EDX

FESEM was carried out using JSM-7100F, Jeol FESEM. The SEM analysis was used to determine surface morphology of the synthesized NPs. The synthesized powders were

dispersed in ethanol and ultra sonicated for 15 min. The solution was then drop casted on Al foil, air dried and then finally placed on copper grid for analysis. To prevent samples charging, a thin gold coating was sputtered onto the samples prior to the analysis. FESEM was coupled with EDX and the sample used for FESEM was used as such for this analysis as well. EDX analysis gave an idea about the elemental composition and the chemical purity of the synthesized NPs.

The image in **figure 7.3(a)** shows individual ZNPs as well as aggregates and exhibit that the ZNPs synthesized are irregular in shape. The SEM images of Cu-ZNPs are shown in **figure 7.3(c)**. These images depict the incorporation of Cu into the crystal lattice of ZnO which change the shape and morphology of ZNPs. The images of Cu-ZNPs were found to be even more agglomerated, therefore, it is difficult to determine the average grain size from the less resolved SEM images.

EDX analysis was conducted for looking at the elemental composition of the synthesized samples and for the confirmation of the successful doping and the formation of ZNPs [represented in **figure 7.3(b and d)**]. EDX signals and their percentage composition of the samples are shown in the **figure 7.3** given below. **Figure 7.3 (b)** shows strong signals of zinc and oxygen, which represents the purity of the synthesized material. For doped ZNPs, copper signals were also found along with zinc and oxygen, which signify copper has been successfully doped. The EDX spectra confirmed the presence of chemical constituents (Zn = 79.52 wt % and O = 20.48 wt % in undoped ZnO; Cu = 8.1 wt %, O = 15.6 wt % and Zn = 76.2 wt % in doped ZnO).

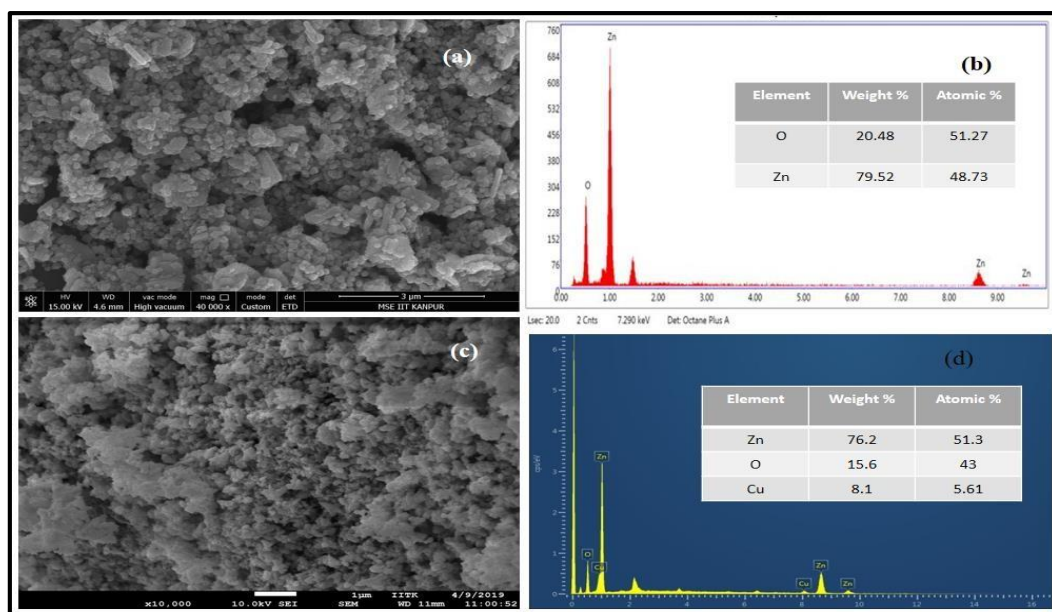


**Figure 7.3: (a and c) FESEM images, (b and d) EDX spectrum of ZNPs and Cu doped ZNPs respectively.**

#### 7.3.1.4 FTIR analysis

The FTIR spectra of the samples were recorded using Perkin Elmer Spectrum Two FT-IR spectrometer. The samples were used either in solid form or thin film. “Attenuated total reflectance” (ATR) mode was used for recording the data. The PIKE MIRacle single reflection horizontal ATR accessory equipped with a ZnSe ATR crystal was used for the analysis. FTIR spectrum was observed to investigate the chemical composition of the samples synthesized as ZNPs and Cu doped ZNPs and for the study of functional groups present in the plant extract used as stabilizer. The phytochemicals, which act as capping agent for synthesis and stabilization of ZNPs are revealed by FT-IR spectroscopic technique. FT-IR plots of pure and Cu-ZNPs are shown in **figure 7.4**. The spectrum range was from  $500\text{ cm}^{-1}$  to  $4000\text{ cm}^{-1}$ . Different peaks were observed at different wave number values. Strong bands were obtained at  $3368$ ,  $2934$ ,  $1569$ ,  $1406\text{ cm}^{-1}$  corresponding to OH stretching vibration of phenol group, CH stretching, C=C stretching of alkyl ether group and N=O bond of secondary amine [Roshmi et al., 2016; Pulipati et al., 2013]. The origin of band at  $543\text{ cm}^{-1}$  is due to metal oxygen bond, which confirms the synthesis of ZnO [Prasad et al., 2018; Kumar et al., 2013]. The phytochemicals present in plant

extract such as alcohols, phenols, amines and others interact with the surface of zinc and provide stability to the synthesized nanoparticles [Kulkarni et al., 2017].

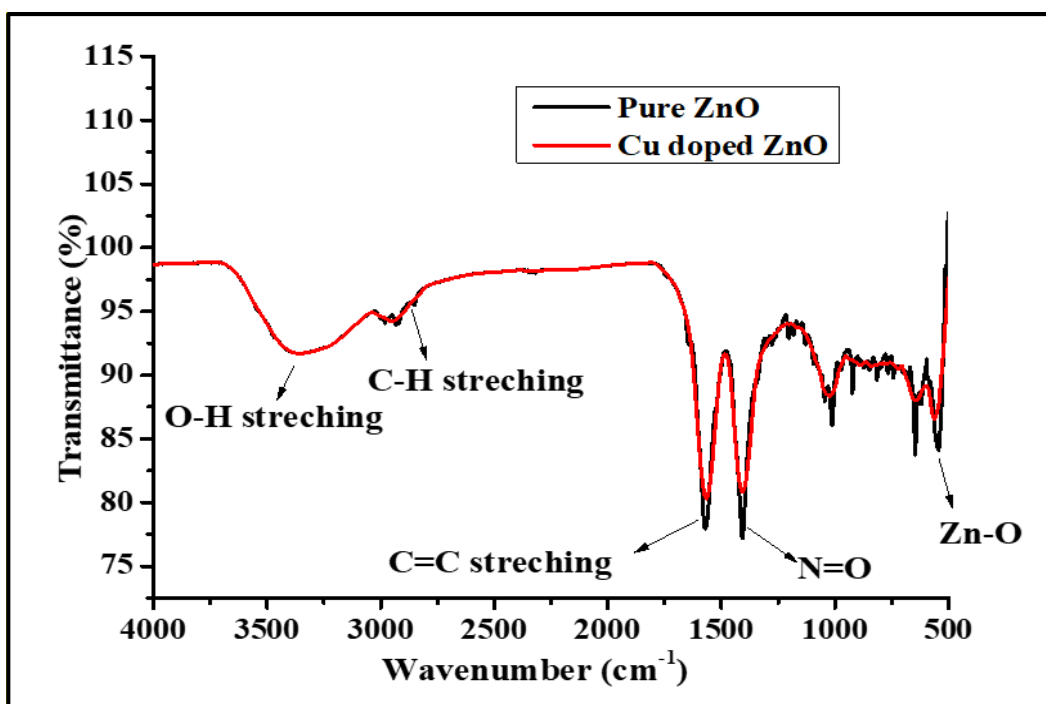


Figure 7.4: FTIR spectrum of pure ZNPs and Cu doped ZNPs.

#### 7.3.1.5 TGA analysis

TGA analytical technique was used to detect the response of particles against rise in temperature. The basic principle of the technique is to raise the temperature of the sample below its melting point. A reduction in the weight of the sample is observed due to evaporation of water and biochemicals present in the plant extract [Suman et al., 2013]. TGA analysis (TGA, Linseis PT 1000) of the synthesized materials was carried out in air by maintaining the heating rate of 10°C per min. from room temperature to 600°C.

For ascertaining heat stability and temperature response of the synthesized NPs, TGA technique was used. Here in TGA study (shown in **figure 7.5**), TGA data show the reduction of mass over a range of temperature. In both the samples (Pure and doped ZNPs), reduction of mass was first observed below a temperature of 100°C. The reduction

of mass occurred due to the evaporation of moisture present on the outer surface of the materials. The second degradation occurred at around 250°C temperature, which was due to the water present internally as well as biomolecules, which acts as stabilizer. The last peak was obtained at 420°C temperature, which might be due to degradation of various other biomolecules as depicted in FTIR spectrum. Hence, from the thermal analysis, it may be concluded that all the prepared samples are thermally stable at higher temperature and also that Cu doping increases the thermal stability of ZnO and hence, the weight loss of pure ZNPs is more compared to that for Cu-ZNPs samples [Chithra et al., 2016].

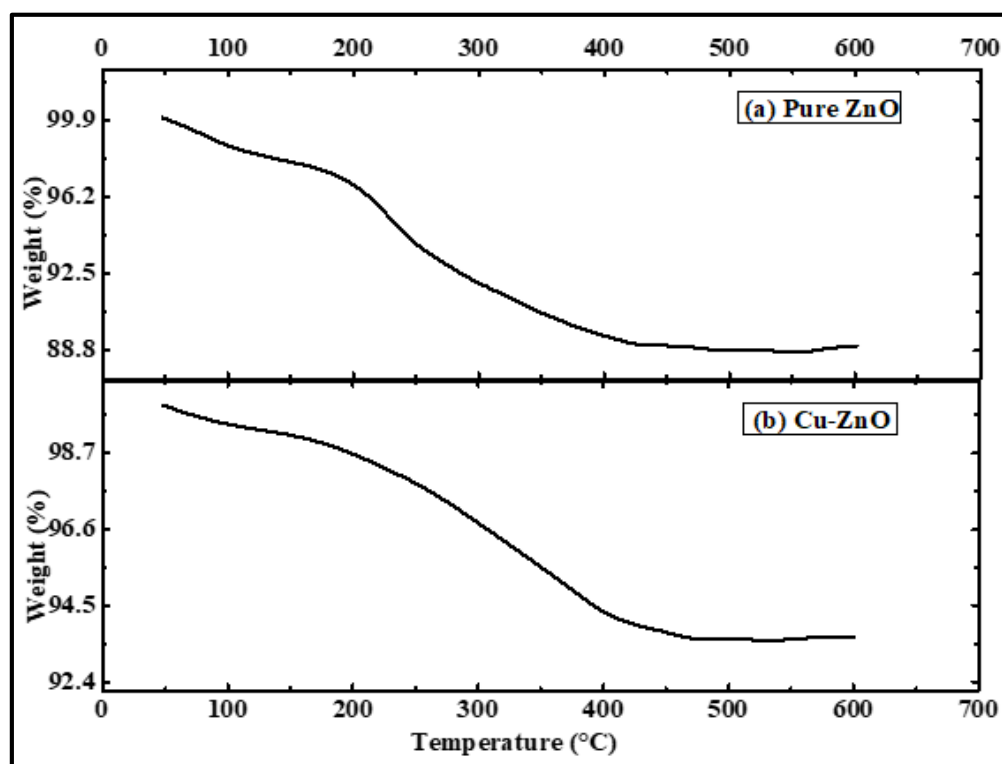


Figure 7.5: TGA curves of (a) pure ZNPs and (b) Cu doped ZNPs.

### 7.3.1.6 TEM analysis

Transmission electron microscopy was carried out using Jeol JEM 1400 (Jeol Ltd., Tokyo, Japan). Sample for carrying out electron microscopy observations was prepared by dispersing the NPs powder in distilled water using ultra sonication. The solution was then

drop casted on a carbon film supported on a Cu grid and was then evaporated under ambience conditions.

**Figure 7.6 (a and b)** shows the TEM micrograph of synthesized ZNPs and Cu-ZNPs respectively, which reveals that particles are very much aggregated and particles of size as small as 10 nm are visible.

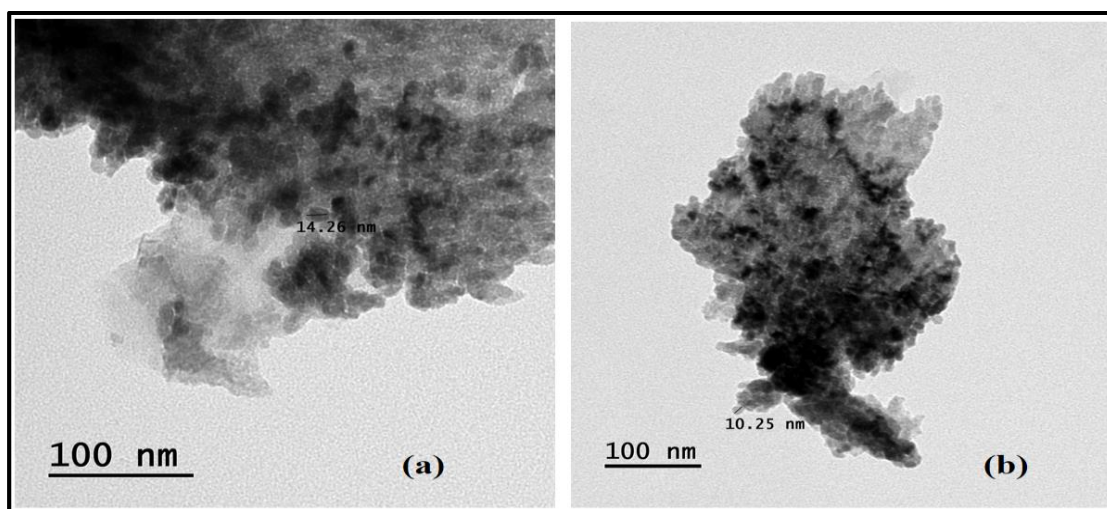


**Figure 7.6: TEM images of (a) pure ZNPs and (b) Cu doped ZNPs.**

### 7.3.2 Optimization of adsorption parameters

All the optimization study was done using 100 mL of 20 mg/L of dye and 0.1 g of adsorbent was added to synthesized nanoparticles. The adsorption process was allowed to run for 180 min.

### 7.3.3 Optimization of pH

The percent removal of CR dye by pure ZNPs and Cu-ZNPs was studied by varying pH in the range from 2 to 10 (**figure 7.7 a**). It was observed that removal efficiency of CR dye by both ZNPs and Cu-ZNPs was in the range of 90-93% for entire pH range (2–10) using both the adsorbents synthesized. Thus, from the abovementioned result, it can be concluded that both the NPs work efficiently in the wide pH range for the removal of CR

dye. It has also been observed that on addition of any of the synthesized nanoparticles, the pH of dye solution automatically comes in the 6.5–7.5 pH range.

#### **7.3.4 Optimization of contact time**

Contact time was optimized by varying the time period from 0 to 180 min. at adsorbent dose 0.10 g for 100 mL CR dye (20 mg/L) as shown in **figure 7.7(b)**. It was observed that with increase in the time of contact the percent removal of CR dye by ZNPs increased. The reason for increase in adsorption with time is, more time allows sufficient contact period for interaction of dye with the adsorbent. The time taken for the removal of dye using ZNPs was observed to be 180 min., while for the process in which Cu-ZNPs were used as adsorbent, approximately 95% of dye was removed in 120 min. time. The result shows that both the nanoparticles act as good adsorbent and remove more than 90% of the dye but the time taken by Cu-ZNPs was comparatively less than that of ZNPs.

#### **7.3.5 Optimization of adsorbent dose**

The efficiency of pure ZNPs and Cu-ZNPs was examined by determining the percent removal of CR dye by varying the concentration of adsorbent in the range of 0.02 to 0.1g for 100 mL of 20 mg/L of CR dye solution. **Figure 7.7 (c)** exhibits the percent removal of CR dye on increasing adsorbent dose. On increasing the concentration of ZNPs, there is an increase in the percentage of removal of CR dye within an optimized time.

#### **7.3.6 Optimization of congo red dye concentration**

Maximum adsorption capacity of CR dye was obtained by optimizing the concentration of dye. The concentration of CR dye was varied in the range of 20–100 mg/L at optimized adsorbent dose and time. The result is depicted in **figure 7.7 (d)**. It revealed that percent removal of CR dye decreases with increase in dye concentration. The active sites on adsorbents get saturated after adsorption of certain concentration of dye and therefore, further adsorption does not take place.

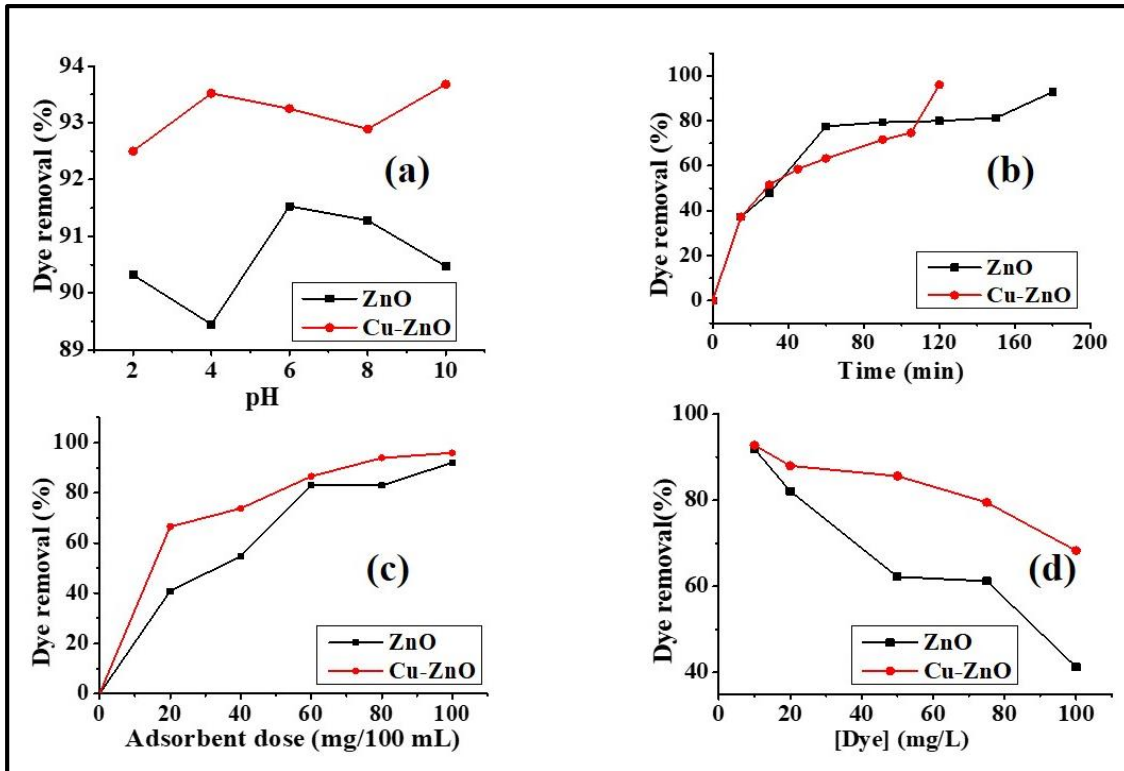


**Figure 7.7: Effect of (a) pH, (b) time, (c) adsorbent dose and (d) dye concentration on percent removal of congo red.**

### 7.3.7 Kinetic study

The mechanism of adsorption of CR dye on the surface of synthesized nanoparticles can be explained by various kinetic models such as pseudo first order and pseudo second order.

Pseudo first order can be represented by the following **equation 7.3**:

$$\log(q_e - q_t) = \log q_e - \left(\frac{k_1}{2.303}\right)t \quad \dots\dots\dots (7.3)$$

Where,  $q_t$  (mg/g) is the adsorption capacity at time  $t$  and  $k_1$  ( $\text{min}^{-1}$ ), kinetic rate constant.

The value of constant  $k_1$ , and  $q_e$  was calculated from linear plot between  $\log(q_e - q_t)$  versus  $t$  (**figure 7.8 a and b**). The dye adsorption process using both the synthesized NPs (ZNPs and Cu- ZNPs) did not follow pseudo first order kinetics as the calculated value of  $q_e$  is not in agreement with experimental value and value of  $R^2$  is smaller as compared to second order kinetics (given in **table 7.1**).

A linear form of pseudo second order kinetics is represented in the **equation 7.4** below.

$$\frac{t}{q_t} = \frac{1}{k_2 q_e^2} + \frac{t}{q_e} \quad \dots\dots\dots (7.4)$$

Where,  $k_2$  ( $\text{g mg}^{-1}\text{min.}^{-1}$ ) is the rate constant of the pseudo-second order. The value of  $k_2$  and  $q_e$  was determined from the graph plotted between  $t/q_t$  versus  $t$  (**figure 7.8 c and d**). The pseudo second order model is in good agreement with adsorption process as the calculated value of  $q_e$  is in agreement with experimental value and value of  $R^2$  is also very high.

**Table 7.1: Kinetic models parameter study of congo red dye adsorption on undoped and Cu doped ZNPs**

| Kinetic models      | Parameter                               | Value of parameters |               |
|---------------------|---|---------------------|---------------|
|                     |   | Pure ZNPs           | Cu doped ZNPs |
| Pseudo first order  | $k_1$ ( $\text{min.}^{-1}$ )            | 0.01                | 0.03          |
|                     | $q_e$ (cal.)                            | 0.25                | 0.30          |
|                     | $R^2$                                   | 0.797               | 0.962         |
| Pseudo second order | $k_2$ ( $\text{g mg}^{-1}\text{min.}$ ) | 0.08                | 0.23          |
|                     | $q_e$ (cal.)                            | 0.40                | 0.37          |
|                     | $R^2$                                   | 0.981               | 0.975         |

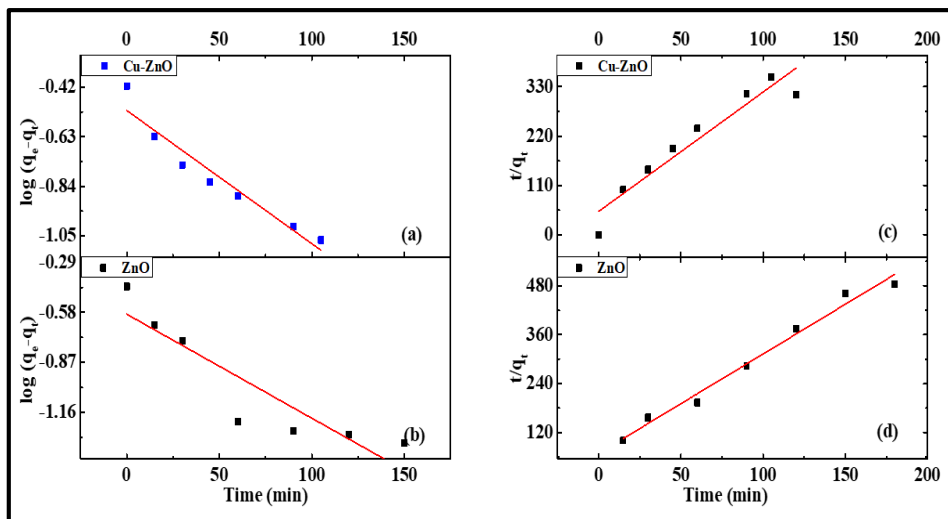


**Figure 7.8: (a and b) Pseudo first order and (c and d) Pseudo second order kinetics for adsorption of congo red dye over synthesized nanoparticles.**

### 7.3.8 Isotherm study

The interaction between the liquid and solid phase of the system is justified by the isotherm study. The adsorption equilibrium of CR dye onto ZNPs and Cu-ZNPs was

studied by carrying out various experiments and the data obtained was explained by mainly three adsorption isotherm models such as Langmuir, Freundlich and Temkin model. Langmuir adsorption model assumes monolayer distribution of dye considering the surface of adsorbent to be homogenous. Langmuir model can be represented in a linear form and is given by **equation 7.5**.

$$\frac{C_e}{q_e} = \frac{1}{q_{\max}b} + \frac{C_e}{q_{\max}} \quad \dots\dots\dots (7.5)$$

Where,  $q_{\max}$  (mg/g) is the maximum monolayer adsorption capacity and  $b$  (L/mg), the Langmuir constant. The curve was plotted between  $C_e$  versus  $q_e$  (**figure 7.9 a**), which gives the value of adsorption model parameters and correlation coefficient ( $R^2$ ) given in **table 7.2**. The feasibility of Langmuir adsorption isotherm was determined by the value of separation factor  $R_L$  [**Sivaraj and Namasivayam, 2001**], which is given by **equation 7.6** shown below:

$$R_L = \frac{1}{1+bC_0} \quad \dots\dots\dots (7.6)$$

In the above equation,  $C_0$  represents the initial concentration of CR dye.

$R_L < 1$  indicates the adsorption to be feasible while  $R_L > 1$  signifies non-feasible reaction and  $R_L = 1$  represents linear adsorption process.

The value of  $R_L$ , in case of CR dye being adsorbed on ZNPs, was found to be 0.129, which exhibit the feasibility of adsorption. In case of Cu-ZNPs, on comparing the data to Langmuir isotherm mode, the value of separation factor was found to be 1, which exhibits linear adsorption.

Freundlich isotherm model is based on the assumption that adsorption of the molecules takes place in multilayer over a heterogeneous surface of adsorbate. The linear form of this model is represented in **equation 7.7**.

$$\log q_e = \log K_f + \frac{1}{n} \log C_e \quad \dots\dots\dots (7.7)$$

Where,  $K_f$  ( $\text{mg g}^{-1}$ ) is Freundlich constant, which defines the adsorption capacity and  $n$ , the heterogeneity factor depicting the intensity of adsorption. The linear plot between  $\log q_e$  versus  $\log C_e$  determines the value of  $K_f$  and  $n$  (**figure 7.9 b**). The value of  $n$  represents whether the reaction is favourable or not. The value of  $n$  in the range of 1 to 10 represents favorable adsorption [**Freundlich, 2013**]. The adsorption of dye on both ZNPs and Cu-ZNPs is a favorable adsorption.

Temkin isotherm model follows the assumption that (a) adsorption of the molecules occurs in monolayer over heterogeneous active sites on the adsorbent surface or (b) binding energy is uniformly distributed due to adsorbent- adsorbate interaction, the heat of adsorption of adsorbed dye molecule decreases linearly with coverage. A linear form of model is expressed by **equation 7.8**.

$$q_e = B \ln K_T + B \ln C_e \quad \dots\dots\dots (7.8)$$

Where,  $B = RT/b$ ,  $b$  is the Temkin constant related to heat of adsorption ( $\text{J mol}^{-1}$ ),  $R$ , universal gas constant ( $8.314 \text{ J mol}^{-1}\text{K}^{-1}$ ) and  $K_T$ , equilibrium binding constant ( $\text{L/g}$ ). The linear plot between  $q_e$  vs  $\ln C_e$  gives the value of  $K_T$  and  $B$  (**figure 7.9 c**).

By comparing the abovementioned isotherm models, it was found that the data obtained in case of ZNPs fitted well to Freundlich and Temkin models. The value of correlation coefficient was found to be high for these two models as compared to Langmuir model having lower value of correlation coefficient.

While in case of Cu-ZNPs, the data does not fit to Temkin isotherm as the value of correlation coefficient is very low but fits well to Langmuir and Freundlich isotherm.

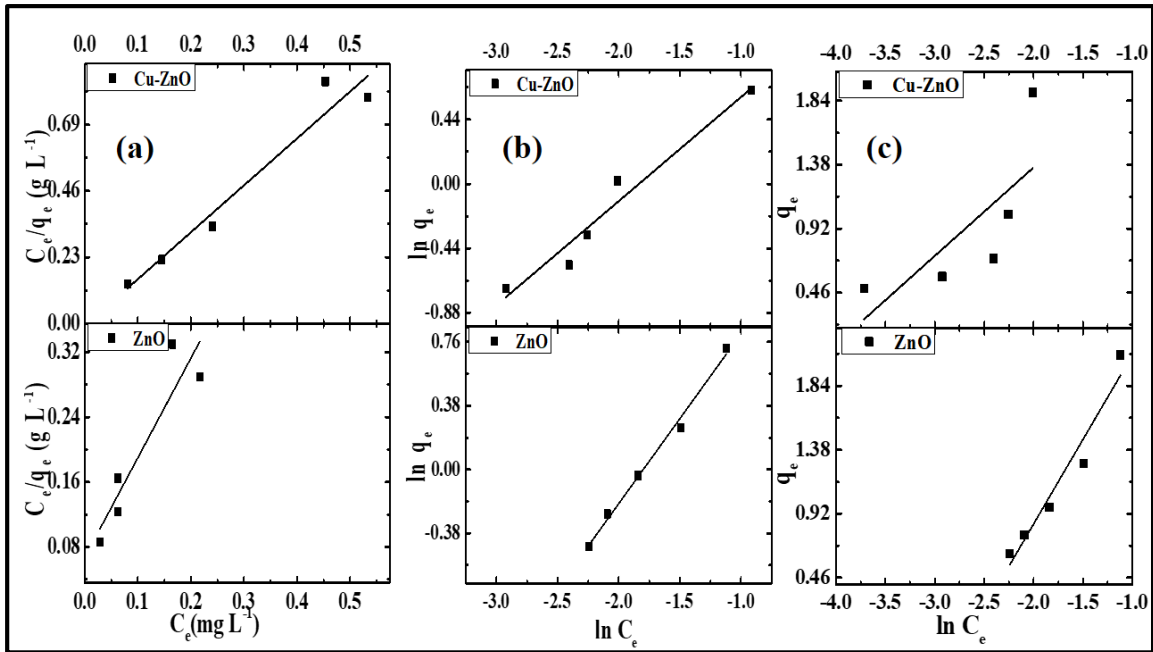


Figure 7.9: (a) Langmuir, (b) Freundlich and (c) Temkin isotherm for adsorption of congo red over ZNPs and Cu doped ZNPs.

Table 7.2: Various adsorptions isothermal models for congo red dye adsorption interpreted by correlation coefficients and adsorption parameters

| Isotherm model | Parameters                                 | Values   |               |
|----------------|--|----------|---------------|
|                |  | PureZNPs | Cu doped ZNPs |
| Langmuir       | $q_{max}$ (mg/g)                           | 0.81     | 0.61          |
|                | $b$ (L/mg)                                 | 18.31    | 0             |
|                | $R^2$                                      | 0.804    | 0.936         |
|                | $R_L$                                      | 0.12     | 1.00          |
|                | $n$  | 1.00     | 1.40          |
| Freundlich     | $K_f \{ (mg\ g^{-1})(L\ mg^{-1})^{1/n} \}$ | 6.19     | 3.68          |
|                | $R^2$                                      | 0.989    | 0.943         |
|                | $B$  | 1.21     | 0.63          |
| Temkin         | $K_T (L\ g^{-1})$                          | 14.81    | 61.65         |
|                | $R^2$                                      | 0.926    | 0.420         |

## 7.4 Conclusions

Both ZnO nanoparticles and Cu doped ZnO nanoparticles were successfully synthesized using *Moringa oleifera* leaf extract and their identity was established using various analytical techniques such as UV- Vis, XRD, FESEM, TEM, etc. All the techniques used in the characterization revealed that Cu was successfully doped into the lattice of ZnO.

Kinetic study of both the nanoparticles showed that the adsorption process on congo red dye using both the undoped and doped ZnO nanoparticles follows pseudo second order kinetics. On calculating the percent removal of dye using both the nanoparticles within an optimized time, it was found that both the nanoparticles act as good and potential adsorbent. The time taken by Cu doped ZnO nanoparticles to achieve maximum adsorption was comparatively less than that of ZnO nanoparticles. The adsorption data obtained for ZnO nanoparticles fitted well to both Freundlich and Temkin model, while for Cu doped ZnO nanoparticles, the data fitted well with Langmuir and Freundlich model.

## References

- Agarwal, H., Menon, S., Kumar, S.V., Kumar, S.R., Sheba, R.D., Lakshmi, T., and Nallaswamy, V.D. (2019). Phyto-assisted synthesis of zinc oxide nanoparticles using *Cassia alata* and its antibacterial activity against *Escherichia coli*. *Biochemistry and Biophysics Reports*, 17, 208–211.
- Ahmed, S., Annu, Chaudhry, S.A., and Ikram, S.A. (2017). A review on biogenic synthesis of ZnO nanoparticles using plant extracts and microbes: A prospect towards green chemistry. *J. Photochem. and Photobio. B: Biology*, 166, 272–284.
- Ba-Abbad, M.M., Kadhum, A.A.H., Mohamad, A.B., Takriff, M.S., and Sopian, K. (2013). The effect of process parameters on the size of ZnO nanoparticles synthesized via the sol-gel technique. *Journal of Alloys and Compounds*, 550, 63–70.
- Bansal, V., Poddar, P., Ahmad, A., and Sastry, M. (2006). Room-temperature biosynthesis of ferroelectric Barium titanate nanoparticles. *J. American Chemical Society*, 10, 11958–11963.
- Chamjangali, M. A., Bagherian, G., Bahramian, B., and Fahimi Rad, B. (2015). Synthesis and application of multiple rods gold–zinc oxide nanostructures in the photocatalytic degradation of methyl orange. *International Journal of Environmental Science and Technology*, 12, 151–160.
- Chandra, H., Patel, D., Kumari, P., Jangwan J.S. and Yadav, S. (2019). Phyto- mediated synthesis of zinc oxide nanoparticles of *Berberis aristata*: Characterization, antioxidant activity and antibacterial activity with special reference to urinary tract pathogens. *Materials Science and Engineering C*, 102, 212-220.
- Chen, M.W., Ding, Wang, J., and Diao, G. (2013). Removal of azo dyes from water by combined techniques of adsorption, desorption, and electrolysis based on a supramolecular sorbent. *Industrial and Engineering Chemistry Research*, 52, 2403–2411.
- Chidambaram, S., Pari, B., Kasi, N., and Muthusamy, S. (2016). ZnO/Ag heterostructures embedded in Fe<sub>3</sub>O<sub>4</sub> nanoparticles for magnetically recoverable photocatalysis. *Journal of Alloys and Compounds*, 665, 404–410.
- Chithra, M.J., Pushpanathan, K., and Nadu, T. (2016). Thermal, structural and optical investigation of Cu-doped ZnO nanoparticles. *Modern Physics Letters B*, 30, 1–13.
- Freundlich, H. M. F. (2013). Over the Adsorption in Solution. *The Journal of Physical Chemistry*, 57.
- Gupta, V.K., Kumar, R., Nayak, A., Saleh, T. A., and Barakart, M. A. (2013). Adsorptive removal of dyes from aqueous solution onto carbon nanotubes: a review, *Advances in Colloid and Interface Science*, 193, 24-34.
- Huang, N., Shu, J., Wang, Z., Chen, M., Ren, C., and Zhang, W. (2015). One-step pyrolytic synthesis of ZnO nanorods with enhanced photocatalytic activity and high

photostability under visible light and UV light irradiation. *Journal of Alloys and Compounds*, 648, 919–929.

Kharissova, O.V., Dias, H.V.R., and Kharisov, B.I. (2013). The greener synthesis of nanoparticles. *Cell*, 31.

Khalafi, T., Buazar, F., and Ghanemi, K. (2019). Phycosynthesis and enhanced photocatalytic activity of zinc oxide nanoparticles toward organosulfur pollutants. *Scientific Reports*, 9, 1–10.

Kulkarni, S., Jadhav, M., Raikar, P., Barretto, D.A., Vootla, S.K., and Raikar, U.S. (2017). Green synthesized multifunctional Ag@Fe<sub>2</sub>O<sub>3</sub> nanocomposites for effective antibacterial, antifungal and anticancer properties. *New J. Chem.*, 41, 9513–9520.

Kumar, R., Kumar, G., and Umar, A. (2013). ZnO nano-mushrooms for photocatalytic degradation of methyl orange. *Materials Letters*, 97, 100–103.

Lachheb, H., Puzenata, E., Houas, A., Ksibib, M., Elalouib, E., and Guillarda, C. (2002). Photocatalytic degradation of various types of dyes (Alizarin S) in water by UV-irradiated titania. *Applied Catalysis*, 39, 75–90.

Li, Z., Chang, P., Jiang, W., Jean, J., and Hong H. (2011). Mechanism of methylene blue removal from water by swelling clays. *Chemical Engineering Journal*, 168, 1193–1200.

Malik, P.K. (2004). Dye removal from wastewater using activated carbon developed from saw dust: adsorption equilibrium and kinetics, *Journal of hazardous material*, 113, 81–88.

Prasad, A.R., Garvasis, J., Oruvil, S.K., and Joseph, A. (2018). Bio-inspired green synthesis of zinc oxide nanoparticles using *Abelmoschus esculentus* mucilage and selective degradation of cationic dye pollutants. *J. Physical and Chemistry of Solids*, 127, 265–274.

Pulipati, S., Parveen, S.H., Babu, R.K., Vagdevi, G., and Babu, S. (2013). Pharmacognostical and physicochemical standardization of leaves of *Spathodea campanulata* P. Beauv. *J. Pharmacognosy and Phytochemistry*, 2, 189–19.

Raveendran, P., Fu, J., Wallen, S.L., Hill, C., and Carolina, N. (2003). Completely 'Green' synthesis and stabilization of metal nanoparticles. *J American Chemical Society*, 139, 13940–13941.

Rekha, P., Muhammad, R., and Mohanty, P. (2015). Sonochemical synthesis of cyclophosphazene bridged mesoporous organosilicas and their application in methyl orange, congo red and Cr (VI) removal. *RSC Advances*, 5, 67690–67699.

Rodríguez, A., García, J., Ovejero, G., and Mestanza, M. (2009). Adsorption of anionic and cationic dyes on activated carbon from aqueous solutions: Equilibrium and kinetics, *Journal of Hazardous Materials*, 172, 1311–1320.

Roshmi, T., Jishma, P., and Radhakrishnan, E.K. (2016). Photocatalytic and

antibacterial effects of silver nanoparticles fabricated by *Bacillus subtilis* SJ 15. *Inorganic and Nanometal Chemistry*, 3174, 901–908.

Saini, R.K., Sivanesan, I., and Keum, Y.S. (2016). Phytochemicals of *Moringa oleifera*: a review of their nutritional, therapeutic and industrial significance. *3 Biotech*, 6, 203.

Sharma, Y.C., Sinha, A.S.K., and Upadhyay, S.N. (2010). Characterization and adsorption studies of *Cocos nucifera* L. activated carbon for the removal of methylene blue from aqueous solutions, *J. Chem. Eng. Data*, 55, 2662–2667.

Singh, B.N., Kumar, A., Rawat, Khan, W., Naqvi, A.H., and Singh, B.R. (2014). Biosynthesis of stable antioxidant ZnO nanoparticles by *Pseudomonas aeruginosa* rhamnolipids. *Plos one*, 9.

Singh, B.R., Singh, B.N., Khan, W., Singh, H.B., and Naqvi, A.H. (2012). Biomaterials ROS-mediated apoptotic cell death in prostate cancer LNCaP cells induced by biosurfactant stabilized CdS quantum dots. *Biomaterials*, 33, 5753–5767.

Sivaraj, K.K.R., and Namasivayam, C. (2001). Orange peel as an adsorbent in the removal of acid violet 17 (acid dye) from aqueous solutions. *Waste Management*, 21, 105–110.

Suman, T.Y., Rajasree, S.R.R., Kanchana, A., and Elizabeth, S.B. (2013). Biosynthesis, characterization and cytotoxic effect of plant mediated silver nanoparticles using *Morinda citrifolia* root extract. *Colloids and Surfaces B: Bio interfaces*, 106, 74–78.

Tanwar, R., Kumar, S., and Kumar, U. (2017). Photocatalytic activity of PANI / Fe<sup>0</sup> doped BiOCl under visible light- degradation of Congo red dye. *Journal of Photochemistry and Photobiology, A: Chemistry*, 333, 105–116.

Tian, F., Wu, Z., Chen, Q., Yan, Y., Cravotto, G., and Wu, Z. (2015). Microwave-induced crystallization of AC/TiO<sub>2</sub> for improving the performance of rhodamine B dye degradation. *Applied Surface Science*, 351, 104–112.

Tripathi, N., Ahmad, R., Song, J. E., Ah Ko, H., Hahn, Y.B., and Khang, G. (2014). Photocatalytic degradation of methyl orange dye by ZnO nanoneedle under UV irradiation, *Materials Letters*, 136, 171–174.

Yagub, M.T., Sen, T.K., Afroze, S., and Ang, H.M. (2014). Dye and its removal from aqueous solution by adsorption: A review. *Advances in Colloid and Interface Science*, 209, 172–184.

Zare, K., Sadegh, H., Ghoshekandi, R.S., Maazinejad, B., Ali, V., Tyagi, I., Agarwal, S., and Gupta, V.K. (2015). Enhanced removal of toxic Congo red dye using multi walled carbon nanotubes: Kinetic, equilibrium studies and its comparison with other adsorbents. *Journal of Molecular Liquids*, 212, 266–271.

## Chapter 8: Conclusions and future prospective

---

A simple, convenient, environment friendly and less energy consuming method was developed to prepare metal/metal oxide nanoparticles using extract obtained from different plants. The nano materials were then used for fabrication of polymer nanocomposites. Different metal/metal oxide nanoparticles such as Ag, ZnO, MnO<sub>2</sub> and CuO were synthesized using extract derived from *Citrus sinensis*, *Moringa oleifera*, *Ficus retusa*. These nanoparticles were characterized using various analytical techniques to study their morphology, structure, size and several other properties. Out of the abovementioned nanoparticles, CuO and  $\alpha$ -MnO<sub>2</sub> nanoparticles were used to develop polymer nanocomposites. These laboratory synthesized materials (nanoparticles and nanocomposites) were applied for wastewater treatment, antimicrobial activities evaluation and for the development of drilling fluids for petroleum industry's drilling operation. The organic dyes released in water bodies were successfully removed using these materials through different processes following varying mechanisms. MnO<sub>2</sub> nanoparticles removed methyl orange and methyl red dyes from their aqueous solutions and these nanoparticles were also used to enhance the properties of polymer membrane. The synthesized polymer nanocomposite was used as photocatalyst for removing eosin yellow and methylene blue dyes from their aqueous solutions. Other than wastewater treatment, these MnO<sub>2</sub> nanoparticles were also used for improving the rheological properties of water-based drilling fluids for drilling operations in petroleum industry.

The incorporation of laboratory synthesized CuO nanoparticles into the chitosan beads enhanced its adsorptive properties for removal of eriochrome black T and methylene blue dyes present in wastewater.

The Ag nanoparticles were capable of removing congo red dye through photocatalytic degradation. These silver nanoparticles also possessed antimicrobial properties and therefore, can be used for medicinal purposes.

Finally, ZnO nanoparticles were doped with Cu and these Cu doped nanoparticles removed congo red dye from its aqueous solution by the process of adsorption.

In future, these nanoparticles can also be applied to remove heavy metal ions such as Hg, Pb, Cd, etc. present in wastewater. Moreover, organic compounds such as p-nitrophenol, polycyclic aromatic hydrocarbons, and pesticides, aliphatic and heterocyclic compounds can also be targeted for degradation into simpler forms using these nanomaterials.





## List of Publications

---

**V. Srivastava**, S. Pandey, A. Mishra, A. K. Choubey, Green synthesis of biogenic silver particles, process parameter optimization and application as photocatalyst in dye degradation, SN Applied Sciences (2019) 1 1722. <https://doi.org/10.1007/s42452-019-1762-z>.

**V. Srivastava**, A. K. Choubey, Synthesis of nanostructured silver particles using *Citrus limetta* peel extract for catalytic degradation of azo dyes through electron relay effect. Adv. Nat. Sci.: Nanosci. Nanotechnol, (2019) 10 045015. <https://doi.org/10.1088/2043-6254/ab52f3>.

**V. Srivastava**, A. K. Choubey, Kinetic and isothermal study of effect of transition metal doping on adsorption of zinc oxide nanoparticles synthesized via green route using *Moringa oleifera* leaf extract. Materials Research Express (2020) 6 12 1250i7. <https://doi.org/10.1088/2053-1591/ab7158>.

**V. Srivastava**, A. K. Choubey, Study of adsorption of anionic dyes over biofabricated crystalline  $\alpha$ -MnO<sub>2</sub> nanoparticles. Environmental Science and Pollution research. Environ Sci Pollut Res (2021) 28 15504–15518. <https://doi.org/10.1007/s11356-020-11622-1>.

**V. Srivastava**, A.K. Choubey. Investigation on enhancement of adsorptive property of pure chitosan beads by immobilization of laboratory synthesized CuO nanoparticles. (Under review in Journal of Molecular Structure)

**V. Srivastava**, M. Beg, A.K. Choubey, S. Sharma. Application of Manganese Oxide nanoparticles synthesized via green route for improved performance of water-based drilling fluids (Under review).

**V. Srivastava**, A.K. Choubey. Novel PVA/Chitosan composite membrane modified using biofabricated  $\alpha$ -MnO<sub>2</sub> nanoparticles for photo catalytic degradation of cationic dyes (Under review).

Reena, Abhinav, **V. Srivastava**, V. Mahto, A.K. Choubey. Experimental investigation of the gelation performance and sandpack study of laboratory synthesized ZnO reinforced PVP/RF gels for water shut-off treatment (Under Review).

### **Book Chapter**

A. K. Choubey, **V. Srivastava**, Herbal Materials as Thermal Energy Storage Materials, Latent Heat-Based Thermal Energy Storage Systems, Materials, Applications and the Energy Market, Apple Academic Press, USA, 2019 (ISBN: 9781771888585).